ADVANCED STEEL CONSTRUCTION

An International Journal

Volume 22 Number 2

April 2026

CONTENTS

Technical Papers

Website: *http://www.hkisc.org*
ISSN 1816-112X
Science Citation Index Expanded, Materials Science Citation Index and ISI Alerting
Cover: Guangzhou Baiyun International Airport T3, China. Photo@ Li Kai-Jian
e-copy of IJASC is free to download at "www.ascjournal.com" in internet and mobile apps.

ADVANCED STEEL CONSTRUCTION

VOL.22, NO.2 (2026)

ADVANCED STEEL CONSTRUCTION

an International Journal

ISSN 1816-112X

Volume 22 Number 2 *April 2026*

ISSN 1816-112X

Science Citation Index Expanded, Materials Science Citation Index and ISI Alerting

Advanced Steel Construction
an international journal

Cover: Guangzhou Baiyun International Airport T3, China. Photo@ Li Kai-Jian
e-copy of IJASC is free to download at "www.ascjournal.com" in internet and mobile apps.

General Information
Advanced Steel Construction, an international journal

Aims and scope

The International Journal of Advanced Steel Construction provides a platform for the publication and rapid dissemination of original and up-to-date research and technological developments in steel construction, design and analysis. Scope of research papers published in this journal includes but is not limited to theoretical and experimental research on elements, assemblages, systems, material, design philosophy and codification, standards, fabrication, projects of innovative nature and computer techniques. The journal is specifically tailored to channel the exchange of technological know-how between researchers and practitioners. Contributions from all aspects related to the recent developments of advanced steel construction are welcome.

Subscription inquiries and change of address. Address all subscription inquiries and correspondence to Member Records, IJASC. Notify an address change as soon as possible. All communications should include both old and new addresses with zip codes and be accompanied by a mailing label from a recent issue. Allow six weeks for all changes to become effective.

The Hong Kong Institute of Steel Construction
HKISC
c/o Prof. SL Chan,
Unit 209B, Photonics Centre, No. 2 Science Park East Avenue,
Hong Kong Science Park, Shatin, N.T., Hong Kong, China.
Tel: 852- 3595 6150 Fax: 852- 3619 7238
Email: ceslchan@connect.polyu.hk Website: *http://www.hkisc.org/*
ISSN 1816-112X
Science Citation Index Expanded, Materials Science Citation Index and ISI Alerting

ISSN 1816-112X

Science Citation Index Expanded, Materials Science Citation Index and ISI Alerting

Advanced Steel Construction
an international journal

VOLUME 22 NUMBER 2 April 2026

Technical Papers

Advanced Steel Construction – Vol. 22 No. 2 (2026) 130–142
DOI:10.18057/IJASC.2026.22.2.1

EXPERIMENTAL AND NUMERICAL ANALYSIS ON THE STRUCTURAL PROPERTIES OF CONCRETE-FILLED RECTANGULAR THIN-WALLED HIGH-STRENGTH STAINLESS-STEEL TUBULAR COLUMNS

Jun Zhao [1], Yang Peng [2], Wei-Chao Zhang [3], Shen-Lan Li [4] and Jun Dong [2,*]

[1] *School of Civil Engineering and Architecture, Changzhou Institute of Technology, Changzhou 213032, China*
[2] *College of Civil Engineering, Nanjing Tech University, Nanjing 211816, China*
[3] *Sinopec Sales Co., Ltd. Lianyungang Petroleum Branch, Lianyungang 222500, China*
[4] *Rural Economic Service Center of Banpu Town, Lianyungang 222241, China*
** (Corresponding author: E-mail: dongjun@njtech.edu.cn)*

ABSTRACT

Exploring high-performance structures suitable for high corrosion marine environment is one of the research priorities in engineering. In order to meet the requirements of the marine environment and reduce costs, thin-walled stainless-steel was used to design a high-performance component. Two stainless-steel lipped channels were welded to form a new stainless-steel tubular column, with concrete filled inside, a high-performance concrete-filled stainless-steel tubular column was designed. Axial compression short column test, finite element analysis of axial compression short columns, axial compression and compression-bending intermediate-length columns were carried in the paper. Six groups of axial compression tests were conducted, results shown that both rectangular stiffening ribs and V-shaped stiffening ribs could enhance the restraint capacity of the external stainless-steel tube. The ultimate capacity of the axial compression short column with bidirectional ribs was 15.04% higher than that of the short column with unidirectional ribs. The axial compression mechanization of short columns, axial compression and compression-bending mechanization of median long column were analyzed by FEM. For axial compression short columns, the main parameters were the size of the V-shaped stiffeners and the compressive strength of the concrete. When the width-to-thickness ratio of the V-shaped stiffener was 8.33 and the angle was 90°, the cross-sectional performance was the best. When the concrete was C80, the peak load was increased by 17.20% compared with C60. For axial compression and compression-bending intermediate-length columns, the main parameters were the slenderness ratio and eccentricity. When the slenderness ratio was in the range of 15.17-91.02, the larger the slenderness ratio, the faster the stiffness degradation. When the eccentricity was in the range of 0.56-3.75, the deformation capacity of intermediate-length columns was better, and the ductility was also better. The recommendation of compression-bending capacity calculation formula was proposed, with high accuracy.

ARTICLE HISTORY

Received: 20 February 2025
Revised: 21 June 2025
Accepted: 26 June 2025

KEYWORDS

High-strength stainless-steel;
Concrete-filled rectangular tubular column;
Axial compression short column test;
Compression-bending;
Finite element analysis

1. Introduction

Seawater and ocean currents could easily cause corrosion and impact, restricting the development of marine engineering [1-3]. High-strength stainless-steel had good mechanical properties and corrosion resistance, which could meet the highly corrosive environmental conditions and reduce the maintenance cost [4-5]. Welding the lipped channels and assembled into a rectangular section, with concrete filled inside, a better performance component with bidirectional ribs could formed [6-8]. It had advantages of light self-weight, strong corrosion resistance and large capacity compared with concrete-filled steel tube [9-10].

Scholars have carried out related experiments and theoretical research on concrete-filled steel tube for decades [11-13]. Lai et al. [14] collected the test data of 41 groups of axial compression short columns, 17 groups of compression-bending members and 4 groups of pure bending members with thin-walled and non-compact sections of concrete-filled steel tubes. A finite element numerical model was established to determine the applicability of AISC 360 for calculating rectangular thin-walled concrete-filled steel tube components. Aslani et al. [15] collected 316 groups of test data of axial compression short columns and axial compression long columns of rectangular and square concrete-filled steel tubes, and calculated the applicability of the Australian design code to the axial compression capacity of high-strength concrete-filled steel tube components. Liew et al. [16] conducted compression-bending experiments on square high-strength steel tube columns. With ultra-high-strength concrete filled inside, the calculated values of the test and different steel reduction factors were calculated. The results showed that high-strength concrete-filled steel tubes could be designed and calculated using the fully plastic bending moment method. Zhou et al. [17] and Zhang et al. [18] found the existence of stiffeners could effectively enhance the bond between concrete and steel tubes and reduce the slip, and could give full play to the material properties and increase the overall working performance of the short columns. Ellobody et al. [19] added stiffeners in rectangular and square concrete-filled high-strength stainless-steel tubular columns to study their mechanical properties. The tests showed that the ductility and strength of stiffened stainless-steel tube concrete columns were greatly improved. Lam et al. [20] conducted axial compression tests of square stainless-steel columns filled with concrete (30-100 MPa). The calculation results of the axial compression capacity of concrete-filled steel tube columns were obtained. Gardner et al. [21] conducted a series of axial compression tests of concrete-filled stainless-steel tubes. The tests found that under the same conditions, the axial compression capacity of concrete-filled stainless-steel tubes was higher than that of concrete-filled steel tubes. Uy et al. [22] conducted axial compression and compression-bending mechanical performance tests of concrete-filled stainless-steel tube short columns. The research showed that the mechanical performance was excellent. Subsequently, B. Uy et al. [23] studied the mechanical performance of thin-walled concrete-filled steel tube columns through experiments. The test results showed that the width-to-thickness ratio corresponding to severe buckling of the steel tube was greater than 100. To sum up, scholars had achieved certain results in cold-formed thin-walled steel tubes with different sections and concrete-filled steel tube components [24-29], but there were no research on tubular columns assembled by lipped channels. Two stainless-steel lipped channels were welded to form a new stainless-steel tubular column, with concrete filled inside, a high-performance concrete-filled stainless-steel tubular column was formed.

This paper designed a new type of concrete-filled rectangular thin-walled stainless-steel tubular columns. It had advantages of strong capacity, simple process, and had abundant raw material reserves. Axial compression short column test, finite element analysis of axial compression short columns, axial compression and compression-bending intermediate-length columns were carried in the paper. The key parameters were analyzed, and the recommended calculation method was also proposed.

2. Axial compression test of short columns

2.1. Design and fabrication of specimens

The external casing was composed of two duplex stainless-steel 2205 lipped channels, and the splicing part was equivalent to unidirectional ribs. To prevent the situation of substandard material strength, the strength grade of the infilled concrete was C60 [20]. The fabrication and curing of core concrete was carried out in accordance with the Code GB/T 50081-2002 [30]. The design scheme was shown in Fig.1. The original cross-section was named RA section. The enhanced component cross-section was named RB section. The cold-formed V-shaped ribs were arranged on the long side. The parameters were

shown in Table 1.

Table 1
Parameters of the specimen

Type	H/mm	B/mm	D/mm	R1/mm	R2/mm	t/mm	b_0/mm	b_0/t	A_s/mm^2	A_c/mm^2	b_s/mm
RA	480	160	140	4	4	3	-	-	1942.5	20430.3	-
RB	480	160	140	1	1	3	54	18	2036.9	19537.1	30

Where，A_s-Area of the stainless-steel tube; A_c-Area of concrete inside.

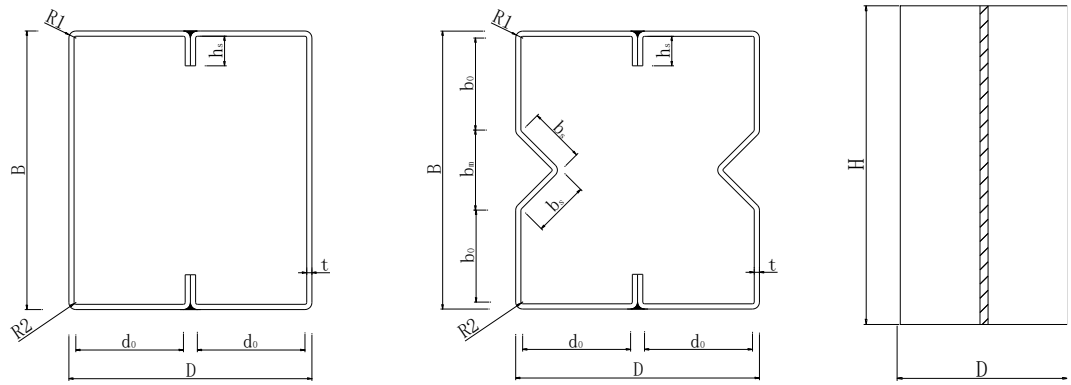

(a) RA section (b) RB section (c) Elevation

Fig. 1 Details of specimens

(a) RA specimens (b) RB specimens

Fig. 2 Processed specimens

Table 2
Actual size of specimens

Specimen	Height H/mm	Section length B/mm	Section breadth D/mm	Average thick-ness of the tube t/mm	Rectangular stiffening ribs length h_s/mm	V-shaped stiffening ribs right-angle edge length b_s/mm	Concrete area A_c/ mm^2	Stainless-steel tube area A_s/ mm^2	Strength and capacity estimate value N_u^i/kN
RA-1	478.5	139.5	161.0	2.83	15.17	-	1832.4	20599.4	2163
RA-2	479.0	140.0	161.5	2.84	16.66	-	1838.9	20743.9	2154
RA-3	479.0	139.5	160.5	2.83	15.67	-	1830.4	20550.4	2160
RB-1	479.0	139.5	160.0	2.79	16.21	30.1	1904.3	19738.7	2515
RB-2	479.0	140.0	159.5	2.84	15.66	30.5	1912.2	19583.8	2517
RB-3	478.5	139.5	160.5	2.83	15.67	30.0	1903.4	19659.6	2520

Before pouring concrete, the actual cross-sectional dimensions of the components were measured first. Fig.2 shows the specimens of the finished preparation. The measured actual cross-sectional dimensions are shown in Table 2.

2.2. Test equipment and loading scheme

2.2.1. Loading equipment

The axial compression test was conducted using a 10,000 kN compression-shear testing machine, as shown in Fig.3. The accuracy of the testing machine was 0.01 kN. The maximum movable distance of the loading end of the testing machine was 450 mm, and the maximum distance between the loading end and the base was 2600 mm. Before the test, it was necessary to set up supports with a height of 1975 mm. Test load and displacement was recorded.

2.2.2. Test equipment and layout of measuring points

The test adopted the DIC-3D 2014a acquisition system, the test equipment and layout of measuring points were shown in Fig.4. The DIC-3D equipment was arranged on the key non-loading surface, and the entire process of component deformation was recorded by the camera. In order to verify the accuracy of the measurement results of the DIC-3D system, four longitudinal strain gauges were arranged and compared with the DIC-3D results. When the strain was large, the strain gauge could only measure the deformation of the initial section. When the deformation is greater than 20,000$\mu\varepsilon$, the strain gauge cannot measure and its results cannot be compared with the results of the DIC-3D [31].

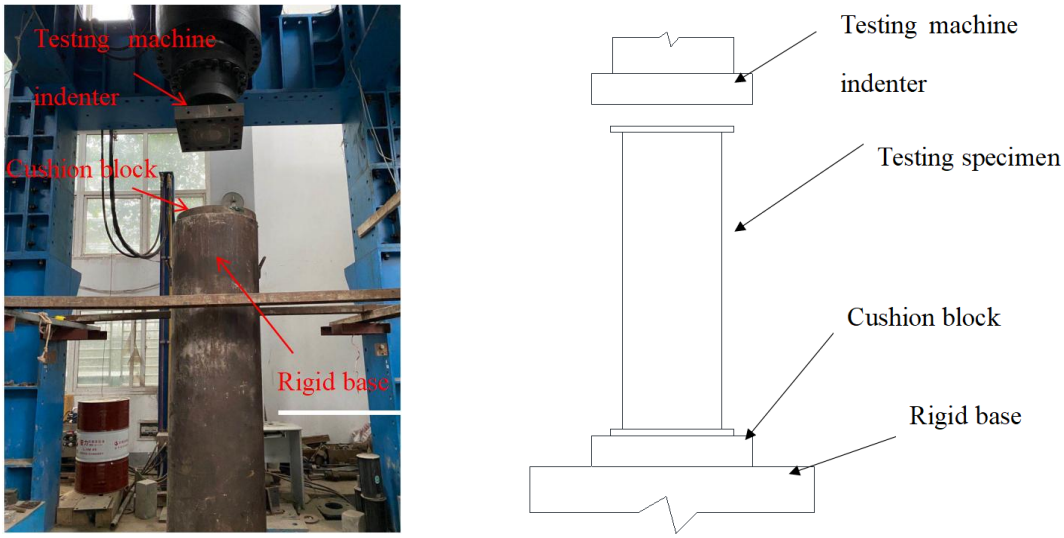

Fig. 3 Loading equipment

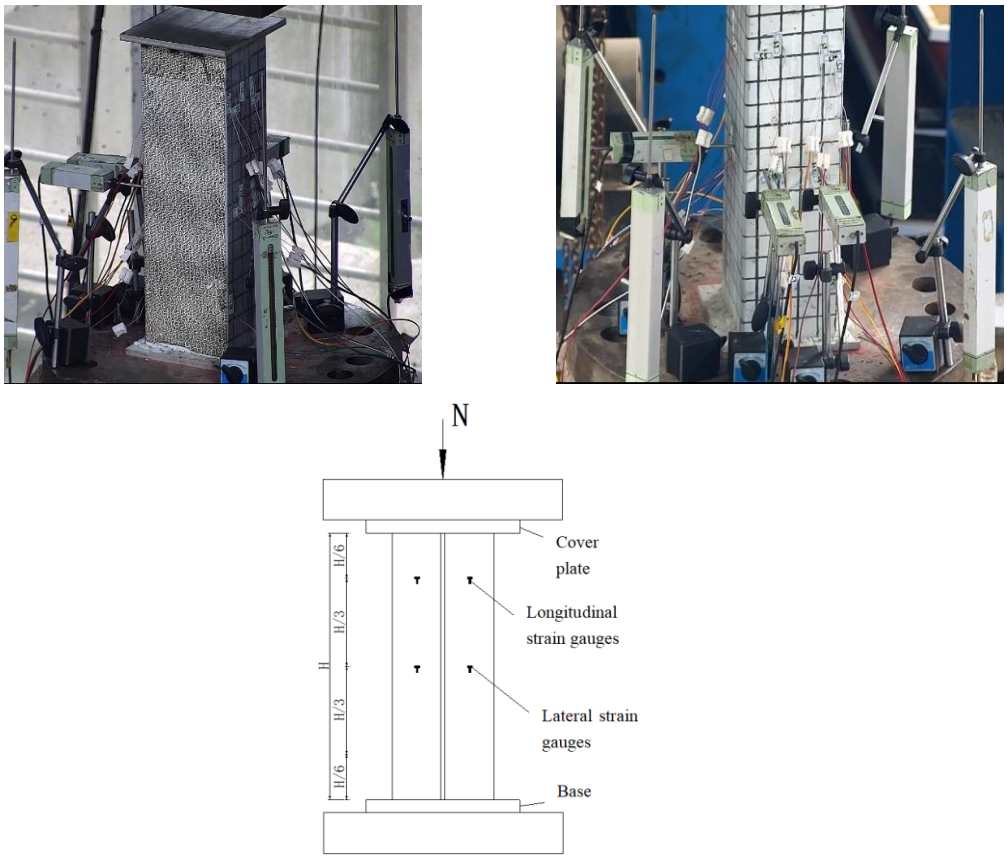

(a) RA specimens

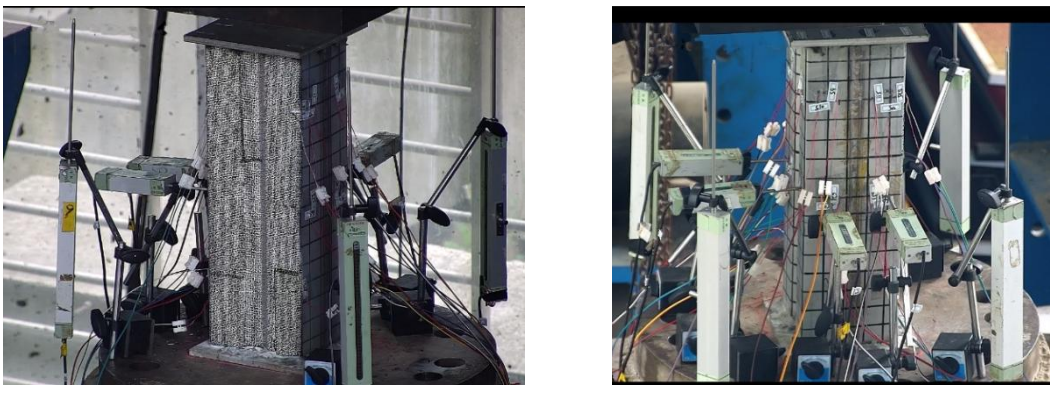

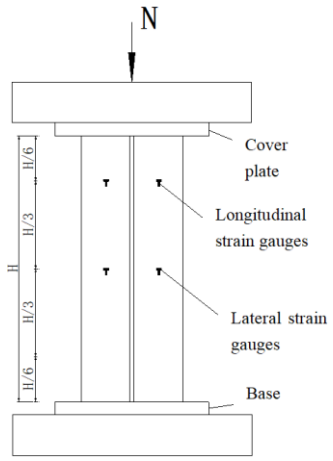

(b) RB specimens

Fig. 4 DIC-3D test equipment and layout of measuring points

Table 3
Detailed loading parameters

Type	Preloading		Stage Ⅰ		Stage Ⅱ			Stage III		Expected total time consumption /min
	Preloading value/kN	Load per level/kN	Ending load /kN	Expected time consumption /min	Load per level/kN	Ending load /kN	Expected time consumption /min	Expected deformation amount/mm	Expected time consumption /min	
RA	110	140	1540	24	110	1980	11	12	6	31
RB	125	160	1760	24	125	2260	9			29

2.2.3. Loading system

The loading scheme adopted the monotonic loading with the combined control of force and displacement, and the loading steps were as follows: (1) Preloading: Preloading to about 5% of the estimated ultimate load to check the stability of the test system and the reliability of the measuring points, and then completely unloaded. (2) First stage: When the load was less than or equal to 70% of the estimated capacity. (3) Second stage: When the load was greater than 70% of the estimated capacity to about 90% of the estimated capacity. (4) Third stage: When the load reached 90% of the estimated ultimate load. The loading parameters of the specific components were shown in Table 3.

2.2.4. Test scheme

The measurement results of the DIC (Digital Image Correlation) equipment were compared with those of the strain gauges and displacement meters to detect the local deformation of the outer wall of the stainless-steel tube during the loading process. The range of the strain gauge was 20,000 (2%). Displacement meters were arranged on the outside and in the middle of the specimen, which were used to measure the longitudinal and transverse total deformations of the specimen respectively. Four displacement meters with a range of 200 mm were arranged on the outside of the specimen, and the displacement meters were parallel to the longitudinal direction of the specimen. The transverse displacement meters were arranged at the H/2 height between the outer cover plate and the bottom plate of the tube wall on the corresponding surface (rectangular rib surface B) of the DIC acquisition system and the adjacent surface of the corresponding surface (non rib surface B or V-shaped rib surface B).

2.3. Test results and analysis

2.3.1. Test process and main phenomena

Fig.5 and Fig.6 showed the situation of concrete spalling after the specimens were cut. The failure mode of the components could be seen in Fig.9-Fig.10. The concrete at the slit did not spall, indicating that the cutting had almost no influence on the actual concrete spalling of the specimens. The failure mode of the internal concrete could clearly represent the state of the specimens after the axial compression test.

For the axial compression short columns of RA and RB in Fig.6, both rectangular stiffeners and V-shaped stiffeners enhanced the restraint capacity of the external stainless-steel tube. The difference was that the failure mode of unidirectional stiffeners was shear failure, while that of bidirectional stiffeners was atypical drum-shaped failure.

Fig. 5 The failure characteristics of RA component

Fig. 6 The failure characteristics of RB component

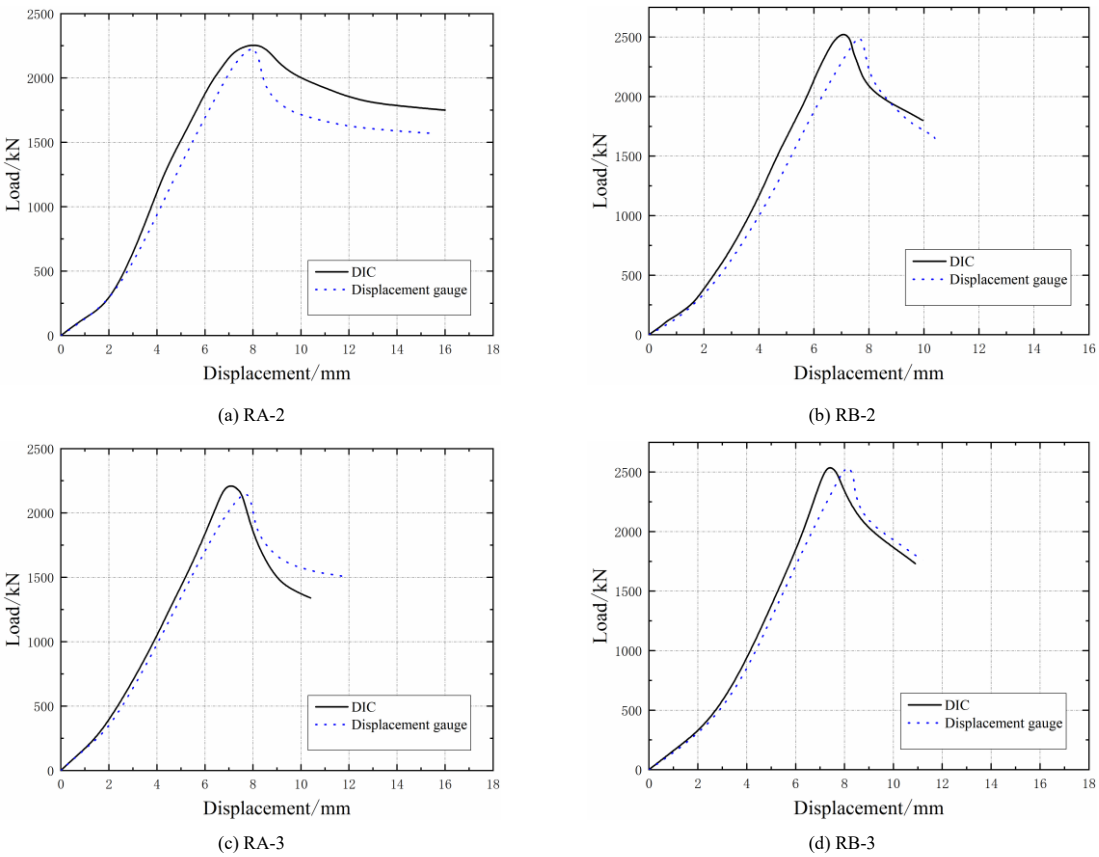

Fig. 7 Comparison of load-displacement curves of experiment and DIC-3D system

Table 4
Comparison of experimental and theoretical values

Specimen	Test value N_{ue}/ kN	Estimate of capacity N'_u/ kN	N'_u/N_{ue}
RA-1	2175	2163	0.994
RA-2	2218	2154	0.971
RA-3	2149	2160	1.005
RB-1	2487	2515	1.006
RB-2	2499	2517	1.007
RB-3	2540	2520	0.992

2.3.2. Test data and analysis

The displacement data obtained from displacement gauges were compared with that of DIC-3D system, as shown in Fig.7. It could be seen that the displacement data of displacement gauges was in good agreement with the DIC-3D system. After calculation, the ultimate capacity of the axial compression short column with bidirectional ribs was 15.04% higher than that of the short column with unidirectional ribs. Stiffeners on the external stainless steel tube changed the buckling state of the component. The unidirectional stiffened component began to buckle when the external stainless-steel tube reached 70% of the ultimate capacity, while the bidirectional stiffened component did not buckle before reaching the ultimate bearing capacity.

2.3.3. Test results

The capacity obtained from the test was compared with the estimated value [26], as shown in Table 4. It was found that the test values agreed well with the theoretical values.

3. Finite element modeling and validation

3.1. Establishment of the FEM

In the verification of the finite element model of the axial compression short column, the stress-strain curves of experiments were adopted and transformed into the true stress-strain curve, as shown in Fig.8. The nominal yield strength f_y was taken as 563 MPa, the elastic modulus E_s was taken as 220087 MPa, and the Poisson's ratio was taken as 0.3 [32]. The concrete and steel pipe grid are 6mm × 6mm, and the end plate grid is 18mm × 18mm. The upper and lower end plates and the high-strength stainless-steel tube were constrained by binding; the upper and lower end plates and the core concrete were in normal "hard" contact; the tube and the core concrete were in "hard" contact. The contact between the tube and the core concrete in the tangential direction, adopted the Coulomb friction model. Considering the surface of the stainless-steel was

relatively smooth and the bonding with the concrete was poor, the interface friction coefficient was taken as 0.2. In ABAQUS analysis, the material with a larger elastic modulus was taken as the master surface in the simulation, and the one with a smaller elastic modulus was taken as the slave surface. Therefore, the high-strength stainless-steel tube was used as the master surface, and the core concrete was used as the slave surface in the simulation. According to the experimental analysis, the straight ribs of the steel tube were in good contact with the core concrete during the failure analysis of the specimen. The straight ribs and the core concrete were constrained by binding (Tie). The weld seams were constrained by binding (Tie). The concrete adopted a plastic damage model with the following parameters: the dilation angle was set to 30° ; the flow eccentricity was 0.1; the ratio of biaxial compressive strength to uniaxial compressive strength was 1.16; the ratio of the second stress invariant in tension to that in compression was 0.667; and the viscosity parameter was set to 0. For the initial geometric defects of median long column compression-bending members, the amplitude calculation was consistent with that of short column under axial compression. The eigenvalue buckling analysis was first carried out, and the lowest-order mode and first-order mode of the analysis results were taken as the initial geometric defects in the model analysis. Considering its overall buckling, the initial geometric defect should also took L/1000 as its overall geometric defect.

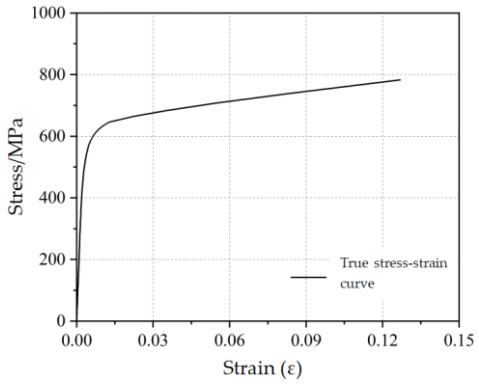

Fig. 8 True stress-strain curve

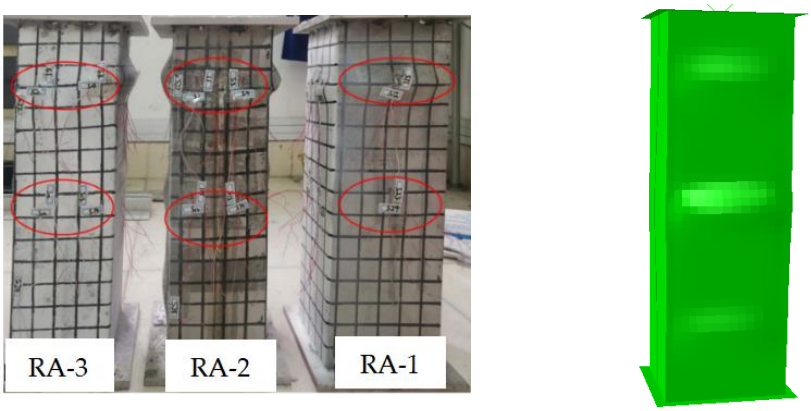

(a) Experiment (b) FEM

Fig. 9 Failure diagram of RA component

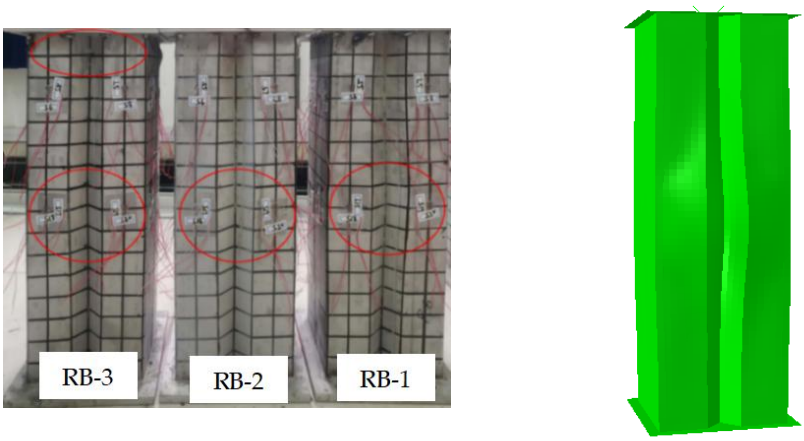

(a) Experiment (b) FEM

Fig. 10 Failure diagram of RB component

3.2. Verification of the FEM

3.2.1. Comparison of failure modes and stress cloud diagrams

At the beginning of the loading, the component was in the elastic stage, and there was no obvious change on the surface of the high-strength stainless-steel tube. As the load increased, when it reached about $0.7N_u$, local buckling occurred in the middle of the RA component. While for the RB component, due to the V-shaped stiffeners, buckling only occurred in the middle of the component when it reached the ultimate capacity. Subsequently, the buckling phenomenon was obvious and the component was damaged, as shown in Fig.9 and Fig.10. The final deformation obtained by FEM (Finite Element Method) was basically consistent with the experiment.

3.2.2. Analysis of the load-displacement curves

Tests and FEM load-displacement curves of RA and RB components were shown in Fig.11. Table 5 listed the ultimate capacities of the two types of components obtained from the experiment and the FEM. Where, N_{exp} represented the ultimate capacity in the experiment, and N_{sim} represented the ultimate capacity in FEM. According to the Table 6, the maximum difference was 8.7%, and the average difference was 4.3%, indicating that the simulation results were reliable. From the failure mode and the load-displacement curve, the finite element model was in good agreement with the experiment, and parameter analysis could be conducted using FEM.

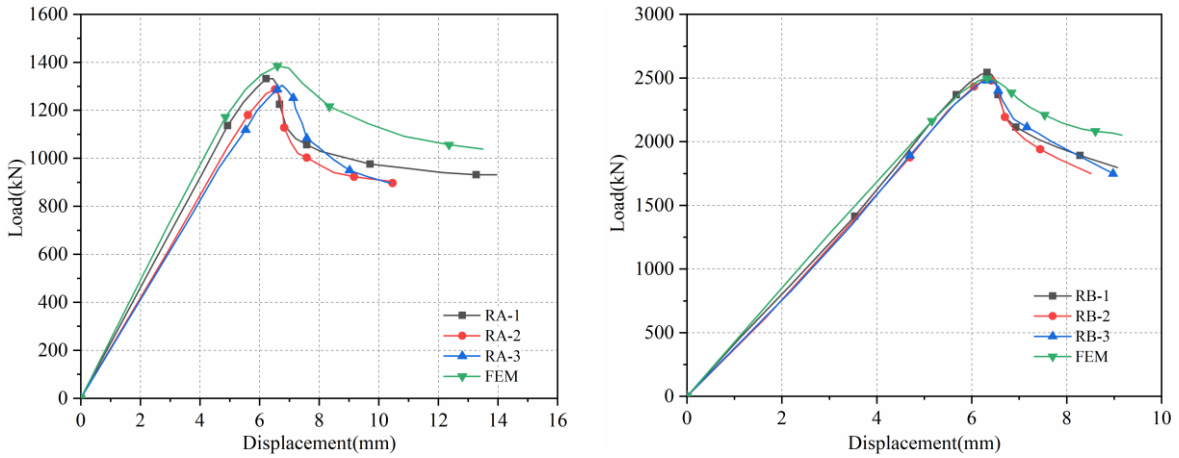

(a) RA type specimens (b) RB type specimens

Fig. 11 Comparison of load-displacement curve

Table 5
Comparison of ultimate capacity between test and FEM

Specimen	Ultimate capacity /kN		N_{exp}/N_{sim}
	N_{exp}/kN	N_{sim}/kN	
RA-1	2175	2355	0.92
RA-2	2218	2355	0.94
RA-3	2149	2355	0.92
RB-1	2487	2492	1.00
RB-2	2499	2492	1.00
RB-3	2540	2492	1.02

4. Numerical analysis of structural performance and compression-bending capacity calculation

4.1. Analysis of axial compression of short columns

4.1.1. Analysis of the loading process

The whole loading process curves of RA and RB components under axial compression load were showed in Fig.12. The peak strain of concrete was about 0.004, which was much larger than the peak strain of 0.0024 of plain concrete under uniaxial compression. The axial compression peak strains corresponding to RA and RB components were 0.00347 and 0.00409 respectively, and the axial compression ultimate capacities were 2355.8 kN and 2497.7 kN. The ultimate capacity was increased by 6.0%. It showed that compared with RA components without stiffeners, the V-shaped stiffeners of RB components had a stronger ability to confine the core concrete and could better improve the ultimate capacity of axial compression. In the descending section, the curve of RB components was gentler compared with that of RA, indicating that V-shaped stiffeners could improve the ductility.

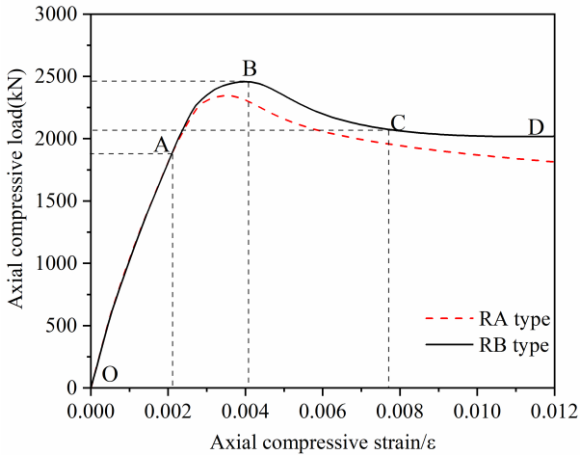

Fig. 12 Axial load-strain relationship curves of RA and RB members

4.1.2. Analysis of the concrete cross-section performance

The greater the lateral restriction provided by the high-strength stainless-steel tube was, the larger the range of the effective confined zone of the core concrete was. Fig.13 showed the Mises stress distribution nephogram of the middle section of the concrete of RA and RB components at the ultimate load. The lateral restriction of RA was mainly concentrated at the corners, right-angle ribs and the center of the section. The diagonal confined zone was synthesized along two directions relying on the stiffness of the right-angle ribs and corners. The lateral restriction of RB was mainly distributed at the corners, right-angle ribs, the corners of V-shaped stiffeners and the center of the section, and the area of the middle confined zone was larger than that of the cross-section of RA, which was about twice the area of the middle confined zone of RA component.

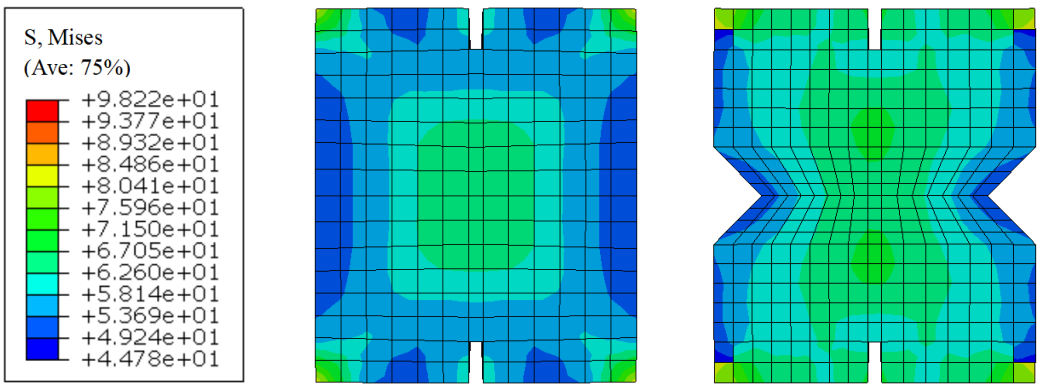

(a) RA specimens (b) RB specimens

Fig. 13 Stress nephogram of middle section of the core concrete

4.1.3. Analysis of the interface performance between stainless-steel and concrete

When the axial load was small, the high-strength stainless-steel tube and the concrete remained in a bonding state and had good contact. As the axial load increased, gaps began to appear. The gaps mainly occurred at the surface and V-shaped stiffener, while the corners and right-angle ribs still maintained a good contact relationship. The cross-sections of RA and RB short columns reaching the ultimate capacity were shown in Fig.14, where P is the midpoint on the edge of the non-ribbed surface (RA) and the V-shaped stiffener surface (RB) of the mid-span section of the short column. The non-ribbed surface of the middle section of the RA short column had already undergone visible bulging, while the RB was not obvious, and at the later stage of loading, the tube and the concrete were separated at P. The deformation and failure of the short column were caused by the buckling of the stainless-steel tube in the middle and the transverse deformation. The relationship between the contact gap and the longitudinal displacement at point P of the RA and RB short columns was shown in Fig.15. At the initial stage of loading, the contact gap of the two types of components remained zero at P. When the ultimate capacity was reached, the contact gap between the tube and the concrete of RA reached 1.68 mm, while the contact gap of RB was only 0.48 mm, indicating that the V-shaped stiffener could greatly alleviate the buckling of the high-strength stainless-steel tube.

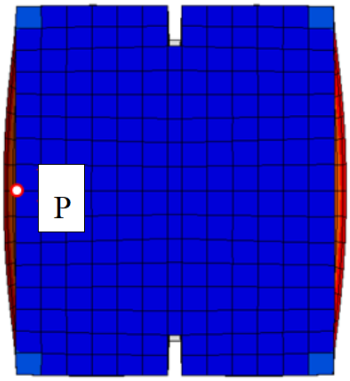

(a) RA type specimens

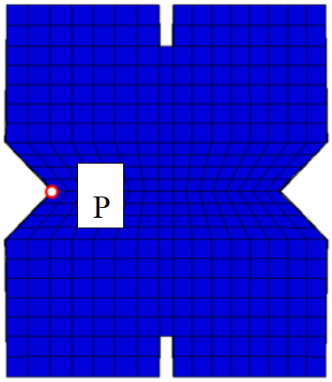

(b) RB type specimens

Fig. 14 Deformation of mid-span section of short column

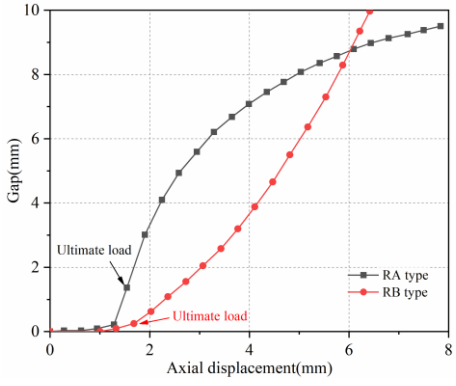

Fig. 15 Contact gap-displacement curve of P point

4.1.4. Analysis of the influence of main parameters

This section conducted a parameter analysis taking the size of the V-shaped stiffeners (including the angle φ and depth h_v), the strength of the core concrete, and the width-thickness ratio of the plate b_0 / t as variables, as shown in Fig.16.

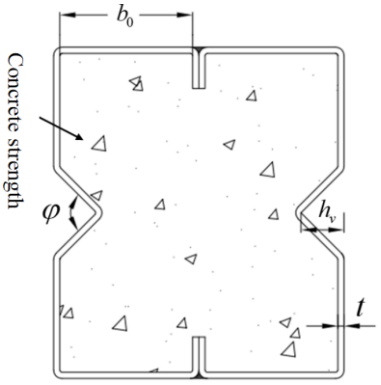

Fig. 16 Details of V-stiffener size

Where, φ were taken as 30°, 45°, 60°, 90°, and 120°, and h_v were taken as 18mm, 19mm, 20mm, 22mm, 24mm, 27mm and 30mm. Fig.17 showed the depth-ultimate load relationship curves of different depths h_v of V-shaped stiffeners. When the angles of V-shaped stiffeners φ were 30°, 45°, and 60° respectively, the ultimate load increased with the increase of the depth. When φ was 90°, the ultimate load slightly decreased with the increase of the depth. While when φ was 120°, the ultimate load decreased rapidly with the increase of the depth. The reason was that: with the continuous increase of the load, the entire component entered the elastic-plastic stage. The Poisson's ratio of the concrete was greater than that of the stainless-steel tube, the transverse deformation of the concrete was greater than that of the stainless-steel tube, and the concrete exerted lateral pressure on the steel tube. When φ was 120°, even if the minimum stiffness of the V-shaped stiffener met the requirements, it was not conducive to improving the stiffness of the steel tube. Compared with the V-shaped stiffeners with small angles, it was more likely to bulge outward under the action of lateral load, indicating that the use of 120° V-shaped stiffener could not effectively improve the confinement effect on the concrete. When the depth was less than 20mm, the section performance increased with the increase of the depth of the V-shaped stiffener. When the depth was greater than 20mm, the section performance decreased with the increase of the depth of the V-shaped stiffener. In particular, when the angle was 90°, the section performance dropped rapidly. After the depth exceeded 25mm, the section performance was lower than that of the 60° section. When the angle of the V-shaped stiffener was 120°, the section performance at any depth was far lower than that of other angles. Therefore, in actual engineering design, angles greater than 90° were avoided.

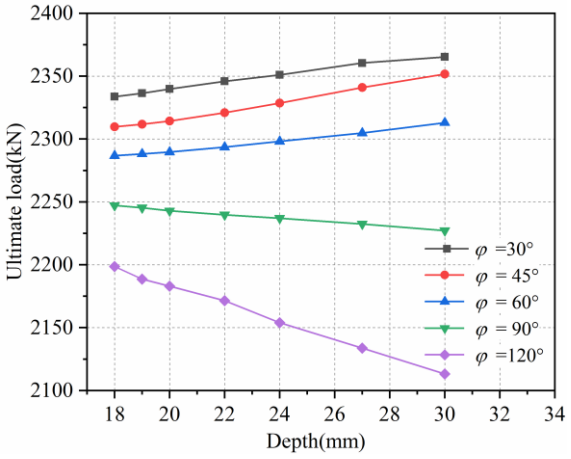

Fig.17 Relationship between V-shaped stiffener depth and ultimate load

Fig.18 showed the relationship between different angles of V-shaped stiffeners and ultimate loads. As φ increased, the ultimate load of the component continuously decreased. The greater h_v, the greater the degree of decrease in the ultimate load. When the depth h_v was small (18-20mm), the

smaller the angle, the smaller the stiffness of the V-shaped stiffener, resulting in a relatively low ultimate capacity. When h_v was small (22-30mm), the larger the angle, the greater the weakening degree of the V-shaped stiffener on the component section, also resulting in a relatively low ultimate capacity. After analysis, the optimal size of the V-shaped stiffener was a depth of 20mm, that is, the width-thickness ratio of the V-shaped stiffener plate was 8.33, and the angle was 90°.

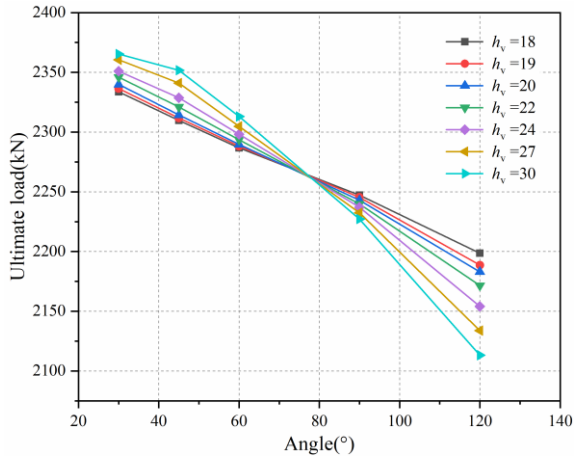

Fig. 18 Relationship between V-shaped stiffener angle and ultimate load

On the basis of determining the size of the V-shaped stiffener, different strengths of high-strength concrete were selected as parameters to analyze their applicability with high-strength stainless-steel tubes, in order to give full play to the mechanical properties of both. The high-strength concrete was taken as C60 to C80 respectively, with a total of 5 sets of components. The specific parameter information was shown in Table 6. The components were assigned according to R-concrete strength. For example: R-C60 indicated that the component had a concrete strength of C60. After analysis, the peak load corresponding to C60 was 2242 kN, and the peak load corresponding to C80 was 2628 kN, with an increase of 17.20%. Fig.19 showed the axial forces by the stainless-steel tube and the concrete under different strengths.

Table 6
Details of concrete strength

Speci-men	*H*/ mm	*B*/m m	*D*/ mm	*t*/ mm	Con-crete grade	f_{ck}/MPa	f_c'/MPa	N_u/kN
RB-60					C60	38.5	49.97	2242.93
RB-65					C65	41.5	54.90	2336.75
RB-70	480	160	140	3	C70	44.5	60.98	2435.78
RB-75					C75	47.5	64.98	2532.10
RB-80					C80	50.2	69.97	2628.77

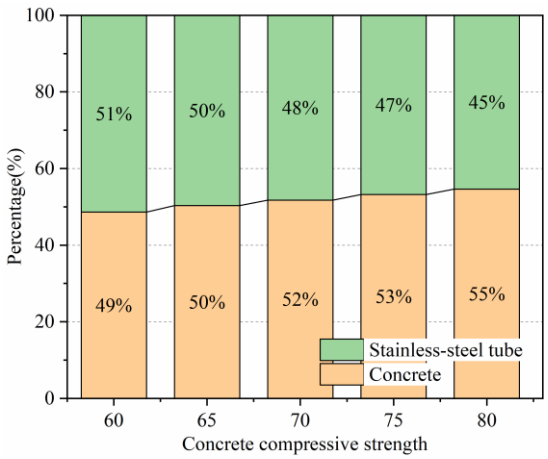

Fig. 19 Ratio of stainless-steel tube to concrete capacity

Different stainless-steel tube thicknesses were chosen to study the influence of different width-thickness ratios of the plate on the axial compression performance of the short columns. The thicknesses were taken as 2.0mm, 2.5mm, 3.0mm, 3.5mm, and 4.0mm. Fig.20 showed the ratio of the average stress of the tube section to the yield strength for different width-thickness ratios of the plate. When the width-thickness ratio was between 18 and 21.3, the average stress of the tube section could reach 0.95 f_y, indicating that the tube could better exert its material properties at this time. Therefore, the width-thickness ratio was recommended to be 18-21.3.

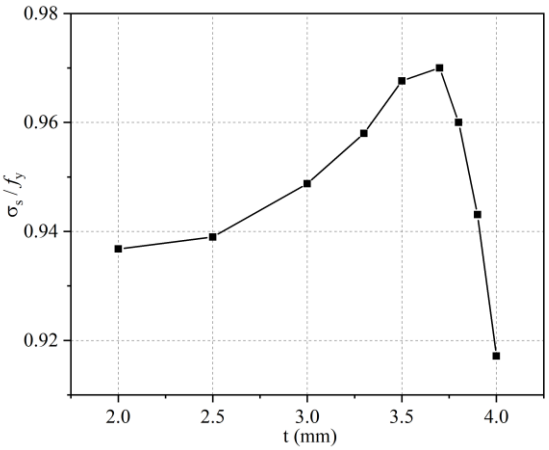

Fig. 20 Ratio of average stress to yield strength of steel tube section with different width-to-thickness ratio of plates

4.2. Analysis of axial compression and compression-bending of intermediate-length columns

4.2.1. Analysis of the concrete cross-section performance

The influence of eccentric load on the cracking of core concrete in medium-long columns was analyzed by the maximum principal plastic strain PEEQ in ABAQUS, as shown in Fig.21. When the eccentric load was $0.25N_u$, the maximum principal plastic strain PEEQ was basically 0, indicating that the core concrete did not crack at this time. When the eccentric load reached $0.63N_u$, tiny cracks occurred near the middle section of the eccentric load, and the component began to enter the elastic-plastic stage. With the continuous increase of the eccentric load, the plastic principal strain of the concrete at the middle section continuously expanded towards the neutral axis, and the component bent significantly in the eccentric direction. When the ultimate eccentric load was reached, the middle section of the concrete part basically cracked.

4.2.2. Analysis of the interface performance between stainless-steel and concrete

Fig.22 was the middle section view of the component, and a limited number of 1 to 9 nodes were selected to analyze the interface characteristics between the high-strength stainless-steel tube and the concrete. The initial gap at the interface between the stainless-steel and the concrete was 0, and the contact pressure was 0. With the increase of the eccentric load, the initial Poisson's ratio (0.3) of the tube was greater than the initial Poisson's ratio (0.2) of the concrete, a gap was generated between the tube and the concrete, and the restraint effect of the concrete by the tube also began to decrease. Fig.23 showed the change process of the gap between the stainless-steel and the concrete at each node of the middle section of the high-strength stainless-steel tube concrete component with the increase of the load. When the longitudinal displacement reached about 0.7mm, the tube and the concrete at the middle section of the V-shaped stiffener surface began to separate. With the increase of the longitudinal displacement, the separation distance between the tube and the concrete at points 4 and 6 of the V-shaped stiffener surface was the most obvious, and there was also a certain separation at point 5. When the longitudinal displacement reached about 3mm, that is, when the ultimate load was reached, the tube and the concrete at the middle section of the right-angle rib surface were basically not separated, while the separation gap at the V-shaped stiffener surface was large, about 2.5mm. When the longitudinal displacement reached about 0.7 mm, the stainless steel tube and concrete at the corners (Points 3 and 7) of the middle section of the stainless steel tube concrete component began to squeeze each other, generating contact pressure. As the longitudinal displacement increased, the contact pressure at the corners increased rapidly. When the longitudinal displacement reached 3 mm, that is, when the bending pressure load reached the ultimate load, the contact pressure at Corners 3 and 7 was the greatest. The contact pressure at the corner (Point 3) of the middle section in the compression zone reached 37 MPa, the contact pressure at the corner (Point 7) of the middle section in the

tension zone reached 25 MPa, and the contact pressure at Point 1 of the middle section in the compression zone of the right-angle rib surface reached 2.9 MPa. Compared with the corner contact pressure, the facial contact pressure was very small and could be ignored.

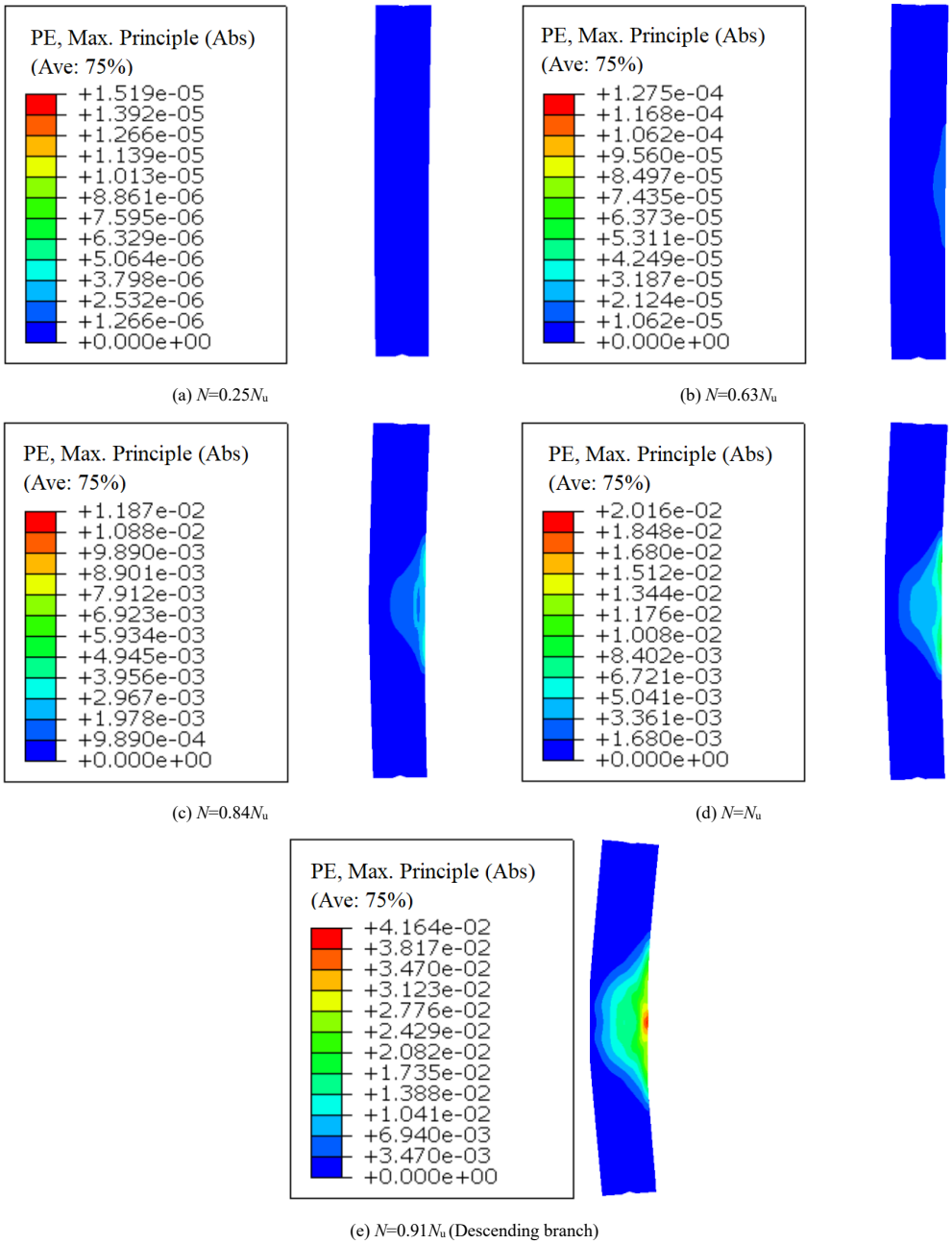

(a) N=0.25N_u (b) N=0.63N_u

(c) N=0.84N_u (d) N=N_u

(e) N=0.91N_u (Descending branch)

Fig. 21 Finite element prediction of cracks and crushing of concrete filled in members

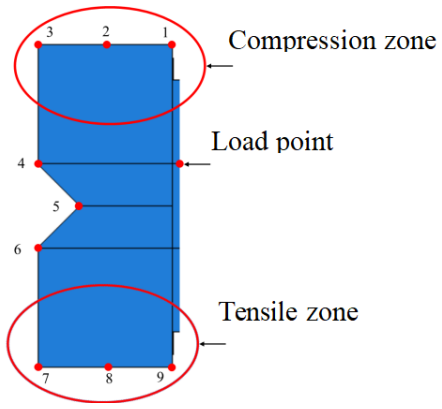

Fig. 22 The middle section of the component

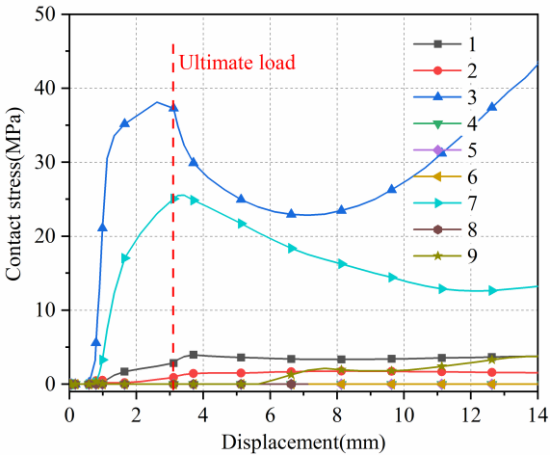

Fig. 23 Relationship of displacement-contact stress of each node in the middle section

4.2.3. Analysis of the influence of main parameters

The corresponding eccentricities were 0, 0.19, 0.38, 0.56, 0.75, 0.94, 1.25, 1.875, 2.5 and 3.75. When the eccentricity was small (e = 0.19), the middle section of the component was entirely in a compressive state. As the eccentricity increased (e = 1.0), the compressive zone of the middle section of the component decreased, and there was a tendency for tension in the direction away from the eccentricity. When the eccentricity increased to 1.25, a tensile zone appeared in the direction of the component away from the eccentricity. When the eccentricity (e = 3.75) was large, the tensile zone of the middle section of the component expanded. At this time, the range of the tensile zone was basically consistent with that of the tensile zone, and the component undergone compressive failure in the compressive zone and tensile failure in the tensile zone. Fig.24 showed the influence of the eccentricity on the ultimate compression-bending capacity of intermediate-length columns. When the eccentricity was less than 0.5, the ultimate compression-bending capacity decreased rapidly. When the eccentricity was greater than 1, the ultimate compression-bending capacity decreased slowly. When the section properties of the components were the same, the larger the slenderness ratio was, the gradually smaller the influence of the eccentricity on the ultimate compression-bending capacity was.

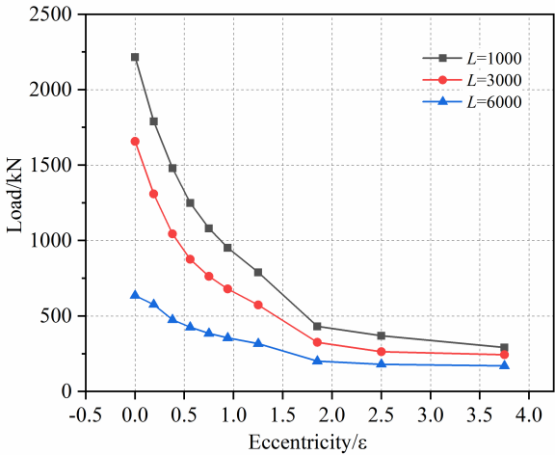

Fig. 24 Effect of eccentricity on ultimate capacity of members

The slenderness ratio was chosen as 15.17, 30.34, 45.51, 60.68, 75.85 and 91.02. The influence of the slenderness ratios was shown in Fig.25. For the same concrete-filled high-strength stainless-steel tubular columns, the peak compression-bending load decreased with the increase of the slenderness ratio. The smaller the slenderness ratio, the faster the peak compression-bending load decreased. Under the same eccentricity, the peak compression-bending load of concrete-filled high-strength stainless-steel tube columns decreased approximately linearly with the increase of the slenderness ratio, and the smaller the eccentricity, the steeper the decrease of the peak compression-bending load. When the eccentricity was 300mm, the peak compression-bending load remained basically unchanged.

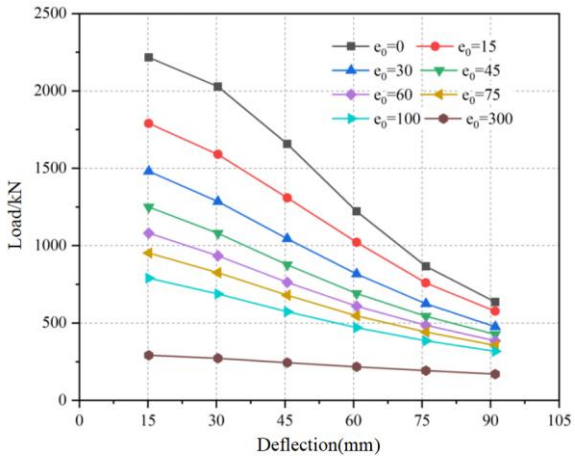

Fig. 25 The change of bending peak load with slenderness ratio

The thicknesses of the stainless-steel tubes were taken as 2mm, 3mm, and 4mm, and the width-thickness ratios of the sub-plates were 33.0, 21.3, and 15.5 respectively. Analyze the influence of the width-thickness ratio, as shown in Fig.26. For the same concrete-filled high-strength stainless-steel tubular column, the peak compression-bending load decreased with the increase of the width-thickness ratio. The smaller the width-thickness ratio of the plate, the faster the peak compression-bending load decreased. Under the same eccentricity, the peak compression-bending load decreased approximately linearly with the increase of the width-thickness ratio of the plate, and the smaller the eccentricity, the steeper the decrease of the peak compression-bending load. When the eccentricity was 300mm, the peak compression-bending load remained basically unchanged.

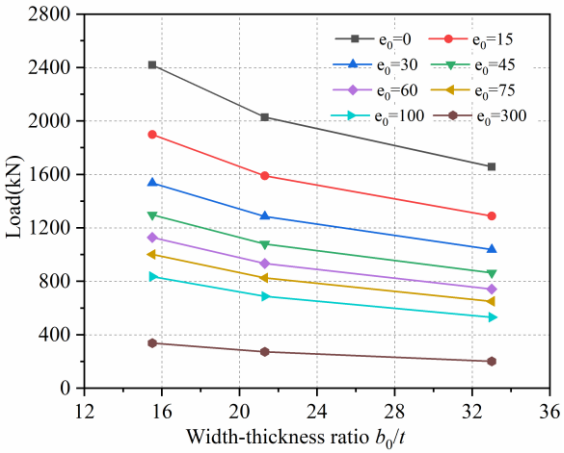

Fig. 26 The change of bending peak load with width-thickness ratio of plate

4.3. Recommendation of compression-bending capacity calculation formula

For the concrete-filled high-strength stainless-steel tubular column, the compression-bending capacity by the Chinese code T/CECS 952 and FEM was calculated. Results showed the dispersion rate between Chinese code T/CECS 952 and finite element calculation results was only 0.06. Therefore, the design formula of the Chinese code T/CECS 952 was modified to make it applicable to the calculation of the compression-bending capacity of median long column with sorbite high-strength stainless-steel S600E (f_y = 600MPa). Fig.27 showed a typical N/N_u-M/M_u relationship curve of concrete-filled stainless-steel tube. There was an equilibrium point C (ζ_0, η_0). With the increase of the slenderness ratio, the equilibrium point C (ζ_0, η_0) became more and more concave and less and less obvious. The main reason was that the influence of the second-order effect became more and more obvious with the increase of the slenderness ratio.

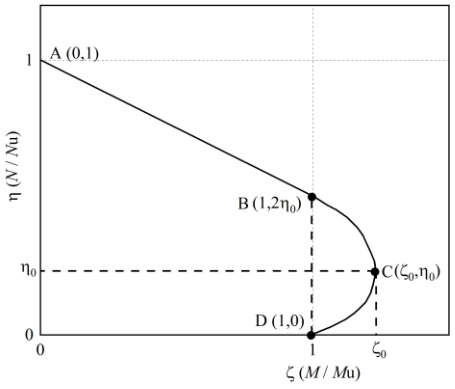

Fig. 27 Typical N/N_u-M/M_u relationship curve

Referred to the Chinese code T/CECS 952, ζ_0, η_0 in the equilibrium point C(ζ_0, η_0) could be approximately expressed as a function of the restraint effect ξ . A linear regression analysis was conducted and the corresponding functional relationship was obtained. For high-strength concrete-filled stainless-steel S600E tubular column, it could be calculated according to Eqs.(1) and (2).

$$\varsigma_0=1+0.11\xi^{-1.15} \quad (1)$$

$$\eta_0=0.1+0.09\xi^{-0.76} \tag{2}$$

The equation suggested in this paper still adopted a two-segment function for representation. Considering the influence of the slenderness ratio, the N/N_u-M/M_u equation of the median long column of concrete-filled high-strength stainless-steel tube could be expressed as Eq.(3).

$$\begin{cases} \dfrac{N}{\varphi\cdot N_u}+(\dfrac{a}{d})\cdot\dfrac{M}{M_u}=1 & \dfrac{N}{N_u}\geq 2\varphi^3\cdot\eta_0 \\ \dfrac{-b\cdot N^2}{N_u^2}-\dfrac{c\cdot N}{N_u}+(\dfrac{1}{d})\dfrac{M}{M_u}=1 & \dfrac{N}{N_u}\leq 2\varphi^3\cdot\eta_0 \end{cases} \tag{3}$$

The comparison between the ultimate capacity of the compression-bending median long column calculated by the proposed calculation method and the finite element calculation results was shown in Fig.28. It could be seen the proposed calculation method was reliable.

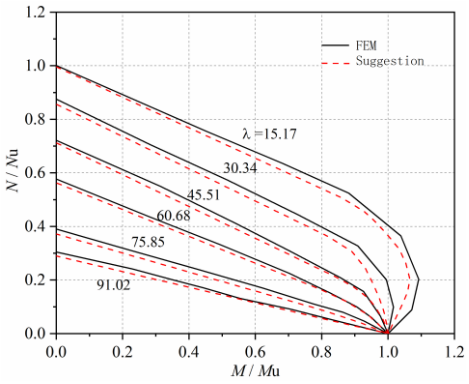

(a) Influence of slenderness ratio on N/N_u-M/M_u curve

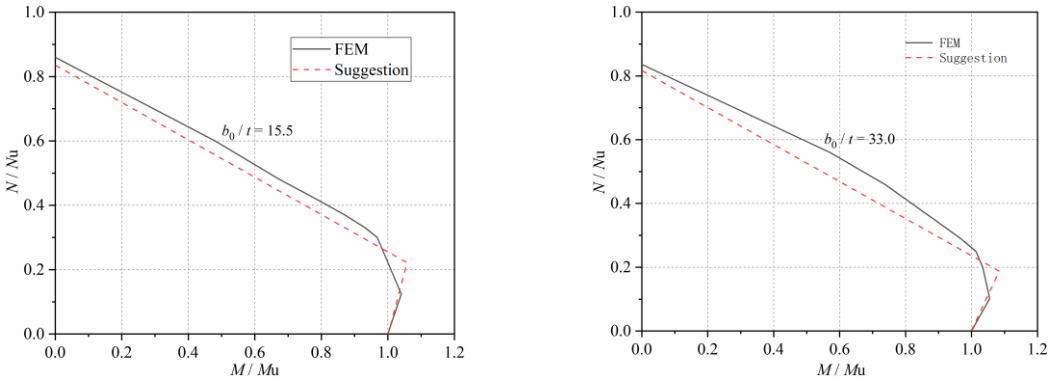

(b) Influence of the width-thickness ratio on the N/N_u-M/M_u curve

Fig. 28 Comparison of N/N_u-M/M_u relationship between the proposed method and FEM

Fig.29 showed the comparison between the proposed calculation method for S600E concrete-filled high-strength stainless-steel tubular columns and the finite element calculation results. Among them, N_{ue} represented the result of the ultimate compression-bending capacity calculated by the finite element method, and N_{u1} represented the result of the ultimate compression-bending capacity calculated by the proposed calculation method. $\overline{x}$ was the average value of N_{ue}/N_{u1}, and σ was the standard deviation of N_{ue}/N_{u1}. Through the comparison, the finite element results of the other components were all slightly smaller than the results of the proposed calculation method. Through calculation, the average value of N_{ue}/N_{u1} for concrete-filled high-strength stainless-steel tubular columns was 1.06, and the standard deviation of N_{ue}/N_{u1} was 0.035. It indicated that the proposed calculation method for calculating the compression-bending capacity was conservative.

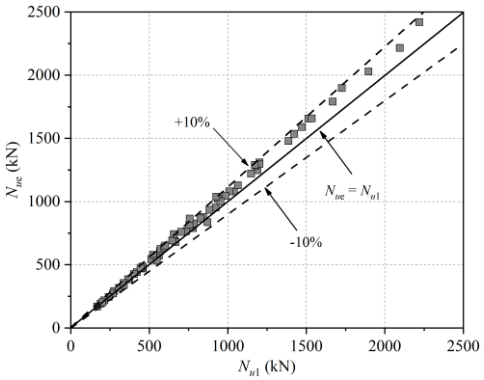

Fig. 29 Comparison between the proposed calculation method and FEM

5. Conclusions

This paper aimed at the environmental requirements of marine engineering. With the purpose of delaying the local buckling of the pipe wall and improving the restraint effect of the core concrete, two new types of concrete-filled thin-walled high-strength stainless-steel tubular columns were designed, the structural performances were studied by experiments and FEM. The main conclusions were as follows:

(1) Stiffeners on the external stainless-steel tube effectively improved the capacity of the axial compression short column. The ultimate capacity of the axial compression short column with bidirectional stiffeners was 15.04% higher than that of the axial compression short column with unidirectional stiffeners.

(2) The most important parameters affecting the axial compression short columns were the size of the V-shaped stiffeners and the strength of the concrete. When the width-thickness ratio of the V-shaped stiffeners was 8.33 and the angle was 90°, the size of cross-section was optimal. When the concrete was C80, the peak load was increased by 17.20% compared with C60.

(3) The most important parameters affecting the axial compression and compression-bending intermediate-length columns were the slenderness ratio and the eccentricity. When the slenderness ratio was between 15.17 and 91.02, the larger the slenderness ratio, the faster the stiffness degradation. When the eccentricity was between 0.56 and 3.75, the column had better deformation capacity and better ductility.

(4) The recommended calculation formula for the compression-bending capacity of medium long columns of concrete-filled thin-walled high-strength stainless-steel tubular columns was proposed, with high accuracy.

Reference

[1] Ayough P, Sulong NHR, Ibrahim Z. Analysis and review of concrete-filled double skin steel tubes under compression. Thin-Walled Struct 2020;148:106495.
[2] Shao ZW, Zha XX, Wan CY. Design method of fire-resistance capacity of reinforced-concrete-filled steel tube column under axial compression. Fire Saf J 2022;129:103572.
[3] Ukanwa KU, Clifton GC, Lim JB, et al. Simple design procedure for concrete filled steel tubular columns in fire. Eng Struct 2018;155:144-156.
[4] Duarte APC, Silva BA, Silvestre N, et al. Tests and design of short steel tubes filled with rubberised concrete. Eng Struct 2016;112:274-286.
[5] Tan QH, Gardner L, Han LH, et al. Fire performance of steel reinforced concrete-filled stainless steel tubular (CFSST) columns with square cross-sections. Thin-Walled Struct 2019;143:106197.
[6] Wang J, Yang Z, Zheng X. Axial compression behavior of square section concrete- filled steel tubes reinforced with internal latticed steel angles. J Constr Steel Res 2024;213:108414.
[7] Chen Z, Zhou J, Jing C, et al. Mechanical behavior of spiral stirrup reinforced concrete filled square steel tubular columns under compression. Eng Struct 2021;226:111377.
[8] Wu LL, Han GH, Sarno LD, et al. Experimental and numerical analysis of L-shaped concrete-filled steel tube stub columns. Structures 2024;69:107351.
[9] Ren QX, Zhou KZ, Li W. Experimental study of clay concrete filled steel tubular stub columns under axial compression. Structures 2024;70:107509.
[10] Chen J, Song SS, Ye J, et al. Axial compressive behaviour and design of concrete-filled wire arc additively manufactured steel tubes. Structures 2024;70:107495.
[11] Ahmed M, Shahin RI, Yehia SA, et al. Nonlinear analysis of square steel-reinforced concrete-filled steel tubular short columns considering local buckling. Struct Concr 2024;1:69-84.
[12] Hu JY, Huang YF, Li WJ, et al. Compressive behaviour of UHPC-filled square high-strength steel tube stub columns under eccentric loading. J Constr Steel Res 2022;198:107558.
[13] Ukanwa KU, Clifton GC, Lim JB, et al. Simple design procedure for concrete filled steel tubular columns in fire. Eng Struct 2018;155:144-156.
[14] Lai ZM, Varma AH, Noncompact and slender circular CFT members: Experimental database, analysis, and design. J Constr Steel Res 2014;101:455-468.
[15] Aslani F, Uy B, Tao Z, Predicting the axial load capacity of high-strength concrete filled steel tubular columns. Steel Compos Struct 2015;19:967-993.
[16] Liew JYR, Xiong M, Xiong D, Design of concrete filled tubular beam-columns with high strength steel and concrete. Structures 2016;8:213-226.
[17] Zhou XH, Liu YJ, Jiang L, Review of the mechanical properties of PBL reinforced rectangular concrete filled steel tube structure. Journal of Chinese Highway 2017;30:45-62.
[18] Zhang N, Liu YJ, Li H, Analysis of local flexion performance of PBL stiffening rectangular concrete filled steel tube. Journal of Building Science and Engineering 2017;34:95-102.
[19] Ellobody E, Nonlinear behavior of concrete-filled stainless steel stiffened slender tube columns. Thin-Walled Struct 2007;45:259-273.
[20] Lam D, Gardner L, Structural design of stainless steel concrete filled columns. J Constr Steel Res 2008;64:1275-1282.
[21] Zhang WF, Gardner L, Wadee MA, On the uniform torsional rigidity of square concrete-filled steel tubular (CFST) sections. Structures 2022;43:249-2521.
[22] Tao Z, Uy B, Analysis and design of concrete-filled stiffened thin-walled steel tubular columns under axial compression. Thin-Walled Struct 2009;47:1544-1556.
[23] Uy B, Strength of concrete filled steel box columns incorporating local buckling progress of building steel structure. J Struct Eng 2003;126:341-352.
[24] Liao JJ, Zeng JJ, Long YL, et al. Behavior of square and rectangular concrete-filled steel tube (CFST) columns with horizontal reinforcing bars under eccentric compression. Eng Struct 2022;271:114899.
[25] Lin L, Wang FC. Investigation of analytical behavior of concrete filled steel tubular (CFST) offshore rock-socketed pile under lateral load. Ocean Eng 2023;277:114279.
[26] Cai YC, Su MN, Chen XR, et al. High strength steel square and rectangular tubular stub columns infilled with concrete. J Constr Steel Res 2021;179:106536.
[27] Lin SQ, Li ZL, Zhao Y. Behavior of eccentrically loaded circular concrete-filled steel tube stub columns with localized corrosion. Eng Struct 2023;288:116227.
[28] Tang HY, Wang HX, Liu Y, et al. Axial compressive property of square and rectangular UHPC-filled duplex stainless steel tube stub columns. Compos Struct 2023;323:117492.
[29] Tang HY, Hou LJ, Yuan ZJ, et al. Eccentric compressive behavior of square concrete-filled stainless steel tube (CFSST) stub columns. Struct 2023;55:1920-35.
[30] GB/T 50081-2002. Standard for test method of mechanical properties on ordinary concrete. Beijing, China: Standard Press of China; 2002.
[31] Peng Y, Zhao J, Chen LS, et al. Residual stress measurement combining blind-hole drilling and digital image correlation approach. J Constr Steel Res 2021;176:106346.
[32] Huang YQ, Yang JJ, Feng RQ, et al. Resistance of cold-formed sorbite stainless steel circular tubes under uniaxial compression. Thin-Walled Struct 2022;179.

Advanced Steel Construction – Vol. 22 No. 2 (2026) 143–152
DOI:10.18057/IJASC.2026.22.2.2

STUDY ON THE FATIGUE PERFORMANCE OF CROSS-WELDED STEEL FABRIC FOR SIMPLE-SUPPORTED BOX GIRDER OF HIGH-SPEED RAILWAY

Chuang Du *, Qi-Hui Gao, Jin-Li Qiao, Xiao-Tong Liu and Didier Nshimiyimana

School of Civil Engineering and Transportation, Hebei University of Technology, Tianjin 300401, China
** (Corresponding author: E-mail: duch_1@sina.com)*

ABSTRACT

By utilizing intelligent construction technology, the production process of the steel fabric for simply - supported box girders in high - speed railways has been upgraded from manual binding to automatic welding. However, welding can affect the fatigue performance of steel bars. To evaluate this impact, fatigue tests were conducted on five groups of specimens as well as the base metal. The test results indicate that fatigue failure occurred at the welded spot, presenting as a brittle failure. As the stress amplitude decreases, the fatigue life of the specimens increases significantly. The fatigue life is more sensitive to stress changes at low - stress amplitudes. When the stress ratio increases, both the fatigue life and the stress amplitude decrease, and the sensitivity of the fatigue life and stress amplitude to the stress ratio gradually increases. On the overall fatigue S - N curve, the stress amplitude corresponding to a fatigue life of 2 million cycles for the welded steel bar was approximately 128.72 MPa. Compared with the base metal, the stress amplitude decreased by 45.75%. The stress amplitude under ultra - high cyclic loading was predicted. The coupling relationship of stress-amplitude stress-ratio fatigue-cycle was fitted and analyzed, relevant equations were derived, and a safety line for the values of stress amplitude and stress ratio was determined.

ARTICLE HISTORY

Received: 26 February 2025
Revised: 26 June 2025
Accepted: 26 June 2025

KEYWORDS

Cross-welded steel bars;
Fatigue test;
S-N curve;
Stress ratio;
Fatigue performance

1. Introduction

With the rapid expansion of the high - speed railway network in China, the construction technology for high - speed railways has also advanced significantly [1-2]. In the simply - supported box girders of high - speed railways, a large number of steel bars are arranged to form a steel fabric. Traditionally, the steel fabric is fabricated manually by workers, which leads to low efficiency, slow construction progress, and high costs. With the advancement of intelligent construction technology in high - speed railway bridge construction[3], automatic spot welding construction has been adopted to substitute the manual binding of steel bars in the construction of steel fabric. This not only significantly enhances construction efficiency, cuts down labor costs, but also speeds up the progress of bridge construction. However, fatigue issues of welded steel bars emerge subsequently[4-5]. Traditional manual construction methods do not damage the steel bars, but automatic spot welding can cause localized damage to the steel bar. When high - speed trains frequently pass over the bridges, the dynamic loads generated may lead to fatigue damage of the steel bars, thereby affecting the operational safety of the entire bridge. Therefore, it is essential to investigate the fatigue performance of welded steel bars[6-8].

For the fatigue performance of welded steel, scholars both at home and abroad have conducted relevant research[9-12]. For welded steel bars, Wang et al. [13] carried out fatigue tests on HRB400 electric arc - welded steel bars. The test results indicated that the fatigue strength decreased slightly as the stress ratio and the diameter of the steel bars increased. The design p - S - N curve of the electric arc - welded steel bars was obtained through fitting. Sheng et al. [14] performed low - frequency and high - frequency fatigue tests on steel bars of different specifications and diameters to derive the S - N curves. Zheng et al. [15] conducted experimental research and analysis on the fatigue strength of flash - butt welding specimens made of HRB500 high strength steel. The fatigue strengths of the base metal and the weldment were determined using the S - N curve and the lifting method. In addition, China's codes also contain relevant provisions regarding the fatigue performance of welded steel bars. In the "Code for Design of Concrete Structures of Railway Bridges and Culverts (TB10092 - 2017)" [16], the fatigue strengths of the base metal, flash - butt welding, electric arc welding, and other welding forms are specified. The allowable fatigue stress amplitudes of the base metal, flash - butt welding, and electric arc welding are 145 MPa, 130 MPa, and 60 MPa respectively. In the "Code for Design of Concrete Structures (GB 50010 - 2010)" [17], the fatigue stress amplitudes of HRB400 steel bars with different stress ratios range from 31 MPa to 175 MPa.

The objects of the above research and codes are only for the base metal or the welded joint of two steel bars in the same straight line. However, in the steel fabric of the simply - supported box girder of the high - speed railway, the steel bar connections are cross - welded spot connections. For this type of cross - welded spot connection, after the steel bars are cross - welded, they remain continuous through - length bars. Only at the welded spot positions of the steel bars, the base metal suffers certain damage. The cross - welded spot connection differs from the aforementioned flash - butt welding steel bars where the two steel bars form a welded joint in the same straight line. For the cross - welded steel bars, Schwarzkopf [18] verified the fatigue limit state and established a fatigue limit state verification method based on the Palmgren - Miner rule. Gu et al. [19, 20] investigated the fatigue performance of welded steel fabrics made of cold - rolled ribbed steel bars (CRB550), hot - rolled ribbed steel bars (HRB400), and high ductility cold - rolled ribbed steel bars (CRB600H), and presented S - N curve equations. Li et al. [21] conducted high cycle fatigue tests on base metal specimens and specimens with welded joints at different stress levels. The fatigue performance of both was analyzed. The S - N curves and p - S - N curves were obtained, and fatigue reliability analysis was performed. As can be seen, although the fatigue performance of cross - welded steel bars has been studied both domestically and internationally, the relevant literature is still very limited. Currently, for the fatigue performance of cross - welded spot steel bars in high - speed railway box girders, there is no relevant code in China. Only in the "Technical Specification for Concrete Structures with Welded Steel Fabric (JGJ114 - 2014)" [22], Article 3.1.7 stipulates that when welded steel fabrics made of CRB550, CRB600H, and HRB400 steel bars are used for plate flexural members, fatigue performance needs to be checked. When the maximum stress of the steel bar does not exceed 300 MPa, the limit value of the fatigue stress amplitude for 2 million cycles can be taken as 100 MPa. It is evident that the codes are very rough and not suitable for the fatigue of cross - welded steel bars in high - speed railway box girders. The research on the fatigue performance of cross - welded steel bars in high - speed railway box girders is still in its initial stage. It is necessary to conduct further in - depth studies on the fatigue performance of cross - welded steel bars.

In this paper, the fatigue performance of cross - welded steel bars was investigated. Based on the test results, the fatigue S - N curve of the cross - welded steel bars was derived through fitting. The research findings offer theoretical support for the operational safety of high - speed railways and serve as a reference for the future formulation of relevant codes. This paper is divided into six parts. Firstly, the “Introduction” summarizes the current research status of the fatigue performance of welded steel bars, with a primary focus on those used in China. Secondly, the “Test Overview” describes the specimens of welded steel bars, including specimen fabrication and testing methods. Thirdly, the “Test results and analysis” mainly focuses on analyzing the test results and the failure of the specimens. Fourthly, the “Fatigue S - N Curves” section theoretically analyzes the fatigue test results and fits the fatigue S - N curves under different working conditions. Fifthly, the “Further study on fatigue performance” mainly explores the fatigue performance of cross - welded steel bars under ultra - high cycle loads and the influence of coupling factors on fatigue life. Finally, the “Conclusion” summarizes the findings of the research in this paper.

2. Test overview

2.1. Specimen design

Referring to relevant literature[19,20], the specimen was designed as a cross - connection of two steel bars. One was a 300 mm long steel bar, and the other was a 40 mm long steel bar, as shown in Fig. 1. According to the diameter of the steel bars, the specimens were divided into five groups, namely M1 - M5. Among them, in the M4 and M5 groups, a 19 mm × 0.9 mm steel strip was welded onto the steel bars, as shown in Table 1. In addition, to compare the effect of welding on the fatigue performance of steel bars, fatigue tests were also conducted on the base metal specimens. Each base metal specimen was 300 mm long and 12 mm in diameter, and there were 3 base metal specimens in total. All specimens were made of HRB400 steel bars.

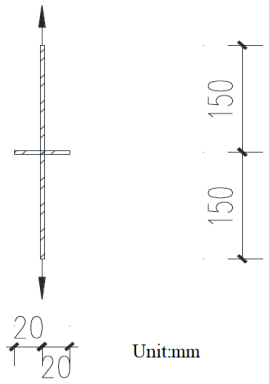

Fig. 1 Detailed specimen dimension

Table 1
Specimen groups

Group	Direction	Diameter /mm
M1	Longitudinal	12
	Transverse	16
M2	Longitudinal	12
	Transverse	12
M3	Longitudinal	12
	Transverse	18
M4	Longitudinal	18
	Transverse	19×0.9 steel strip
M5	Longitudinal	12
	Transverse	19×0.9 steel strip
Base metal	Longitudinal	12

2.2. Fatigue loading scheme

Fatigue tests were conducted under different stress ratios and stress amplitudes. For each of the specimen groups from M1 to M5, there were many working conditions, and two specimens were used for each working condition, resulting in a total of 126 specimens. The stress ratio had three levels: 0.1, 0.2, and 0.4. The stress amplitude was set at intervals of 100 MPa, with a maximum stress of 400 MPa to cover the stress range of the HRB400 steel bars. The working conditions of the fatigue tests are presented in Table 2.

Based on the loading mode of fatigue load, fatigue tests can be classified into constant amplitude loading and variable amplitude loading. In this test, constant amplitude loading was adopted, as shown in Fig. 2. The fatigue test was carried out at room temperature. The steel bars were subjected to tension - tension loading with a sinusoidal load at a frequency of 20 Hz. According to Chinese codes [22, 23], the test would be terminated if the specimen had not fractured after reaching 2 million cycles. Three specimens were prepared for the fatigue test of the base metal. The maximum stresses were set at 400 MPa, 350 MPa, and 300 MPa respectively, and the stress ratio was set at 0.2, as shown in Table 2. The fatigue loading mode of the base metal was the same as that of the welded specimens.

Table 2
Fatigue test working conditions of M1~M5 and base metal

Stress ratio	Maximum stress /MPa	Minimum stress /MPa	Stress amplitude /MPa	Number of specimens	Note
0.1	400	40	360	2	M1~M5
	300	30	270	2	
	200	20	180	2	
	100	10	90	2	
0.2	400	80	320	2	
	300	60	240	2	
	200	40	160	2	
	100	20	80	2	
0.4	400	160	240	2	
	300	120	180	2	
	200	80	120	2	
	100	40	60	2	
0.2	400	80	320	1	Base metal
	350	70	280	1	
	300	60	240	1	

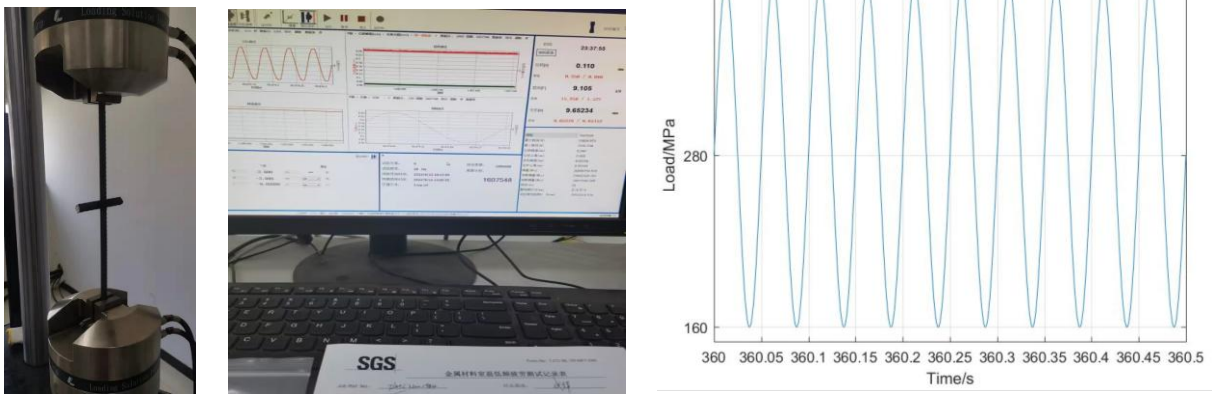

(a) Fatigue testing (b) Data acquisition (c) Load history diagram of fatigue test

Fig. 2 Fatigue test

3. Test results and analysis

3.1. Static test

To assess the impact of welding on the static mechanical properties of steel bars, three cross-welded specimens were randomly chosen for the static tensile test prior to the fatigue test. The yield strength and ultimate tensile

strength values of the specimens are presented in Table 3. As shown in Table 3, the static strength of the specimens did not decrease. This indicates that the static properties of the steel bars were not significantly affected by welding. The possibility that the static strength of the steel bars could decrease due to welding factors, which could in turn affect the fatigue performance, was ruled out.

Table 3
Static test results

	M1	M2	M3
Yield strength /MPa	400	445	435
Ultimate strength /MPa	635	675	635

3.2. Specimen failure diagram

The failure diagrams of the static and fatigue tests of the specimens are shown in Fig. 3. As shown in Fig. 3(a), when the specimen was subjected to static tension, the failure occurred at the non-welded position. The specimen exhibited an obvious necking fracture, and the steel bar yielded, which was a typical ductile failure. As shown in Fig. 3(b), when the specimen was subjected to a fatigue load, the failure occurred at the cross-welded position. Part of the cross-section was smooth, while the other part was relatively rough. A corrugated fatigue fracture could be observed. The reason for this lies in the fatigue damage process. Firstly, there were welding defects at the welded position of the specimen. Welding would cause local heating of the steel bar, and the uneven temperature field would lead to local plastic deformation of the steel bar. After welding, residual stress and stress concentration were generated in the steel bar. The area with residual stress and stress concentration near the welding point of the steel bar was a pre-existing defect. It was easy for this area to form the initial source of fatigue. Under the action of the fatigue load, fatigue micro-cracks originated from the fatigue source and propagated. As the number of repeated loads increased, the crack propagation zone was gradually formed. The interface within the crack propagation zone was continuously rubbed and squeezed under the cyclic load, thus forming a smooth section area. When the crack propagation zone had propagated to the critical size, the remaining area of the steel bar was insufficient to bear the external fatigue load, and the specimen suddenly fractured. Unlike the ductile failure of the specimen under static tension, fatigue failure was a sudden brittle failure, which posed a hazard.

(a) Static failure of specimens

(b) Fatigue failure of specimens

Fig. 3 Comparison of static and fatigue failure

Table 4
Fatigue test results of the M1 group

Stress ratio	Specimen number	Number of cycles /×10^4	Fracture position	Specimen number	Number of cycles	Fracture position
0.1	M1-0.1-400-1	9.4188	Non-welded area	M1-0.1-400-2	10.2685	Welding position
	M1-0.1-300-1	35.557	Welding position	M1-0.1-300-2	44.9155	Welding position
	M1-0.1-200-1	200	No fracture	M1-0.1-200-2	200	No fracture
	M1-0.1-100-1	200	No fracture	M1-0.1-100-2	200	No fracture
0.2	M1-0.2-400-1	7.3595	Welding position	M1-0.2-400-2	9.3068	Welding position
	M1-0.2-300-1	43.3597	Welding position	M1-0.2-300-2	41.6827	Welding position
	M1-0.2-200-1	200	No fracture	M1-0.2-200-2	200	No fracture
	M1-0.2-100-1	200	No fracture	M1-0.2-100-2	200	No fracture
0.4	M1-0.4-400-1	19.6338	Welding position	M1-0.4-400-2	18.9725	Welding position
	M1-0.4-300-1	176.6307	Welding position	M1-0.4-300-2	62.464	Welding position
	M1-0.4-200-1	200	No fracture	M1-0.4-200-2	200	No fracture
	M1-0.4-100-1	200	No fracture	M1-0.4-100-2	200	No fracture

Note: M1 represents the grouping number, 0.1 represents the test stress ratio, 400 represents the maximum stress, and 1 indicates that it is the No.1 specimen under the working condition. No fracture indicates that the specimen is not damaged by fatigue after 2 million cycles and the test is terminated.

3.3. Fatigue test results

Based on the aforementioned fatigue test scheme, the fatigue test was carried out, and the test results of the M1 group are presented in Table 4. The results of the other groups are similar and will not be listed here. The test data points are plotted on the double - logarithmic coordinate system, as shown in Fig. 6 below. For the test working condition with a maximum stress of 400 MPa, it is evident from the test results that fatigue damage occurred in all specimen groups. For the test working condition with a maximum stress of 300 MPa, only one specimen in the M3 group with a stress ratio of 0.1 reached 2 million cycles without fatigue failure, while the rest of the specimens experienced fatigue failure. For the test working condition with a maximum stress of 200 MPa, most of the specimens did not undergo fatigue failure after 2 million cycles. For the test working conditions with a maximum stress below 200 MPa, no fatigue failure occurred in any of the specimens. At a stress ratio of 0.1 and a maximum stress of 200 MPa, the stress amplitude was 180 MPa. Accordingly, it can be predicted that the stress amplitude for 2 million cycles at a stress ratio of 0.1 should be greater than 180 MPa. Similarly, it can be predicted that the stress amplitudes for 2 million cycles at stress ratios of 0.2 and 0.4 should be higher than 160 MPa and 120 MPa, respectively.

4. Fatigue S-N curves

4.1. Fatigue S-N curve fitting method

There are several fitting models for the fatigue S - N curve of steel bars. Currently, the mathematical expressions of the fatigue S - N curve are mainly the exponential function, power function, and three - parameter power function [24-25], which correspond to the single - logarithm linear model, double - logarithm linear model, and double - logarithm three - parameter power function model, respectively. Additionally, based on the double - logarithmic linear model, a double - logarithmic polyline model is derived by setting an inflection point at a certain location. Considering the advantages and disadvantages of each model and referring to the European standard "Design of Steel Structures - Part 1 - 9: Fatigue EN 1993 - 19:2005" [26], the fatigue S - N curve in this study is fitted using the double - logarithmic polyline model, with a fatigue life of 2 million cycles as the inflection point. The fatigue S - N curve of the double - logarithmic polyline model consists of two straight - line segments. The first segment is represented by a line segment with a steeper slope, corresponding to a fatigue life of less than 2 million cycles. It is fitted using the least - squares method based on the power - function curve equation.

$$NS^m = \mathrm{C} \tag{1}$$

In the above equation, m and C are two constants determined experimentally. In this paper, the relationship between the number of fatigue cycles and the stress amplitude is investigated. The stress amplitude is defined as $S = \Delta\sigma = \sigma_{max} - \sigma_{min}$. Taking the logarithm for both sides of Equation (1), Equation (2) is derived as follows.

$$lgN = \mathrm{b} + \mathrm{m}lg\Delta\sigma \tag{2}$$

From equation (2), it is evident that the exponential function expression is equivalent to the linear relationship between $lg\Delta\sigma$ and lgN in semi - logarithmic coordinates. Therefore, the model obtained by this method is generally referred to as a linear model, which represents the nonlinear relationship in a linear logarithmic equation.

The second segment is represented by a line segment with a slope m=m+2, corresponding to a fatigue life of more than 2 million cycles. The reason for setting the slope m=m+2 is that the stress amplitude at a low-stress level is not simply linearly related to that at a high-stress level, A commonly used approach is to adopt m=m+2 as the slope to reflect the characteristics of fatigue life at low-stress level[27].

Considering the survival rate (i.e., reliability), the fatigue S-N curve is corrected. A common method is to add the deviation obtained from test point statistics to equation (2) [28], as shown in Equation (3). In the Equation (3), $c = \alpha m_N\sqrt{1-\theta^2}$, where m_N is the logarithm mean squared deviation of the cycle number, and θ is the correlation coefficient. When $\alpha = 2$, the survival rate is 97.7%.

$$lgN = \mathrm{b} + \mathrm{m}lg\Delta\sigma + \mathrm{c} \tag{3}$$

4.2. Fatigue S-N curve of base metal

The fatigue test results of the base metal are presented in Fig. 4. As can be seen, when the stress amplitude decreased from 320 MPa to 280 MPa, the fatigue life increased by 253,300 cycles, a 2.53 - fold increase. When the stress amplitude decreased from 280 MPa to 240 MPa, the fatigue life increased by 1,458,500 cycles, a 4.48 - fold increase. It is evident that the stress amplitude has a significant impact on the fatigue life, and the number of fatigue cycles decreases nonlinearly as the stress amplitude increases. According to the test results, the rate of decrease in fatigue life in the stress amplitude range of 240 MPa to 280 MPa is higher than that in the range of 280 MPa to 320 MPa, indicating a higher sensitivity of fatigue life to low - stress amplitudes.

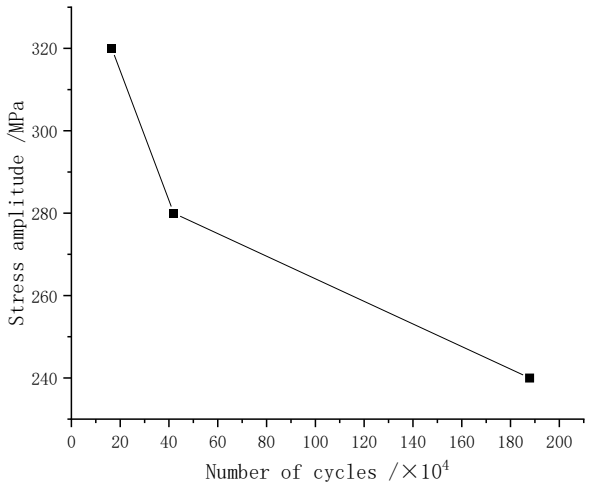

Fig. 4 Fatigue test results of base metal

The fatigue S - N curves of the base metal were derived through fitting based on the fatigue test results, as presented in Table 5. These curves were plotted out in a double - logarithmic coordinate system, as shown in Fig. 5. The stress amplitude corresponding to a fatigue life of 2 million cycles calculated by the fitting curve was approximately 236.49 MPa. After correcting the fitting results according to a survival rate of 97.7%, the fatigue stress amplitude for 2 million cycles was approximately 230.16 MPa. Notably, this value was higher than the stress amplitude of 156 MPa for HRB400 steel bars specified in the "Code for Design of Concrete Structures"[17] under the condition of a stress ratio of 0.2.

Table 5
Fatigue S-N curve equation for base metal

Fatigue S-N curve	R-squared of fitting	Stress amplitude for 2 million cycles /MPa		
		Test value	Correction value	Decrease rate
lg*N*=26.40113-8.46742lg*Δσ* (*N*≤2000000) lg*N*=31.14876-10.46742lg*Δσ* (*N*≥2000000)	0.99	236.49	230.16	2.75%

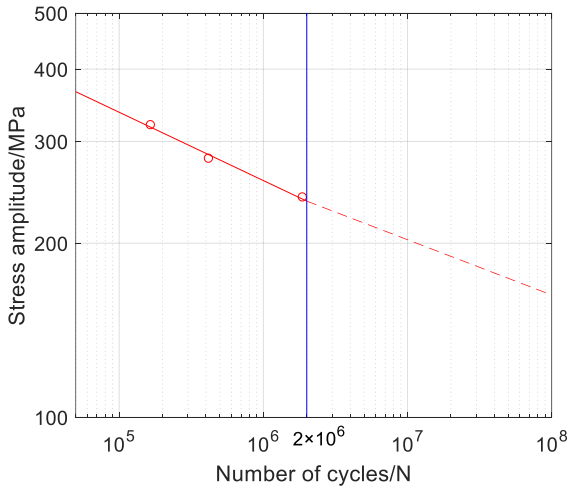

Fig. 5 Fatigue S-N curve of base metal

4.3. Fatigue S-N curve analysis under each working condition

Based on the test results, the fatigue S - N curves of Groups M1 - M5 under different stress ratios were fitted, as presented in Table 6. The calculated stress amplitude for 2 million cycles ranges from a minimum of 91.87 MPa in the M4 group under the stress ratio of 0.4 to a maximum of 194.03 MPa in the M1 group under the stress ratio of 0.1, with an average stress amplitude of 147.61 MPa. After correcting the fitting results according to a survival rate of 97.7%, the modified stress amplitudes were obtained. The stress amplitudes of each group decreased to varying degrees, ranging from approximately 3.36% to 24.87%, with an average decrease of 12.09%. The modified minimum stress amplitude was 81.19 MPa, the maximum was 186.10 MPa, and the average was 130.36 MPa.

Comparing with the conclusions drawn from the analysis of test results in Section 3.3 above, where the stress amplitudes for 2 million cycles at the three stress ratios should be higher than 180 MPa, 160 MPa, and 120 MPa, the stress amplitudes obtained from the fatigue S - N curves were lower. This indicates that the stress amplitudes obtained by the linear fitting method are relatively conservative.

From the fitted curve, it can be clearly seen that when the stress amplitude was constant, the fatigue life decreased with the increase of the stress ratio. This law was particularly evident in M1 to M4. For M5, the fatigue S - N curve corresponding to a stress ratio R=0.4 was higher. Moreover, the fatigue S-N curves fitted for the stress ratios R=0.2 and R=0.1 showed relatively higher coincidence compared with the stress ratio R=0.4, indicating that as the stress ratio increased, the sensitivity of fatigue life to the stress ratio gradually increased.

Table 6
Fatigue S-N curves for each group with different stress ratios

Groups	Stress ratios	Fatigue S-N curve	R-squared of fitting	Strss amplitude for 2 million cycles /MPa		
				Test value	Correction value	Decrease rate
M1	0.1	$\lg N=17.45131-4.87366\lg\Delta\sigma$ ($N\leq2\times10^6$) $\lg N=22.02704-6.87366\lg\Delta\sigma$ ($N\geq2\times10^6$)	0.984	194.03	186.10	4.09%
	0.2	$\lg N=19.16802-5.68836\lg\Delta\sigma$ ($N\leq2\times10^6$) $\lg N=23.69199-7.68836\lg\Delta\sigma$ ($N\geq2\times10^6$)	0.990	182.80	176.66	3.36%
	0.4	$\lg N=19.30300-5.88915\lg\Delta\sigma$ ($N\leq2\times10^6$) $\lg N=23.71856-7.88915\lg\Delta\sigma$ ($N\geq2\times10^6$)	0.841	161.36	139.69	13.43%
M2	0.1	$\lg N=13.92056-3.48984\lg\Delta\sigma$ ($N\leq2\times10^6$) $\lg N=18.28725-5.48984\lg\Delta\sigma$ ($N\geq2\times10^6$)	0.574	152.53	114.59	24.87%
	0.2	$\lg N=17.26281-4.88849\lg\Delta\sigma$ ($N\leq2\times10^6$) $\lg N=21.74754-6.88849\lg\Delta\sigma$ ($N\geq2\times10^6$)	0.799	174.73	147.88	15.37%
	0.4	$\lg N=15.23831-4.17604\lg\Delta\sigma$ ($N\leq2\times10^6$) $\lg N=19.51858-6.17604\lg\Delta\sigma$ ($N\geq2\times10^6$)	0.766	138.08	114.91	16.78%
M3	0.1	$\lg N=15.50731-4.10088\lg\Delta\sigma$ ($N\leq2\times10^6$) $\lg N=19.99721-6.10088\lg\Delta\sigma$ ($N\geq2\times10^6$)	0.967	175.77	165.28	5.97%
	0.2	$\lg N=12.71205-3.02412\lg\Delta\sigma$ ($N\leq2\times10^6$) $\lg N=16.95197-5.02412\lg\Delta\sigma$ ($N\geq2\times10^6$)	0.813	131.81	112.39	14.73%
	0.4	$\lg N=16.70012-4.80759\lg\Delta\sigma$ ($N\leq2\times10^6$) $\lg N=21.02623-6.80759\lg\Delta\sigma$ ($N\geq2\times10^6$)	0.998	145.56	143.21	1.62%
M4	0.1	$\lg N=13.29931-3.29484\lg\Delta\sigma$ ($N\leq2\times10^6$) $\lg N=17.54733-5.29484\lg\Delta\sigma$ ($N\geq2\times10^6$)	0.978	133.05	121.23	8.89%
	0.2	$\lg N=13.6621-3.44057\lg\Delta\sigma$ ($N\leq2\times10^6$) $\lg N=17.94108-5.44057\lg\Delta\sigma$ ($N\geq2\times10^6$)	0.950	137.88	119.51	13.32%
	0.4	$\lg N=10.24624-2.00962\lg\Delta\sigma$ ($N\leq2\times10^6$) $\lg N=14.17256-4.00962\lg\Delta\sigma$ ($N\geq2\times10^6$)	0.998	91.87	81.19	11.62%
M5	0.1	$\lg N=13.32842-3.29892\lg\Delta\sigma$ ($N\leq2\times10^6$) $\lg N=17.58884-5.29892\lg\Delta\sigma$ ($N\geq2\times10^6$)	0.885	134.96	119.74	11.28%
	0.2	$\lg N=14.36774-3.77073\lg\Delta\sigma$ ($N\leq2\times10^6$) $\lg N=18.64633-5.77073\lg\Delta\sigma$ ($N\geq2\times10^6$)	0.899	137.82	123.29	10.54%
	0.4	$\lg N=16.66334-4.72691\lg\Delta\sigma$ ($N\leq2\times10^6$) $\lg N=21.04773-6.72691\lg\Delta\sigma$ ($N\geq2\times10^6$)	0.962	155.67	145.67	6.42%

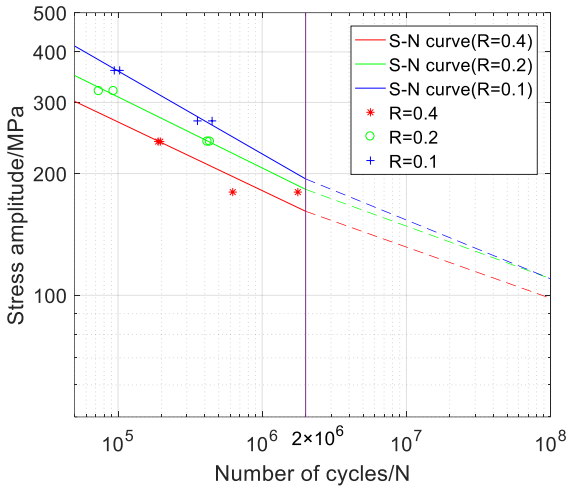

(a) Fatigue S-N curves for M1

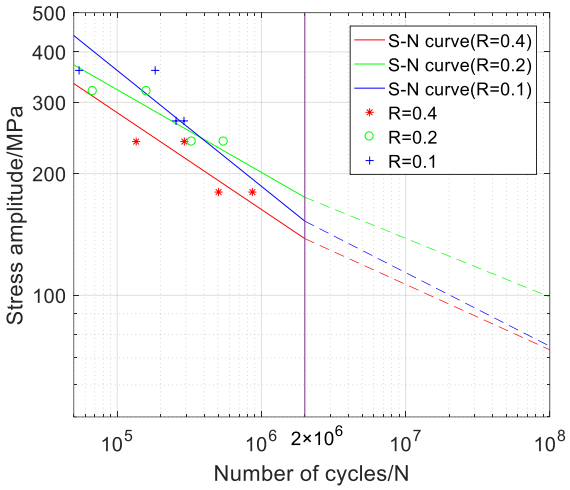

(b) Fatigue S-N curves for M2

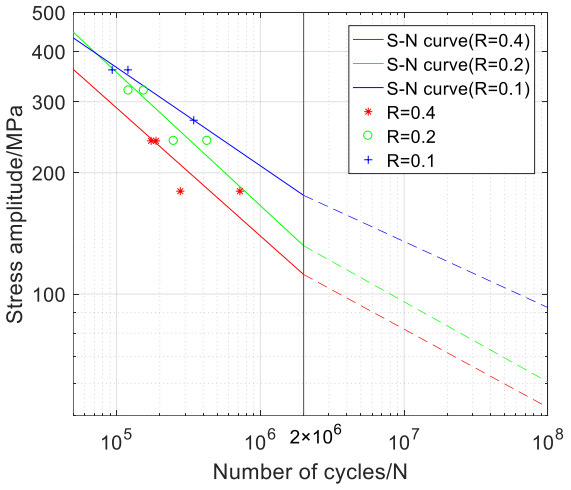

(c) Fatigue S-N curves for M3

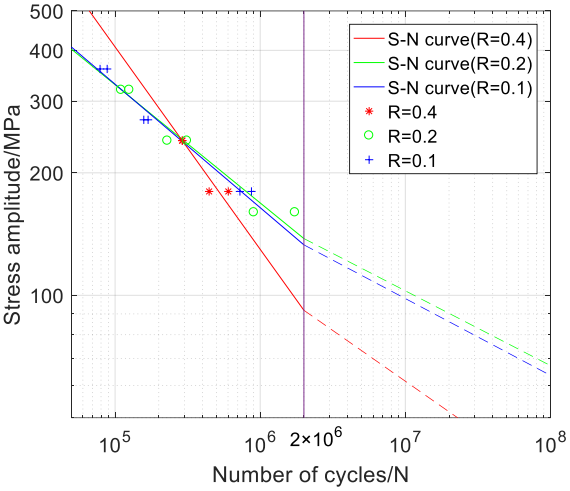

(d) Fatigue S-N curves for M4

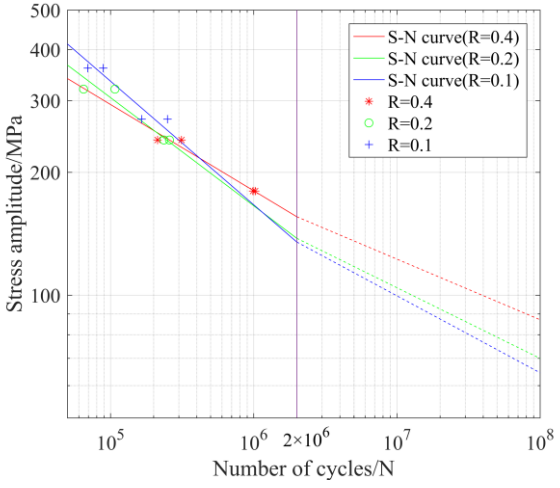

(e) Fatigue S-N curves for M5

Fig. 6 Fatigue S-N curves for each group with different stress ratios

The stress amplitudes of the five groups under different stress ratios were analyzed. Based on the stress amplitude and stress ratio for 2 million cycles in Table 6, the relationship curve was fitted and presented in Table 7. Sheng et al [14] combined his test results with the suggested values of stress amplitude and stress ratios in the "Code for the Design of Concrete Structures" [17] to fit the relationship curve between stress amplitude and stress ratio. To facilitate comparison, the curves provided by Sheng et al. were equivalently transformed. Similarly, corresponding equations were fitted according to the values specified in the code. The comparison among the test results of this paper, the stress amplitude stress ratio curves from the literature [14], and the code [17] is shown in Fig. 7. It can be observed that the smaller the stress ratio, the smaller the slope of the curve, and the sensitivity of the fatigue stress amplitude to the stress ratio gradually decreased as the stress ratio increased.

4.4. Analysis of total fatigue S-N curve

In Section 4.3 above, the fatigue S - N curve analysis was conducted for each working condition of Groups M1 - M5. To gain an overall understanding of the fatigue performance of cross - welded steel bars, all test data under various working conditions were integrated to fit the fatigue S - N curve, as presented in Table 8. The fatigue S - N curves of the cross - welded steel bars as a whole and the base metal are shown in Fig. 8. It is evident that welding has a significant impact on the fatigue performance of steel bars, notably reducing their fatigue life. As the stress amplitude increases, the fatigue life of the welded steel bars decreases rapidly, much faster than that of the base metal. The stress amplitude of the cross - welded steel bars for 2 million cycles is 128.72 MPa, while that of the base metal is 236.49 MPa. The stress amplitude of the cross - welded steel bars is 45.75% lower than that of the base metal.

Based on a survival rate of 97.7%, the fitting results were corrected. After correction, the stress amplitude of the welded steel bars for 2 million cycles was 100.49 MPa, while that of the base metal was approximately 230.16 MPa. The stress amplitude of the welded steel bars was 56.34% lower than that of the base metal. In literature [20], the reported stress amplitude was 156.64 MPa. In the European code [29], the specified stress amplitude was about 100.04 MPa, and in the German code [30], it was around 99.17 MPa. These results are summarized in Table 9. Evidently, the modified test results were lower than those reported in literature [20] and close to the values specified in the codes [29-30].

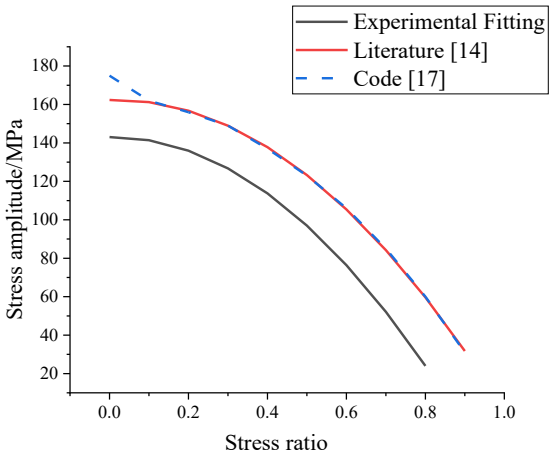

Fig. 7 Stress amplitude stress ratio relationship curve

Table 7
Stress amplitude stress ratio relationship equation

Item	Equation	Note
Experimental Fitting	$\Delta\sigma = -188.82\rho^2 + 2.25\rho + 143.049$	In the equation: ρ indicates the stress ratio, and $\Delta\sigma$ indicates the stress amplitude.
Literature [14]	$\Delta\sigma = -167.44\rho^2 + 5.6\rho + 162.32$	
Code [17]	$\Delta\sigma = -138.63\rho^2 - 27.2\rho + 170.16$	

Table 8
Fatigue S-N curve for total cross-welded steel bars

Fatigue S-N curve equation	R-squared of fitting	Stress amplitude for 2 million cycles and decreasing rate			
		Test value /MPa	Decreasing rate/MPa	Correction value/MPa	Decreasing rate/%
lg$N$=12.80034-3.08075lg$\Delta\sigma$ (N≤2×10⁶) lg$N$=17.01964-5.08075lg$\Delta\sigma$ (N≥2×10⁶)	0.796	128.72	45.75	100.49	56.34

Table 9
Summary and comparison of stress amplitude

Item	Test	Test correction	Base metal	Literature [20]	Code[29]	Code[30]
Stress amplitude /MPa	128.72	100.49	230.16	156.64	100.04	99.17

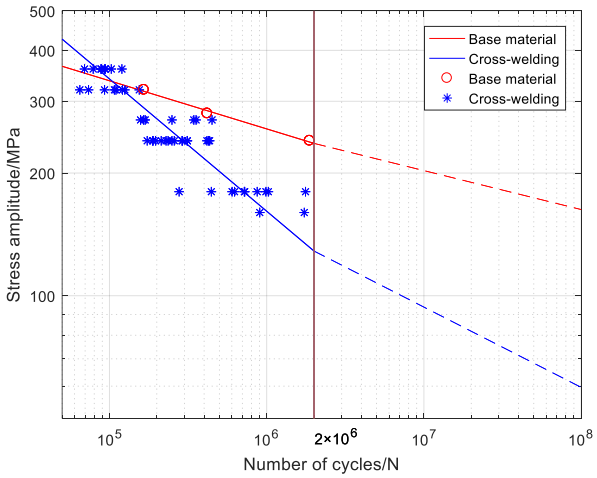

Fig. 8 Comparison of fatigue S-N curves between welded steel bar and base metal

5. Further study on fatigue performance

5.1. Ultra-high cycle stress amplitude

The existing codes use 2 million fatigue cycles as an important indicator to measure the fatigue life of steel bars in building structures. However, high - speed railways operate at high speeds and with high frequency. In an actual simply - supported box girder, the number of fatigue cycles of steel bars may far exceed 2 million. Currently, China's high - speed railway codes do not explicitly specify the fatigue life of steel bars. In this paper, it is assumed that a high - speed train runs on a high - speed railway line every 5 minutes. According to the design service life of 100 years, the number of fatigue cycles of steel bars will exceed 10 million. The literature [20, 31-32] has indicated that the number of high - speed train operations can reach hundreds of millions within the design service life. Evidently, using 2 million cycles as an indicator of fatigue life does not meet the actual needs of high - speed railway operation. Therefore, the stress amplitude under ultra - high cyclic loads should be studied.

The stress amplitudes from this test and different literatures under different fatigue cycle numbers under ultra - high cyclic loads are listed in Table 10. The stress amplitude under ultra - high cyclic loads is predicted from the fatigue S - N curve obtained in Section 4. For comparison, based on relevant literatures, the inflection point of the fatigue curve was set at 10 million cycles. When the number of fatigue cycles exceeded 10 million, the stress amplitude of the steel bar dropped below 80 MPa. Considering the survival rate, the corrected stress amplitude was only 59.60 MPa, which was 42.46% lower than the results reported in literature [19], but close to the results specified in the codes [29-30]. It can also be observed from Fig. 9 that the test results in this paper lie between the results reported in literatures [19- 20] and those specified in the codes [29-30]. The modified curve shows a high degree of consistency with the fatigue S - N curves given in the codes [29-30].

Table 10
Stress amplitude at ultra-high cycle load

No.	Source	Fatigue S-N curve	Stress amplitude for different fatigue cycles /MPa						
			1×10^6	2×10^6	4×10^6	6×10^6	8×10^6	10^7	10^8
1	Test	$\lg N=12.80034-3.08075\lg\Delta\sigma$ ($N<10^7$) $\lg N=17.01964-5.08075\lg\Delta\sigma$ ($N\geq10^7$)	161.20	128.72	102.79	90.11	82.08	76.34	48.52
2	Test correction	$\lg N=12.80034-3.08075\lg\Delta\sigma$ ($N<10^7$) $\lg N=16.56588-5.08075\lg\Delta\sigma$ ($N\geq10^7$)	125.85	100.49	80.25	70.35	64.08	59.60	37.88
3	Literature [20]	$\lg N=14.7811-3.8639\lg\Delta\sigma$ ($N<10^7$) $\lg N=18.8081-5.8639\lg\Delta\sigma$ ($N\geq10^7$)	187.33	156.56	130.85	117.82	109.36	103.23	69.70
4	Literature [20]	$\lg N=19.5581-5.9792\lg\Delta\sigma$ ($N<10^7$) $\lg N=23.7563-7.9792\lg\Delta\sigma$ ($N\geq10^7$)	185.16	164.89	146.84	137.21	130.77	125.98	94.40
5	Literature [19]	$\lg N=12.3214-3.0\lg\Delta\sigma$ ($N<10^7$) $\lg N=15.8690-5.0\lg\Delta\sigma$ ($N\geq10^7$)	127.98	101.58	80.62	70.43	63.99	59.40	37.48
6	Code[29]	$\lg N=12.3016-3.0\lg\Delta\sigma$ ($N<10^7$) $\lg N=15.8360-5.0\lg\Delta\sigma$ ($N\geq10^7$)	126.05	100.04	79.40	69.37	63.02	58.51	36.91
7	Code [30]	$\lg N=12.2902-3.0\lg\Delta\sigma$ ($N<10^7$) $\lg N=15.8170-5.0\lg\Delta\sigma$ ($N\geq10^7$)	124.95	99.17	78.71	68.76	62.47	58.00	36.59

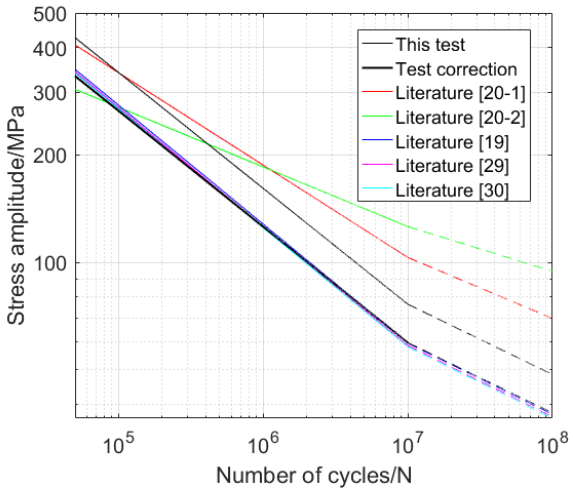

Fig. 9 Comparison of the fatigue S-N curve for cross-welded steel bars

5.2. Analysis of multi-factor coupling influence on fatigue life

The effects of stress amplitude and stress ratio on fatigue life were derived from the test results and fitting fatigue S-N curves. In the three-dimensional coordinate system, taking the stress - amplitude, stress - ratio, and fatigue - cycle as coordinate parameters, the curved surfaces of three influencing factors were fitted. The curved surfaces equation is listed in Equation (4), the fitting R variance is 0.7127, and the curved surface of stress - amplitude stress - ratio fatigue - cycle is shown in Fig. 10 (a). From Fig. 10 (a), the characteristics of the three factors can be observed. When the stress - amplitude is smaller, the fatigue - cycle is higher and the stress - ratio is larger, the curvature of the surface is larger, indicating that in the low-stress amplitude region with high fatigue life, the fatigue - cycle is more sensitive to the stress - amplitude. The greater the stress ratio is, the stronger the sensitivity is.

The intersection line between a plane representing 2 million fatigue cycles and the surface was determined. This intersection line was projected onto the stress - amplitude stress - ratio plane, and the relationship curve between stress - amplitude and stress - ratio was obtained, as shown in Fig. 10 (b). The curve divides the coordinate system into two regions. The values of stress - amplitude and stress - ratio in the region below the curve meet the requirement of 2 million cycles. Under the corresponding working conditions of stress - amplitude and stress - ratio in this region, the fatigue performance of cross - welded steel bars can be ensured.

A comparison of the stress - amplitude stress - ratio curves between Fitting Method 1 in Section 4.3 (Fig. 7) and Fitting Method 2 (Fig. 10) is presented in Fig. 11. As can be observed from Fig.11, there was little difference between the two methods in the stress ratio range of 0 to 0.4, and the error was within 10%. However, the difference between the two methods gradually increased when the stress ratio exceeded 0.4.

Based on the fatigue S - N curve obtained through the linear fitting method in Table 6, the fatigue lives under different working conditions were obtained and compared with the experimental results. The average error was 31.12%. When the fatigue lives obtained by the three - dimensional fitting method were compared with the experimental results, the average error was 18.54%. The three - dimensional fitting method outperforms the linear fitting method in the stress ratio range of 0 to 0.4. In actual engineering, fatigue cyclic loads with a stress ratio greater than 0.4 are rare, and the available data is insufficient. Accurately predicting the stress - amplitude stress - ratio relationship may require more test data for support.

$$f(x,y)=p_{00}+p_{10}x+p_{01}y+p_{20}x^2+p_{11}xy+p_{30}x^3+p_{21}x^2y \quad (4)$$

Where x is the stress amplitude, y is the stress ratio, and the coefficients are taken as shown in Table 11.

Table 11
Curvilinear equation coefficients

Parameter	p_{00}	p_{10}	p_{01}	p_{20}	p_{11}	p_{30}	p_{21}
Coefficients Value	1.218×10^7	-1.231×10^5	4.951×10^6	422.3	4.472×10^4	- 0.4767	- 106.4

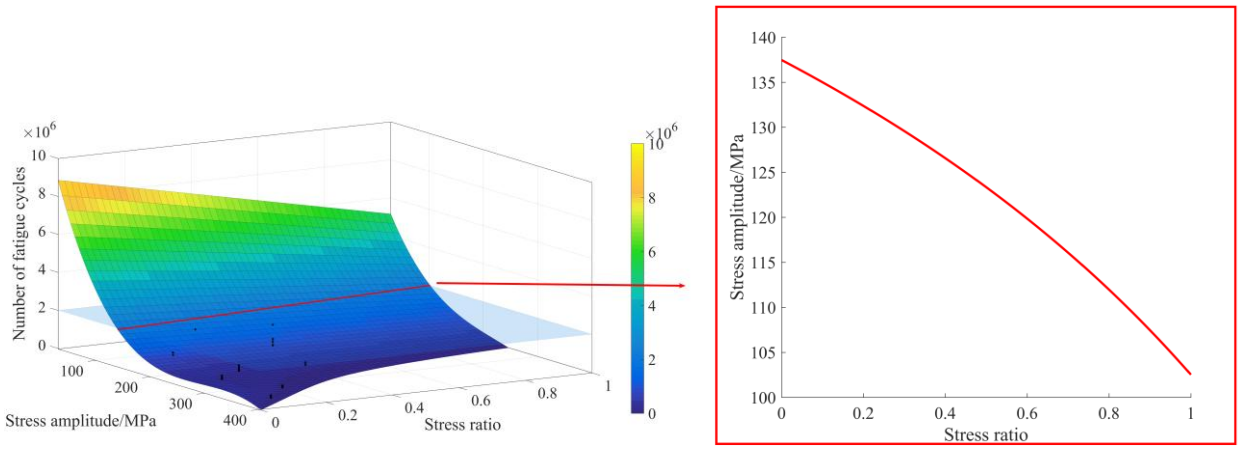

(a) Surface of stress-amplitude stress- ratio fatigue-cycle (b) Line for stress-amplitude stress- ratio

Fig. 10 The curved surface of stress-amplitude stress- ratio fatigue-cycle

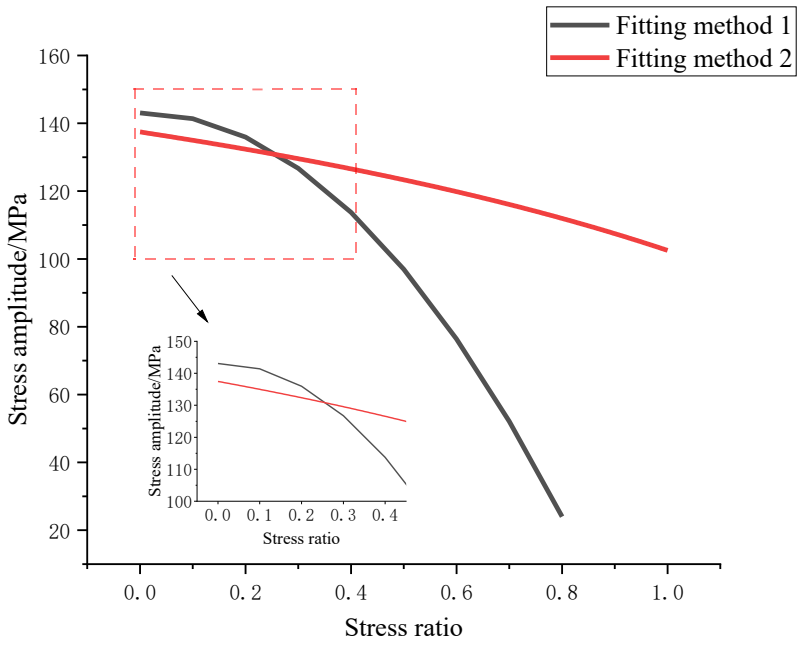

Fig. 11 Comparison of stress-amplitude stress-ratio curve

6. Conclusions

For the fatigue performance of steel bars in the simply - supported box girders of high - speed railways, this paper conducts experimental research and theoretical analysis on cross - welded steel bars and the base metal. The main conclusions of this study are as follows.

(1) Welding does not have a significant impact on the static strength of the specimens. The failure modes of the specimens indicate that in static tensile tests, failure occurs at the non - welded positions, which is a typical necking ductile failure. In contrast, fatigue failure occurs at the welded spots and is a brittle failure.

(2) Stress amplitude and stress ratio are two crucial factors influencing the fatigue life. The greater the stress amplitude, the lower the fatigue life. At low stress amplitudes, the fatigue life exhibits higher sensitivity. As the stress ratio increases, the fatigue life decreases, the stress amplitude reduces, and the sensitivity of both the fatigue life and the stress amplitude to the stress ratio gradually increases.

(3) The fatigue S - N curve of the base metal indicates that the number of fatigue cycles decreases non - linearly as the stress amplitude increases. For a fatigue life of 2 million cycles, the stress amplitude of the base metal is approximately 230.16 MPa, while the stress amplitudes of specimens M1 - M5 range from 91.87 MPa to 194.03 MPa. Based on a survival rate of 97.7%, the modified stress amplitudes range from 81.19 MPa to 186.10 MPa, with an average value of 130.36 MPa. The overall stress amplitude of all specimens is 128.72 MPa. After correction, this value drops to 100.49 MPa, which is 45.75% lower than that of the base metal.

(4) The stress amplitude under ultra - high cycle loading is predicted. When the number of fatigue cycles exceeds 10 million, the stress amplitude drops below 80 MPa. After correction, it reaches 59.60 MPa. The coupling relationship among stress-amplitude, stress-ratio, and fatigue-cycle is fitted and analyzed, and the relevant formula is derived. A comparison between the two fitting methods is conducted. Finally, a safety line for stress-amplitude and stress-ratio is established.

Acknowledgments

This work was funded by the Science Research Project of Hebei Education Department (Grant No. ZD2022140) and the Natural Science Foundation in Hebei Province (Grant No. E2024202216).

References

[1] H.-B. Liu, S. Li, L. Xu, and Z.-B. Yu, “Identification of wheel-rail forces on high-speed railways based on physical model and hybrid recursive neural networks,” *Engineering Structures*, vol. 338, p. 120547, 2025.

[2] J.-J. Deng, H.-Y. Zhai, and Z.-J. Wang, “Vulnerability evaluation of high-speed railway network under wind disasters,” *Reliability Engineering and System Safety*, vol. 264(PA), p.111323, 2025.

[3] C.-F. Lu, J.-F. Liu, Y.-H. Liu, and Y.-M. Liu,“ Intelligent construction technology of railway engineering in China,” *Frontiers of Engineering Management*, vol.6,no.02,pp.503-516, 2019.

[4] T. Skriko, K. Lipiäinen, A. Ahola, H. Mettänen,and T. Björk, “Fatigue strength of longitudinal load-carrying welds in beams made of ultra-high-strength steel,” *Journal of Constructional Steel Research*, vol.179, p.106563, 2021.

[5] Z.-Y. Jie, W.-J. Wang, P. Zhuge, Y.-D. Li, and X. Wei, "Fatigue properties of inclined cruciform welded joints with artificial pits," *Advanced Steel Construction*,vol.17,no.01,pp. 20-27, 2021.
[6] A. Aloisio, D. Lavorato, J.-Q. Xue, J.-J. Wu, A. Rasulo, B. Briseghella, and C. Nuti, "The role of overstrength in welded joints for rebar substitution in damaged RC columns," *Construction and Building Materials*, vol.409, p.133952, 2023.
[7] Y.-Z. Jiang, Z.-Y. Xin, D.-Y. Wang, and T. Ou, "Structural fatigue performance of L-shaped support in continuous welded stainless steel roof system," *Journal of Constructional Steel Research*, vol.214, p.108507,2024.
[8] Q. Cheng, Z.-A. Yao, H.-Y. Chen, D.-W. Liu, M.-Y. Lin, Q. Zhao, and B. Zhang, "Study on corrosion fatigue degradation performance of welded top plate-U rib of cross-sea steel box girder," *Buildings*, vol.13, p.7, 2023.
[9] M. Gu, L.-W. Tong, X.-L. Zhao, and Y.-F. Zhang, "Numerical analysis of fatigue behavior of welded cfchs T-joint," *Advanced steel construction*, vol. 10, no. 04, pp. 476-496, 2014.
[10] H. Miao, T.Yamashita,K. Ushioda, S. Tsutsumi,Y. Morisada,and H. Fujii,"Improving fatigue property of linear friction welded cruciform joints of low carbon steel," *Journal of Manufacturing Processes*,vol.338,pp. 55-64, 2025.
[11] H.-L. Luo, K.-C. Qu, C. Yu, Q.-H. Kan, and G.-Z. Kang, "Experimental study on multiaxial ratchetting-fatigue interaction of SUS301L stainless steel tubular welded joint," *International Journal of Fatigue*, vol. 186, p.108411, 2024.
[12] W.- Z. Wang, Z.-Y. Jie, G. -J. Yu, L.- F. Xiao, and Y. -Z. Fan, "Unified fatigue life calculation of Q460c steel fillet weld cruciform joints considering fatigue crack initiation and propagation," *Advanced Steel Construction*, vol. 20, no. 03, pp. 222-231, 2024.
[13] Y.-F., Wang, W. Wang, and Y.-Q. Liu, "Experimental research on the fatigue performance of lapped welded splices of high strength reinforcing bars," *Journal of Railway Engineering Society*, vol. 38, no. 03, pp. 113-117, 2021.
[14] X.-W. Sheng, W.-Q. Zheng, and J.-Z. Lei, "Experimental study on fatigue behavior of high strength steel bars connected by flash butt welding in railway engineering," *China Civil Engineering Journal*, vol. 50,no. 12, pp. 56-61, 2017.
[15] W.-Q. Zheng, and X.-W. Sheng, "Welding properties for HRB500 high-strength steel bars connected by flash butt welding," *China Civil Engineering Journal*, vol. 52, no. 07, pp. 22-29, 2019.
[16] TB 10092-2017, "Code for the Design of Concrete Structures for Railway Bridges and Culverts," China Railway Publishing House Co., Ltd. 2017.
[17] GB 50010-2010, "Code for Design of Concrete Structures," China Construction Industry Press, 2016.
[18] M. Schwarzkopf, "Fatigue design of tack-welded mesh reinforcing bars," *Structural Engineering International*, vol. 5, no. 02, pp. 102-106, 1995.
[19] W.-L. Gu, and Z.-L. Lin, "Experimental research on fatigue properties of welded fabric," *Building Structure*, vol. 42, no. 01, pp. 105-107+90, 2012.
[20] W.-L. Gu, and A.-P. Zhu, "Experimental Research on Fatigue S-N Curves of Welded Fabric," *Construction Technology*, vol. 46, no. 04, pp. 71-74+103, 2017.
[21] C. Li, G.-S. Liu, and S.-Y. Wang, "Experimental Study on Fatigue Properties of Welded Steel Fabric," *Bulletin of Science and Technology*, vol. 38, no. 08, pp. 79-84,2022.
[22] JGJ 114-2014, "Technical specification for concrete structures reinforced with welded steel fabric," China Construction Industry Press, 2014.
[23] GB/T 28900-2022, "Test methods of steel for reinforcement of concrete," State Administration for Market Regulation, 2022.
[24] H. Esmaeili,M. Avateffazeli,M. Haghshenas,and R. Rizvi. "A Hybrid Framework for Characterizing and Benchmarking Fatigue S-N Curves in Aluminum Alloys by Integrating Empirical and Data-Driven Approaches,"*Fatigue & Fracture of Engineering Materials & Structures*, vol. 48,no. 1, pp. 44-59, 2024.
[25] M. Agrawal,M. Gupta,R T D. Prabhakaran, and P. Mahajan, "A comparative study of static and fatigue performance of glass and basalt fiber reinforced epoxy composites," *Polymer Composites,* vol. 45,no. 4, pp. 3551-3565, 2024.
[26] BS-EN 1993-1-9:2005, "Design of steel structures —Part 1-9: Fatigue,"U.K.: GEN, 2005.
[27] W.-Z. Yao, X.-W. Li, P.-S. Dong, "Fatigue-resistant design theory and method for welded structures," China Machine Press, 2017.
[28] JGJ/T 27-2014, "Standard for test methods of welded joint of reinforcing steel bars," China Construction Industry Press,2014.
[29] CEN. EN 1992-1-1. "Eurocode 2: Design of concrete structures—Part 1–1: general rules and rules for buildings," European Committee for Standardization, Brussels, 2004.
[30] DIN 1045-1, "Tragwerke aus Beton, Stahlbeton und Spannbeton Teil 1: Bemessung und Konstruktion," 2008.
[31] J.-X. Wen, H.-J. Li, F.-L. Huang, Z.-Q. Yang, Z. Wang, and Z.-L. Yi, "Fatigue Performance Test System for Ballastless Track Concrete of High Speed Railway," *Railway Engineering*, vol. 62, no. 12, pp. 7-11, 2022.
[32] J.-W. Zhang, C.-B. Cai, S.-Y. Zhu, M.-Z. Wang, Q.-L. He, S.-F. Yang, and W.-M. Zhai, "Experimental investigation on dynamic performance evolution of double-block ballastless track under high-cycle train loads," *Engineering Structures*, vol. 254, p. 113872, 2022.

Advanced Steel Construction – Vol. 22 No. 2 (2026) 153–169
DOI:10.18057/IJASC.2026.22.2.3

EXPERIMENTAL STUDY ON FLEXURAL PERFORMANCE OF LARGE-SECTION PARTIALLY ENCASED COMPOSITE BEAM WITH WEB OPENINGS

Hong-Xin Liu [1, 2], Ping Yang [3], Yu-Kun Yang [4], Jie Li [5], Ya-Ming Li [1, 2], Shui-Zhong Jia [1, 2] and Xiao-Meng Xie [4, *]

[1] *Shanghai Institute of Architectural Design and Research Co., Ltd., Shanghai 200041, China*
[2] *Shanghai Engineering Research Center of Spatial Structure, Shanghai 200041, China*
[3] *The Government Investment Project Proxy Construction Center of Kangbashi District, Ordos City, Erdos 017000, China*
[4] *Shanghai Jieyi Construction Technology Co., Ltd., Shanghai 201311, China*
[5] *Tongji University, Shanghai 201206, China*
** (Corresponding author: E-mail: xiexiaomeng2024@163.com)*

ABSTRACT

To investigate the effect of openings on the flexural performance of large-section partially encased composite beams (referred to as large-section PEC beams), static tests were conducted on five large-section PEC beams with different configurations. The study focused on the influence of web openings in the primary and secondary beams on the flexural performance, ductility, and failure modes of the specimens under four-point bending. The results indicate that under static loading, all specimens exhibited good ductility, with strength-to-yield ratios ranging from 1.18 to 1.30, and retained some strength reserves after reaching the yield load. Web openings slightly reduced the load-bearing capacity and sectional stiffness of the specimens. The strain in the main steel component and the concrete strain along the section height approximately exhibited a linear distribution, conforming to the plane section assumption. A finite element model was developed based on the test results. The load-deflection curves and stress contours matched well with the experimental results, and the error between the simulated and experimental ultimate load-bearing capacities was within 10%. The flexural load-bearing capacity calculated using the proposed method for large-section PEC beams with web openings showed minor deviations from the experimental values, with minimal influence from size effects, confirming the safety and reliability of the adopted formulas.

ARTICLE HISTORY

Received: 16 March 2025
Revised: 29 June 2025
Accepted: 2 July 2025

KEYWORDS

Large-section PEC beams;
Failure mode;
Flexural capacity;
Ductility;
Finite element analysis

1. Introduction

Steel-concrete composite beams represent a hybrid structural form that integrates the high compressive capacity of concrete with the tensile strength and ductility of steel materials [1–4]. These composite systems have seen broad adoption in bridge engineering, industrial buildings, and various civil structures due to their excellent stiffness, strong load-bearing ability, and limited deformation under service loads [5–8]. A specific form of such systems, known as partially encased composite (PEC) members, is produced by embedding shear connectors into the flanges of steel profiles and casting concrete around them [9]. During the prefabrication process, PEC components require only lateral formwork, thereby simplifying the construction procedure. The concrete confined within the flange regions significantly mitigates the likelihood of both overall and local buckling, thus contributing to a higher structural capacity [10–11]. When compared to traditional steel components, PEC beams display marked improvements in fire resistance [12–13], as well as notable enhancements in flexural and shear behavior [14–15], which has led to growing interest in their application both in domestic and international contexts.

To date, extensive research has been carried out on the mechanical behavior and practical applications of PEC beams. Nakamura et al. [16] demonstrated that, compared with conventional I-section steel beams, the flexural and shear load-bearing capacities of PEC beams are increased by factors of 2.08 and 2.98, respectively. Through both experimental studies and numerical modeling, He et al. [17–18] identified that PEC beams with corrugated steel webs possess enhanced shear resistance and greater fracture modulus, and further introduced a corresponding shear capacity calculation approach. Nardin et al. [19] focused on how construction methods influence the flexural behavior of PEC beams, concluding from experimental observations that bottom bolts contribute to an increase in fracture modulus. In a study by Kindmann et al. [20], 12 PEC beams featuring different cross-sectional configurations were subjected to bending tests, which confirmed that concrete encased within flanges contributes positively to both flexural stiffness and capacity. Furthermore, the adoption of advanced concrete materials with improved tensile performance has led to notable enhancements in the flexural behavior of steel-concrete composite beams [21–23]. Hao et al. [24] performed shear tests on PEC-UHPC composite beams, revealing their exceptional performance in resisting shear forces.

Compared to traditional steel beams, PEC beams exhibit improved load-bearing capacity and ductility. However, the concrete poured into the web increases the component's weight and cost, and the segmented casting process required for PEC beams reduces construction efficiency. To address these issues, it is common practice to introduce web openings in the steel web. These openings serve multiple engineering purposes: they reduce structural self-weight, facilitate the passage of mechanical, electrical, and plumbing (MEP) systems through the beam, and eliminate the need for flipping the beam for casting—thus enabling one-sided formwork and continuous concrete pouring, which significantly improves constructability and efficiency. Compared to traditional PEC beams, PEC beams with web openings enhance material utilization and simplify construction. Recent studies have begun to explore this configuration. Zhao et al. [25], for instance, proposed two new types of honeycomb PEC beams and investigated the effects of web openings, compressed steel flanges, and filled concrete on the mechanical performance of beams.

However, their study was limited to small-span specimens with relatively modest cross-sectional dimensions. In practical applications, large-section PEC beams are often needed to satisfy increasing span and load requirements that exceed the capacity of conventional PEC configurations. These large-section beams also benefit from web perforations, which help reduce self-weight and support single-pass, one-sided casting without flipping, thereby improving production efficiency. In this study, experimental and finite element investigations were conducted on large-section PEC beams with various forms and sizes of process openings in the web. The failure modes, load-bearing capacity, main steel strain, component deformation, and ductility were analyzed to examine the influence of web openings on the flexural performance of large-section PEC beams. A calculation method for the flexural load-bearing capacity of large-section PEC beams was also proposed.

2. Experimental program

2.1. Specimen design

The specimens were developed in accordance with the *Technical Specification for Partially Encased Steel-Concrete Composite Structures* (T/CECS 719—2020) [26], and were labeled as PECB1 (primary beam), PECB2 (secondary beam), PECB3 (primary beam with web openings type 1), PECB4 (secondary beam with web openings), and PECB5 (primary beam with web openings type 2). All tested beams feature cross-sectional heights greater than 600 mm, thus qualifying as large-section PEC beams. The main steel members were fabricated using Q355-B steel, while HRB400 steel was utilized for both tie rods and anti-crack reinforcement. C30-grade concrete was applied in the web regions. The designed span length l_0 was 10,800 mm for PECB1, PECB3, and PECB5, and 7,200 mm for PECB2 and PECB4. Fig. 1 provides the detailed structural layout of each specimen.

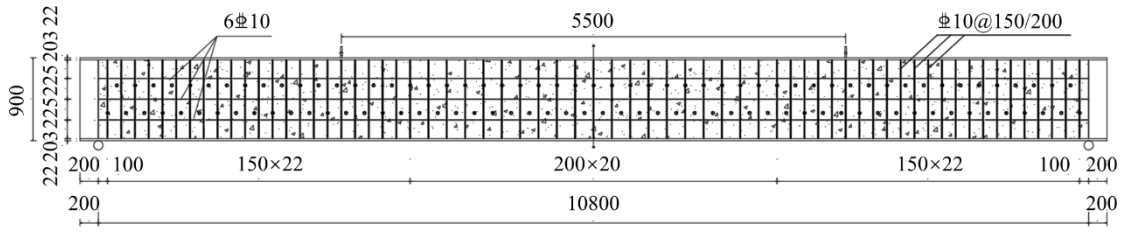

(a) Specimen PECB1 elevation

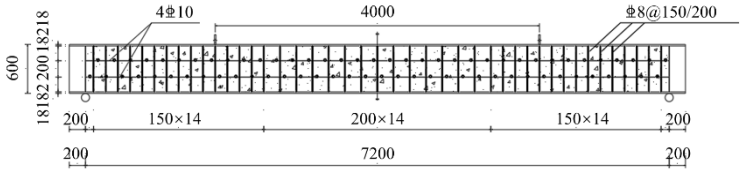

(b) Specimen PECB2 elevation

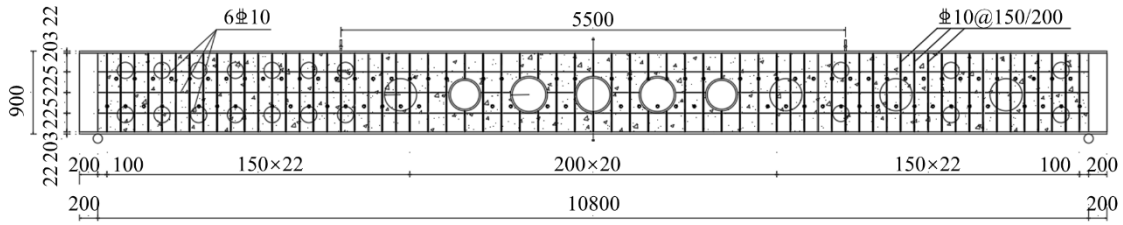

(c) Specimen PECB3 elevation

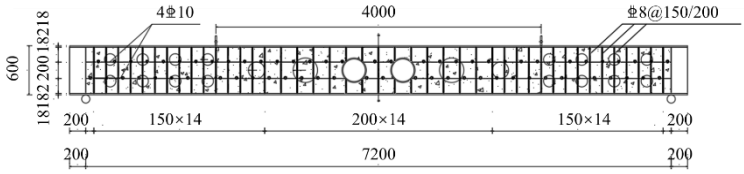

(d) Specimen PECB4 elevation

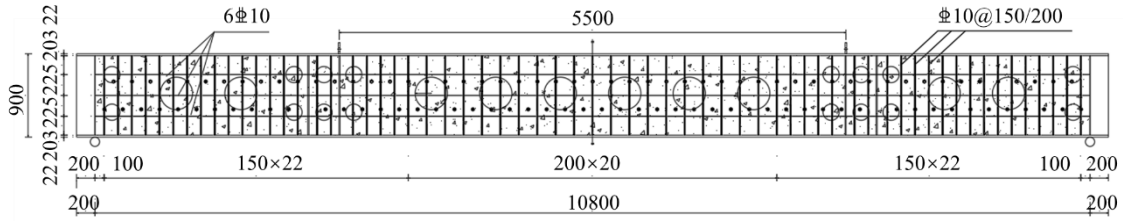

(e) Specimen PECB5 elevation

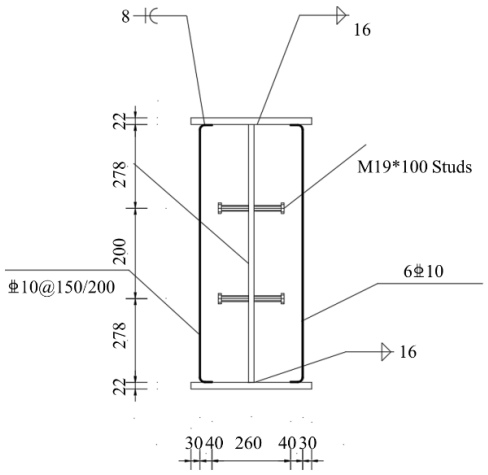

(f) Middle section of main beam span

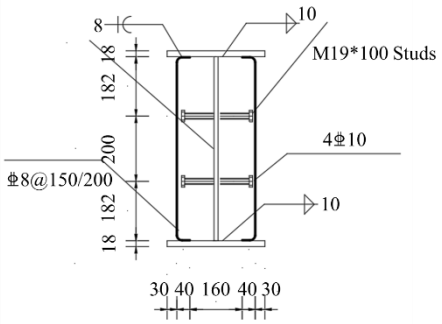

(g) Mid-span section of secondary beam

Fig. 1 Schematic diagram of PEC beams

Table 1
Basic parameters of specimen design

Number	Calculated length l_0 /mm	Height h_a / mm	Width b_f / mm	Flange thickness t_f / mm	Web thickness t_w / mm	Steel ratio / %	Web opening ratio / %
PECB1	10800	900	400	22	18	8.63	-
PECB2	7200	600	300	18	12	9.04	-
PECB3	10800	900	400	22	18	8.63	15.36
PECB4	7200	600	300	18	12	9.04	17.98
PECB5	10800	900	400	22	18	8.63	14.56

The key geometric and material parameters are summarized in Table 1. In specimen PECB3, web openings included five unfilled holes at midspan with a diameter of 400 mm, quarter-span holes of 350 mm, and additional openings of 175 mm. For PECB4, midspan openings measured 300 mm in diameter (with two left unfilled), quarter-span openings were 200 mm, and the remaining were 140 mm. In contrast, PECB5 adopted a midspan opening diameter of 350 mm and 175 mm for the others, with all web perforations fully filled with concrete to accommodate the casting process. The spacing of tie rods was arranged at 200 mm within the pure bending region and reduced to 150 mm in the bending-shear transition zone. The steel ratio for the section was computed exclusively based on the cross-sectional area of structural steel components.

2.2. Material properties

The material property tests for the concrete were conducted in the Building Materials Laboratory at Tongji University, following the national standard testing method "Standard for Test Methods of Physical and Mechanical Properties of Concrete" (GB/T50081-2019)[27]. Under the same curing conditions, the compressive strength of the concrete cube is 31.1 MPa. The material properties of the steel were determined according to the "Tensile test method for metal materials at room temperature " (GB/T 228.1-2010) [28]. Standard tensile tests were performed using the universal testing machine in the Structural Engineering Laboratory at Tongji University, with the loading apparatus shown in Fig. 3. All steel plates used for the specimens were taken from the same batch of steel and were cut into proportional samples for testing. The yield strength f_y, ultimate strength f_u, and elastic modulus E of the steel materials with different thicknesses are listed in Table 2.

Table 2
Material properties of steel

Number	t/mm	f_y/MPa	f_u/MPa	E/MPa
1	12	408.13	524.31	231378
2	18	390.81	488.79	223478
3	22	408.49	499.13	215244

2.3. Loading protocol and measurement

Specimens PECB1, PECB3, and PECB5, which have larger spans and higher cross-sectional load-bearing capacities, were subjected to monotonic loading using two 350-ton actuators. The loading points were located at the one-third points of the span, with the specific loading setup shown in Fig. 2(a). Specimens PECB2 and PECB4, which have smaller spans and lower cross-sectional load-bearing capacities, were tested using a single 350-ton actuator. The vertical concentrated load applied by the actuator was distributed to the test specimens through a rigid distribution beam. The loading points were located at one-third of the calculated span, with the specific loading setup shown in Fig. 2(b). To achieve simply supported boundary conditions, one end of the specimens was configured as a sliding hinge support, while the other end was a fixed hinge support.

(a) Loading device of PECB1, PECB3 and PECB5 specimens

(b) Loading device of PECB2 and PECB4 specimens

Fig. 2 Specimen loading diagram

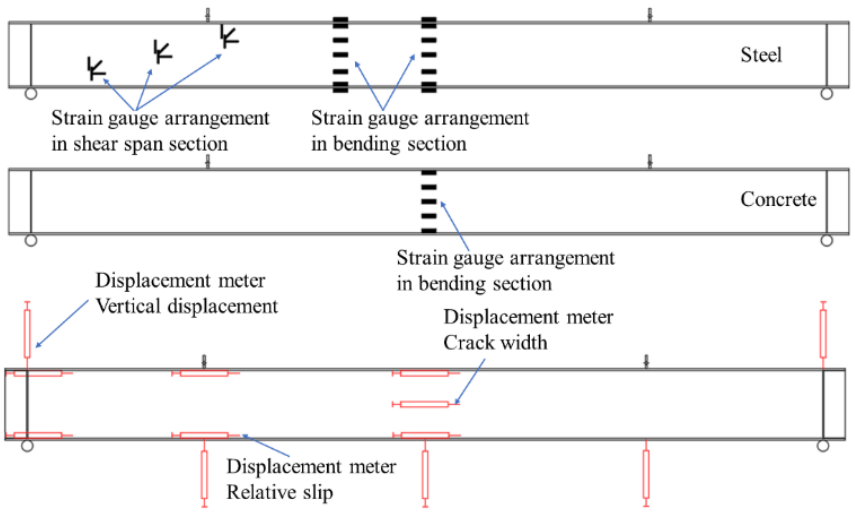

Fig. 3 Displacement gauge and strain gauge layout

The formal loading process adopted a force-controlled loading phase followed by a displacement-controlled loading phase. For specimens PECB1, PECB3, and PECB5, each of the two jacks applied 60 kN per loading step (approximately 0.05 P_u, where P_u is the ultimate load of the beam) at a loading rate of 20 kN/min. For specimens PECB2 and PECB4, the load per step was 30 kN (approximately 0.05 P_u) at a loading rate of 10 kN/min. After reaching half

of the estimated ultimate load (calculated as the yield load using the transformed section method), the control mode was switched to displacement-controlled loading, with each step increasing by 5 mm at a rate of 5 mm/min. Loading continued until the specimen failed, ensuring that the deflection at the loading point exceeded 300 mm within the effective stroke of the jack. The specific layout of the test measurement points is shown in Fig. 3.

3. Experimental results analysis

3.1. Failure pattern of specimen

Specimen PECB1 entered the cracked working stage after being loaded to 348.2 kN (approximately 0.11 P_u). The midspan deflection at this point was 5.35 mm (l_0/2019). At 1397.3 kN (approximately 0.45 P_u), the maximum midspan crack width reached the serviceability limit (0.3 mm), and the midspan deflection was 28.88 mm (l_0/374). At 2640.8 kN (approximately 0.85 P_u), the midspan deflection exceeded the serviceability limit (l_0/200), and the yield strain (2700 με) was reached in the upper and lower steel flanges. The midspan deflection was 81.62 mm (l_0/132). At 3090.2 kN (P_u), partial spalling of the top surface concrete at the midspan occurred. The midspan deflection exceeded 1/50 of the calculated span, meeting the failure criteria for the specimen, and the test was terminated. The pure bending zone at the final failure of specimen PECB1 is shown in Fig. 4.

Specimen PECB2 entered the cracked working stage after being loaded to 193.5 kN (approximately 0.11 P_u), with a midspan deflection of 4.04 mm (l_0 /1881). At 1276.6 kN (approximately 0.70 P_u), the midspan deflection exceeded the serviceability limit (l_0/200), reaching 48.57 mm (l_0/156). At 1560.9 kN (approximately 0.86 P_u), the maximum crack width on both sides of the midspan reached the serviceability limit (0.3 mm). The upper and lower steel flanges achieved the yield strain (2400 με), and the midspan deflection was 79.33 mm (l_0/96). At 1813.6 kN (P_u), slight spalling occurred on the top surface concrete at the midspan. The midspan deflection exceeded 1/50 of the calculated span, reaching the failure criteria for the specimen, and the test was terminated. The pure bending zone at the final failure of specimen PECB2 is shown in Fig. 5.

(a) Specimen failure diagram

(b) North side area

(c) Mid-span region

(d) South side area

Fig. 4 Final failure state of specimen PECB1

(a) Specimen failure diagram

(b) North side area

(c) Mid-span region

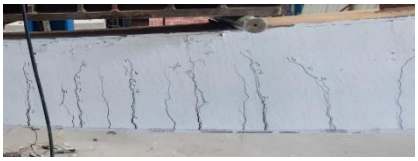

(d) South side area

Fig. 5 Final failure state of specimen PECB2

(a) Specimen failure diagram

(b) North side area

(c) Mid-span region

(d) South side area

Fig. 6 Final failure state of specimen PECB3

Specimen PECB3 entered the cracked working stage after being loaded to 339.9 kN (approximately 0.11 P_u), with a midspan deflection of 5.70 mm (l_0/1896). At 2140.4 kN (approximately 0.69 P_u), the midspan deflection approached the serviceability limit (l_0/200), and the maximum crack width on both sides reached the serviceability limit (0.3 mm). The midspan deflection was 53.37 mm (l_0/202). At 2463.8 kN (approximately 0.79 P_u), the upper and lower steel flanges achieved the yield strain (2700 με), and the midspan deflection was 86.63 mm (l_0/125). At 3107.9 kN (P_u), abnormal noises were heard, and partial spalling occurred on the top surface concrete at the midspan. The midspan deflection exceeded 1/50 of the calculated span, meeting the failure criteria, and

the test was terminated. The pure bending zone at the final failure of specimen PECB3 is shown in Fig. 6.

Specimen PECB4 entered the cracked working stage after being loaded to 413.9 kN (approximately 0.23 P_u), with a midspan deflection of 10.17 mm (l_0 /708). At 1244.5 kN (approximately 0.70 P_u), the midspan deflection exceeded the serviceability limit (l_0/200), reaching 36.82 mm (l_0/195). At 1450.6 kN (approximately 0.82 P_u), the maximum crack width on both sides of the midspan reached the serviceability limit (0.3 mm), and the midspan deflection reached 79.33 mm (l_0/96). At 1627.5 kN (0.92 P_u), the upper and lower steel flanges achieved the yield strain (2700 με), and the midspan deflection reached 117.65 mm (l_0/61). At 1776.7 kN (P_u), partial spalling occurred on the top surface concrete at the midspan, and cracks at the web openings became more pronounced. The midspan deflection exceeded 1/50 of the calculated span, meeting the failure criteria, and the test was terminated. The pure bending zone at the final failure of specimen PECB4 is shown in Fig. 7.

(a) Specimen failure diagram (b) North side area

(c) Mid-span region (d) South side area

Fig. 7 Final failure state of specimen PECB4

Specimen PECB5 entered the cracked working stage after being loaded to 646.8 kN (approximately 0.21 P_u), with a midspan deflection of 10.17 mm (l_0 /708). At 2284.7 kN (approximately 0.74 P_u), the upper and lower steel flanges achieved the yield strain (2700 με), the midspan deflection exceeded the serviceability limit (l_0/200), and the maximum crack width on both sides of the midspan reached the serviceability limit (0.3 mm). The midspan deflection was 71.17 mm (l_0/152). At 3100.1 kN (P_u), partial spalling occurred on the top surface concrete at the midspan. The midspan deflection exceeded 1/50 of the calculated span, meeting the failure criteria, and the test was terminated. The pure bending zone at the final failure of specimen PECB5 is shown in Fig. 8.

Compared with the unfilled specimen PECB3, PECB5 exhibited significantly different cracking behavior in the region surrounding the web openings. Due to the presence of concrete infill, no radiating or diagonal cracks were observed extending from the hole edges. Instead, the cracks remained primarily vertical and concentrated in the pure bending zone, with more uniform distribution and smaller crack widths. This indicates that the concrete filling within the web openings helped to redistribute internal stresses and reduce stress concentrations at the hole periphery, thereby effectively suppressing the development of radial cracks. The improved crack pattern also contributed to more stable crack propagation and delayed local damage near the openings, as evidenced by the relatively intact concrete surface shown in Fig. 8.

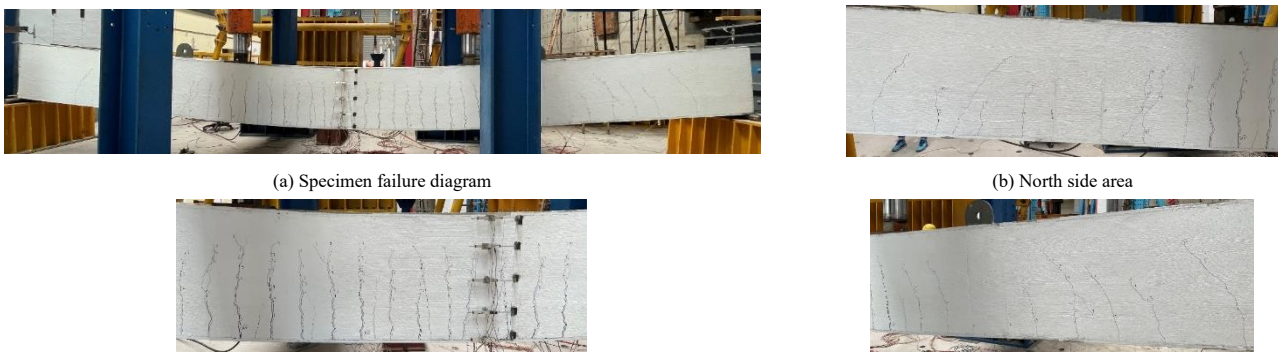

(a) Specimen failure diagram (b) North side area

(c) Mid-span region (d) South side area

Fig. 8 Final failure state of specimen PECB5

In summary, all five specimens initially exhibited concrete cracking, followed by steel flange yielding and eventual spalling of the top concrete surface at midspan, with midspan deflections exceeding the failure criteria. Notably, in specimens with unfilled web openings such as PECB3, the altered load transfer path around the openings led to the formation of radiating cracks extending downward from the hole edges. These cracks were accompanied by wider crack widths and more pronounced spalling and bulging of the concrete above the openings. In contrast, specimens with filled openings, such as PECB5, exhibited predominantly vertical cracks without significant radiating patterns, and the surrounding concrete remained largely intact. These observations indicate that concrete infill effectively mitigates local stress concentrations and inhibits the development of radial cracking.

3.2. Load-mid-span deflection curve

Fig. 9 presents the load–midspan deflection curves for the test specimens, which can be clearly divided into two behavioral phases. (1) Elastic Stage: Prior to the yielding of the tensile flange, the concrete is effectively restrained by the main steel structure and the reinforcement, resulting in slow crack initiation and negligible stiffness degradation. During this phase, the load–deflection relationship remains largely linear. (2) Elasto-plastic Stage: Once the tensile flange yields, the specimen enters a stage characterized by inelastic behavior. Cracks in the web concrete begin to propagate rapidly, diminishing their structural contribution and causing a gradual reduction in sectional stiffness. The corresponding deflection curve develops noticeable inflection points and deviates from linearity, showing increased midspan displacement and clear bending deformation. With continued loading, the bottom flange of the main steel component undergoes strain hardening, which helps maintain the flexural capacity of the section. Subsequently, as the upper flange yields, partial spalling of the concrete at the midspan top surface is observed. At this stage, the deflection approaches the allowable limit, marking the termination point of the test.

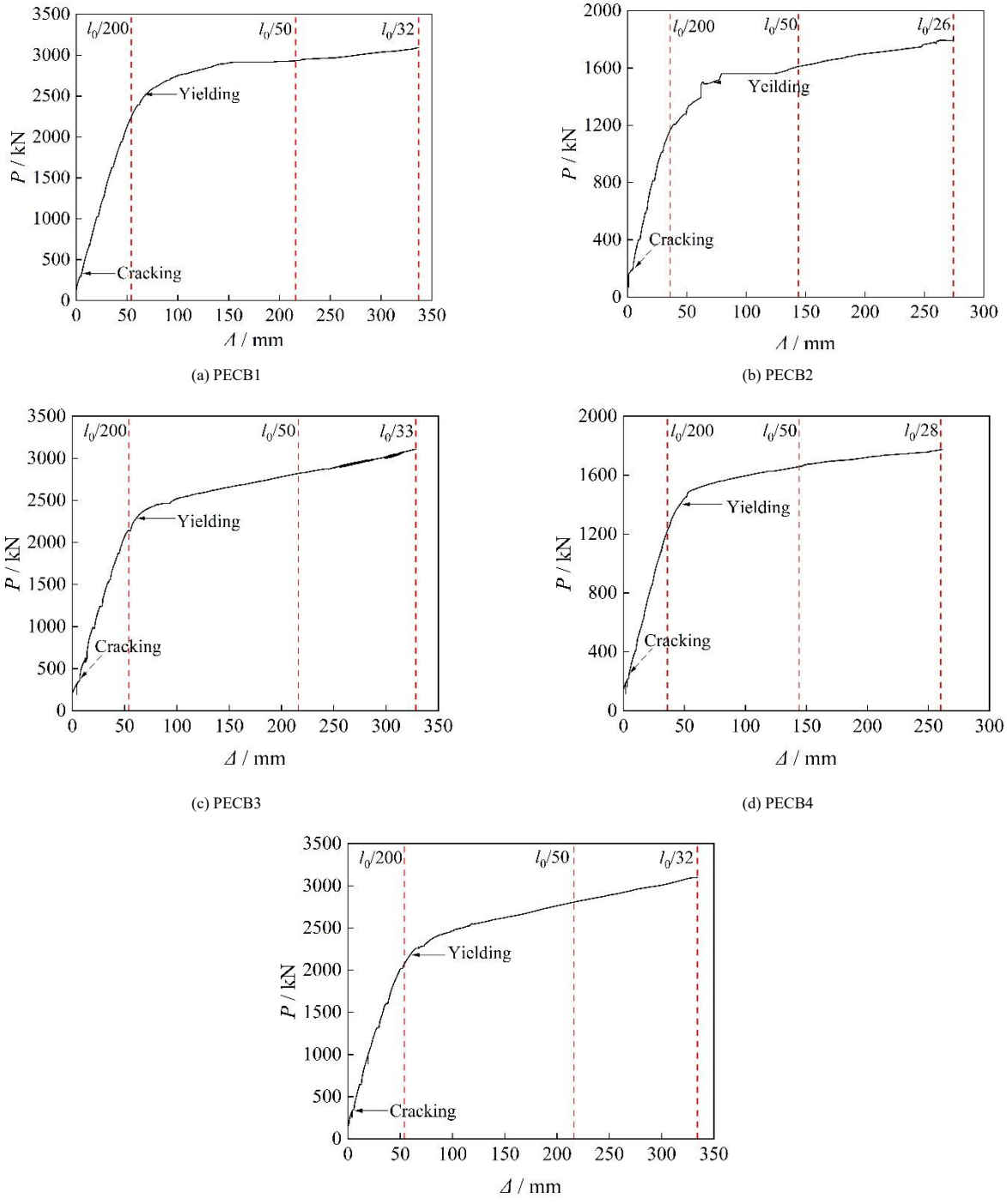

Fig. 9 Load-mid-span deflection curve

By comparing the load-midspan deflection curves of specimens with and without web openings, it was observed that the initial stiffness showed minimal differences. This limited variation arises because, although the presence of web openings reduces the cross-sectional rigidity of the primary steel structure, the effect is largely offset by the presence of concrete infill and added reinforcement. Once the specimens enter the yielding phase, PECB1 exhibits marginally higher load-carrying capacity than PECB3 and PECB5. Nevertheless, at the ultimate failure point, their capacities converge to nearly identical values. Meanwhile, PECB2 and PECB4 display similar curve patterns without notable divergence. These findings suggest that while web openings cause a slight decrease in load-bearing capacity, their overall influence remains minor. This is attributed to the fact that the flexural resistance of PEC beams is predominantly governed by the steel flanges, web, and concrete, with the web itself contributing a comparatively smaller share.

3.3. Bearing capacity analysis

Based on the load-midspan deflection curves of the specimens, the load-bearing capacities and displacements at characteristic points are summarized in Table 3. The theoretical cracking load P_{cr}' was calculated using the "Technical Specification for Partially Encased Composite Steel-Concrete Structures" (T/CECS 719—2020)[26], while the actual cracking load P_{cr} was obtained experimentally. The theoretical yield load P_y' was calculated using the yield stress obtained from material tests based on the edge yield criterion, and the actual yield load P_y was measured experimentally using the Park method. The theoretical ultimate load P_u' was derived using the full-section plasticity criterion, and the actual ultimate load P_u was determined experimentally. The ductility coefficient μ was used to evaluate the ductility performance of the specimens, defined as $\mu=\Delta_u/\Delta_y$, where Δ_u is the ultimate displacement, and Δ_y is the yield displacement.

As shown in Table 3: (1) The experimental load values at characteristic points of the specimens were higher than the calculated values, indicating that the load-bearing capacity can be determined using the edge yield criterion and the full-section plasticity criterion. (2) The cracking load of the specimens ranged from 0.1 P_u to 0.2 P_u, indicating early cracking. This was likely due to the presence of initial cracks in the concrete. However, the crack development

met the requirements of the specifications, and the load-bearing capacity exceeded 0.7 P_u at the normal serviceability limit state. (3) The overstrength ratio of the specimens ranged from 1.18 to 1.30, indicating that the specimens retained a certain strength reserve after reaching the yield load. (4) All specimens exhibited stable post-yield behavior and excellent ductility, with ductility coefficients exceeding 4.0, indicating strong deformation capacity and energy dissipation potential suitable for seismic design applications. (5) Compared to specimen PECB1, the yield strength of specimens PECB3 and PECB5 decreased by 6.0% and 8.4%, respectively, while their yield displacements increased by 5.2% and 6.0%, respectively. The yield strength and yield displacement of specimens PECB2 and PECB4 showed minimal differences, indicating that large-section PEC beams are more significantly affected by web openings in the steel section.

Table 3
Bearing capacity and displacement of characteristic points

Number	Web opening ratio / %	Stiffness /N·mm^{-1}	Cracking load / kN		Yielding load / kN		Δ_y/mm	P_y / P_y'	Ultimate load /kN		Δ_u / mm	P_u / P_u'	P_u / P_y	μ
			P_{cr}'	P_{cr}	P_y'	P_y			P_u'	P_u				
PECB1	-	33516	155.4	348.2	2185.4	2605.9	77.75	1.19	2734.5	3090.2	336.88	1.07	1.19	4.33
PECB2	-	23804	88.7	193.5	1241.6	1504.2	63.19	1.21	1474.4	1813.6	274.38	1.32	1.21	4.34
PECB3	15.36	29947	155.4	339.9	2185.4	2450.3	81.82	1.12	2734.5	3107.9	328.44	1.31	1.27	4.01
PECB4	17.98	24997	88.7	201.5	1241.6	1511.1	60.45	1.22	1474.4	1776.7	261.27	1.14	1.18	4.32
PECB5	14.56	28953	155.4	323.4	2185.4	2386.6	82.43	1.09	2734.5	3100.1	334.16	1.13	1.30	4.05

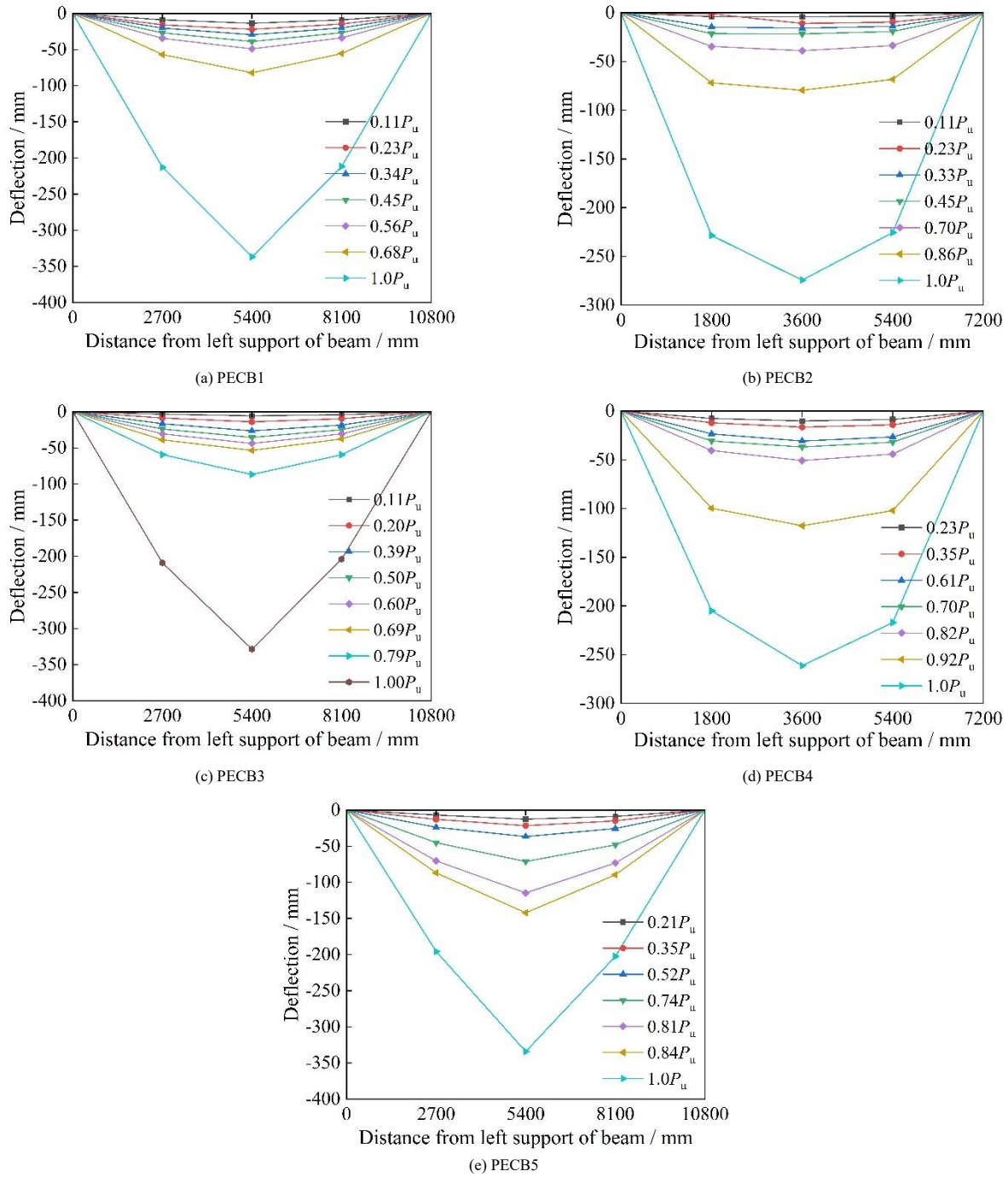

(a) PECB1

(b) PECB2

(c) PECB3

(d) PECB4

(e) PECB5

Fig. 10 Specimen deformation

3.4. Deformation analysis

Beams with good ductility can absorb a certain amount of energy after reaching their yield or maximum load-bearing state, exhibiting strong post-yield deformation capacity and providing clear warnings or deformations before failure. Fig. 10 illustrates the vertical deformations at various locations on the specimens, and the following observations can be made: (1) All specimens exhibited excellent ductility, with ductility coefficients exceeding 4.0, indicating strong ductile performance. (2) When the load reached approximately 0.7P_u, the deflection reached the serviceability limit state deflection value (l_0/200). (3) At the initial loading stage, specimen deformations were minimal, with similar deflections observed at the 1/4-span and 3/4-span points. Before the yield load, the deformations of the specimens gradually increased at a slow rate. After reaching the yield load, the rate of deflection growth significantly increased, indicating that the specimens had entered the elasto-plastic stage.

3.5. Cross-section strain distribution

To evaluate the distribution pattern of deformation along the cross-sectional height of the main steel member and concrete in the pure bending zone of large-section PEC beams under load, two control cross-sections were established in the pure bending zone of the specimens. Strain gauges (BX120-100AA) were evenly spaced and arranged on the concrete and web, while displacement meters with a range of 10 mm were evenly spaced and installed on the surface of the concrete on the opposite side. Both strain gauges and displacement meters were placed on the concrete surface to account for potential damage to the strain gauges due to tensile cracking when the deformation of the concrete became significant, as displacement meters can still roughly measure the progression of concrete strain. The strain development of the steel flanges under load is illustrated in Fig. 11. At the initial loading stage, the strain in the flanges generally exhibited a linear increase with the load. When the load reached approximately 0.7P_u to 0.8 P_u, the strain in both the upper and lower flanges reached the yield strain. Upon further loading, the flange strain increased rapidly, and the strain curve began to show an inflection point, consistent with the load-deflection curve at mid-span.

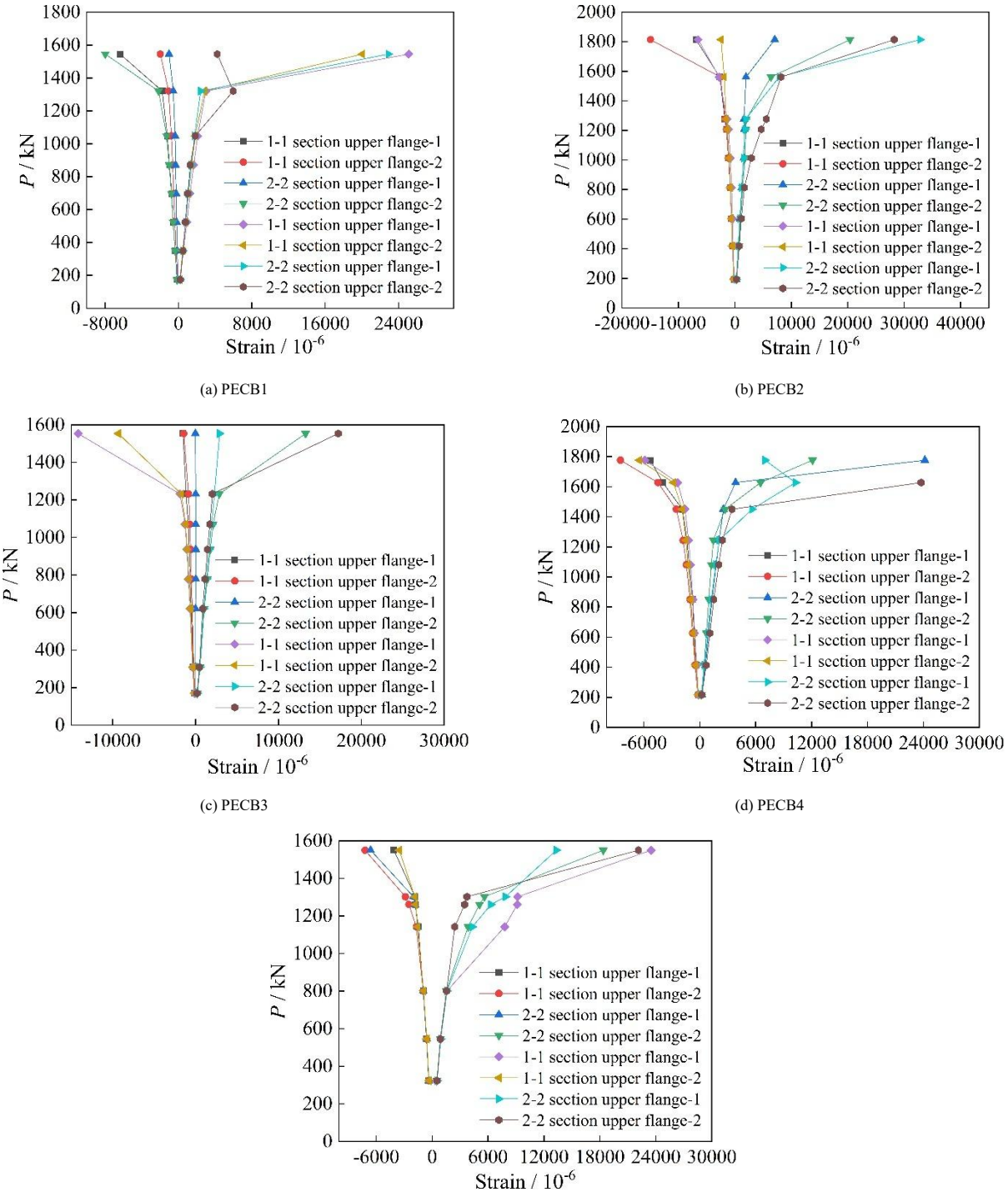

(a) PECB1

(b) PECB2

(c) PECB3

(d) PECB4

(e) PECB5

Fig. 11 Flange strain of the specimen

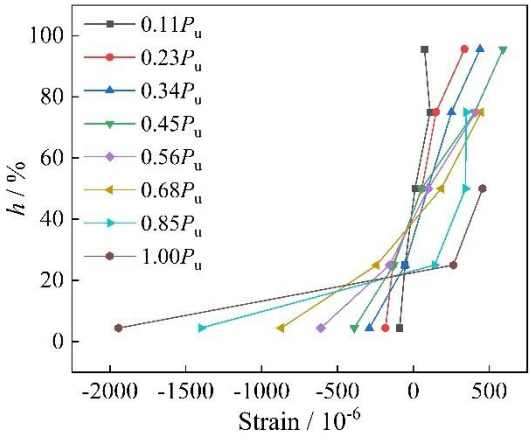

(a) PECB1

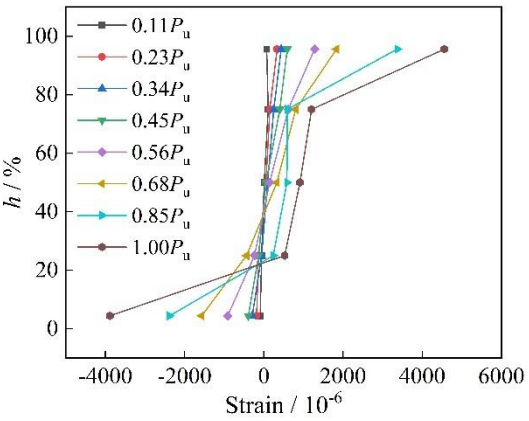

(a) PECB1

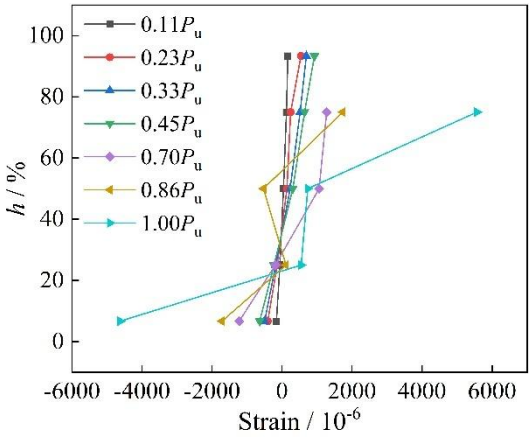

(b) PECB2

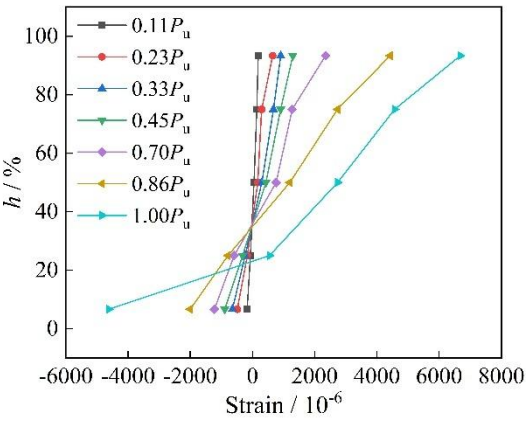

(b) PECB2

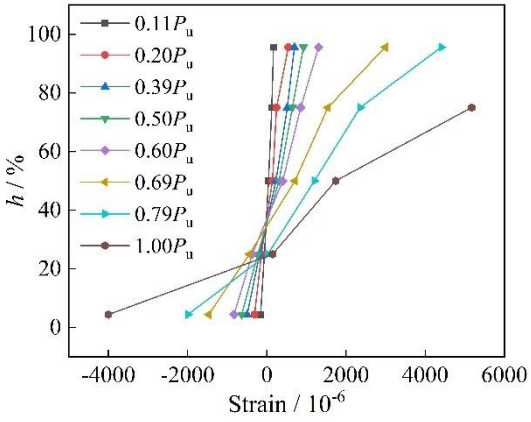

(c) PECB3

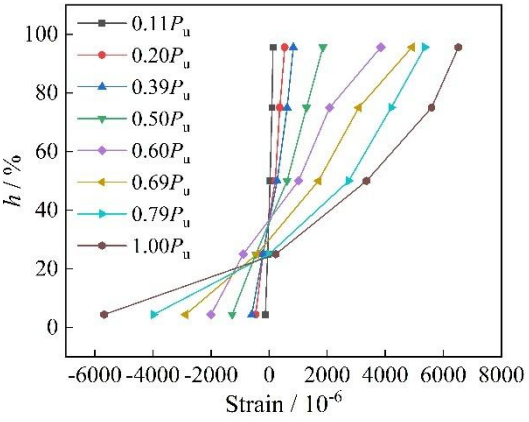

(c) PECB3

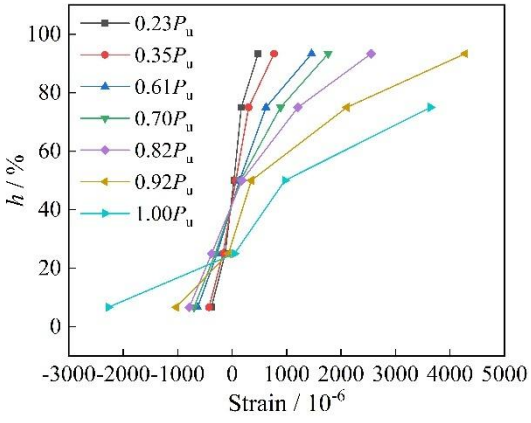

(d) PECB4

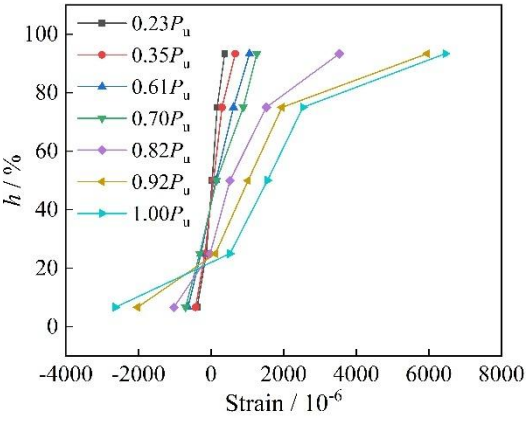

(d) PECB4

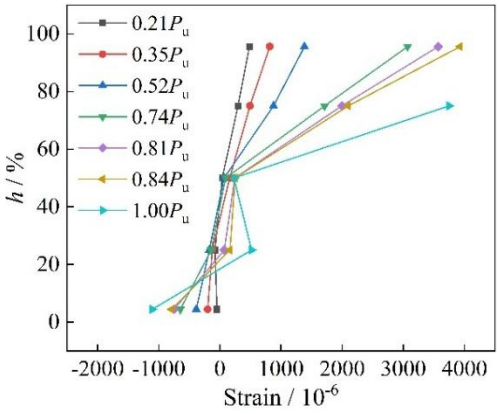

(e) PECB5

Fig. 12 Strain of section steel web

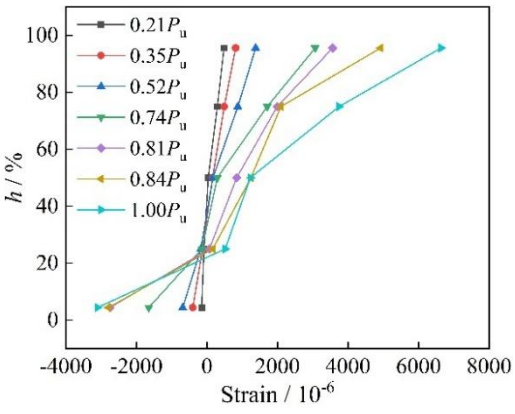

(e) PECB5

Fig. 13 Concrete strain

Fig. 12 and Fig. 13 illustrates the strain curves of mid-span concrete and steel along the cross-sectional height, where h represents the height from the lower flange. Before reaching a load of $0.7P_u$, the neutral axis of the cross-sections for specimens PECB1, PECB3, and PECB5 was approximately located at a height of 450 mm. For specimens PECB2 and PECB4, the neutral axis was approximately located at a height of 250 mm, and the strains in concrete and steel along the cross-sectional height conformed to the plane section assumption. After the load reached $0.7P_u$, the tensile strain in the concrete increased, the neutral axis of the cross-section shifted significantly upward, and severe cracking occurred in the web concrete, leading to stress redistribution and a somewhat nonlinear strain distribution across the cross-section.

4. Finite element analysis of large-section PEC beams

4.1. Finite element modelling

This numerical model is developed to replicate the failure behavior of PEC beams subjected to quasi-static loading. It integrates multiple geometric elements and force interactions. The steel reinforcement and link components are represented using the two-node three-dimensional truss element (T3D2), while the concrete and steel beam components are modeled with eight-node solid hexahedral elements featuring reduced integration (C3D8R). A structured meshing strategy is employed, applying a consistent element size of 100 mm across all components, including steel, concrete, links, longitudinal reinforcement, and construction steel. Details of the mesh partitioning are illustrated in Fig. 14.

As shown in Fig. 14, the finite element model adopted a uniform mesh size of 100 mm, which was selected based on both the geometric features of the specimens and practical considerations of simulation accuracy and computational efficiency. Given that the web opening diameters ranged from 175 mm to 400 mm, and the steel web thickness was between 12 mm and 22 mm, the chosen mesh size ensures that even the smallest openings are discretized by at least 6–8 elements along the diameter. This resolution is generally sufficient to capture the stress concentration and deformation gradients near discontinuities such as holes and thin webs. Additionally, finer mesh sizes were evaluated during preliminary simulations, but no significant improvement in global load–displacement response was observed, while computational cost and convergence difficulties increased. The selected 100 mm mesh size provided stable performance and successfully reproduced key structural responses observed in the experiments.

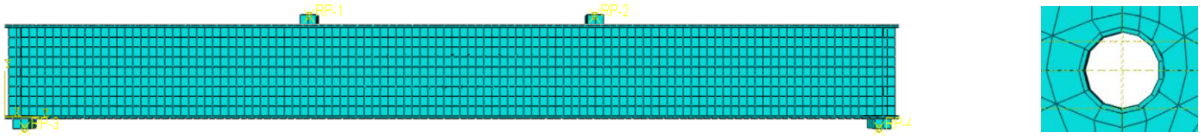

(a) Overall mesh division

(b) Mesh division at the opening

Fig. 14 Finite element model and mesh division

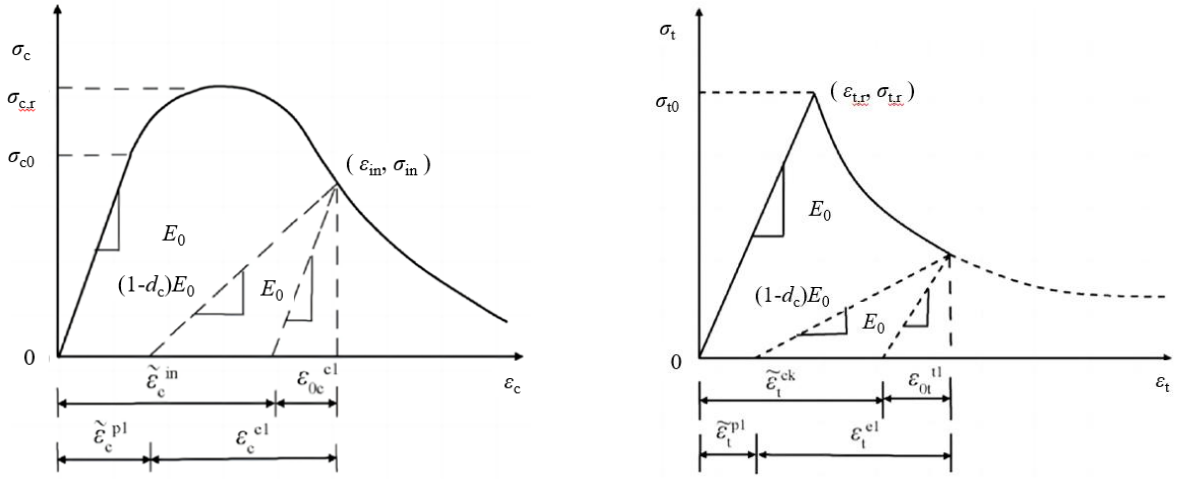

(a) Single-axis compression

(b) Single-axis tension

Fig. 15 Stress-strain relationship of concrete in CDP model

The concrete plastic damage model (CDP) is adopted to simulate concrete behavior. According to the study conducted by Chang Xinquan from Southeast University [29], excluding the damage factor can notably shorten the computation time, though it may introduce deviations in the descending segment of the concrete stress–strain response when compared to experimental observations. The constitutive models for concrete in both compression and tension, along with the corresponding damage factors, are defined based on the provisions of the "Code for Design of Concrete Structures" (GB 50010—2010) [30], and are illustrated in Fig. 15. For the CDP model, key parameters include a dilation angle of 35°, a flow potential eccentricity of 0.15, a viscosity parameter of 0.0015, a biaxial-to-uniaxial compressive yield strength ratio of 1.16, and a stress invariant ratio (K_c) of 0.6667 along the tension-compression meridian. In addition, the mechanical response of reinforcement bars and steel sections is represented using a bilinear stress–strain model in the simulation process.

In the finite element model, a paired contact interaction is defined between the concrete and steel components. Tangential behavior follows Coulomb friction theory with a friction coefficient set to 0.5, while normal interaction is modeled using hard contact. The flanges are permitted to separate outwardly from the concrete but are restricted from penetrating inward. Additionally, the ends of the link elements are rigidly connected to the flanges of the steel beam, whereas the longitudinal reinforcement bars are anchored into the end plates, all of which are embedded within the concrete. These end plates are modeled as rigid bodies, ensuring no deformation, and are bound to both the steel beam ends and concrete ends through section binding.

4.2. Comparison of numerical simulation and experimental results

4.2.1. Contrastive analysis of load-deflection curves

Fig. 16 presents the load-deflection comparison curves between the numerical simulation results and the experimental results for the bending test specimens of large-section PEC beams. It can be observed that the finite element simulation performs well, as the experimental curves align closely with the simulation curves, indicating that the selected computational model accurately captures the entire bending process of the large-section PEC beams.

To strengthen the numerical validation, Table 4 has been added to provide a comprehensive quantitative comparison between FEM simulation results and experimental data for all five specimens. The comparisons include yielding load (P_y), yielding displacement (Δ_y), ultimate load (P_u), and ultimate displacement (Δ_u), along with their respective percentage errors.

The results demonstrate that the FEM model achieves high accuracy in predicting both load and displacement at key response stages. Specifically, the error in yielding load remains within ±5% for most specimens, with the exception of PECB5 (7.82%). The error in yielding displacement is also generally low, ranging from 0.49% to 8.84%. Ultimate load predictions are particularly accurate for PECB2, PECB3, and PECB5, with errors below 1.2%, while PECB1 and PECB4 show larger deviations (11.71% and –16.97%, respectively), likely due to variations in local failure modes and damage propagation not fully captured in the model.

Moreover, the predicted ultimate displacements (Δ_u) show excellent agreement with the experimental values for all specimens, with maximum deviation below ±0.35%. This further confirms the model's capability to simulate deformation behavior under large deflections.

As noted in Fig. 16, the simulation and experiment exhibit good agreement in the overall shape of the load–displacement curve, particularly during the loading stage. However, discrepancies become apparent during the unloading phase. These deviations are mainly attributed to simplifications in the constitutive models of concrete and steel, which do not fully capture post-peak stiffness degradation, microcrack-induced softening, and interface debonding effects. Additional refinement, such as incorporating damage-plasticity models or cohesive zone elements, may improve the unloading phase simulation accuracy in future work.

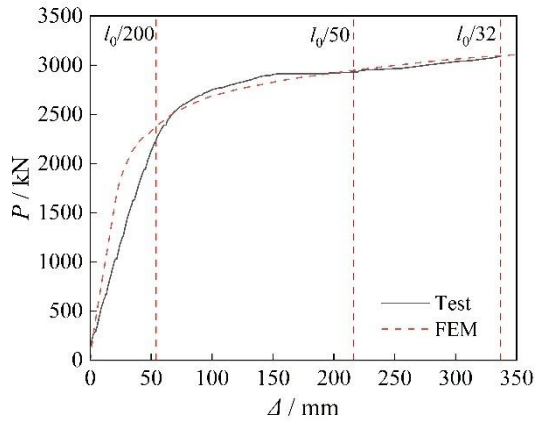

(a) PECB1

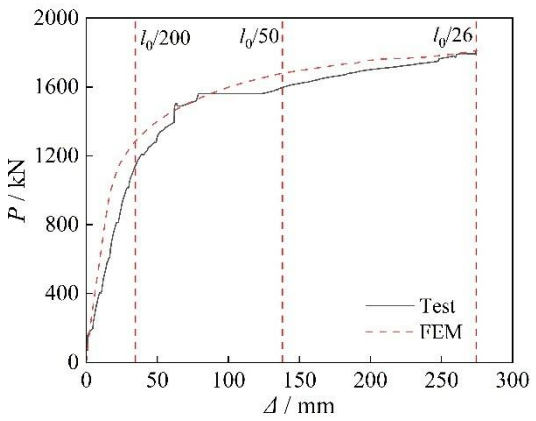

(b) PECB2

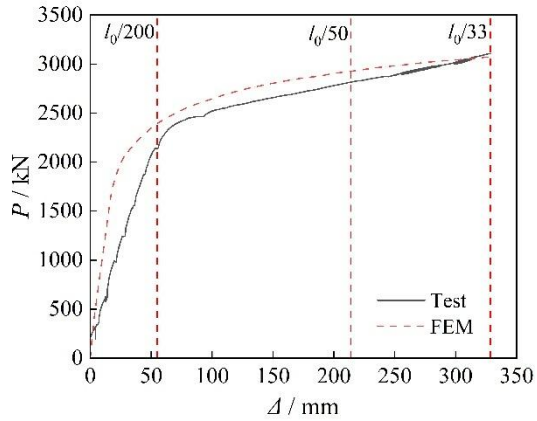

(c) PECB3

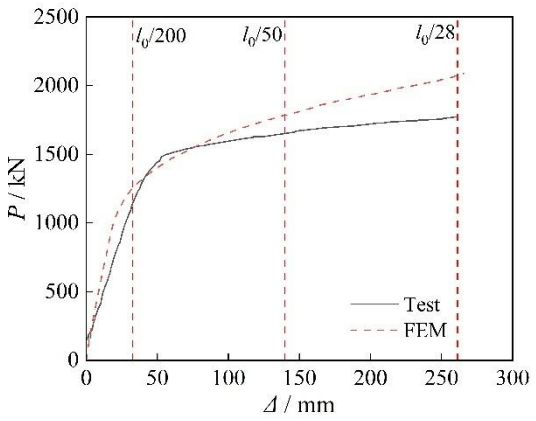

(d) PECB4

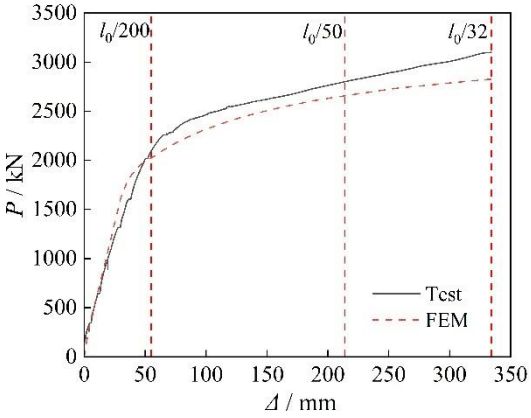

(e) PECB5

Fig. 16 Load-deflection curve comparison diagram

Table 4
Comparison between FEM simulation and experimental results

Number	Yielding load / kN		Mirror / %	Yielding displacement / mm		Mirror / %	Ultimate load /kN		Mirror / %	Ultimate displacement / mm		Mirror / %
	P_y^{FEM}	P_y		Δ_y^{FEM}	Δ_y		P_u^{FEM}	P_u		Δ_u^{FEM}	Δ_u	
PECB1	2521.5	2605.9	3.24	69.87	77.75	10.14	2734.5	3097.1	11.71	336.43	336.88	0.13
PECB2	1443.5	1504.2	4.04	57.88	63.19	8.40	1810.9	1813.6	0.15	275.01	274.38	-0.23
PECB3	2546.2	2450.3	-3.91	77.85	81.82	4.85	3073.3	3107.9	1.11	328.90	328.44	-0.14
PECB4	1446.2	1511.1	4.29	56.19	60.45	7.05	2078.2	1776.7	-16.97	262.19	261.27	-0.35
PECB5	2199.9	2386.6	7.82	78.83	82.43	4.37	2826.5	3100.1	8.83	334.48	334.16	-0.10

4.2.2. Stress distribution

Fig. 17 and Fig. 18 present the stress contour diagrams of the large-section PEC beam bending specimens under their ultimate load-bearing condition. In these figures, the maximum concrete stress is observed within the compression zone at the mid-span, with stress levels gradually diminishing toward the support ends. Similarly, the stress distribution in the steel sections shows a decreasing trend from the center of the beam outwards toward both sides.

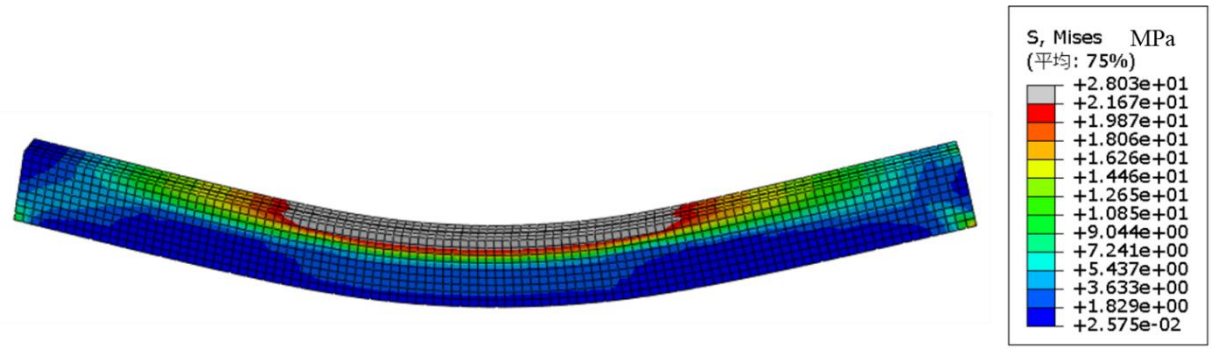

(a) PECB1

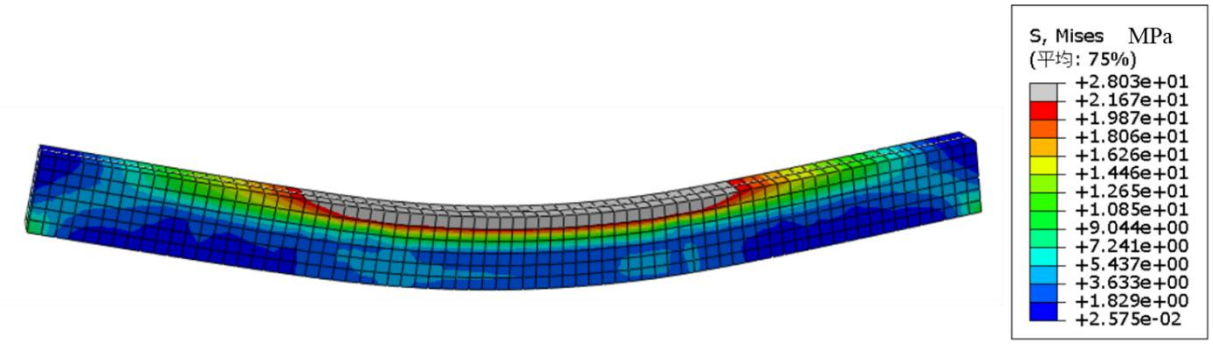

(b) PECB2

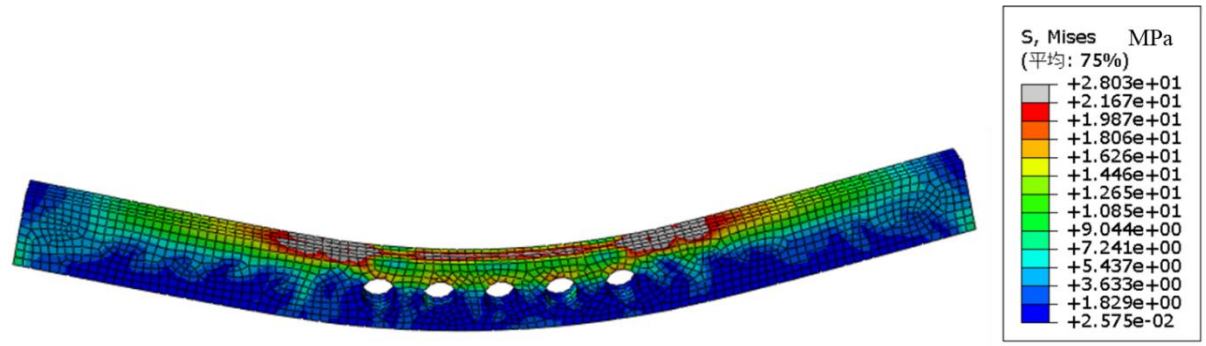

(c) PECB3

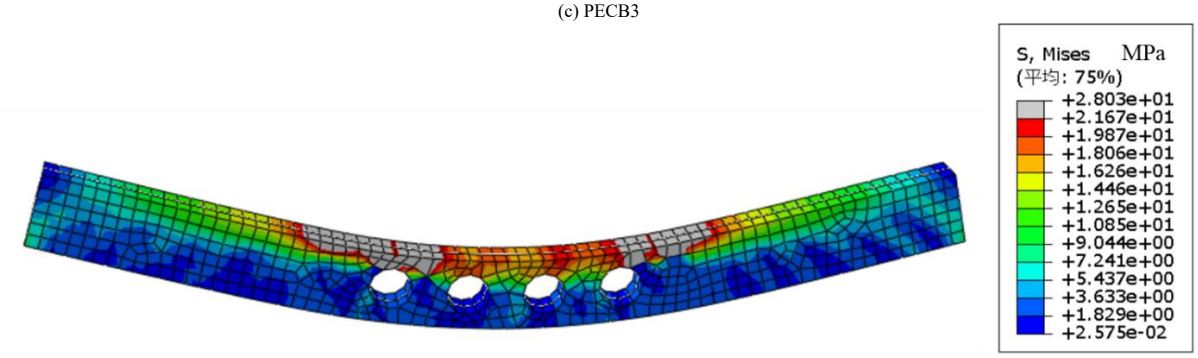

(d) PECB4

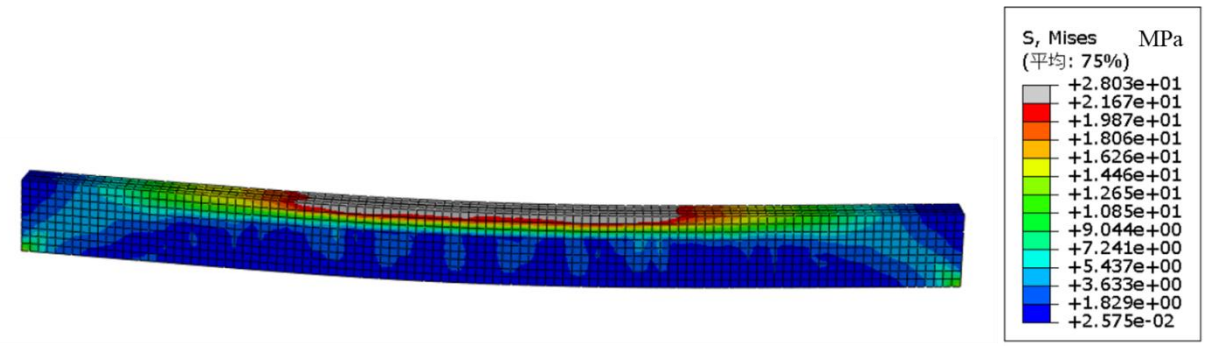

(e) PECB5

Fig. 17 Stress heat map of concrete

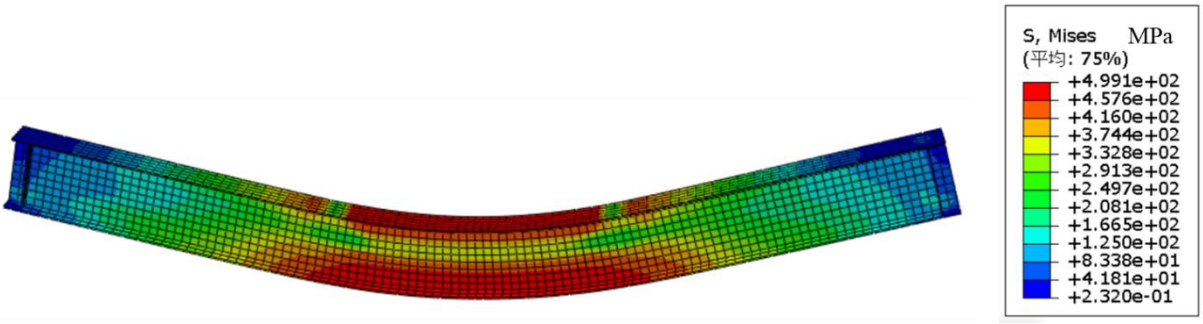

(a) PECB1

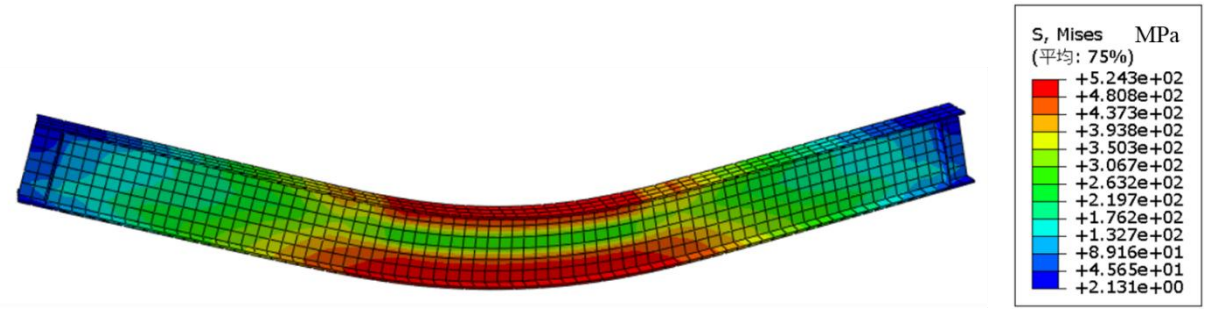

(b) PECB2

(c) PECB3

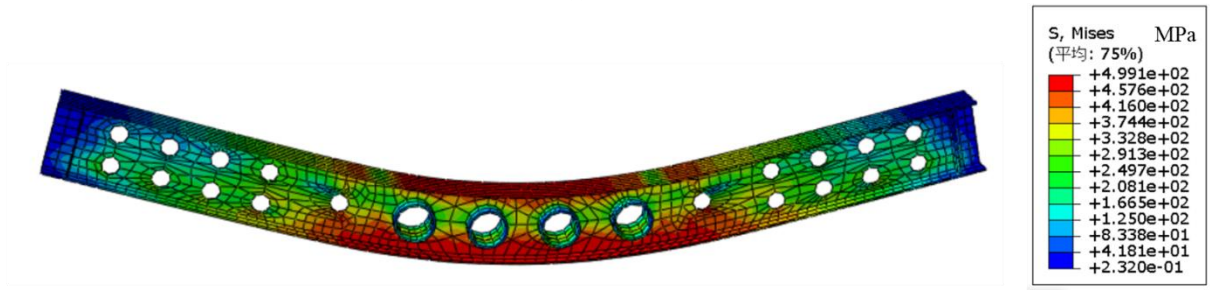

(d) PECB4

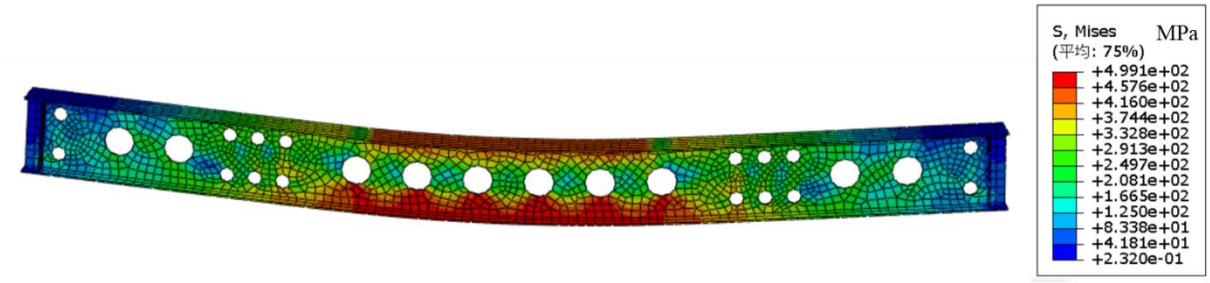

(e) PECB5

Fig. 18 Stress heat map of steel

4.2.3. Strain distribution

The plastic damage model for concrete does not simulate crack formation directly at the integration points. Instead, it visualizes crack propagation through contour representations. The direction of crack growth is determined based on the equivalent plastic strain, with the crack plane vector oriented parallel to the direction in which the maximum plastic strain occurs. The progression of cracks is presented using the distribution of maximum plastic strain values.

As shown in Fig. 19, three representative crack patterns are provided to illustrate the damage evolution process in the web concrete of large-section PEC beams. Taking specimen PECB1 as a case in point, when the applied load reaches 345 kN, tensile damage initiates at the bottom mid-span region, indicating the onset of cracking in the specimen. With the load increasing to 1400 kN, the area of tensile yielding expands, and the damage zone continues to grow. At 2100 kN, no additional tensile cracks are observed, suggesting crack saturation on the tensile side. The simulated crack development closely mirrors the observed experimental behavior, thereby confirming the accuracy and reliability of the established finite element model.

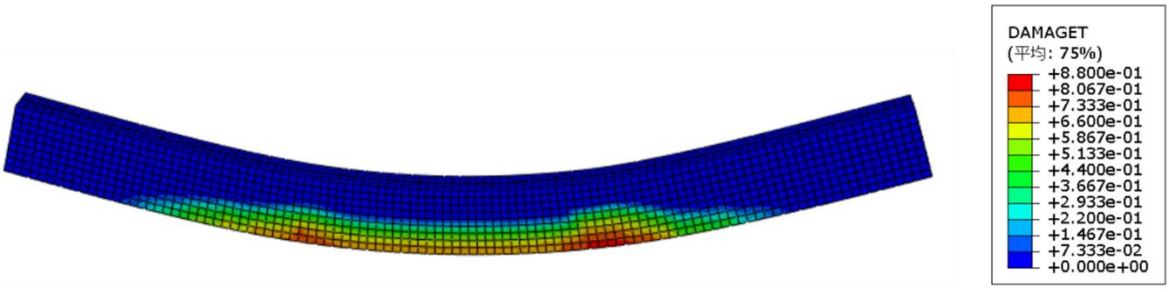

(a) P = 345 kN

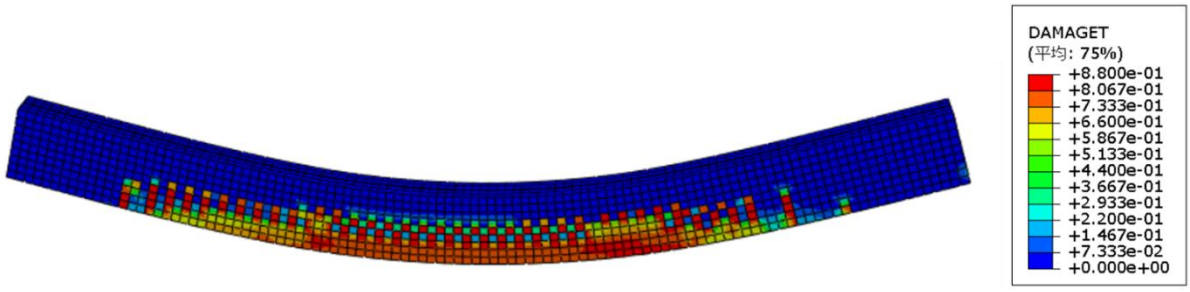

(b) P = 1400 kN

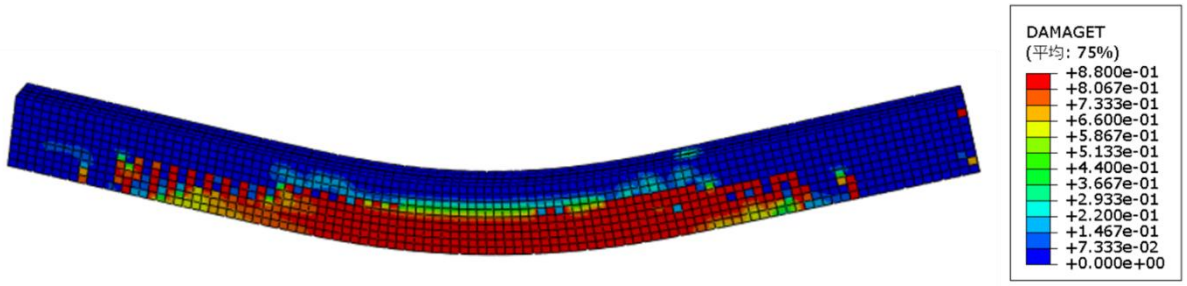

(c) P = 2100 kN

Fig. 19 Tensile strain diagram of concrete of PECB1

5. Flexural bearing capacity calculation of large-section PEC beams

The stress distribution and some parameters of the large-section PEC beam cross-section are shown in Fig. 20. During the process of reaching the ultimate load capacity, the neutral axis of the specimen continuously shifts upward, and the height of the compression zone decreases. The cross-section above the neutral axis is under compression, while the section below the neutral axis is under tension, with both the flanges and the tensile reinforcement reaching their yield strength.

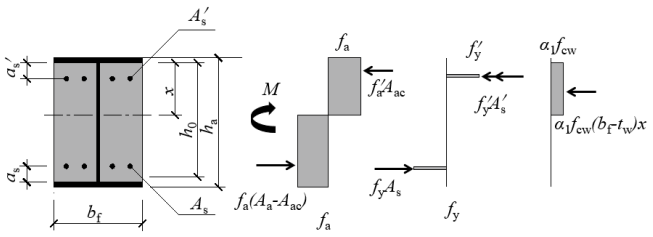

Fig. 20 Section diagram and equivalent rectangular stress diagram of large-section PEC beams

The formulas for calculating the flexural capacity of large-section PEC beams are provided in Equations (1)–(5), and the calculated results are shown in Table 5.

$$M_u = \alpha_1 f_{cw}(b_f - t_w)\frac{x^2}{2} + f_y A_s(h_a - x - 2t_f - a_s) + f_y' A_s'(x - a_s') + f_a S_{at} + f_a' S_{ac} \quad (1)$$

$$\alpha_1 f_{cw}(b_f - t_w)x + f_y' A_s' + f_a' A_{ac} - f_y A_s - f_a(A_a - A_{ac}) = 0 \quad (2)$$

$$2a_s' \le x \le \xi_b h_0 \quad (3)$$

$$\xi_b = \frac{1}{1 + \dfrac{f_y + f_a}{2 \times 0.003 E_s}} \quad (4)$$

$$A_{ac} = t_w x + b_f t_f \quad (5)$$

In these formulas: M_u represents the design value of the flexural capacity of the cross-section (N·mm); f_{cw} is the axial compressive strength design value of the concrete in the web of the main steel member (N/mm^2); x is the distance from the neutral axis of the composite section to the compression edge of the concrete (mm); h_a、b_f、t_w、t_f are the height, flange width, web thickness, and flange thickness of the main steel section of the beam (mm), respectively. α_1 is the influence coefficient of compressive stress in the compression zone; f_y、f_y' are the design values of tensile and compressive strengths of the reinforcement (N/mm^2); f_a、f_a' are the design values of tensile and compressive strengths of the main steel section of the beam (N/ mm^2); A_s、A_s' are the cross-sectional areas of the tensile and compressive reinforcement (mm^2), respectively; A_a、A_{ac} are the total cross-sectional area of the main steel section and the cross-sectional area of the compression zone of the main steel section (mm^2), respectively. a_s、a_s' are the distances from the resultant force point of the tensile reinforcement to the tensile edge of the concrete and from the resultant force point of the compressive reinforcement to the compressive edge of the concrete (mm), respectively. S_{at}、S_{ac} are the section plastic moment of the tensile and compressive areas of the main steel section relative to the plastic neutral axis of the composite section (mm^3), respectively. h_0 is the effective height of the concrete section (mm); E_a、E_s are the elastic moduli of the main steel section and the reinforcement (N/mm^2), respectively.

Table 5
The calculation results of flexural capacity are compared with the experimental results

Number	M / (kN·m)	M_u / (kN·m)	M / M_u
PECB1	5561.28	4922.12	1.13
PECB2	2296.32	1769.29	1.30
PECB3	5594.22	4922.12	1.14
PECB4	2132.04	1769.29	1.21
PECB5	5580.18	4922.13	1.13

Note: M is the test value (mid-span bending moment corresponding to ultimate load P_u).

As shown in Table 5, the experimental results for specimens PECB1, PECB3, and PECB5 were 1.13 to 1.14 times the calculated values, while those for PECB2 and PECB4 reached 1.30 and 1.21 times, respectively. These results suggest that the size effect has a measurable, though not dominant, influence on the flexural behavior of PEC beams. Specifically, the relatively higher capacity margins observed in smaller specimens (PECB2 and PECB4) may be attributed to localized constraint effects, increased relative reinforcement ratios, and reduced span-to-depth ratios, which tend to artificially enhance flexural strength. In contrast, large-section specimens (PECB1, PECB3, PECB5) exhibit more distributed cracking patterns and reduced confinement effects, leading to more realistic structural responses. This trend aligns with existing findings in the literature [31–33], which indicate that smaller-scale specimens often overestimate structural performance due to boundary and scale-induced anomalies. Overall, the good agreement between calculated and experimental values confirms the validity and safety of using the full-section plastic theory for estimating the flexural capacity of large-section PEC beams with web openings.

The average stiffness method was used in this study to calculate the average stiffness B of the specimens, and the stiffness calculations for specimens PECB3, PECB4, and PECB5 excluded the web opening regions. When calculating the equivalent sectional moment of inertia I_{ucr} for the uncracked section of large-section PEC beams and I_{cr} for the cracked section, the web concrete of the main steel member was equivalently transformed into the steel web. The calculation formulas are as follows:

$$I_{eq} = (I_{ucr} + I_{cr})/2 \quad (6)$$

In the formulas, I_{eq} represents the stiffness obtained through calculation. Using structural mechanics, the stiffness can be applied to derive the mid-span deflection f_1 of the specimen at $0.7P_u$, which is then compared with the experimentally determined mid-span deflection f at $0.7P_u$. The specific results are shown in Table 6. The deflection formula for the specimen is as follows:

$$f_1 = \frac{Pa\left(3l_0^2 - 4a^2\right)}{48B} \quad (7)$$

In the formula, f_1 is the deflection of the specimen at $0.7P_u$, l_0 is the calculated span of the specimen, a is the shear span length of the specimen, P is the load applied at the loading point, and B is the average stiffness of the specimen.

Table 6
The calculation results of mid-span deflection are compared with the test results

Number	I_{eff} / mm^4	I_{gross} / mm^4	Opening efficiency factor I_{eff}/I_{gross}	f / mm	f_1 / mm	f/f_1
PECB1	9.42×10^8	9.42×10^8	1.00	51.18	32.75	0.64
PECB2	1.80×10^8	1.80×10^8	1.00	46.65	23.94	0.51
PECB3	9.42×10^8	8.41×10^8	0.89	56.39	41.16	0.73
PECB4	1.80×10^8	1.88×10^8	1.05	36.80	29.32	0.80
PECB5	9.42×10^8	8.13×10^8	0.86	58.89	41.08	0.70

As shown in Table 6, the ratio of theoretical to experimental deflection values is consistently less than 1, indicating that in the elastoplastic stage, the calculated values tend to underestimate the actual deformation of the beams. This deviation is particularly evident in specimens with web openings (e.g., PECB3 and PECB5), where increased deflection is observed due to reduced sectional stiffness caused by perforation. To quantitatively explain this behavior, an opening efficiency factor I_{eff} / I_{gross} was introduced, where I_{eff} is estimated based on the measured average stiffness, and I_{gross} is the theoretical moment of inertia of the unperforated steel section. Given that flexural stiffness *EI* governs mid-span deflection, the calculated efficiency factors show a clear correlation with the increased deflection ratios. For example, PECB3 and PECB5, with efficiency factors of 0.894 and 0.864 respectively, correspond to increased deflection ratios f_1 / f of 0.73 and 0.70. This demonstrates that the reduction in stiffness due to web openings directly leads to larger displacements under load.

In addition, PECB2—although a solid-web specimen—exhibited the largest deflection prediction error, with f_1 / f =0.51, corresponding to a 49% underestimation. This is primarily attributed to its relatively small cross-section, which makes the specimen more sensitive to early cracking, stiffness degradation, and boundary condition effects. Moreover, the current deflection formula is based on linear elastic assumptions and does not incorporate stiffness loss from concrete cracking or localized damage. Therefore, for small-section or low-stiffness members, the simplified stiffness estimation method is less accurate. To improve predictive accuracy, future work should consider using effective moment of inertia approaches, nonlinear moment–curvature analysis, or segmental stiffness models that better reflect the post-cracking behavior of the composite section.

Therefore, the use of opening efficiency factors provides a practical design-oriented metric to assess the impact of web openings on flexural stiffness and deflection, and allows engineers to control allowable deformation levels in accordance with structural performance requirements. This refinement helps address the underestimation issue of the theoretical model and aligns well with the experimental trends observed in Table 6.

6. Conclusions

This study performed four-point bending tests on large-section PEC beams to evaluate how variables such as cross-sectional size, presence of web openings, and different opening configurations influence their failure modes, deflection response, flexural strength, ductility, and strain distribution along the section height. The principal findings are as follows:

（1）The inclusion of web openings introduces some degree of reduction in the bearing capacity of large-section PEC beams; however, the overall weakening effect is relatively minor. Compared with specimen PECB1, specimens PECB3 and PECB5 exhibited reductions in yield strength by 6.0% and 8.4%, respectively, while PECB2 and PECB4 showed no appreciable change.

（2）All tested specimens achieved ductility coefficients exceeding 4.0, indicating that large-section PEC beams possess excellent ductile behavior. The strain profiles of the primary steel elements and the surrounding concrete along the vertical section height display an approximately linear trend, consistent with the plane section assumption.

（3）The load–deflection responses and stress contour distributions from finite element simulations aligned closely with the experimental observations. The discrepancy between the simulated and measured ultimate bearing capacities was within 10%, confirming both the credibility of the adopted model and its effectiveness in capturing the flexural response of large-section PEC beams.

（4）Size effect exerts a notable influence on the flexural characteristics of PEC beams. Although large-section specimens show narrower flexural capacity margins compared to smaller counterparts, the calculated values still range from 1.13 to 1.30 times the experimental results, validating the safety and conservativeness of the proposed prediction method.

（5）The computed mid-span deflections using the reduced stiffness averaging method deviated from experimental data but did not affect the assessment of the serviceability limit state. In practice, the partial stiffness reduction caused by web openings should be considered during design to ensure structural performance.

Author Contributions

Conceptualization, Hongxin Liu; Methodology, Yukun Yang; Software, Jie Li; Resources, Yaming Li and Hongxin Liu; Writing – original draft, Shuizhong Jia; Writing – review & editing, Xiaomeng Xie; Visualization, Jie Li; Funding acquisition, Ping Yang, Yaming Li and Hongxin Liu. All authors have read and agreed to the published version of the manuscript.

Funding

Scientific Research Project of Shanghai Science and Technology Commission (21DZ1203002), Project of East China Construction Group Co., LTD. (Class 20-1-0073-Junction)

Data Availability Statement

The original contributions presented in the study are included in the article, further inquiries can be directed to the corresponding author.

Conflicts of Interest

The authors declare no conflicts of interest.

References

[1] Huang H, Xue C, Zhang W, et al. Torsion design of CFRP-CFST columns using a data-driven optimization approach[J]. Engineering Structures, 2022, 251: 113479. 10.1016/j.engstruct.2021.113479
[2] Liu J, Lyu F, Ding F X, et al. Energy dissipation of steel–concrete composite beams subjected to vertical cyclic loading[J]. Adv. Steel Constr, 2022, 18: 658-669. 10.18057/IJASC.2022.18.3.3
[3] Yan J B, Kang E C, Xie J. Behaviours of steel-concrete composite beams at low temperatures: materials and structures[J]. Adv Steel Constr, 2023, 19(4): 353-365. 10.18057/IJASC.2023.19.4.4
[4] Tian Y, Liu D, Chen X, et al. Damage evolution of steel-UHPC composite beams using AE and DIC techniques[J]. Journal of Constructional Steel Research, 2025, 224: 109163. 10.1016/j.jcsr.2024.109163
[5] Yang Y, Lin B, Zhang W. Experimental and numerical investigation of an arch–beam joint for an arch bridge[J]. Archives of Civil and Mechanical Engineering, 2023, 23(2): 101. 10.1007/s43452-023-00645-3
[6] Du Z L, Liu Y P, He J W, et al. Direct analysis method for noncompact and slender concrete-filled steel tube members[J]. Thin-Walled Structures, 2019, 135: 173-184. 10.1016/j.tws.2018.11.007
[7] Chen Z, Niu X, Liu J, et al. Seismic study on an innovative fully-bolted beam-column joint in prefabricated modular steel buildings[J]. Engineering Structures, 2021, 234: 111875. 10.1016/j.engstruct.2021.111875
[8] Li G C, Chen B W, Yang Z J, et al. Axial behavior of high-strength concrete-filledhigh-strength square steel tubular stub columns[J]. Adv Steel Constr, 2021, 17(2): 158-168. 10.18057/IJASC.2021.17.2.6
[9] Yao Y, Huang H, Zhang W, et al. Seismic performance of steel-PEC spliced frame beam[J]. Journal of Constructional Steel Research, 2022, 197: 107456. 10.1016/j.jcsr.2022.107456
[10] Chen Y, Li W, Fang C. Performance of partially encased composite beams under static and cyclic bending[J]. Structures, 2017, 9(FEB.): 29-40. 10.1016/j.istruc.2016.09.004
[11] Jiang Y, Hu X, Hong W, et al. Experimental study and theoretical analysis of partially encased continuous composite beams[J]. Journal of Constructional Steel Research, 2016, 117: 152-160. 10.1016/j.jcsr.2015.10.009
[12] Wang Z, Ye Y, Ma Y, et al. Experimental and finite element flexural performance study of HPEC beam[J]. Journal of Constructional Steel Research, 2023, 211: 108189. 10.1016/j.jcsr.2023.108189
[13] Ahn J K, Lee C H. Fire behavior and resistance of partially encased and slim-floor composite beams[J]. Journal of Constructional Steel Research, 2017, 129: 276-285. 10.1016/j.jcsr.2016.11.018
[14] He J, Wang S, Liu Y, et al. Mechanical behavior of a partially encased composite girder with corrugated steel web: Interaction of shear and bending[J]. Engineering, 2017, 3(6): 806-816. 10.1016/j.eng.2017.11.005
[15] Piloto P A G, Ramos-Gavilán A B, Gonçalves C, et al. Experimental bending tests of partially encased beams at elevated temperatures[J]. Fire Safety Journal, 2017, 92: 23-41. 10.1016/j.firesaf.2017.05.014

[16] Nakamura S, Momiyama Y, Hosaka T, et al. New technologies of steel/concrete composite bridges[J]. Journal of Constructional Steel Research, 2002, 58(1): 99-130. 10.1016/s0143-974x(01)00030-x
[17] He J, Liu Y, Lin Z, et al. Shear behavior of partially encased composite I-girder with corrugated steel web: Numerical study[J]. Journal of Constructional Steel Research, 2012, 79: 166-182. 10.1016/j.jcsr.2012.07.018
[18] He J, Liu Y, Chen A, et al. Bending behavior of concrete-encased composite I-girder with corrugated steel web[J]. Thin-walled structures, 2014, 74: 70-84. 10.1016/j.tws.2013.08.003
[19] De Nardin S, El Debs A L H C. Study of partially encased composite beams with innovative position of stud bolts[J]. Journal of Constructional Steel Research, 2009, 65(2): 342-350. 10.1016/j.jcsr.2008.03.021
[20] Kindmann R, Bergmann R, Cajot L G, et al. Effect of reinforced concrete between the flanges of the steel profile of partially encased composite beams[J]. Journal of Constructional Steel Research, 1993, 27(1-3): 107-122. 10.1016/0143-974x(93)90009-h
[21] Barros J A O, Figueiras J A. Flexural behavior of SFRC: testing and modeling[J]. Journal of materials in civil engineering, 1999, 11(4): 331-339. 10.1061/(ASCE)0899-1561(1999)11:4(331)
[22] Li V C. Engineered cementitious composites (ECC) material, structural, and durability performance[M]. 2008.
[23] Yoo D Y, Yoon Y S. Structural performance of ultra-high-performance concrete beams with different steel fibers[J]. Engineering Structures, 2015, 102: 409-423. 10.1016/j.engstruct.2015.08.029
[24] Hao N, Yang Y, Xue Y, et al. Shear performance of partially encased composite beams with high-strength steel and UHPC[J]. Journal of Constructional Steel Research, 2023, 211: 108217. 10.1016/j.jcsr.2023.108217
[25] Zhao B, Huo H, Ran C, et al. Flexural behavior of castellated partially encased composite (PEC) beams[J]. Journal of Constructional Steel Research, 2024, 214: 108509. 10.1016/j.jcsr.2024.108509
[26] Technical specification for partially clad steel-concrete composite structures: T/CECS 719-2020 [S]. Beijing: China Architecture and Construction Press, 2020. (in Chines)
[27] Test method standard for physical and mechanical properties of concrete: GB/T50081-2019[S]. Beijing: Standards Press of China, 2019. (in Chines)
[28] Tensile test method for metal materials at room temperature GB/T 228-2010 [S]. Beijing: Standards Press of China, 2010. (in Chines)
[29] Chang Xinquan, Wang Xin, Liu Changyuan, Wu Zhishen. Reliability evaluation of finite element Model for flexural performance of RC beams reinforced by Prestressed FRP plates [J]. Journal of Nanjing University of Technology (Natural Science Edition), 2021, 43(03): 318-328. (in Chines)
[30] Specification for design of concrete structures: GB 50010-2010 [S]2015 edition. Beijing: China Architecture and Construction Press, 2015. (in Chines)
[31] Rao G A, Vijayanand I, Eligehausen R. Studies on ductility of RC beams in flexure and size effect [C] // Proceedings of the 6th International Conference on Fracture Mechanics of Concrete and Concrete Structures. Catania: 2017.
[32] Zheng XF. Experimental Study on Dimensional effect of bending performance of high-strength concrete beams [D]. Dalian: Dalian University of Technology, 2011. (in Chines)
[33] Alca N, Alexander S D B, MacGregor J G. Effect of size on flexural behavior of high-strength concrete beams[J]. Structural Journal, 1997, 94(1): 59-67. 10.14359/461

Advanced Steel Construction – Vol. 22 No. 2 (2026) 170–180
DOI:10.18057/IJASC.2026.22.2.4

INFLUENCE OF WELDING RESIDUAL STRESS ON AXIAL MECHANICAL PROPERTIES OF HOLLOW SPHERICAL JOINTS

Ren-Zhang Yan [1,*], Hao-Ping Ji [1], Shuai Wang [2], Xiao-Qiang Jin [1] and Lin Song [3]

[1] *School of Civil Engineering, Chongqing Jiaotong University, Chongqing 400074, China*
[2] *Chongqing Aerospace Polytechnic, Chongqing 400021, China*
[3] *China Metallurgical Construction Engineering Group Co., LTD, Chongqing 400037, China*
**(Corresponding author: E-mail: rz_yan@cqjtu.edu.cn)*

ABSTRACT

Significant welding residual stresses (WRS) exist at the sphere-pipe welds of welded hollow spherical joints (WHSJ), adversely affecting their axial mechanical performance. However, due to the complex distribution pattern of residual stress, quantitatively assessing their impact on joint axial stiffness and load-bearing capacity has been challenging. This study employs a combined approach of theoretical derivation and model testing to examine and reveal the influence mechanisms and quantitative influence patterns of sphere-to-pipe welding residual stress on the axial mechanical properties of hollow spherical joints. It was found that welding residual stress reduces joint axial stiffness by 1.97% – 54.7% and load-bearing capacity by 2.27% – 24.4%. Furthermore, the detrimental effect of welding residual stress on axial performance decreases with increasing hollow sphere diameter (D), increases with increasing wall thickness (t), and exhibits a contrasting trend with increasing steel pipe diameter (d): its effect on axial stiffness initially increases then decreases, whereas its effect on load-bearing capacity initially decreases then increases.

ARTICLE HISTORY

Received: 18 February 2025
Revised: 2 July 2025
Accepted: 18 July 2025

KEYWORDS

Welded hollow spherical joints;
Welding residual stress;
Axial stiffness;
Axial compressive capacity;
Experimental study

1. Introduction

Welded hollow spherical joints (WHSJ), developed by Professor Liu X.L.(1991), have been widely used in various spatial grid structures. These joints consist of a core hollow sphere connected to multiple pipes through welded joints. Notably, the core hollow sphere itself is fabricated by welding two hemispherical shells [1]. However, significant WRS exist at the sphere-pipe butt welds, adversely affecting the axial mechanical properties of the joints. This has prompted extensive research by numerous scholars.In terms of overall structural performance, Wang X.(1996) considers the axial stiffness and bending stiffness of the joints when analyzing the grid of welded spherical joints. Through finite element analysis, it is found that after considering the stiffness of the welded spherical joints, the deflection of the grid structure is reduced, and the influence of the axial stiffness on the deflection is greater than that of the bending stiffness[2]; Zhang J.L.(2003) introduces the stiffness model of WHSJ in the design of geodesic and Cavite reticulated shell structures, and analyzes that the joint stiffness has a significant impact on the buckling load and ultimate load of the structure[3,4]. Kang J.'s(2008) research shows that the structural bearing capacity is reduced after considering joint stiffness in geodesic and saddle reticulated shells with initial defects[5,6]. Li F.(2014) establishes a numerical analysis model of semi-rigid joint cylindrical grid mega-structure and analyzes the static performance of the axial semi-rigid, bending semi-rigid and double semi-rigid structures of joints. It is found that the structural bearing capacity decreased by about 15% after considering the superposition effect of bending stiffness and axial stiffness[7]. Su Y.H.(2005) points out that variations in joint axial stiffness significantly influence the load-bearing capacity of latticed shell structures[8]. These studies show that the stiffness of WHSJ has a non-negligible impact on the overall performance of the structure.

In order to accurately evaluate the stiffness of WHSJ, many scholars have conducted extensive studies on their mechanical properties. Yan X.Y.(2021) explores the axial stiffness, bending stiffness, bearing capacity and ultimate tensile and compressive properties of H-beam WHSJ by combining numerical analysis with experimental studies[9,10];Liu H.B.(2018) investigated the axial performance of H-beam WHSJ, conducting a comprehensive analysis of the effects of material strength, geometric dimensions, and stiffening ribs on joint mechanical properties. The study further proposed corresponding calculation methods[11]; Zhao Z.W.(2021), Han Q.H.(2016) and Yan X.Y.(2019) analyze the axial stiffness and bending stiffness of WHSJ under different stress states, and establish relevant calculation formulas[12-14]; In addition, scholars such as Zhao Z.W.(2018), Lu J.(2018), Huang B.S.(2021) and Liu H.B.(2020) also examine the mechanical properties of WHSJ under extreme conditions such as corrosion, fire and high temperature, and achieve rich research results[15-20].

Due to the structural characteristics of WHSJ, their performance is affected by many factors, and many scholars have also conducted studies on these factors. Luo Y.F.(1995) finds that the joint volume has an important influence on the structural stress and buckling morphology[21]; Dong S.L.(2005) conducts an in-depth study on the bearing capacity of WHSJ, proposes a practical calculation method, and points out that the welding quality at the sphere-pipe butt welds is an important factor for the joint stiffness[22,23]; Liao J.(2010) considers the size and quality of various WHSJ and finds that they have different degrees of influence on the joint stiffness and bearing capacity[24]; Wang X.(2000) not only examines the axial and bending stiffness of joints, but also analyzes the influence of the size of joint region on the stiffness and elastic buckling load of grid structure, and concludes that the joint stiffness is related to many factors such as the stress condition, geometric dimensions, and rod size[25]. In summary, the quality of welds at the sphere-pipe butts of the WHSJ is one of the important factors affecting its performance.

Recent studies have further investigated the residual stress distribution at sphere-to-pipe welds and its structural effects. Zhao Z.W. (2016) employed numerical simulations to analyze how residual stresses influence joint performance and the mechanical properties of single-layer latticed shells. The research demonstrated that residual stresses reduce both joint stiffness and structural load-bearing capacity[26]. Yan R.Z. (2023) established a residual stress distribution model for hollow spherical joint welds, complemented by experimental analyses of its impact on bending performance. The results confirmed that residual stresses adversely affect joint bending stiffness and load-bearing capacity, with the degree of influence varying according to joint geometric size[27,28].This study demonstrates that WRS will reduce the bending stiffness and bearing capacity of joints, and the degree of influence varied with the changes in the structural size of joints.

Through literature review, it is found that the current calculation methods for the axial stiffness and bearing capacity of WHSJ are mainly based on experimental analysis, and the results have certain variations. At the same time, there are few studies that consider the influence of WRS. Therefore, based on the previous studies, this paper further explores the influence of WRS on the axial mechanical properties of WHSJ through a combination of theoretical deduction and experimental studies, and clarifies the influence mechanism of WRS on the axial stiffness and ultimate bearing capacity of joints.

2. Specimen design of welded hollow spherical joint

2.1. Joint design

To ensure the representativeness of the research results, the study selected WHSJ commonly used in engineering, with particular focus on the influence of key parameters: hollow sphere diameter (D), wall thickness (t), and steel pipe diameter (d) on joint axial stiffness and ultimate bearing capacity. Axial performance tests were conducted on five groups of specimens (see Table 1 for

detailed parameters). All specimens employed seamless steel pipes with identical dimensions: 470 mm in length and 6 mm in wall thickness on each side.

When welding the steel pipe and the hollow spheres, a single-pass three-layer arc welding is used to simulate the actual engineering, and the hemispherical butt weld of the hollow spheres is avoided. To facilitate loading application in the welded hollow spherical joint model tests and avoid interference with the hemispherical butt welds of the hollow sphere, the specimens were fabricated by connecting the hollow sphere to two steel pipes at a 180° included angle. A 200mm×200mm loading end plate is set at the end of the steel pipe to connect the support. Fig. 1 is a schematic diagram of the specimen structure, in which the grooved plate is mainly used to arrange the displacement sensor. The hollow spheres and steel pipes of all specimens are made of Q235 steel. During the production of the hollow spheres, the WRS generated by welding the two hemispheres is eliminated through heat treatment and static standing.

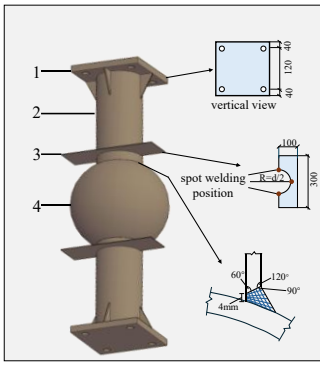

(a) Tectonic diagram
1.fixed end-plate; 2.seamless steel pipe;
3. grooved plates for measuring points;
4.welded hollow sphere.

(b) Photographs of specimens

Fig. 1 Diagram of test pieces

Table 1
Specimen parameters

Number	Specimen number	Ultrasonic impact	Name	*D*/mm	*t*/mm	*d*/mm	Theoretical value of bearing capacity N_R/kN
1	SJ1	No	experiment group	300	8	89	346
	SJ1-D	Yes	control group				
2	SJ2	No	experiment group	350	8	89	329
	SJ2-D	Yes	control group				
3	SJ3	No	experiment group	300	8	114	488
	SJ3-D	Yes	control group				
4	SJ4	No	experiment group	300	10	114	610
	SJ4-D	Yes	control group				
5	SJ5	No	experiment group	300	8	140	656
	SJ5-D	Yes	control group				

Note: Specimens labeled "SJ *i*" (where " *i* " = 1, 2, …, 5) denote the test specimens, with" *i* " indicating the test group index. Correspondingly, "SJ *i*-D" (" *i* "= 1, 2, …, 5) represent the control specimens paired with "SJ *i*". These underwent ultrasonic impact treatment to mitigate WRS immediately after sphere-pipe welding.

2.2. Preparation of control group specimens

To investigate the influence of WRS on the axial performance of the joints, ultrasonic impact method (UIM) was first applied to the sphere-to-pipe welds of the five control group specimens upon completion of fabrication. This treatment aimed to reduce WRS within the welds and the adjacent heat-affected zone. The fundamental principle of UIM involves utilizing high-frequency, high-efficiency, and focused ultrasonic energy to induce sufficient compressive plastic deformation and grain refinement in the metal surface layer. This process alters the WRS field, thereby reducing, homogenizing, or eliminating the residual stresses. In this study, a TY20-80 ultrasonic impact instrument was employed to mitigate WRS in the weld regions. As illustrated in Fig. 2, the UIM treatment involved continuously impacting the weld and heat-affected zone using an impact gun operating at 20,000 Hz, traversing at a uniform speed of 2 cm/min. During the process, the impact gun was maintained perpendicular to the weld, ensuring continuous contact between the impact pin and the weld seam. Detailed test principles and operational procedures are documented in reference [28].Subsequently, to quantify the WRS in all specimens, measurements were taken using an SC21B 3D stress magnetic scanner prior to conducting the axial compression tests. The SC21B scanner operates based on the magnetostrictive effect of ferromagnetic materials, enabling non-destructive measurement of the initial stress within steel components, with a measurement resolution of 1 MPa. The research group had previously conducted relevant UIM and magnetic testing [29].This paper only lists some important results as the basis for the analysis of this paper.

Fig. 2 ultrasonic impact weld process

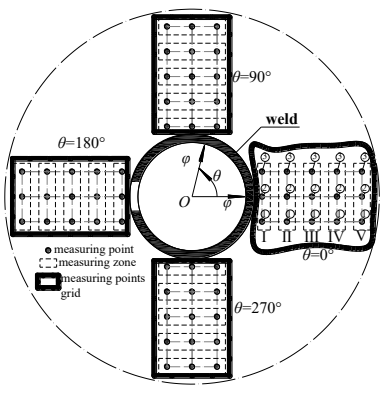

(a)vertical view

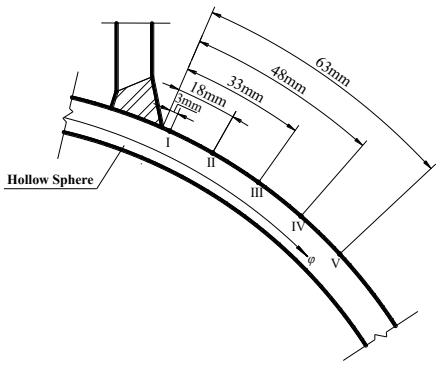

(b)section

Fig. 3 Layout of measuring points of residual stress

Table 2
$\theta = 180$ ° WRS test results

Number	Specimens	Measuring point	Experiment group(SJ*x*)/MPa				Control group(SJ*x*-D)/MPa				β
			$\sigma_{i,\theta}$	$\sigma_{i,\varphi}$	$\sigma_{i,equ}$	$\sum\sigma_{i,equ}$	$\sigma'_{i,\theta}$	$\sigma'_{i,\varphi}$	$\sigma'_{i,equ}$	$\sum\sigma'_{i,equ}$	
1	SJ1 /SJ1-D	I	-26	-96	86	504	-13	-74	68	296	41%
		II	79	-191	241		40	-100	125		
		III	44	-77	106		24	-43	59		
		IV	34	-34	60		19	-22	35		
		V	12	6	11		10	6	9		
2	SJ2 /SJ2-D	I	-29	-82	72	513	-35	-45	41	300	41%
		II	104	-181	249		44	-90	118		
		III	57	-102	139		41	-68	95		
		IV	27	-19	40		21	-17	33		
		V	2	-12	13		2	-12	13		
3	SJ3 /SJ3-D	I	39	-65	91	506	31	-47	68	313	38%
		II	67	-185	225		29	-105	122		
		III	39	-120	143		27	-80	97		
		IV	7	-6	11		7	-7	12		
		V	-7	-39	36		-2	-15	14		
4	SJ4 /SJ4-D	I	-40	-56	50	375	-47	-49	48	248	33%
		II	62	-165	203		44	-83	111		
		III	42	-73	100		29	-58	76		
		IV	3	-12	13		1	-8	9		
		V	10	7	9		5	3	4		
5	SJ5 /SJ5-D	I	-49	-117	102	415	-34	-43	39	296	29%
		II	59	-159	195		42	-92	119		
		III	41	-52	81		38	-45	71		
		IV	28	26	27		36	-26	54		
		V	10	0	10		15	8	13		

Note:
① The number *x* in the table represents the specimen group number, which is 1~5 respectively;
② $\sigma_{i,\theta}$ and $\sigma_{i,\varphi}$ are the circumferential and longitudinal WRS of the test group specimens at the measuring point *i* respectively;
③ $\sigma'_{i,\theta}$ and $\sigma'_{i,\varphi}$ are the circumferential and longitudinal WRS of the control group specimens at the measuring point i respectively;
④$\sigma_{i,equ}$ and $\sigma'_{i,equ}$ are the equivalent WRS of the test group and control group specimens at the measuring point *i* respectively, $\sigma_{i,equ} = \sqrt{(\sigma_{i,\theta})^2 + (\sigma_{i,\phi})^2 - \sigma_{i,\theta} \cdot \sigma_{i,\varphi}}$
⑤ β is the reduction rate of WRS, $\beta = \left(\sum\sigma_{i,equ} - \sum\sigma'_{i,equ}\right) / \sum\sigma_{i,equ}$

When measuring WRS via the magnetic method, a measurement point grid was established on the hollow sphere surface as shown in Fig. 3 to comprehensively characterize the stress distribution pattern. Starting from the weld initiation point, grid units were positioned at 90° intervals along the circumferential direction. Each unit contained five measurement points uniformly spaced longitudinally and three points arranged circumferentially. During measurement, the circumferential stress value at each longitudinal position was determined by averaging the three circumferential measurement points. Due to repeated heating from the welding heat source at the arc-extinguishing point, significant fluctuations occurred in residual stress measurements. Therefore, the measurement grid at $\theta = 180°$ (away from these critical zones) was selected for analysis. Residual stress results for all five specimen groups at this location are presented in Table 2.

It can be seen from Table 2 that ultrasonic impact has a certain effect on eliminating the WRS of the welded hollow spherical joint, which can reduce the WRS of the hollow spherical joint by 29%~41%.

3. Analytical calculation of the influence of WRS on the axial mechanical properties of WHSJ

In order to clarify the influence of WRS on the axial mechanical properties of WHSJ, it is necessary to derive the axial stiffness and bearing capacity of WHSJ analytically before conducting experiments. The research team has established the distribution pattern of WRS of WHSJ in various sizes by using the aforementioned magnetic test and finite element simulation. The relevant results have been reported in detail in[27] This paper will directly use the results to analyze the influence of WRS on the axial mechanical properties of WHSJ.

3.1. Calculation of axial stiffness considering the influence of WRS

The axial stiffness *K* of the joint is the ratio of the axial load *N* to the axial deformation *u* of the joint domain, which can be calculated using Eq. (1). The WHSJ are composite connections formed by welding steel pipes to hollow spherical bodies. The axial deformation within the joint region, denoted as *u*, arises from the combined axial deformation of the steel pipe u_s and the hollow sphere δ_0. Assuming these deformations are independent, the total axial deformation *u* under axial load *N* results from the additive combination of u_s and δ_0 acting in series, as expressed in Eq. (1).

$$K = \frac{N}{u} = \frac{N}{u_s + \delta_0} \tag{1}$$

3.1.1. Joint domain range considering the influence of WRS

The influence of WRS on the joint is mainly concentrated in the sphere-pipe connection weld and the nearby heat-affected zone. Taking SJ1 as an example, Fig. 4 is the WRS distribution pattern diagram of SJ1 established by the research team in the early stage. It can be seen that the maximum WRS appears near the weld, and the WRS in the remaining areas will decrease rapidly as its position moves away from the weld. If 5% of the material yield strength is used as the basis for whether the WRS can be ignored to judge the influence zone of the WRS, the weld affected zone of SJ1 can be obtained as the blue area shown in Fig. 4. At this time, the influence zone height of the steel pipe is h_0 = 106mm, and the influence zone of the hollow spherical shell is $\varphi = 49.83°$.The

WRS distribution pattern of the other specimens is similar to that of SJ1, except that the specific influence range h_0 and φ of each group of specimens will change with the geometric structure size of the joint. Since this paper mainly examines the influence of WRS on the axial bearing performance of the joint, the axial deformation of the joint is mainly calculated in the blue area shown in Fig. 4. Due to space limitations, the following deduction is based on SJ1. The distribution of WRS and the deduction process of the axial mechanical properties of the joints of the other groups of specimens are completely similar to those of SJ1.

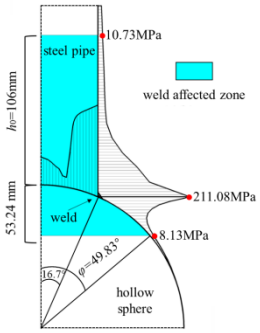

Fig. 4 Pattern of residual stress distribution in SJ1 von Mises welding

3.1.2. Calculation of u_s

To accurately calculate the axial deformation of the welded affected zone of the steel pipe, the distribution law of the axial WRS in the welded affected zone of the steel pipe, i.e., the range of height h_0, should be clarified first. As shown in Fig. 5(a), the axial WRS distribution diagram on the typical section of the steel pipe in SJ1 is shown. Obviously, the axial WRS in the steel pipe is anti-symmetrically distributed along the center of the steel pipe wall thickness (position with r = 41.5mm), and the residual stress is the largest at about 3.5mm from the weld (z = 3.5mm), and the residual stress value has been reduced to less than 10MPa at 100mm from the weld (z = 100mm).

To simplify calculations, the nonlinear axial WRS within the steel pipe is equivalently homogenized as a uniform stress along its thickness direction. As illustrated in Fig. 5(b), the simplification involves dividing the WRS into tensile and compressive zones along the thickness direction based on stress characteristics, with monotonically varying stresses in each zone. The nonlinear stresses in these zones are then homogenized into uniform stresses σ_w using Eq. (2), following the principle of equivalent resultant force. This equivalent treatment preserves the mechanical nature of each zone. Since the resultant force of the equivalent stress matches that of the actual distributed stress, the overall impact remains consistent, ensuring that the influence trend of residual stress on joint mechanical behavior does not deviate significantly. However, applying Eq. (2) for simplification requires identical processing of nonuniform stresses at all height positions along the pipe's longitudinal direction. Fig. 4 reveals that WRS also varies nonlinearly along the pipe height. Accurate computation necessitates discretizing the pipe into numerous segments along its height, resulting in a computationally intensive process. To enhance efficiency, two extreme cases of uniformly distributed residual stress along the height are considered: ① Assume that the axial WRS in the range of height h_0 of the steel pipe is distributed according to the law at z = 3.5mm; ② Assume that the axial WRS in the range of height h_0 of the steel pipe is distributed according to the law at z = 100mm. Although the simplified stress distribution differs from reality, the mechanical nature at each location aligns with actual conditions. The selected stress values represent the maximum and minimum extremes of the actual distribution, bounding the upper and lower limits of the true stress. Consequently, the actual WRS lies between cases ① and ②, and the actual axial deformation u_s within height h_0 must lie between the results computed for these two cases.

$$\sigma_w = \frac{\int_{r=d/2}^{r=d/2+t/2} \sigma \cdot dr}{t/2} \tag{2}$$

In the formula, σ_w is the equivalent uniformly-distributed WRS, σ is the actual WRS, d is the inner diameter of the steel pipe, and t is the wall thickness of the steel pipe. For SJ1, when simplified according to case ①, σ_w = 85.2MPa is calculated, and when simplified according to case ②, σ_w=3.3MPa is calculated.

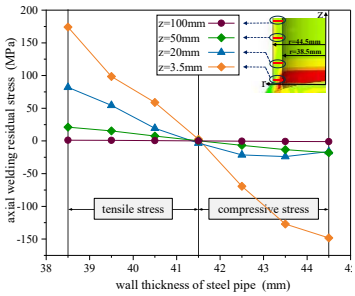

(a) Distribution of axial weld residual stresses in a typical cross-section of steel pipe

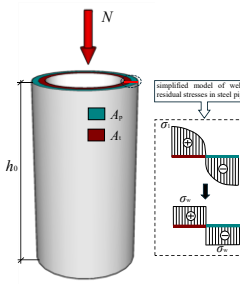

(b) Distribution of weld residual stresses before and after simplification of pipe section

Fig. 5 Residual stress distribution in welded SJ1 steel pipe

After simplification in the above manner, the cross section A within the height range of the steel pipe h_0 will be divided into two parts: The compression circumferential region A_p near the outside and the tension circumferential region A_t near the inside, as shown in Fig. 5(b). Obviously, A=A_p+A_t. When the WRS is not considered, the axial deformation within the height range of the steel pipe h_0 under the action of the axial force N can be calculated according to Eq. (3):

$$u_0 = \frac{Nh_0}{EA} \tag{3}$$

When considering the influence of WRS, if the proportional limit load of the steel pipe is assumed to be N_e, the axial force of the steel pipe under the action of N will go through two stages:

i 0~N_e stage: The entire cross section of the steel pipe is under pressure, that is, the compressive stress in the A_p region is less than the yield strength of the steel at this stage, and can share N with the A_t region. When N reaches N_e, the compressive stress in the A_p region just reaches the yield strength f_y, that is, $N_e/A+\sigma_w=f_y$. At this time, the axial deformation u_1 generated within the height range of the steel pipe h_0 can be calculated according to Eq. (4):

$$u_1 = \frac{N_e h_0}{EA} = \frac{(f_y - \sigma_w)\cdot h_0}{E} \tag{4}$$

ii N_e~N stage: In this stage, the stress value in the A_p region is the steel yield strength f_y, which will no longer increase, and plastic deformation will continue to occur. N is only borne by the A_t region. When the load reaches N, the axial displacement u_2 within the height range of the steel pipe h_0 is calculated according to Eq. (5):

$$u_2 = \frac{(N - N_e)h_0}{EA_t} \tag{5}$$

The axial displacement of the steel pipe during the entire loading process is:

$$u_s = u_1 + u_2 \tag{6}$$

For SJ1, A=1564mm^2, then A_p=A_t=782mm^2, and h_0=106mm, f_y=235N/mm^2, E=2.06×105N/mm^2, when simplified according to the above cases ① and ②, σ_w is 85.2MPa and 3.3MPa respectively. According to Eq. (3), u_0=3.29×10^{-4}×N is obtained for the steel pipe when the influence of WRS is not considered for SJ1.

According to Eqs. (4)-(6), the simplified N_e and u_s of SJ1 according to case ① are:

$$N_e = (f_y - \sigma_w)A = 234.3 \text{ (kN)} \tag{7}$$

$$u_s = 6.58\times10^{-4}\times(N-N_e)+0.08 \text{ (mm)} \tag{8}$$

According to case ②, the simplified N_e and u_s are:

$$N_e = (f_y - \sigma_w)A = 362.4 \text{ (kN)} \tag{9}$$

$u_s = 6.58\times10^{-4}\times(N-N_e)+0.12$ (mm) (10)

3.1.3. Calculation of δ_0

Similarly, to evaluate the influence of WRS on the axial deformation of the hollow sphere, the distribution pattern of residual stress within the spherical shell must first be defined. Following the same procedure applied to simplify u_s, the WRS in the hollow spherical joint is partitioned into distinct zones based on tensile and compressive characteristics, with stresses in each zone homogenized into uniform values.

Since the longitudinal and circumferential stresses in the hollow spherical shell will cause the vertical deformation, the distribution patterns of WRS in the hollow spherical shell along two directions are first extracted. As shown in Figs. 6(a)-(b), they are the distribution characteristics of longitudinal and circumferential WRS in the SJ1 hollow spherical shell established by the research team in the early stage. It can be seen that the WRS in the SJ1 hollow spherical shell has the following distribution law: the longitudinal WRS is roughly anti-symmetrically distributed along the wall thickness direction of the sphere with the center line of the wall thickness, that is, within the range of φ=0°~36°, the longitudinal WRS is transformed from tension to compression from the inner surface to the outer surface of the hollow sphere, and the maximum value is obtained at φ=27°, while in the range of φ=36°~90°, the opposite is true; the distribution of circumferential WRS along the wall thickness direction is mainly compressive stress inside and outside the circumferential seam, and the maximum value is obtained at φ=31°. Section 3.1.1 has made it clear that the influence zone of the SJ1 hollow spherical shell is within the range of φ=49.83°. As with the deformation analysis of steel pipes, the maximum residual stress and the minimum residual stress within the influence zone are taken for analysis. Specifically, when considering the most adverse effect of WRS, it is assumed that the WRS within the influence zone of the hollow sphere is uniformly distributed, and the longitudinal and circumferential WRS are distributed according to the conditions at φ=27° and φ=31° respectively; when considering the minimum effect of WRS, the longitudinal and circumferential WRS within the influence zone are distributed according to the conditions at φ=36° and φ=49° respectively, as shown in Fig. 6(c). To simplify the analysis, the longitudinal and circumferential residual stresses are simplified to the uniform distribution mode shown in Fig. 6(d) according to the principle that the tensile and compressive forces are equivalent.

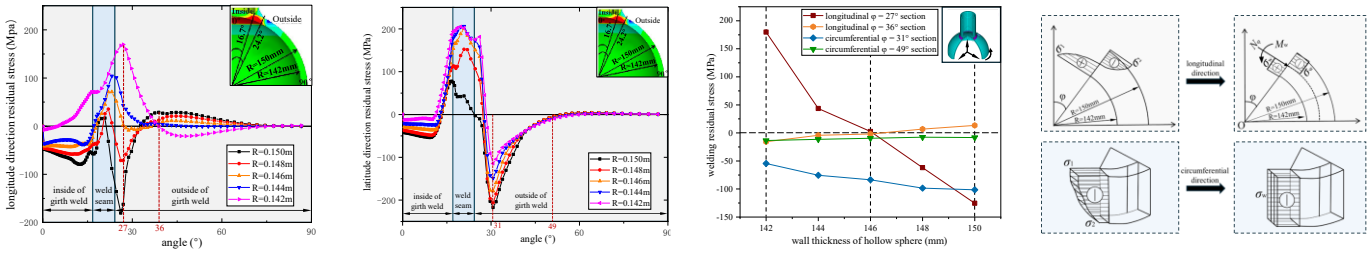

(a) WRS along the wall thickness of the SJ1 shell in the longitudinal direction

(b) Residual weld stress in the circumferential direction along the wall thickness of SJ1 spherical shells

(c) WRS distribution in a typical cross-section of a SJ1 spherical shell

(d) simplified weld residual stress distribution in the meridional and circumferential sections of the spherical shells

Fig. 6 Residual stress distribution of welded SJ1 spherical shells

The hollow sphere is mainly subjected to the axial force N transmitted by the steel pipe. Since the rigidity of the steel pipe and the surrounding spherical shell is relatively large, in order to simplify the analysis, the spherical shell within the steel pipe is regarded as a rigid body[23]. The internal force of the axial force N in the spherical shell can be decomposed into the longitudinal and circumferential membrane forces N_φ and N_θ, the bending moments M_φ and M_θ rotating around N_φ and N_θ, and the transverse shear force Q_φ pointing to the center of the sphere, and the longitudinal and circumferential shear forces S_φ and S_θ. Since the hollow sphere is highly symmetrical, S_φ and S_θ are both equal to 0. If the change of internal force along the thickness direction of the spherical shell is ignored and the mid-surface of the spherical shell is taken as the surface of internal force action, the distribution of internal force of the spherical shell is shown in Fig. 7, and the relationship between N and each internal force can be expressed by Eqs. (11)-(15)[13].

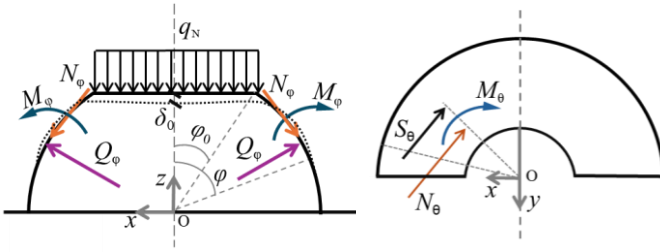

(a) Internal force distribution profile of a spherical shell

(b) Top view of internal force distribution in a spherical shell

Fig. 7 Distribution of internal forces in the spherical shell

$$N_\varphi = \frac{(1+\mu)N\cot\varphi}{\beta_s\sin\varphi_0}\cdot e^{\beta_s(\varphi_0-\varphi)}\cdot(\cos\beta_s\varphi_0\cos\beta_s\varphi+\sin\beta_s\varphi_0\sin\beta_s\varphi)-\frac{N\sin\varphi_0}{\sin^2\varphi} \tag{11}$$

$$N_\theta = \frac{(1+\mu)N}{\sin\varphi_0}\cdot e^{\beta_s(\varphi_0-\varphi)}\cdot[(\cos\beta_s\varphi_0-\sin\beta_s\varphi_0)\cos\beta_s\varphi+(\cos\beta_s\varphi_0+\sin\beta_s\varphi_0)\sin\beta_s\varphi]+\frac{N\sin\varphi_0}{\sin^2\varphi} \tag{12}$$

$$Q_\varphi = -\frac{(1+\mu)N}{\beta_s\sin\varphi_0}\cdot e^{\beta_s(\varphi_0-\varphi)}\cdot(\cos\beta_s\varphi_0\cos\beta_s\varphi+\sin\beta_s\varphi_0\sin\beta_s\varphi) \tag{13}$$

$$M_\varphi = \frac{(1+\mu)DN}{4\beta_s^2\sin\varphi_0}\cdot e^{\beta_s(\varphi_0-\varphi)}\cdot[(\cos\beta_s\varphi_0+\sin\beta_s\varphi_0)\cos\beta_s\varphi+(\sin\beta_s\varphi_0-\cos\beta_s\varphi_0)\sin\beta_s\varphi] \tag{14}$$

$$M_\theta = \frac{\mu(1+\mu)DN}{4\beta_s^2\sin\varphi_0}\cdot e^{\beta_s(\varphi_0-\varphi)}\cdot[(\cos\beta_s\varphi_0+\sin\beta_s\varphi_0)\cos\beta_s\varphi+(\sin\beta_s\varphi_0-\cos\beta_s\varphi_0)\sin\beta_s\varphi] \tag{15}$$

In the formula, $\beta_S=\sqrt[4]{\frac{3\left(1-\mu^2\right)D^2}{4t^2}}$; φ_0 is the opening angle at the top of the spherical shell, that is, the surrounding range of the steel pipe; μ is the Poisson's ratio, D is the outer diameter of the spherical shell; t is the wall thickness of the hollow sphere.

According to the theory of elastic thin shell , the work done by the internal forces N_φ, N_θ, M_φ, M_θ, and Q_φ of the hollow spherical shell in their respective directions can be expressed as:

$$W_{N_\varphi}=\int_0^{2\pi}\int_0^{\frac{\pi}{2}}\frac{1}{Et}\left(N_\varphi^2-\mu N_\varphi N_\theta\right)A_1A_2\cdot d\theta d\varphi \tag{16}$$

$$W_{N_\theta}=\int_0^{2\pi}\int_0^{\frac{\pi}{2}}\frac{1}{Et}\left(N_\theta^2-\mu N_\varphi N_\theta\right)A_1A_2\cdot d\theta d\varphi \tag{17}$$

$$W_{Q_\varphi}=\int_0^{2\pi}\int_0^{\frac{\pi}{2}}\frac{2(1+\mu)}{Et}Q_\varphi^2A_1A_2\cdot d\theta d\varphi \tag{18}$$

$$W_{M_\varphi}=\int_0^{2\pi}\int_0^{\frac{\pi}{2}}\frac{12}{Et^3}\left(M_\varphi^2-\mu M_\varphi M_\theta\right)A_1A_2\cdot d\theta d\varphi \tag{19}$$

$$W_{M_\theta}=\int_0^{2\pi}\int_0^{\frac{\pi}{2}}\frac{12}{Et^3}\left(M_\theta^2-\mu M_\varphi M_\theta\right)A_1A_2\cdot d\theta d\varphi \tag{20}$$

In the above formula, A_1 and A_2 are Lame coefficients. In the spherical shell, $A_1=D/2$, $A_2=(D/2)\cdot\sin\varphi$, and E is the elastic modulus.

According to Fig. 7(a), when the upper boundary of the hollow spherical shell produces a vertical displacement of δ_0, according to the principle of virtual work:

$$N\delta_0=W_{N_\varphi}+W_{N_\theta}+W_{Q_\varphi}+W_{M_\varphi}+W_{M_\theta}$$

Combining the above formulas, the vertical displacement δ_0 of the hollow spherical shell under the axial load N can be solved as:

$$\delta_0=\left\{\int_0^{2\pi}\int_0^{\frac{\pi}{2}}\left[\frac{1}{Et}\left(N_\phi^2-\mu N_\phi N_\theta\right)+\frac{1}{Et}\left(N_\theta^2-\mu N_\phi N_\theta\right)+\frac{12}{Et^3}\left(M_\phi^2-\mu M_\phi M_\theta\right)+\frac{12}{Et^3}\left(M_\theta^2-\mu M_\phi M_\theta\right)+\frac{2(1+\mu)}{Et}Q_\phi^2\right]A_1A_2d\theta d\phi\right\}\times\frac{1}{N} \tag{21}$$

Assume that the internal forces in the spherical shell caused by WRS are $N_{w\varphi}$, $N_{w\theta}$, $M_{w\varphi}$, $M_{w\theta}$, $Q_{w\varphi}$, $S_{w\varphi}$, and $S_{w\theta}$ respectively. Now SJ1 is taken as an example to illustrate the calculation method considering the influence of WRS.

After the WRS is simplified in the above way, the calculation of N_φ work considering the influence of $N_{w\varphi}$ can refer to the calculation idea of steel pipe in Section 3.1.2, that is, the cross section $A_{s\varphi}$ within the t thickness range of the spherical shell is divided into two areas: The compression circumferential area $A_{p\varphi}$ close to the outside and the tension circumferential area $A_{t\varphi}$ close to the inside, as shown in Fig. 6(d), $A_{s\varphi}=A_{p\varphi}+A_{t\varphi}$. When considering the influence of WRS, assuming that the proportional limit load of the spherical shell longitudinal membrane force is $N_{e\varphi}$, the spherical shell force under the action of the longitudinal force N_φ will go through two stages:

i 0~$N_{e\varphi}$ stage: The entire cross section of the spherical shell is compressed in the longitudinal direction, that is, the compressive stress in the $A_{p\varphi}$ region at this stage is less than the yield strength of the steel, and can share N_φ with the $A_{t\varphi}$ region. When N_φ reaches $N_{e\varphi}$, the compressive stress in the $A_{p\varphi}$ region just reaches the yield strength f_y, that is, $N_{e\varphi}/A_{s\varphi}+\sigma_{w\varphi}=f_y$. At this stage, the work done by N_φ is calculated according to Eq. (22):

$$W_1=\int_0^{2\pi}\int_0^{\frac{\pi}{2}}\frac{1}{Et}\left(N_{e\varphi}^2-\mu N_{e\varphi}N_\theta'\right)A_1A_2\cdot d\theta d\varphi \tag{22}$$

ii $N_{e\varphi}$~N_φ stage: In this stage, the stress value of the $A_{p\varphi}$ region is the steel yield strength f_y, and the resultant force $N_p=f_yA_{p\varphi}$ no longer increases. Plastic deformation will continue to occur, and N_φ is only borne by the $A_{t\varphi}$ region. In this stage, the work done by N_φ consists of two parts: the elastic region and the plastic region, which can be calculated according to Eq. (23):

$$W_2=\int_0^{2\pi}\int_0^{\frac{\pi}{2}}\left\{\frac{2}{Et}\left[\left(N_\varphi-N_{e\varphi}\right)^2-\mu\left(N_\varphi-N_{e\varphi}\right)N_\theta'\right]+\frac{2}{Et}\left(N_p^2-\mu N_pN_\theta'\right)\right\}A_1A_2\cdot d\theta d\varphi \tag{23}$$

Among them , as shown in Fig. 6(d), the simplified circumferential WRS is uniformly distributed in the same direction, so $N_{w\theta}=\sigma_{w\theta}A_{s\theta}$.Then the work N_φ considering the WRS can be calculated according to Eq. (24):

$$W_{N_\varphi}=W_1+W_2 \tag{24}$$

As shown in Fig. 6(d), the simplified resultant force of the longitudinal WRS is almost 0, and the effect on the work done by the circumferential WRS can be ignored. Therefore, the work done by N_θ considering the WRS can be calculated according to Eq. (25):

$$W_{N_\theta}=\int_0^{2\pi}\int_0^{\frac{\pi}{2}}\frac{1}{Et}\left[\left(N_\theta+N_w\right)^2-\mu N_\varphi\left(N_\theta+N_w\right)\right]A_1A_2\cdot d\theta d\varphi \tag{25}$$

In the theoretical analysis, the influence of the wall thickness of shell on the internal force is ignored, and it is assumed that all internal forces act on the mid-surface of the shell. As shown in Fig. 6(d), the longitudinal WRS $\sigma_{w\varphi}$ is distributed anti-symmetrically on the mid-surface of the shell. According to the moment balance principle, there must be a bending moment $M_{w\varphi}$ caused by $\sigma_{w\varphi}$ at the φ section, and its magnitude can be calculated according to Eq. (26):

$$W_{M_\varphi}=\frac{1}{4}t\sigma_{w\varphi}A_s\varphi \tag{26}$$

As shown in Fig. 6(d), the circumferential WRS does not cause bending moment on the mid-surface of the spherical shell and there is no distribution of tangential WRS , so $M_{w\theta}=Q_{w\varphi}=S_{w\varphi}=S_{w\theta}=0$. When the WRS of spherical shell is considered, the vertical displacement δ'_0 of the spherical shell can be calculated according to Eq. (27):

$$\delta_0'=\frac{W_{N_\varphi}+W_{N_\theta}+W_{M_\varphi}}{N} \tag{27}$$

For SJ1, D=300mm, t=8mm, φ_0=16.7°, β_s=5.57, f_y=235N/mm^2, $A_{s\theta}$=1833.76mm^2, $A_{s\varphi}$=3315.84mm^2, and $A_{p\varphi}=A_{t\varphi}$ =1657.92mm^2, considering that the residual stress value of the φ=27° section is relatively large, in order to facilitate the solution, the internal force of this section is taken for quantitative analysis. Then according to Eqs. (11)-(15), the internal force of the spherical shell at the φ=27° section of SJ1 without considering the influence of WRS is calculated: $\varphi=-1.38\times N$, $N_\theta=1.38\times N$, $M_\varphi=-3.84\times N\times10^{-25}$, $M_\theta=-1.15\times N\times10^{-25}$, and $Q_\varphi=-0.52\times N\times10^{-25}$. Since the values of M_φ、M_θ, and Q_φ are all small, their influence on the axial stiffness of the spherical shell can be ignored, and $M_\varphi=M_\theta=Q_\varphi=0$ can be directly assumed. Then, according to Eq. (27), when the WRS is not considered, the spherical shell $\delta_0=2.36\times10^{-3}\times N$ is obtained.

According to the simplified method mentioned above, when considering the influence of the maximum WRS: $\sigma_{w\varphi}=63.9$MPa, $\sigma_{w\theta}=-83.62$MPa, $N_{e\varphi}=(f_y-\sigma_{w\varphi})A_{s\varphi}=567.34$(kN), and $N_\theta'=N_\theta+\sigma_{w\theta}A_{s\theta}=1.38\times N-153.34$, then according to Eq. (27), $\delta'_0=3.2\times10^{-3}\times N+0.21$ is calculated; When considering the influence of the minimum WRS: $\sigma_{w\varphi}=6.43$MPa, $\sigma_{w\theta}=-9.87$MPa, $N_{e\varphi}=(f_y-\sigma_{w\varphi})A_{s\varphi}=758$(kN), and $N_\theta'=N_\theta+\sigma_{w\theta}A_{s\theta}=1.38\times N-18.1$, then according to Eq. (27), $\delta'_0=2.41\times10^{-3}\times N+0.12$ is calculated.

3.1.4. Calculation of K

When considering the distribution of maximum WRS of SJ1, the spherical

shell $N_{c\varphi}$ is 567.34kN. During the loading process, the longitudinal force of the spherical shell is always in the elastic stage, while the steel pipe N_e is only 234.3kN. Therefore, it is advisable to take the theoretical bearing capacity of joint N=346kN to make a quantitative analysis of the axial stiffness of joint. When the WRS is not considered, the vertical displacement of the steel pipe u_0=3.29×N×10^{-4} = 0.11(mm), the vertical displacement of the spherical shell δ_0=2.36×N×10^{-3} = 0.82(mm), and the axial stiffness of the joint is:

$$K_0 = \frac{N}{u_0 + \delta_0} = 3.72\times10^5 (\mathrm{N/mm}) \tag{28}$$

When considering the influence of the maximum WRS, the vertical displacement of the steel pipe is u_s = 6.58×10^{-4}×(N-N_e)+0.08 = 0.15(mm), and the vertical displacement of the spherical shell is δ'_0=3.2×N×10^{-3}+0.21 = 1.32(mm), then the axial stiffness of the hollow joint is:

$$K_1 = \frac{N}{u_0 + \delta_0} = 2.35\times10^5 (\mathrm{N/mm}) \tag{29}$$

When considering the influence of the minimum WRS, the vertical displacement of the steel pipe is u_s = u_0 = 3.29×N×10^{-4}=0.11 (mm), and the vertical displacement of the spherical shell is δ'_0 = 2.41×10^{-3}×N+0.08 = 0.91(mm), then the axial stiffness of the joint is:

$$K_2 = \frac{N}{u_0 + \delta_0} = 3.39\times10^5 (\mathrm{N/mm}) \tag{30}$$

The maximum weakening degree β_k of the axial stiffness of the SJ1 joint caused by WRS is 36.8%, and the minimum weakening degree β_k is 8.9%. That is, the theoretical weakening degree of the axial stiffness of the SJ1 joint caused by WRS is between 8.9% and 36.8%.It should be noted that the aforementioned computational procedure simplifies the distribution pattern of WRS, assuming uniform distributions of key stress values at the extreme minimum and maximum levels within the joint region. While the resulting range of joint stiffness reduction bounds the actual scenario, this range is conservatively broad. The computational process for all other specimen groups (e.g., SJ2–SJ5) follows an identical approach to SJ1 and is thus omitted here.

3.2. Influence of WRS on ultimate bearing capacity of joints

Assuming that the welded hollow spherical joint mainly suffers from punching shear failure under axial load, and the vertical shear stress τ plays a controlling role on the punched surface, the joint will suffer from punching shear failure when the shear stress on the punching surface reaches the yield strength[23], as shown in Fig. 8. According to the von-Mises equivalent stress theory, when the equivalent stress of the shear stress on the punched surface exceeds the yield strength of the material, the joint is considered to be damaged. In order to analyze the influence mechanism of WRS on the ultimate compressive bearing capacity of the hollow spherical joint, a micro-segment is taken on the circumferential punched surface of the hollow spherical joint for analysis, as shown in Fig. 9.

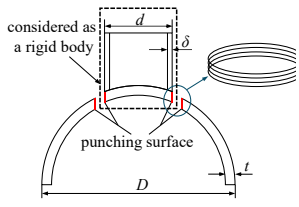

Fig. 8 Schematic diagram of punching damage of welded hollow sphere joint

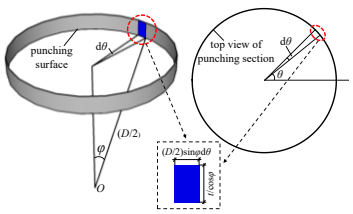

Fig. 9 Schematic diagram of punched surface differential segments

Assume N_u is the ultimate bearing capacity. From the geometric relationship, the length of the micro-segment is t/cosφ and the width is (D/2)sinφdθ. The stress resultant on the micro-segment can be calculated according to Eq. (31). Then, it is integrated along the circumferential direction of the hollow spherical joint. The theoretical ultimate bearing capacity of the joint based on the shear stress destruction model of the punched surface can be calculated according to Eq. (32).

$$\mathrm{d}N_u = \tau\left(\frac{t}{\cos\varphi}\right)\left(\frac{D}{2}\right)\sin\varphi\mathrm{d}\theta \tag{31}$$

$$N_u = \int_0^{2\pi}\tau\left(\frac{t}{\cos\varphi}\right)\left(\frac{D}{2}\right)\sin\varphi\mathrm{d}\theta = \tau\pi D\tan\varphi = \frac{f_y}{\sqrt{3}}\pi D\tan\varphi \tag{32}$$

Assume that N_w represents the resultant force of WRS on the punched surface, and similarly it can be calculated according to Eq. (33):

$$N_w = \int_0^{2\pi}\tau_w\left(\frac{t}{\cos\varphi}\right)\left(\frac{D}{2}\right)\sin\varphi\mathrm{d}\theta = \tau_w\pi D\tan\varphi \tag{33}$$

In the formula: τ_w is the equivalent tangential residual stress on the punched surface.

When WRS exists on the punched surface, the maximum bearing capacity of WHSJ can be calculated by Eq. (34):

$$N'_u = N_u - N_w \tag{34}$$

The degree of weakening of the ultimate bearing capacity of Welded hollow spherical joints by WRS β_N can be calculated by Eq. (35):

$$\beta_N = \frac{N_u - N'_u}{N_u}\times100\% \tag{35}$$

Based on the previous studies of the research group, the data of tangential WRS on the SJ1 punched surface are extracted and the distribution curve is drawn as shown in Fig. 10. It can be seen that the tangential residual stress on the punched surface changes with the thickness in a gradient manner. The closer to the weld, the larger the value is, and the maximum value appears at the starting point of welding. Except for the starting point of welding, the tangential WRS is basically equal. The WRS of each layer is regarded as the same value, and the equivalent tangential WRS of the punched surface of this layer is taken as the principle of equal resultant force of the layer. To simplify the calculation, two extreme cases are analyzed: ① Assume that the tangential WRS on the punched surface is distributed according to the law of the welding layer; ② Assume that the tangential WRS on the punched surface is distributed according to the law at a distance t from the welding layer. Of course, the actual distribution law of WRS on the punched surface is also between ① and ②, and the impact on the ultimate bearing capacity of the joint is also between ① and ②. It is worth noting that the calculation formula for the bearing capacity of joint given by Eq. (34) is completely based on theoretical derivation and lacks experimental correction. The calculation result may not be completely consistent with the actual situation, but it can reflect the impact trend to a certain extent and provide guidance for the experimental research in this paper.

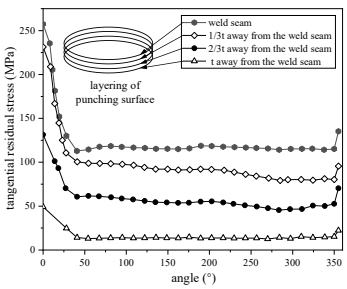

Fig. 10 Residual weld stress distribution in the tangential direction on the punched surface of SJ1

For SJ1, when simplified according to the above cases ① and ②, τ_w is 118.4MPa and 14.3MPa respectively. According to Eq. (33), the resultant force N_w of WRS on the SJ1 punched surface is 267.7kN and 32.3kN respectively. According to Eq. (32), the ultimate bearing capacity of joint N_u is 306.7kN when the WRS is not considered. According to Eq. (34), the maximum bearing capacity N_u' of SJ1 is 39kN and 274.4kN respectively. According to Eq. (35), β_N is 87.2% and 10.5% respectively. According to the calculation results, the

theoretical weakening degree of WRS on the ultimate bearing capacity of SJ1 joint will be between 10.5% and 87.2%.

4. An experimental study on axial bearing performance of WHSJ

Given the nonlinear distribution of WRS within the joint and the coexistence of tensile and compressive stresses, the preceding theoretical calculations employed necessary approximations. While these simplifications capture the influence trend of WRS on the axial load-bearing behavior of WHSJ, they cannot quantify its magnitude. To rigorously assess the quantitative impact of WRS on joint axial performance, an experimental investigation on the axial behavior of WHSJ was conducted.

4.1. Test design of axial loading

4.1.1. Loading plan

In order to simulate the axial force of the joint, two sets of hinged supports are designed to be connected to the loading end plates of the upper and lower ends of the specimen by bolts, then the upper hinged support is connected to the reaction frame crossbeam by screws, and a pressure sensor is placed between the hinged support and the crossbeam; the lower hinged support is directly placed on a 200-ton pneumatically controlled hydraulic jack, as shown in Fig. 11, which is a diagram of the test loading device.

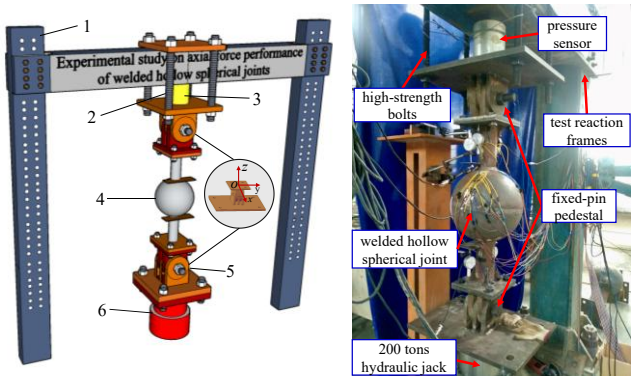

(a) Schematic diagrams test reaction frames;2.high-strength bolts; 3.pressure sensor; 4.welded hollow spherical joint; 5.fixed-pin pedestal;6. 200 tons hydraulic jack

(b) Photographs of loading device diagram

Fig. 11 Loading device diagram

The test loading adopts monotonic static loading. Reference [31]calculates the theoretical axial compressive bearing capacity N_R of each group of specimens according to Eq. (36), which is listed in Table 1 of Section 2.1. Since N_R has taken into account a certain degree of safety, the actual loading load P=1.6N_R is taken, and the loading is divided into 14 levels. Before loading to 0.6P, it increases step by step by 0.1P; after 0.6P, it increases step by step by 0.05P to capture the destruction mode of the joint. Before formal loading, it is preloaded to 0.4P and then unloaded to eliminate the gap between the specimen and the loading system.

$$N_R = \eta_0\left(0.29 + 0.54\frac{d}{D}\right)\pi t d f \tag{36}$$

In the formula: η_0 is the adjustment coefficient of bearing capacity of large-diameter hollow spherical joint, when D≤500mm, η_0=1.0; f is the design value of steel strength, f=215N/mm^2.

4.1.2. layout of measuring points

In order to obtain the axial bearing performance of the joint, the axial deformation of the joint during the loading process should be measured. Therefore, four groups of displacement meters are arranged on the joint according to Fig. 12. At this time, the axial displacement w of the joint can be calculated according to Eq. (37).

$$w = (w_3 + w_4)/2 - (w_1 + w_2)/2 \tag{37}$$

In the formula: w_1~w_4 are the axial deformation values measured by 4 groups of displacement meters.

Since there are certain errors in the specimen production and loading device, eccentricity is inevitable during the loading process. In order to examine the eccentricity of each group of specimens, 4 groups of strain gauges are symmetrically arranged on the upper and lower steel pipes; at the same time, in order to track the stress changes of the joint during the loading process, strain rosettes are arranged on the WHSJ, as shown in Fig. 12.

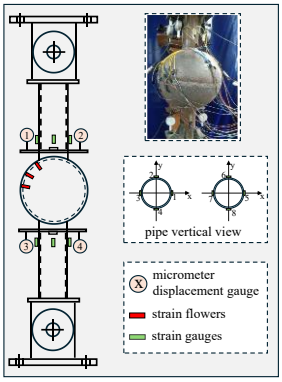

Fig. 12 Layout of measurement points

4.2. test results

4.2.1. Load-displacement curve

The axial deformation of each group of specimens during the loading process is extracted and calculated, and its variation curve along the loading process is plotted, as shown in Fig. 13.

As can be seen from Fig. 13, the axial deformation of each group of specimens changes similarly during the loading process, and their load-displacement curves can be divided into the elastic stage, the elastoplastic stage, and the descending stage. Taking SJ1 as an example, in the initial stage of loading, that is, when the axial displacement increases from 0 to about 1 mm, the axial deformation of the joint increases linearly with the load, and the joint is in the elastic stage as a whole; When the load increases to 208 kN, that is, 0.6P, the joint deformation changes nonlinearly with the load, the displacement increase rate is greater than the load increase rate, and the joint enters the elastoplastic stage; When the load increases to 255 kN, that is, about 0.7P, the joint will enter the plastic stage, and the plastic zone will continue to expand. Even if the load is reduced, the deformation will continue to increase, and then the joint will be damaged.

In addition, as shown in Fig. 13, the load-displacement curves of the control specimens exhibit steeper slopes in the elastic stage than those of the test specimens, indicating higher axial stiffness. Concurrently, the control group demonstrates greater peak loads, confirming superior ultimate load-bearing capacity. These results verify that WRS undermines both the axial stiffness and ultimate bearing capacity of the joints.

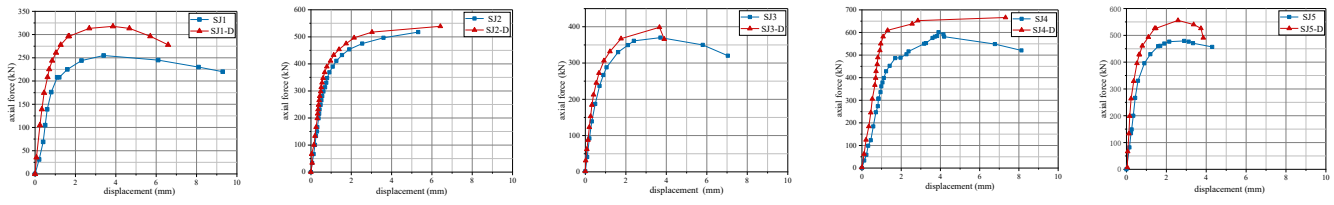

SJ1 & SJ1-D SJ2 & SJ2-D SJ3 & SJ3-D SJ4 & SJ4-D SJ5 & SJ5-D

Fig. 13 Load-displacement curve

4.2.2. Axial stiffness and ultimate bearing capacity of joint

To quantify the influence of WRS on the axial mechanical properties of WHSJ, the elastic axial stiffness and ultimate compressive capacity were extracted from test and control specimens using a graphical method. Taking SJ1 and SJ1-D as examples (Fig. 14): First, fit the load-displacement curve and draw a horizontal line through the peak load point to determine the ultimate capacity N_u. Then, draw a tangent to the elastic segment from the origin, intersecting the peak horizontal line at points A and B. The slopes OA and OB represent the elastic axial stiffness K and K_{Urr}, respectively. The parameters for all specimen groups, calculated via this method, are listed in Table 3. For comparative analysis, Table 3 also includes theoretical values of the axial stiffness and ultimate capacity reduction rates for the five specimen groups.

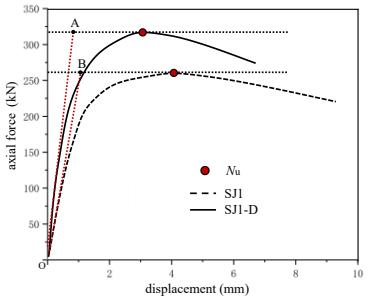

Fig. 14 Calculation of axial stiffness and ultimate compressive load capacity of hollow sphere joint by graphical method

Table 3
Experiment results of axial mechanical properties

number	test specimen	test values K(10^3N/mm)	test values N_u(kN)	control specimen	test values K_{Urr} (10^3N/mm)	test values N_{Urr} (kN)	β_K		β_N	
							test results	theoretical results	test results	theoretical results
1	SJ1	206.11	255.24	SJ1-D	249.8	317.63	21.24%	8.9%~36.8%	24.44%	10.5%~87.2%
2	SJ2	400.18	517.57	SJ2-D	457.8	538.84	14.40%	10.5%~41.7%	4.11%	3.46%~85.2%
3	SJ3	271.24	389.62	SJ3-D	333.03	398.46	22.78%	11.5%~39.6%	2.27%	4.1%~86.3%
4	SJ4	377.9	601.2	SJ4-D	584.6	666.46	54.7%	11.5%~57.3%	10.85%	10.17%~88.8%
5	SJ5	447.88	479.28	SJ5-D	456.69	555.86	1.97%	6.7%~61.1%	15.98%	11.2%~88.2%

Note: ① K in the table is the elastic axial stiffness of the joints in the test group, and K_{Urr} is the elastic axial stiffness of the joints in the control group; ② N_u in the table is the ultimate bearing capacity of the joints in the test group, and N_{Urr} is the ultimate bearing capacity of the joints in the control group; ③ β_K is the weakening rate of axial stiffness, $\beta_K = \frac{(K_{Urr} - K)}{K} \times 100\%$; ④ β_N is the weakening rate of ultimate bearing capacity, $\beta_N = \frac{(N_{Urr} - N_u)}{N_u} \times 100\%$.

1) Effect of WRS on axial mechanical properties of joints

As indicated in Tables 2 and 3, a 30%–40% reduction in WRS in the test specimens enhances the axial stiffness of WHSJ by approximately 1.97%–54.7% and increases their ultimate bearing capacity by approximately 2.27%–24.44%. Compared to theoretical derivation, the experimental results exhibit generally lower values. This discrepancy stems from simplifications in the theoretical model: WRS throughout the joint were partitioned into distinct tensile and compressive zones, with nonlinear stresses in each zone homogenized into uniform values. Additionally, ultrasonic impact treatment failed to achieve complete elimination of WRS in control specimens, resulting in partially retained stresses that further contributed to the reduced experimental values.

Specifically, the axial stiffness of the SJ1 joint increased by 21.24%, and the ultimate bearing capacity increased by 24.44%. The degree of influence is consistent with the influence range of theoretical derivation , indicating that the WRS does affect the axial mechanical properties of the hollow spherical joint, but the specific degree of influence is relatively discrete. In particular, when the WRS of the two groups of specimens 1 and 2 in Table 3 is reduced by 41%, the increase degree of the axial stiffness and ultimate bearing capacity of the joint is quite different. The reason is mainly because the sphere diameters D of the two groups of specimens 1 and 2 are different. Obviously, the structural dimensions of the joint will affect the distribution of WRS, and then the degree of influence on the axial mechanical properties of the joint will also be affected. The other groups of specimens also showed similar situations, which shows that the degree of influence of WRS on the axial mechanical properties of the joint is related to the structural dimensions of the joint.

2) Effect of WRS on axial mechanical properties of joints with the change of structural dimension

① Effect of WRS on axial properties of joints with variation of D

In order to investigate the influence of WRS on the axial mechanical properties of the joint when the diameter D of the hollow sphere changes, the specimens of group 1 and group 2 are selected for analysis. The t and d of the specimens of group 1 and group 2 are exactly the same, and D is 300 and 350 mm respectively. The variation trend of β_K and β_N of the two groups of specimens with D is plotted, as shown in Fig. 15(a).

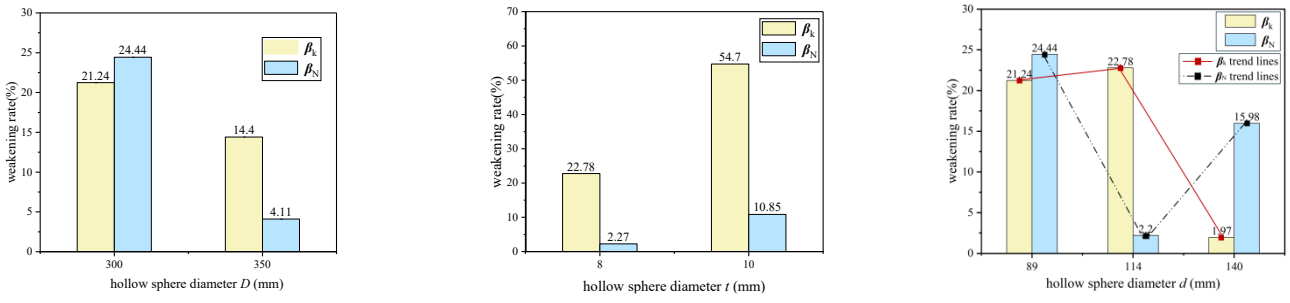

(a) D (b) t (c) d

Fig. 15 Trend of the effect of WRS on the axial mechanical properties of the joints with the variation of geometrical configuration dimensions

As shown in Fig. 15(a), when the hollow sphere diameter D is different, the weakening rate of the WRS on the axial stiffness of joint exceeds 10%, with the maximum weakening of 21.24%; but as D increases, the weakening degree of the WRS on the axial stiffness of joint is decreasing, and the weakening rate when D=300mm is about 1.5 times that when D=350mm. In terms of ultimate bearing capacity, when D=300mm, the weakening of the ultimate bearing capacity by WRS is most obvious, and the weakening rate reaches 24.44%, but as D increases, the weakening degree is also decreasing, and the weakening rate when D=300mm is about 6 times that when D=350mm. It can be seen that the ultimate bearing capacity of small-diameter WHSJ is more affected by WRS, while the influence of WRS on the axial stiffness of joint is insensitive to the change of D.

② Effect of WRS on axial properties of joints with t

Two sets of test results, 3 and 4, are selected to analyze the influence of WRS on the axial mechanical properties of joints as the wall thickness t of hollow sphere changes. The D and d of the two sets of specimens 3 and 4 are exactly the same, and t is 8 and 10 mm respectively. Draw the changing trends of β_K and β_N in groups 3 and 4 with t, as shown in Fig. 15(b). It can be seen from Fig. 15(b) that when the wall thickness t of hollow sphere changes, the WRS weakens the axial stiffness and ultimate bearing capacity of the joint more

significantly, especially the maximum impact on the axial stiffness is as high as 54.7 %; Specifically, the weakening rate at t = 10 mm is approximately 2.4 times that at t = 8 mm. In terms of ultimate bearing capacity, the weakening rate at t = 10 mm is about 5 times that at t = 8 mm. It can be seen that as the wall thickness t increases, the influence of WRS on the axial mechanical properties of WHSJ increases significantly, and as t increases, the influence of WRS on the ultimate bearing capacity of the joint accounts for dominant position, its influence is about twice the influence on the axial stiffness of the joint.

③ Effect of WRS on axial properties of joints with d

In order to examine the influence of WRS on the axial mechanical properties of joints as the steel pipe diameter d changes, the test results of groups 1, 3 and 5 are selected. The D and t of these three groups of specimens are exactly the same, and d is 89, 114 and 140mm respectively. The changing trends of β_K and β_N of each group of specimens with d are shown in Fig. 15(c). It can be seen that when d changes, the maximum weakening rate of the WRS on the axial stiffness of the joint is 22.8%, and the maximum weakening rate on the ultimate bearing capacity of the joint is 24.44%; as d changes, the maximum weakening rate of the WRS on the ultimate bearing capacity of the joint is 22.8%. The degree of influence on axial mechanical properties shows obvious differences. Specifically, when the steel pipe diameter d increases from 89mm to 114mm, the influence of WRS on the axial stiffness of the joint is basically the same, but the weakening rate on the ultimate bearing capacity drops significantly, that is, the weakening rate when d = 89mm is about d = 11 times of 114mm; When the steel pipe diameter d increases from 114mm to 140mm, the degree of weakening of the axial stiffness of the joint by the WRS is significantly reduced, but the degree of weakening of the ultimate bearing capacity is significantly increased, that is, when d = 114mm, the effect of the WRS on the axial stiffness The weakening rate of WRS on the ultimate bearing capacity is about 12 times that of d = 140mm. When d = 140mm, the weakening rate of WRS on the ultimate bearing capacity is about 7 times that of d = 114mm. Overall, as the steel pipe diameter d increases, the degree of weakening of the joint axial stiffness by WRS first increases and then decreases, and the degree of weakening of the ultimate bearing capacity first decreases and then increases.

4.2.3. Destruction mode

As shown in Fig. 16, the destruction modes of each group of specimens are not exactly the same. They can be roughly divided into three categories: The first category is that when the hinge support cannot rotate around the support x-axis and the axial force is mainly eccentric along the y-axis, the sphere-pipe connection area of the hollow sphere will generate a large shear force during loading. SJ1 and SJ2 in Fig. 16 are such cases; The second category is when the axial force is mainly eccentric along the x-axis direction, because the hinge support can rotate in this direction (around the y-axis), the steel pipe tilts during loading, and one side of the weld is concave and the other side is convex during destruction. SJ1-D, SJ4 and SJ5 belong to this category; The third category is that the eccentricity is always small during loading, the specimen is loaded to destruction, the steel pipe is evenly sunken into the hollow sphere, and punching shear failure mainly occurs. SJ2-D, SJ3, SJ3-D, SJ4-D and SJ5-D all belong to this category. In order to accurately examine the eccentricity of each group of specimens during the test, 4 groups of strain gauges are symmetrically arranged on the upper and lower steel pipes. Taking SJ1 as an example, according to the strain collected from the steel pipe during loading, the initial eccentricity of the joint is calculated to be only 1.5 mm. The other groups of specimens also had different degrees of initial eccentricity, but their influence is not significant compared with the structure dimension of joint.

Fig. 16 Actual view of specimen destruction

Note: x-x in the Fig.16 indicates observation along a direction perpendicular to the y-y axis shown in Fig. 12; y-y indicates observation along a direction perpendicular to the x-x axis shown in Fig. 12.

In addition, it can be seen from Fig. 16 that for the test specimens in the test group, namely, SJ1~SJ5 specimens, all three destruction modes may occur; But for the control group specimens, except SJ1-D, all belong to the third category of destruction mode. The second category of destruction occurred in specimen SJ1-D, mainly because the loading process produced a large eccentricity along the x-axis. It can be seen that when each specimen has a certain initial eccentricity, the test group specimens and the control group specimens show significantly different destruction modes, indicating that the initial eccentricity is not the only factor of the destruction mode of specimen. The WRS at the sphere-pipe connection weld also has a certain influence on the destruction mode of the joint. The specific influencing mechanism is as follows:

When the WRS is not considered or the residual stress value is small, the destruction of the hollow spherical joint under axial load begins at the outer surface of the sphere-pipe connection. After the outer surface reaches yield, a plastic zone is formed and develops to the inner surface. As the load increases, the inner surface also enters the plastic stage and expands to the outer surface. When the plastic zones of the inner and outer surfaces converge, the hollow spherical joint undergoes uniform shear failure [23], as shown in Fig. 17(a). When there is non-negligible WRS on the hollow spherical joint, the existence of WRS will interfere with the shear stress distribution on the punched surface, resulting in unequal distribution of shear stress on the circumferential shear surface of joint. The unevenly distributed WRS and the stress generated by the external load will cause the outer surface of the weld starting point to yield first, and then gradually expand to the inner surface, while other circumferential areas still have a certain resistance and no large plastic deformation occurs. Under the combined effect of this circumferential uneven deformation, the hollow spherical joint will eventually be damaged by bias pressure, and the distribution of WRS on the punched surface is larger, as shown in Fig. 17(b). The research team found in the previous studies that the distribution of WRS on the punched surface of the other groups of specimens is generally similar to that of SJ1, and there is only a difference in value with the structure dimension of joint. Therefore, the specimens of the test group in Fig. 16 all suffered different degrees of bias pressure damage under the influence of WRS.

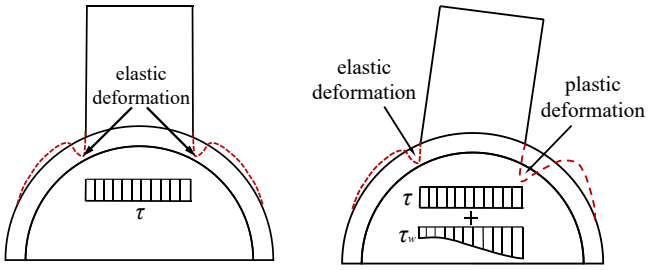

(a)Uniform deformation (b) Uneven deformation

Fig. 17 Schematic diagram of the effect of WRS on the damage mode of the specimen

5. Conclusion

The large number of sphere-pipe connection welds on WHSJ will cause complex WRS in the joints. This paper conducts theoretical derivation and experimental research on the influence of WRS on the axial mechanical properties of WHSJ. The main research conclusions are as follows:

1) The influence mechanism of WRS on the axial stiffness and axial compressive bearing capacity of WHSJs is clarified through theoretical derivation. Theoretically, WRS can reduce the axial stiffness of WHSJ by about 8.9%~36.8%, and the axial compressive ultimate bearing capacity by about 10.5%~87.2%.

2) The axial bearing performance test of WHSJ is carried out. The results show that WRS can reduce the axial stiffness of WHSJ by about 1.97%~54.7%, and the axial compressive ultimate bearing capacity by about 2.27%~24.4%, and will affect the destruction mode of the joint.

3) The influence of WRS on the axial mechanical properties of the joint as the change of structural dimensions of joint is revealed. The influence of WRS on the axial stiffness and axial compressive ultimate bearing capacity of the joint decreases with the increase of the diameter D of hollow sphere, and increases with the increase of the wall thickness t. As the diameter d of the steel pipe increases, the influence on the axial stiffness first increases and then decreases, while the influence on the axial compressive ultimate bearing capacity first decreases and then increases.The influence of steel pipe diameter d on the axial mechanical performance of WHSJ follows a non-monotonic trend. With increasing d, its effect on axial stiffness initially intensifies then diminishes, while its impact on axial compressive ultimate bearing capacity first decreases and subsequently increases.

Acknowledgments

Supported by the Science and Technology Research Program of Chongqing Municipal Education Commission (Grant No. KJQN202403002)

Reference

[1] Liu X.L. and Chen Z.H., Connection between spherical tubes of welded hollow spherical joints of space truss, J.Steel Const, 04, (1991) 52-54. (in Chinese).
[2] Wang X., Dong S.L. and Wan H.Y., Analysis of influence of welding spherical joint stiffness on internal force and deflection of grid, J.Spatial Structures, 2(4),(1996) 34-40 (in Chinese).
[3] Zhang J.L. and Zhao J.C., Influence of joint stiffness on buckling of short-line linear single-layer spherical shell, J.Building Technique Development, 30(3), (2003) 8-9 (in Chinese).
[4] Zhang J.L. and Zhao J.C., The influence of joint stiffness exerted on the stability of Kiewite-type singlelayer reticulated shells, J. Spatial Structure, 10(2), (2004) 43-45, (in Chinese).
[5] Kang J. and Song Z.S., The influence of joint stiffness on the stability of geodesic single-layered reticulated shells with initial in perfection, J. Sichuan Building Science, 34(1), (2008) 42-46, (in Chinese).
[6] Kang J., Zhao J. and Song Z.S., The influence of joint stiffness on the stability of hyperbolic paraboloid reticulated shells with initial in perfection, J.Low Temperature Architecture Technology, (6), (2005) 47-49, (in Chinese).
[7] Li F., Lou Q.L. and Liu T., Study on static performance of cylindrical giant grid structure based on node stiffness, J. Journal of Xi'an University of Architecture and Technology:Natural Science Edition, 46(5), (2014) 682-686, (in Chinese).
[8] Su Y.H., Research on the Effect of Joints Stiffness on the Stability of Reticulated Shells, D. College of Civil Engineering, Southeast University, Nanjing, China, (2005).(in Chinese).
[9] Yan X.Y., Duan Y. and Zhang Y.X., Chen Z.H., Study on compressive bearing capacity and axial stiffness of welded hollow spherical joints with H-shaped steel member, J. Engineering Structures, 203, (2020) 109821.
[10] Yan X.Y., Duan Y. and Cheng Z.H., Liu H.B., Flexural capacity and bending stiffness of welded hollow spherical joints with H-beams, J. Engineering Structures, 24(05), (2021) 1024-1039.
[11] Liu H.B., Ying J.J. and Chen Z.H., Zhou Y., Ultimate tensile and compressive performances of welded hollow spherical joints with H-beam, J.Journal of Constructional Steel Research, 150, (2018) 195-208.
[12] Zhao Z.W., Dai B.Z. and Xu H., Li T.H., Bending capacity of corroded welded hollow spherical joints with considering interaction of tension force and bending moment, J.Structures, 34, (2021) 2656-2664, 10.
[13] Han Q.H., Liu Y.M. and Xu Y., Stiffness characteristics of joints and influence on the stability of single-layer latticed domes, J.Thin-Walled Structures, 107 (2016) 514-525.
[14] Yan X.Y., Zhang Q.W. and Qi G.C., Study on bending stiffness of welded hollow spherical joints based on bending loading states, J. Chinese Journal of Applied Mechanics, 38(01), (2019) 35-44, (in Chinese).
[15] Zhao Z.W., Liu H.Q. and Liang B., Bending capacity of corroded welded hollow spherical joints, J. Thin-Walled Structures, 127, (2018) 523-539.
[16] Lu J., Liu H.B. and Cheng Z.H., Behavior of welded hollow spherical joints after exposure to ISO-834 standard fire, J. Journal of Constructional Steel Research, 140, (2018) 108-124.
[17] Huang B.S., Lu M. and Cao Y.F., Yang F., Experimental study on residual performance of welded hollow spherical joints subjected to axial compression after a fire, J.Structures, 30, (2021) 996-1005.
[18] Liu H.B., Lu J. and Cheng Z.H., Residual behavior of welded hollow spherical joints after exposure to elevated temperatures, J. Journal of Constructional Steel Research, 137, (2017) 102-118.
[19] Liu H.B., Zhao Y. and Wang L. Cheng Z.H., Axial compression properties of welded hollow spherical joints with H-beams under high temperature, J. Journal of Constructional Steel Research, 169 (2020) 10605.
[20] Liu H.B., Zhang Y.J. and Wang L., Cheng Z.H., Mechanical performance of welded hollow spherical joints at elevated temperatures, J.ADVANCED STEEL CONSTRUCTIO 16(1), (2020) 1-12.
[21] Luo Y.F. and Sheng Z.Y., Effects of the joint size of the reticulated shell on its loading capacity, J. Journal of Tongji University, 1(23), (1995) 21-25, (in Chinese).
[22] Dong S.L., Xing L. and Zhao Y., Load-carrying capacity and practical calculation method of welded hollow spherical joints connected with square steel tubes, J. Journal of Building Structures, 26(6), (2005) 27-37, (in Chinese).10.3321/j.issn:1000-6869.2005.06.005.
[23] Dong S.L., Tang H.J. and Zhao Y., Loadcarrying capacity and practical calculation method for welded hollow spherical joints subject to combine axial force and bending moment, J. Journal of Civil Engineering Society, 38(1), (2005) 21-30, (in Chinese).
[24] Liao J. and Zhang Y.G., The study of bilinear model for loading-deformation curve of welded hollow spherical joints, J. Spatial Structures. 16(02), (2010) 31-38. (in Chinese).
[25] Wang X., Dong S. and Wan H.Y., Finite element analysis of the stiffness of welded ball joints, J.Journal of Zhejiang University (Engineering Edition). (01), (2000) 79-84.
[26] Zhao Z.W., Zhu H. and Chen Z.H., Mechanical behavior of single-layer reticulated shell connected by welded hollow spherical joints with considering welding residual stress, J. Welding in the World, 60(1), (2016) 61-69.
[27] Yan R.Z., Zhang C.L. and Wang S., Distribution of residual stress in the sphere-pipe connection welds of welded hollow spherical joints, J. Advanced Steel Construction. 19(3), (2023) 262-272.
[28] Yan R.Z., Yu Z.Y. and Wang S., Liu J.Q., Influence of welding residual stress on bending resistance of hollow spherical joints, J. Journal of Constructional Steel Research. 208, (2023)
[29] Jin X.Q. Distribution of WRS in Hollow Sphere Joints and its Influence on Joint Axial Stiffness, D. Chongqing Jiaotong University, Chongqing, China, (2019). (in Chinese).
[30] Huang K.Z. Plate and shell theory, M. Tsinghua University Press. Beijing. China, (1987).
[31] Ministry of Housing and Urban-Rural Development of the People's Republic of China. Technical specification for space grid structure: JGJ 72010, S. China Construction Industry Press, Beijing China, (2010).

Advanced Steel Construction – Vol. 22 No. 2 (2026) 181–197
DOI:10.18057/IJASC.2026.22.2.5

THEORETICAL FULL-PROCESS CALCULATION AND ANALYSIS FOR SUBCOMPONENTS IN END-PLATE-BOLTED BEAM-COLUMN JOINTS

Kang Ma [1,*], Yi-Ming Gao [1], Zhuo Wang [1], Ruo-Yang Wu [2], Hai-Feng Yu [1], Pan Xu [1] and Yong Li [1]

[1] *School of Civil Engineering, Hebei Province Housing Construction Projects Regeneration Technology Innovation Center, Hebei University of Science and Technology, Shijiazhuang 050018, China*
[2] *Consor Engineers, Herriman, Utah 84096, USA*
** (Corresponding author: E-mail: luya4426@126.com)*

ABSTRACT

Existing theoretical rotational curve calculation methods for end plate-bolted joints often overlook component-level load transfer mechanisms and full deformation processes. This paper introduces a full-process subcomponent analysis method, which systematically evaluates the force-deformation behavior of joint domains, bolts, end plates, and stiffeners at critical failure stages. Simplified models and formulas are developed to calculate the load-bearing capacity and rotation angles of each component. The proposed method was validated through experiments, numerical simulations, and a practical engineering case. The results show that the proposed method accurately predicts joint rotational behavior, with the end plate thickness and bolt configuration significantly influencing load distribution. By revealing the load transfer mechanisms and clarifying the physical meaning of each component's role in joint rotation, the findings of this study provide a robust theoretical foundation for holistic structural analysis and large-scale computation of steel structures.

ARTICLE HISTORY

Received: 5 December 2024
Revised: 7 July 2025
Accepted: 18 July 2025

KEYWORDS

End plate bolted joint;
Beam-column joint;
Full component process;
Theoretical calculation

1. Introduction

Steel structures have increasingly become the preferred choice for prefabricated construction due to their modularity and structural efficiency, with beam-column joints serving as crucial components for load transfer and overall stability. Among joint types, end-plate-bolt connections are widely adopted in steel construction because of their ability to resist both static and seismic loads through elastic-plastic deformation mechanisms [1]. These connections typically involve welding end plates to beam ends and securing them to column flanges with bolts, as illustrated in Fig. 1, which shows commonly used configurations such as double-extended, single-extended, and flush end plates [2,3].

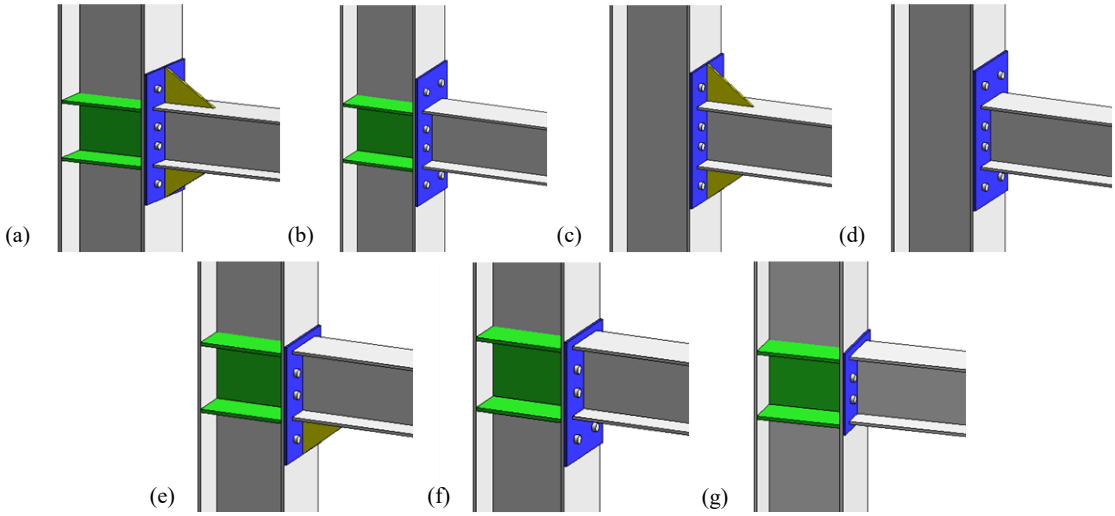

Fig. 1 Different types of end-plate-bolted joints. (a) Double-extended end plate with column web and end plate stiffeners;(b) Double-extended end plate with column web stiffeners; (c) Double-extended end plate with end plate stiffeners;(d) Double-extended end plate without column web or end plate stiffeners; (e) Single-extended end plate with column web and single-sided end plate stiffeners; (f) Single-extended end plate with column web stiffeners; (g) Flat end plate with column web stiffeners

Although previous studies on end-plate-bolted joints have significantly advanced our understanding of their overall mechanical behavior, two key limitations remain:

(i) Component-level mechanism gaps: Most studies have focused on global joint performance, overlooking the independent deformation characteristics and load-transfer mechanisms of subcomponents (e.g., joint domain, bolts, end plates, and stiffeners) across different loading stages (i.e., elastic, elastoplastic, and plastic).

(ii) Elastoplastic stage understudy: Although the elastic-stage capacity of individual components is well-documented, the subsequent elastoplastic deformation processes and their synergistic effects remain poorly understood [4-6].

To address these gaps, this paper introduces a full-process subcomponent analysis method that systematically evaluates the force-deformation behavior of four key components, namely, the joint domain, bolts, end plates, and stiffeners, from initial loading to ultimate failure. By integrating finite element analysis (FEA) with theoretical modeling, the proposed approach: develops simplified mechanical models for each component, delineating their deformation stages using stress-strain curve inflection points. Additionally, a component-wise superposition method is proposed to derive the joint's complete moment-rotation curve, accounting for both elastic and elastoplastic responses. The proposed model was validated through experimental tests and parametric studies on end plate/column flange thickness effects.

Unlike traditional component methods (e.g., EC3 [7,8]), which primarily focus on elastic-stage stiffness and ultimate capacity, this paper provides a unified framework for analyzing the full deformation process and component interactions. The findings of this study offer a robust theoretical foundation for optimizing joint designs in seismic-resistant steel structures, balancing computational efficiency with mechanical accuracy.

2. Calculation methods

2.1. Tests

2.1.1. Test specimen and loading configuration

In the tests, Q345 steel was used as the component material, with a column web stiffener thickness of 12 mm. The dimensions are shown in Figs. 2(a) and 2(b), which depict the beam-column joint configuration with a 10 mm thick 300 mm-wide end plate, M20 bolts, and an 83 mm bolt spacing. Low-cycle reverse loading was implemented using a self-balanced frame at the Structural Laboratory of Hebei University of Science and Technology, Hebei, China. As shown in Fig. 2(c), the test setup consists of a column horizontally fixed and a beam end loaded by a hydraulic actuator. The loading protocol followed the PRC industry standard Building Seismic Test Procedure JGJ/T101-2015 [8], as depicted in Fig. 2(c). In the figure, t_{ep} represents the end plate thickness, and t_{sr} represents the stiffening rib thickness.

2.1.2. Displacement point layout

The displacement measurement points were arranged as shown in Fig. 2(c). D1 was located at the center line of the loading, while D2 was positioned 250 mm away from the end plate. The difference in the measurement results between D2 and D1 was used to calculate the inclination angle of the steel beam. D3 and D4 were located at the lower flange of the column, while D5 and D6 were located at the upper flange of the column to measure the relative rotation of the joint domain. The calculation method followed the procedure outlined by Shi et al. [9].

2.1.3. Test phenomena and results

Observations of the loading process revealed that, at a displacement of 16 mm, yielding deformation occurred in the end plate accompanied by a noticeable separation from the column flange, as depicted in Figs. 3(a) and 3(b). As the displacement reached 64 mm, the end plate exhibited increased bending deformation, resulting in a more pronounced separation from the column flange, with a maximum bending deformation of approximately three times that observed at yielding. The displacement and load of the servo-hydraulic loading system were recorded, and the force-displacement hysteresis and skeleton curves were plotted, as shown in Fig. 3(c).

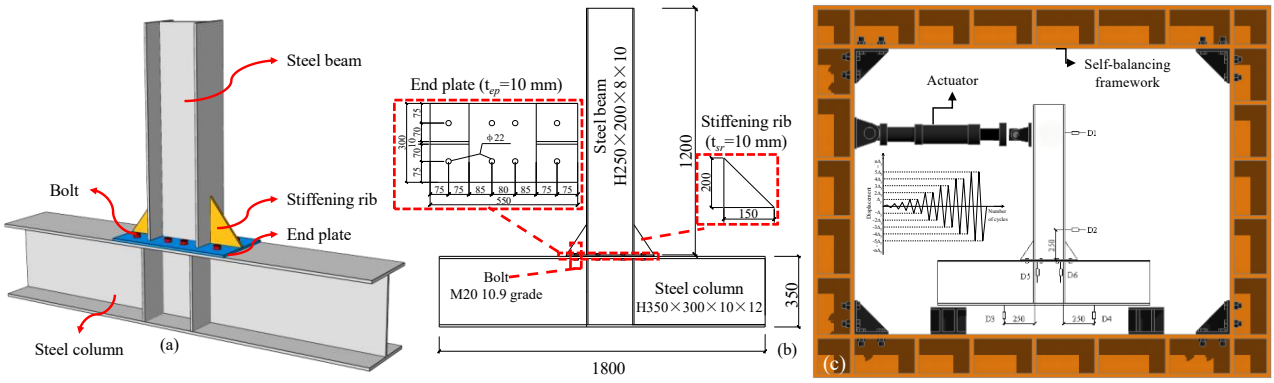

Fig. 2 Test joint diagram: (a) schematic; (b) dimension diagram; (c) test setup

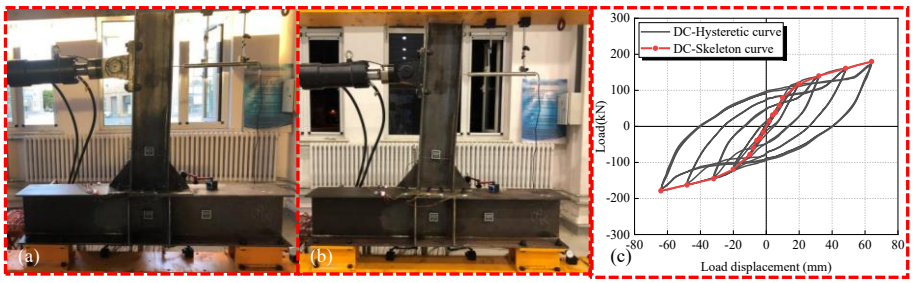

Fig. 3 Test phenomena for Δ = (a) 16 and (b) 64 mm.(c) Hysteresis and skeleton curves

2.2. Finite-element simulation

2.2.1. Modeling method

The material constitutive model adopts the von Mises yield criterion, which is defined as the equivalent stress that reaches the uniaxial tension yield stress when the material is subjected to a triaxial stress state, indicating the onset of yielding. Von Mises hardening was considered, with mixed hardening chosen as the hardening rule. The steel plate material properties are listed in Table. 1. Bonded constraints were selected for the welded connections, while surface contact constraints were chosen for components with only surface contact. Solid-model meshing was performed using C3D8R elements.

Table 1
Steel plate material properties

Steel plate thickness (mm)	Yield strength (N/mm^2)	Ultimate strength (N/mm^2)
12	373	504
10	356	488
8	329	456

When defining the contact properties of each contact component, binding constraints can be selected for welding, and surface-to-surface contact constraints can be selected for components with only surface-to-surface contact. When setting the binding or surface-to-surface contact constraints, it is necessary to define the contact pair and select the master and slave surfaces. The stable convergence calculation of the model is related to the master and slave surface selection.

The more symmetrical and regular the grid division, the better the model convergence and the faster the calculation progress. Additionally, this can effectively improve the numerical analysis accuracy. For parts with a simple stress distribution or less important parts, the mesh size can be increased, which reduces the calculation time. The bolt and hole division needs to be more regular, which facilitates convergence and improves the simulation accuracy.

In the test, bolts were utilized to fix the beam and column flanges, with three orthogonal translational displacement constraints ($U_x = U_y = U_z = 0$) applied to the bolt nodes to simulate rigid anchoring, as illustrated in Fig. 4(a). This figure shows the bolt constraints and loading configuration, where the bolt positions are fully fixed in all horizontal directions to mimic the experimental setup. For the loading mechanism, the entire beam end surface was kinematically coupled to a reference point, allowing the application of prescribed displacement loads at this point in strict accordance with the low-cycle reverse loading protocol specified in JGJ/T101-2015. This coupling strategy ensures uniform force distribution across the beam end, aligning with the test's loading characteristics and enabling accurate simulation of the cyclic deformation process.

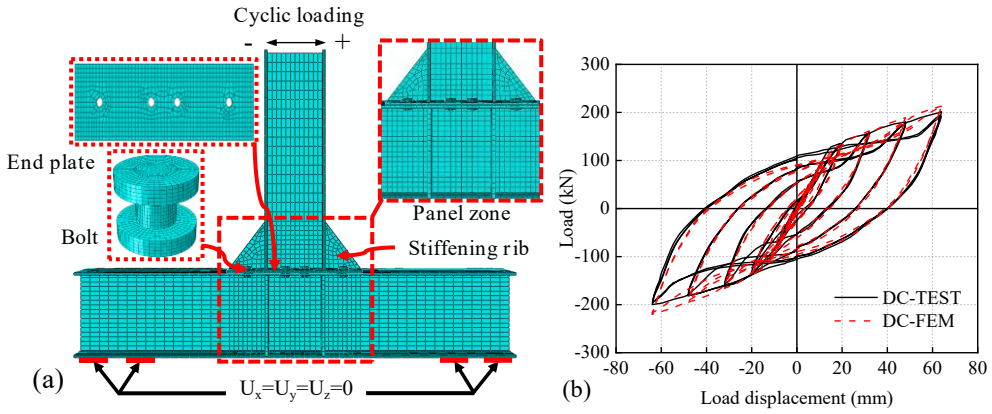

Fig. 4 Finite element simulation: (a) boundary conditions and loading positions; (b) test and simulation results

2.2.2. Finite element validation

A comparative analysis of the test (TEST) and finite-element model (FEM) simulation results of the hysteresis curves is presented in Fig. 4(b), which depicts the force displacement hysteresis loops and moment rotation curves of the specimens. As can be seen, the FEM results closely trace the TEST data, with both exhibiting nearly identical hysteretic shapes and key characteristic points (e.g., yield load, ultimate load, and post-peak deformation). Notably, the simulated end plate bending deformation and nut tilting phenomena shown in Fig. 4(b) align well with the experimental observations shown in Figs. 3(a) and 3(b), validating the FEM's ability to capture the joint's nonlinear behavior, including the stiffness degradation and energy dissipation characteristics under cyclic loading. This close agreement confirms the reliability of the numerical approach in predicting the mechanical response of end -plate-bolted joints. Both the TEST and FEM results exhibited phenomena such as end plate bending deformation, and nut tilt, as shown in Fig. 5, indicating that the established joint specimen model is reliable and accurate.

Based on the test and FEA results, 16 parametric FEMs were established to analyze the stress distribution and deformation properties of the joint domain, bolts, end plate, and reinforcement rib components during the loading process. Simplified stress analysis diagrams were generated to obtain a comprehensive theoretical moment-rotation calculation method. The established FEMs are listed in Table. 2.

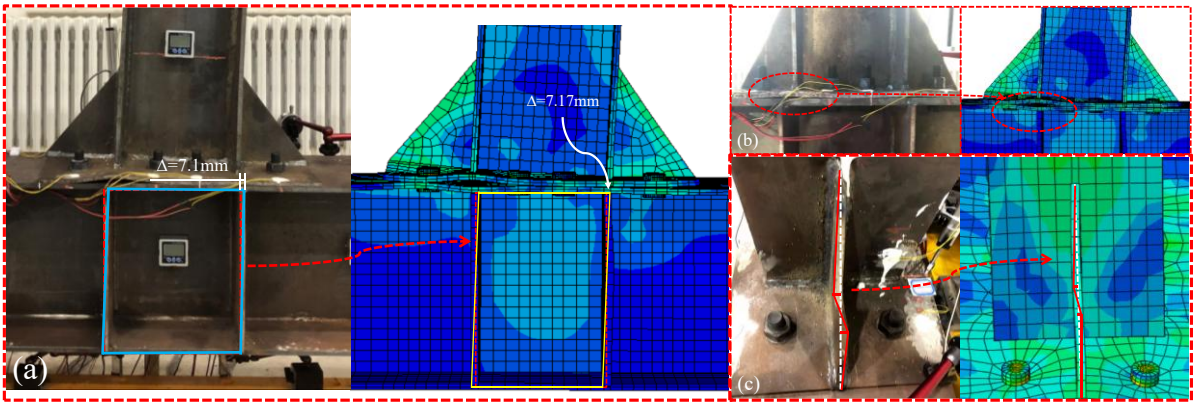

Fig. 5 Comparison between test and finite-element failure modes: (a) joint domain; (b) end plate; (c) stiffening rib

Table 2
Parametric finite-element models

No.	End plate thickness (t_{ep}/mm)	Column flange thickness (t_{cf}/mm)	Model components requiring analysis
1	12	12	Joint-domain, End-plate, Stiffener, and Bolt series
2	14	14	Joint-domain, End-plate, Stiffener, and Bolt series
3	16	16	Joint-domain, End-plate, Stiffener, and Bolt series
4	18	18	Joint-domain, End-plate, Stiffener, and Bolt series
5	20	20	Joint-domain, End-plate, Stiffener, and Bolt series
6	22	22	Joint-domain, End-plate, Stiffener, and Bolt series
7	24	24	Joint-domain, End-plate, and Bolt series
8		12	Bolt series
9	10	14	Bolt series
10		16	Bolt series
11		12	Bolt series
12	12	14	Bolt series
13		16	Bolt series
14		12	Bolt series
15	14	14	Bolt series
16		16	Bolt series

2.2.3. Mesh sensitivity analysis

To address mesh dependency, a comparative analysis of three mesh densities was conducted during finite-element modeling: (i) Coarse Mesh: Element size increased by 50% relative to the basis mesh; (ii) Basis Mesh: Reference mesh adopted in this study (C3D8R elements, regular division for bolts and holes); and (iii) Refined Mesh: Element size reduced by 50% relative to the basis mesh.

As shown in Fig. 6, the Basis Mesh demonstrates excellent agreement with the experimental results (TEST) [10], exhibiting initial rotational stiffness and ultimate moment deviations of less than 6% and 4%, respectively, which are within engineering tolerances. Using the Refined Mesh marginally improves accuracy (<2% deviation) but incurs a threefold increase in computational time. Furthermore, the Coarse Mesh significantly underestimates the ultimate moment (12% deviation) and exhibits stiffness divergence, confirming its inadequacy for reliable predictions. In conclusion, the Basis Mesh balances accuracy and computational efficiency, validating its use in the subsequent numerical analyses.

3. Results and discussion

3.1. Joint domain stress-deformation comprehensive analysis

3.1.1. Calculation sketch

The joint domain stiffness is a crucial parameter for assessing its deformation capacity. Pan et al. [11] suggested that when there is a significant disparity in the heights of the beam and column sections, the bending deformation of the joint domain should be considered in stiffness calculations. However, for standard beam and column dimensions, considering only shear deformation can yield sufficiently accurate results. For column joints with stiffeners, such as flange plates and web stiffeners, the stress deformation can be simplified to that of a short column under a moment couple, as illustrated in Fig. 7. The analysis was divided into the bending deformation of the column flange and shear deformation of the column web. The stress-deformation process of the joint domain was divided into three stages: elastic shear-bending deformation, yielding shear deformation, and post-yielding.

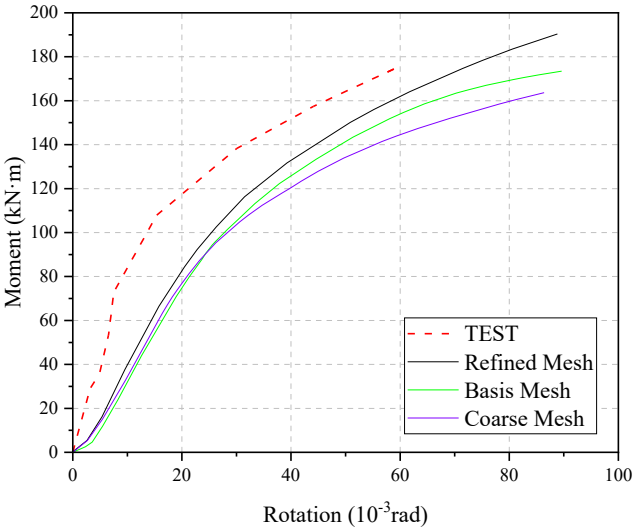

Fig. 6 Moment-rotation curves for the mesh sensitivity analysis

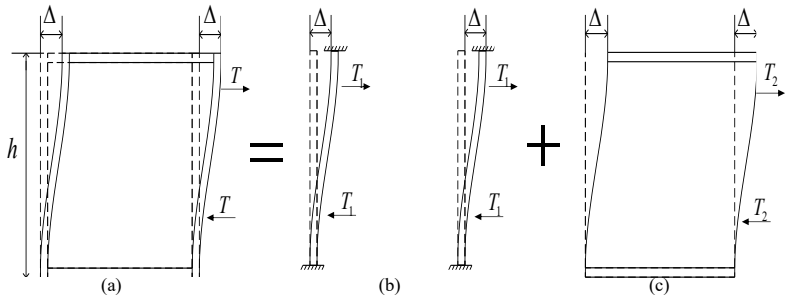

Fig. 7 Calculation diagram ($T = T_1+T_2$): (a) joint domain; (b) flange; (c) web plate

3.1.2. Elastic shear-bending deformation stage

The Chinese steel structure design code [12] provides a calculation method for the yield-bearing capacity of bidirectional bending joint domains. The following steps were taken to calculate the initial rotational stiffness of the joint domain in accordance with the bearing capacity calculation method provided by the steel structure design code.

First, the normalized width-to-thickness ratio of the prescribed joint domain $\lambda_{n,s}$ was determined as follows:

$$h_c/h_b \geq 1,\quad \lambda_{n,s} = \frac{h_b/t_w}{37\sqrt{5.34+4\left(h_b/h_c\right)^2}}\frac{1}{\sqrt{\frac{f_y}{235}}} \tag{1}$$

$$h_c/h_b \leq 1,\quad \lambda_{n,s} = \frac{h_b/t_w}{37\sqrt{4+5.34\left(h_b/h_c\right)^2}}\frac{1}{\sqrt{\frac{f_y}{235}}} \tag{2}$$

where h_b and h_c represent the beam and web calculation heights, respectively.

According to the normalized width-to-thickness ratio $\lambda_{n,s}$ of the joint domain subjected to shear, the shear strength f_{ps} of the joint domain was determined as follows:

$$\lambda_{n,s} \leq 0.6,\quad f_{ps} = \frac{4}{3}f_v \tag{3}$$

$$0.6 \leq \lambda_{n,s} \leq 0.8,\quad f_{ps} = \frac{1}{3}(7-5\lambda_{n,s})f_v \tag{4}$$

$$0.8 \leq \lambda_{n,s} \leq 1.2,\quad f_{ps} = \left[1-0.75(\lambda_{n,s}-0.8)\right]f_v \tag{5}$$

where f_v is the steel shear yield strength, $\lambda_{n,s}$ is the normalized width-to-thickness ratio of the joint domain subjected to shear, and f_{ps} is the joint domain shear strength.

The conversion relationship for the design strength values of the steel materials adopts the conversion relationships listed in Table. 3.

Table 3
Conversion relationships for the steel design strength

Material	Stress type		Conversion control
Steel	Tensile, compressive, and flexural resistance	Q235	$f = f_y/1.090$
		Above Q235	$f = f_y/1.125$
	Shear resistance		$f_v = f_y/\sqrt{3}$

The final bending capacity of the joint domain is as follows:

$$M_{b1}+M_{b2} \leq f_{ps}V_p, V_p = h_{b1}h_{c1}t_w \tag{6}$$

where h_{b1} and h_{c1} represent the height of the beam and column flange heights, respectively.

When the joint domain shear strain reaches the yield strain, $\gamma = \gamma_y$, the shear rotation angle of the joint domain reaches φ_{sy}. Therefore, the initial joint domain rotational stiffness for shear rotation is

$$K = K_i = \frac{M_{b1} + M_{b2}}{\varphi_{sy}} \tag{7}$$

To consider the shear deformation of the steel column webs and flanges under uniaxial bending conditions in the elastic stage, referring to Wang et al. [13-14], the joint domain rotational stiffness can be defined as follows:

$$K = \frac{T}{\Delta} l^2, \quad \tau = G\gamma, \quad \gamma = \frac{\Delta}{l} = \frac{f_y}{G}, \quad G = \frac{E}{2(1+\mu)} \tag{8}$$

$$T_1 = \frac{12EI_{cf}\Delta}{l^3} \tag{9}$$

$$T_2 = A_{cfb}\tau = \frac{A_{cfb}E\Delta}{2l(1+\mu)} \tag{10}$$

The initial joint domain rotational stiffness for shear rotation is:

$$K = K_i = \frac{l^2}{1+\frac{l}{H_C}}\left[\frac{12E(I_{cf1}+I_{cf2})}{l^3} + \frac{A_{cfb}E}{2l(1+\mu)}\right] \tag{11}$$

The corresponding bending capacity of the joint domain at this point is:

$$M = (2T_1 + T_2)l \tag{12}$$

where G is the steel shear modulus, E is the steel elastic modulus, E_h is the steel strain-hardening modulus, and H_c is the selected column segment length.

3.1.3. Yield shear deformation stage

After yield shear deformation in the joint domain, the joint domain rotational stiffness changed. For this type of change, referring to Krawinkler et al. [15], modifications were made to the corresponding calculation formulas for $\beta = 1\text{-}H_c/l$, as follows:

$$K = K_P = 1.3\times\left[\frac{12EI_{cf1}}{5t_{cf1}\beta} + \frac{12EI_{cf2}}{5t_{cf2}\beta}\right]\times\left(\frac{4\min\{t_{cf1}, t_{cf2}\}}{\max\{t_{cf1}, t_{cf2}\}}\right) \tag{13}$$

In this study, we assumed that the stiffness remains constant until the shear strain reaches $3\gamma_y$. Accordingly, the ultimate plastic moment at which this state is reached is:

$$M_p = K_i\gamma_y + 2K_p\gamma_y \tag{14}$$

where β is the adjustment coefficient for the shear's contribution to the joint domain shear resistance, l is the lever arm of the shear force in the joint domain, t_{cf} is the column flange thickness, and I_{cf} is the moment of inertia of the column flange section.

3.1.4. Post-yielding stage

For a joint domain exceeding the yield moment, as the material enters the strain-hardening stage, the coefficient is adjusted according to the stiffness in the plastic stage, as follows:

$$K = \frac{E_h}{E}K_i \tag{15}$$

where K is the joint domain rotational stiffness, E is Young's modulus, and E_h is the steel strain-hardening modulus.

3.1.5. Moment-rotation curve

The results obtained using the proposed theoretical calculation method were compared with the FEM and test results for validation. The comparison between the joint domain moment-rotation models is shown in Fig. 8. The FEM simulation and test results are in good agreement with the theoretical calculation results. However, as the column flange thickness increased, the relative error tended to increase, indicating that the simplified joint domain shear deformation model may underestimate the influence of geometric nonlinearity in thick-plate scenarios. This discrepancy is attributed to the theoretical model's neglect of three-dimensional (3D) stress states in the column flange and the actual welding residual stresses not being considered in the analysis.

The results obtained from the theoretical calculation method (TCM) described above were compared with the FEM and test results in a stage-by-stage basis to validate the proposed theoretical model. The comparison between the moment and rotation models is shown in Fig. 9.

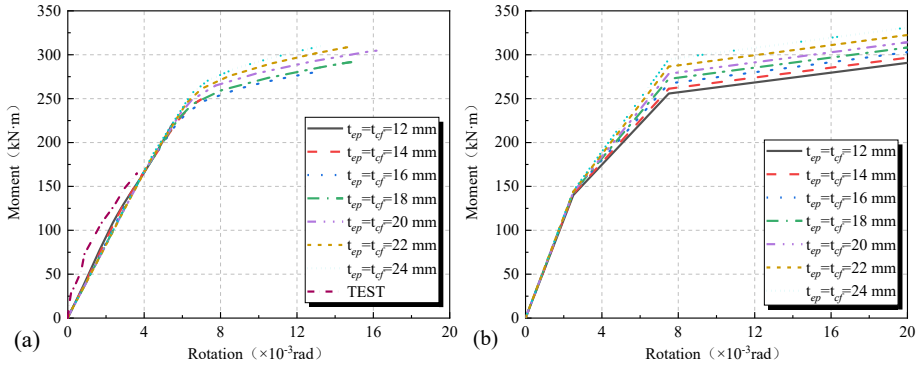

Fig. 8 Joint domain moment-rotation model: (a) finite-element simulation and test results; (b) theoretical calculation results

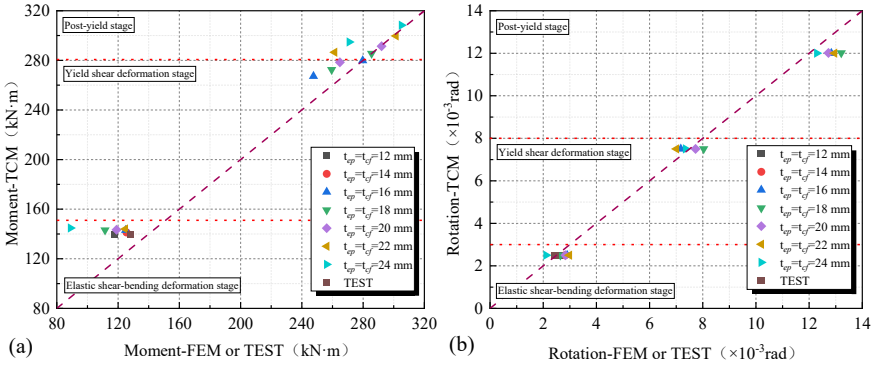

Fig. 9 Results for characteristic points of the joint domain. (a) moment; (b) rotation

3.1.6. Influence of material grade on the joint domain mechanical performance

Hysteretic Behavior

Under cyclic loading, the hysteretic curves of panel zones constructed with Q235, Q345, Q355, and Q460 steel were compared (Fig. 10). The results show that increasing the material strength leads to a marginal improvement in the energy-dissipation capacity, with the hysteretic loop area increasing by approximately 5%-8% from Q235 to Q460. However, this enhancement is significantly less than the theoretical strength increase, indicating that material strength is not the dominant factor governing the panel zone performance.

Mechanism Analysis

The limited improvement in the energy-dissipation capacity with increasing material grade is predominantly governed by local buckling, where panel zones exhibit out-of-plane deformation and instability (as visible in the test observations shown in Figs. 3 and 5) before fully utilizing the material's yield strength, particularly in thin-walled configurations ($t_{cf} \leq 16$ mm). This aligns with the theoretical model's acknowledged limitation in terms of underestimating the geometric nonlinearity and 3D stress states in thick plates, as discussed in Section 3.1.5, as buckling initiates at lower loads due to inherent geometric imperfections. Concurrently, welding residual stresses introduce initial tensile stresses near welds, accelerating plastic deformation and buckling onset, even in high-strength steels like Q460. Additionally, shear deformation dominance constrains the impact of material strength, as shear capacity scales less significantly with grade compared to tensile strength, and the panel zone's aspect ratio (h_b/h_c) limits shear-driven energy dissipation. Finally, stiffener configuration effects overshadow the material grade effects: increasing the stiffener thickness (t_{sr}) enhances the stability more effectively than upgrading the steel strength, as evidenced in the model's emphasis on geometric parameters for resisting buckling, whereas high-strength steel (e.g., Q460) alone cannot mitigate premature instability without corresponding thickness or stiffening adjustments.

Engineering Implications

For seismic design, prioritizing the stiffener configuration and thickness optimization is more effective than upgrading the material grade alone. While high-strength steel (e.g., Q460) may delay bolt failure, it does not mitigate panel zone buckling unless accompanied by increased plate thickness or stiffening. This aligns with the proposed full-process subcomponent method's emphasis on integrating geometric and material factors.

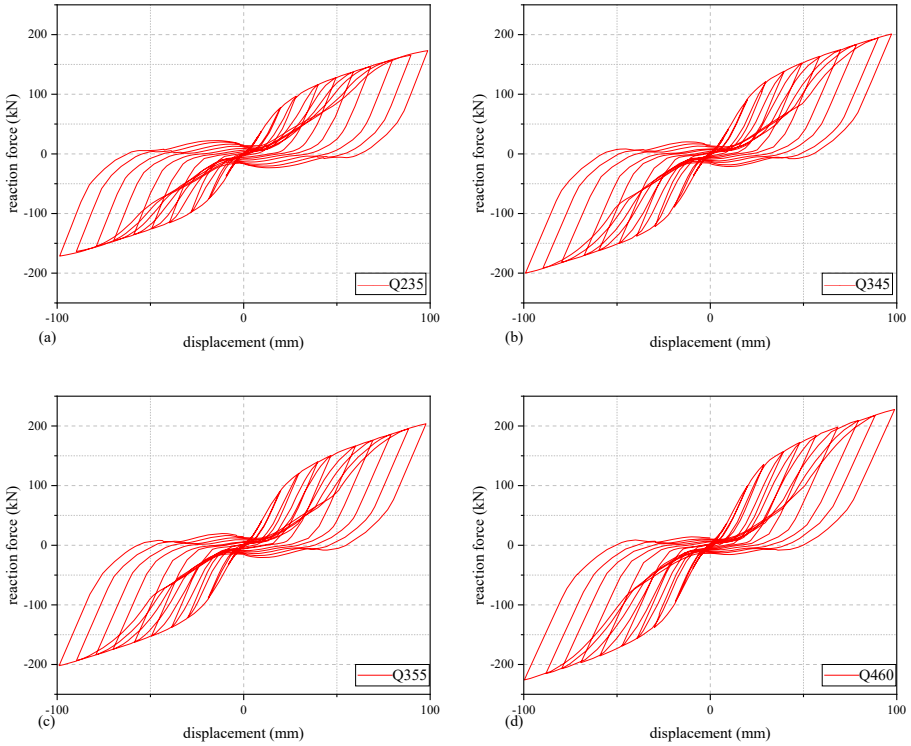

Fig. 10 Node hysteresis curves for steel with different strength grades: (a)Q235; (b)Q345; (c)Q355; (d)Q460

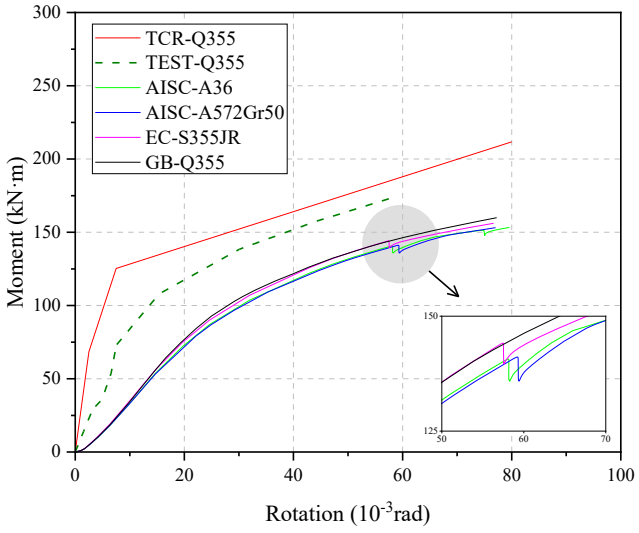

Fig. 11 Comparison of the bending moment and angle curves under different specifications

3.1.7. Validation extension to diverse steel grades

To address material validation limitations, the theoretical calculation method (TCR) was extended to steels from three design codes: Q355 (GB), A36/A572Gr50 (AISC), and S355JR (Eurocode) using ABAQUS simulations. The moment-rotation curves (Fig. 11) demonstrate close alignment between the TCR predictions, experimental data, and FEA results. Notably, the TCR consistently overestimates the experimental moments by 7%-10% at the same rotation angle, providing a conservative safety margin. This stems from its subcomponent superposition approach, which decomposes the joint into end plates, bolts, and panel zones. As shown in Fig. 11, the curves for different steel grades exhibit similar trends, verifying that the TCR can directly integrate material properties from any standard without empirical calibration. This modular design approach ensures generality for global engineering practice.

3.2. Comprehensive bolt stress and deformation analysis

When high-strength bolts with friction-type connections are used, pre-tensioning is necessary during tightening. This pre-tensioning induces compressive strain in the end plate and column flanges. As external loads are applied to the end plate, these compressive strains change. The stress state of the bolts in the tension zone could be categorized into three stages: contact, rigid separation, and complete separation between the end plate and column

flange.

3.2.1. End plate and column flange in the bolted zone in contact

After the bolts are tightened, a pre-tensioning force is generated, as shown in Fig. 12(a), which depicts the bolts in a state of initial tension that pulls the end plate and column flange tightly together. This creates a compressive force between the two plates, where the force from the bolt's pre-tension is balanced by the pressure between the plate surfaces.

When the end plate is subjected to external loads, it begins to separate from the column flange, as illustrated in Fig. 12(b). As the plates start to pull apart, the compressive force between them decreases, while the tension force in the bolt increases. As can be seen, the bolt is under higher tension due to the applied load, with the end plate slightly lifted from the column flange but still in partial contact. A comparison between Figs. 12(a) and 12(b) visually demonstrates how the bolt's tension increases as the joint transitions from a pre-tensioned state to one bearing external loads, highlighting the crucial role of bolt tension in resisting separation and maintaining joint integrity.

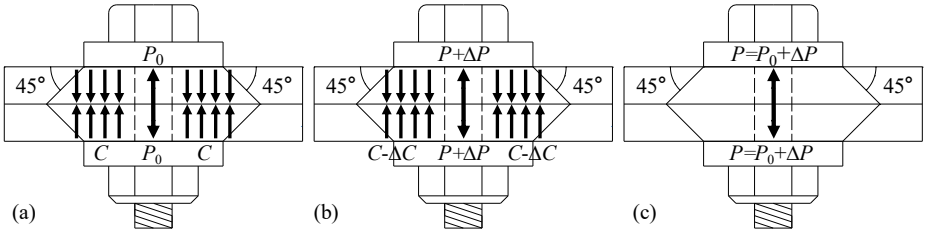

Fig. 12 Tensile force on the bolt's internal force: (a) only pre-tensioning force; (b) pre-tensioning force with tensile force; (c) pre-tensioning force disappeared

In the absence of external forces, the end plate and column flange are in contact. Under the action of a compressive force, the end plate and column flange undergo slight deformations. The pre-tensioning force of the bolt is in constant contact with the end plate and column flange. Therefore, the end plate, column flange, and bolt undergo slight deformations of the same magnitude. The slight deformation Δl caused by the compressive force can be calculated as follows:

$$P_0 = C, \quad \Delta l = \frac{C}{\lambda A_{bt'} E} L_{bt'} = \frac{P_0}{\lambda A_{bt'} E} L_{bt'} \tag{16}$$

When the end plate is subjected to a certain tensile force, separation occurs between the end plate and column flange. At this point, the decrease in the compressive force decreases the compressive microdeformation. However, the tensile force increases the tension force acting on the bolt. The change in tensile force F, actual increase in tension force ΔP, and bolt elongation Δl_i are calculated as follows:

$$F = \Delta P + \Delta C, \ \Delta P = \Delta l_i \cdot k_{bt}, \ \Delta l_i = \frac{\Delta C}{\lambda A_{bt'} E_{bt'}} \tag{17}$$

3.2.2. End plate and column flange in the bolted zone in the critical separation state

As shown in Fig. 12(c), at this point, the end plate is on the verge of separating from the column flange under the action of the tensile force, resulting in the absence of a compressive force between the end plate and column flange. The tension force T, elongation deformation Δl_i, and tensile strain ε_0 of the bolt are calculated as follows:

$$\Delta C = C = P_0, \ T = P_0 + \Delta P, \ \Delta P = \Delta l_i \cdot k_{bt}, \ \Delta l_i = \Delta l, \ \varepsilon_0 = \frac{\Delta l}{L_{bt'}} \tag{18}$$

where ε_0 is the bolt separation strain.

3.2.3. End plate and column flange in the bolted zone in a separation state

After reaching the state where the end plate and column flange are separated, the bolt stress and deformation calculation can be simplified and analyzed as the uniaxial tension of the bolt. Under the action of the tensile force, when the bolt reaches its tensile yield strength, the tension force T_i and resulting elongation deformation Δl_i of the bolt can be calculated as follows:

$$T_i = f_{bt',y} A_{bt'} \tag{19}$$

$$\Delta l_i = \frac{\Delta P}{E_{bt'} A_{bt'}} L_{bt'} \tag{20}$$

3.2.4. Bolt internal force and bending capacity calculation

After analyzing the stress and deformation of individual bolts under a tensile force, the effect of bending moment loads on individual bolts in the entire end-plate-bolt connection of the beam-column joint was further studied and analyzed. This involves establishing a relationship between the load on individual bolts and bending moment. This approach facilitates a better design of the load-bearing capacity of the bolts required in the end -plate-bolt connection joint.

First, based on the FEM results, the influence of the end plate and column flange thicknesses on the bolt internal forces was analyzed. Four bolt regions on one side were selected for analysis: the outer tension extension (BL), inner tension extension (NL), outer compression extension (BY), and inner compression extension (NY) regions. As shown in Fig. 13, as the end plate and column flange thicknesses change, there is a significant change in the bolt internal forces and maximum bending capacity of the joint. A comparison of the FEM simulation results revealed that the influence of the plate thickness variation on the development of the bolt internal forces was in stages, with 10-12, 12-16, 16-20, and 20-26 mm as the different stages. Therefore, stage points were selected for analysis.

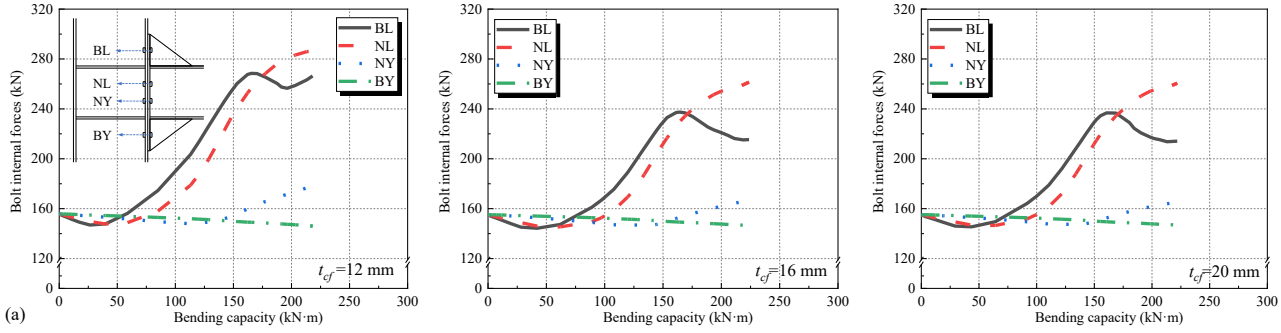

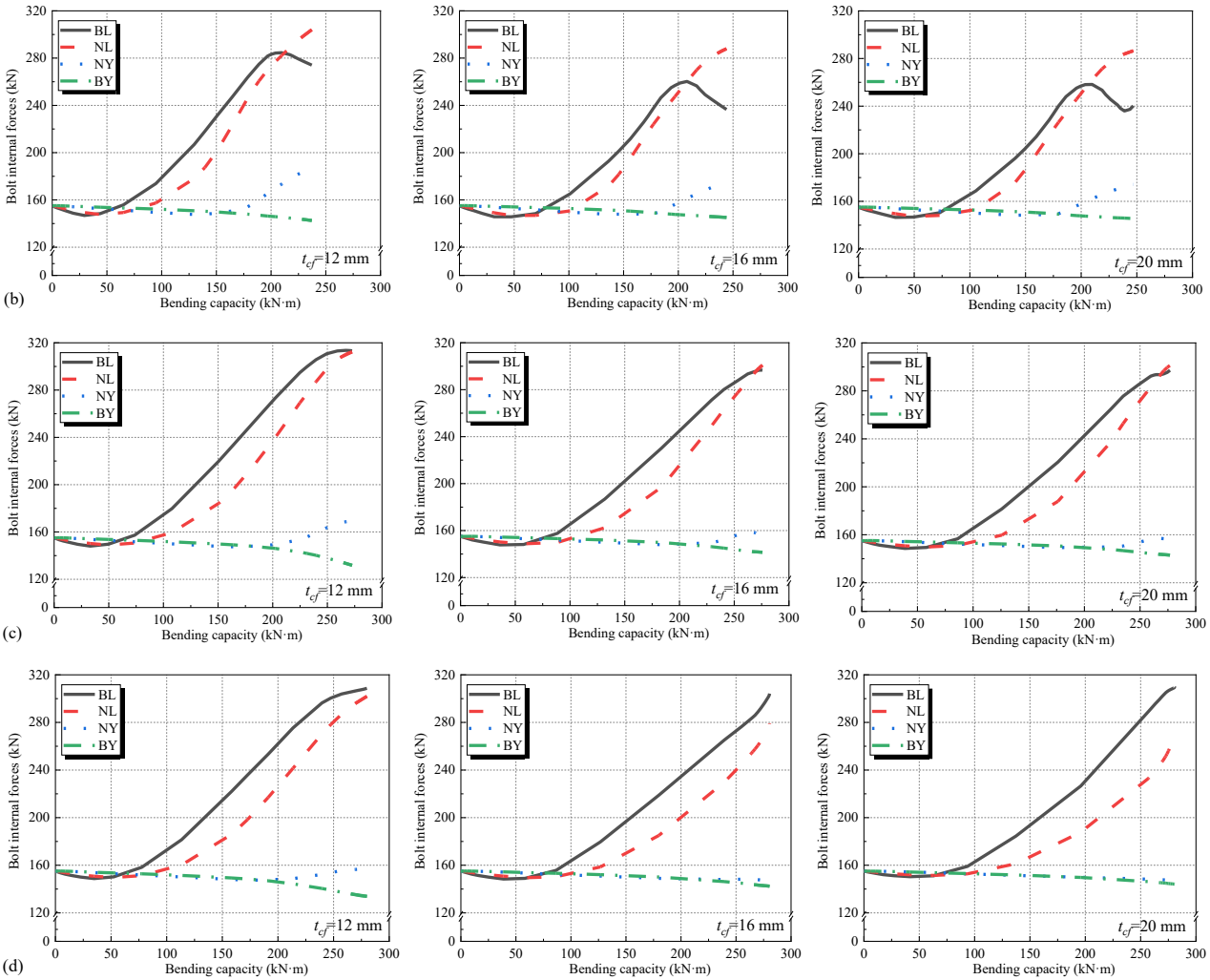

Fig. 13 Variations in bolt internal forces according to different end plate thicknesses (t_{ep}):(a)-(d) 10, 12, 16, and 20 mm, respectively

For an end plate thickness of 10 mm, the end plate fell within the thin plate range. As shown in Fig. 13(a), as the column flange thickness increases from 12 to 20 mm, the maximum internal force of the bolt on the inner side of the tension flange decreases gradually, similar to the maximum internal force of the bolt on the outer side of the tension flange. Initially, the bolt internal force on the outer side of the tension flange exceeded that on the inner side. However, after the bending moment reached 160 kN·m, the bolt internal force on the outer side of the tension flange began to decrease, indicating that the end plate underwent significant deformation at this point. The bolt internal force on the inner side of the compression flange continued to decrease when the bending moment was in the 0-150 kN·m range. However, when the bending moment reached 150 kN·m, the internal force began to increase, indicating that the bolt on the inner side of the compression flange was subjected to tension.

For an end plate thickness of 12 mm, the end plate still fell within the thin-plate range, and its stress and deformation were essentially the same as those for an end plate thickness of 10 mm. As shown in Fig. 13(b), as the column flange thickness increases from 12 to 20 mm, the variation in the bolt internal forces is similar to that at an end plate thickness of 10 mm. However, for an end plate thickness of 10 mm, the bolt internal force on the outer side of the tension flange was initially greater than that on the inner side. When the bending moment reached 160 kN·m, the internal force of the bolt on the outer side of the tensile flange decreased. For an end plate thickness of 12 mm, the bolt internal force on the outer side of the tension flange started to decrease only after the bending moment reached 200 kN·m.

For an end plate thickness of 16 mm, the end plate fell within the medium-thickness range, and its stress and deformation changed accordingly. As shown in Fig. 13(c), as the column flange thickness increases from 12 to 20 mm, the maximum internal forces of the bolts on both the inner and outer sides of the tension flange gradually decrease. Initially, the bolt internal force on the outer side of the tension flange exceeded that on the inner side. However, towards the end, the bolt internal force on the outer side of the tension flange became almost equal to that on the inner side. The bending moment required for the bolt on the inner side of the compression flange to experience tension increased as the column flange thickness increased.

For an end plate thickness of 20 mm, the end plate fell within the thick-plate range, and its stress and deformation changed further. As shown in Fig. 13(d), as the column flange thickness increases from 12 to 20 mm, the maximum internal force of the bolt on the inner side of the tension flange gradually decreases. However, the maximum internal force of the bolt on the outer side of the tension flange increased as the column flange thickness increased. The bolt internal force on the outer side of the tension flange was greater than that on the inner side, and the difference between them increased with the column flange thickness.

This analysis revealed that decreasing end plate and column flange thicknesses led to increased bolt internal forces under the same bending load, due to the lever effect in thin plates. Thicker end plates improved the bolts' load capacity, as they required a higher bending moment for plastic deformation. During joint rotation, bolts on the compressed inner side transitioned from no tension to tension, shifting the rotation center toward the compressed flange. The tensile forces in bolts on either side of the tension flange exhibited similar trends but differed by approximately 1.2 times. These trends varied with end plate thickness, requiring separate equations for thin, medium, and thick plates.

Previous studies and analyses have analyzed calculation models and formulas for force distribution on bolt groups[16]. Different design calculation methods are provided in the design codes of different countries for the bolt-group force distribution in the end-plate-bolted connections of beam-column joints. The parameters used in the equations are shown in Fig. 14.

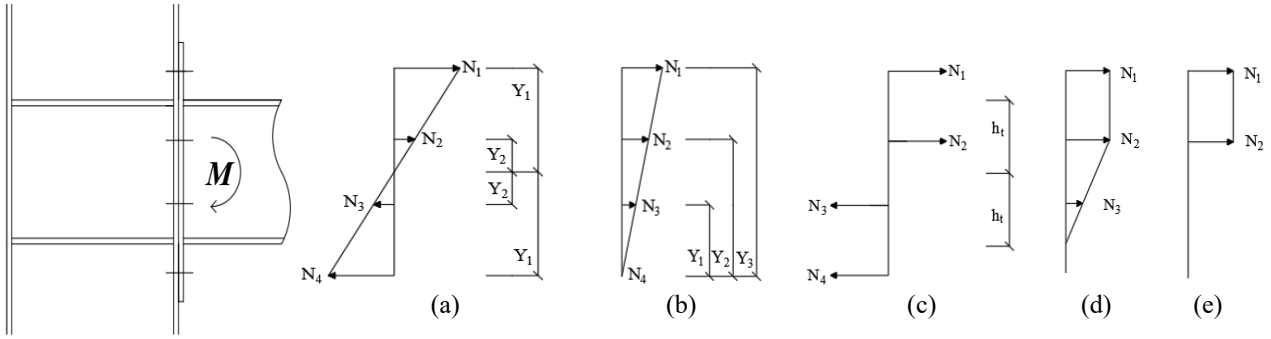

Fig. 14 Force distribution in bolt groups: (a) friction-type high-strength bolts [17]; (b) bearing-type high-strength bolts [17]; (c) JGJ 82-2011; (d) BS5950; (e) AISC358

In the Chinese Steel Structural Connection Joint Design Manual [17], the bolt-group force distribution in the end plate-bolted connections of beam-column joints under bending moment loads is divided according to bolt type: friction-type and bearing-type high-strength bolts. The maximum tensile force N_1 carried by a single row of bolts at different positions can be calculated as follows:

$$N_1 = \frac{My_1}{\sum y_i^2} \le N_t^b \tag{21}$$

In the Chinese Technical Specification for High-Strength Bolt Connections in Steel Structures (JGJ 82-2011) [18], the bolt-group categorization is not based on bolt type. Instead, it is divided based on the tension and compression zones. The maximum tensile force N_t carried by a single row of bolts in the tension zone can be calculated as follows:

$$N_t = \frac{M}{n_t h_t} \le N_t^b \tag{22}$$

In the British [20] and American [21] standards, the internal forces distribution in a row of bolts in a bolt group under bending moment loads can be calculated as follows:

$$M = \sum (N_t h) \tag{23}$$

where M is the bending-resistance capacity of the connection, n_t is the total number of bolt rows in the tension zone, N_t^b is the maximum tensile-load-bearing capacity of a single row of bolts, and h is the distance from each row of bolts to the pressure line of action.

By parametrically analyzing the relationship between the bolt internal forces and the joint bending-resistance capacity, as shown in Fig. 13, and considering existing specifications, the relationship between the bolt internal forces and the joint bending-resistance capacity can be redefined based on the end plate thickness. For thin plates, the method outlined in the Technical Specification for High-Strength Bolt Connections in Steel Structures was used, as shown in Fig. 15(a), with an additional factor of 1.2 to account for the influence of leverage forces. The calculation method for friction-type high-strength bolts outlined in the Connection Joint Design Manual was used for medium and thick plates.

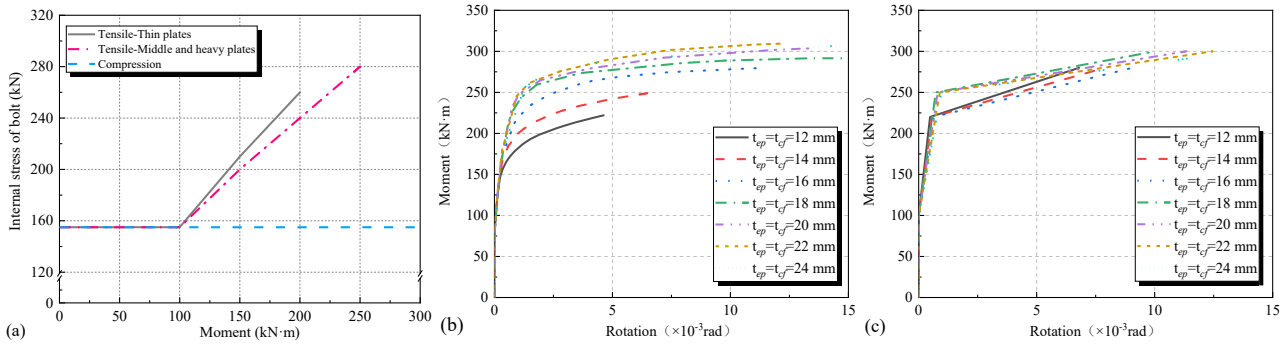

Fig. 15 Bolt moment-rotation curves. (a) bolt internal forces and joint bending resistance; (b) finite-element analysis results; (c) theoretical calculation results

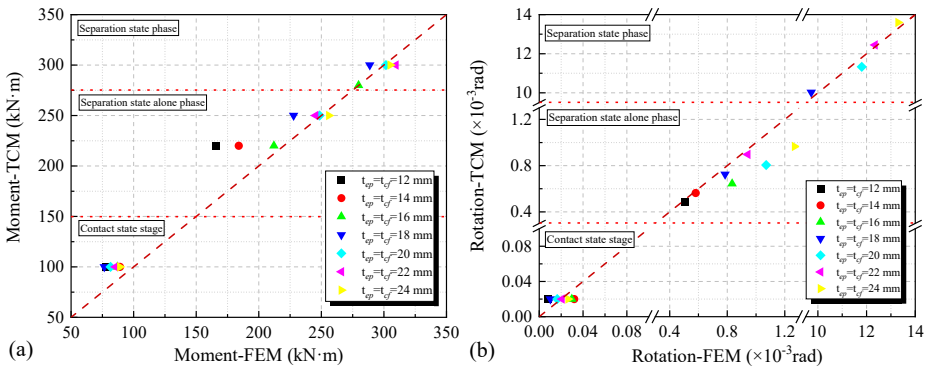

Fig. 16 Bolt results for (a) moment and (b) rotation.

3.2.5. Bolt moment-rotation curve

A comparison between the bolt moment-rotation models is illustrated in Figs. 15(b) and 15(c). As can be seen, the FEA results closely match the theoretical calculation results as the plate thickness increases [22]. However, as the end plate and column flange thicknesses decreased, the disparity between the results gradually increased [23]. This is primarily due to the

unaccounted "lever effect" caused by significant end plate bending, which amplifies bolt tension in reality but is overly simplified in the theoretical model. Conversely, for thick end plates (t_{ep}≥20 mm), the theoretical and numerical results closely align, suggesting that the model performs better when end plate stiffness dominates the deformation mechanism.

To validate the proposed theoretical model, the results obtained from the theoretical calculations (TCM) were compared with those from the FEM based on the aforementioned theoretical calculation methods. The results are shown in Fig. 16.

3.2.6. Parametric analysis for different bolt configurations

Three parametric bolt schemes (Plans A-C) and a control group were designed, with the configurations shown in Fig. 17 and parameters listed in Table 4. Fig. 18 shows their moment-rotation curves, demonstrating high similarity in ultimate capacity and stiffness degradation. As shown in Fig. 18, even with a 20% increase in outer-to-inner distance (Plan A) or a 25% reduction in inner spacing (Plan B), the curves remain nearly overlapping. This consistency arises from end plate geometric constraints (Fig. 17) and multi-component synergy, which dilute spacing effects.

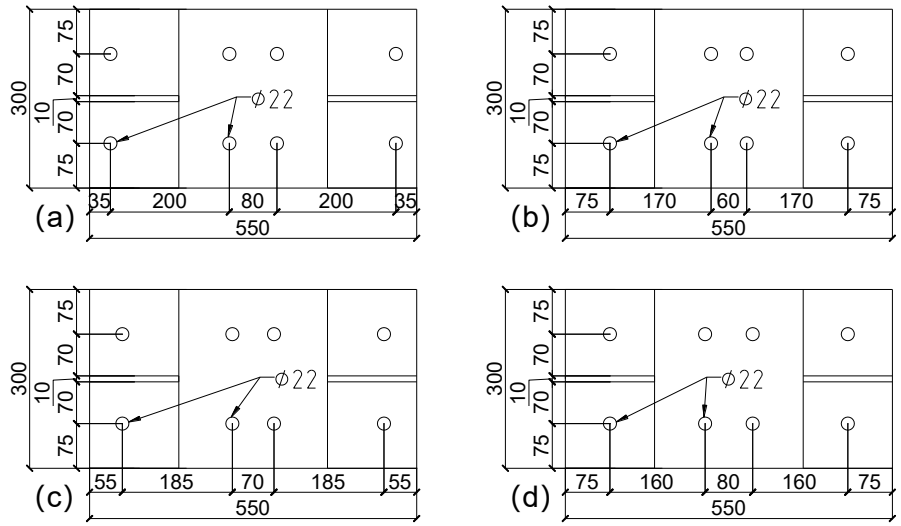

Fig. 17 End plate diagrams under different bolt arrangement plans: (a)-(c) Plans A-C, respectively; (d) TEST and Control group

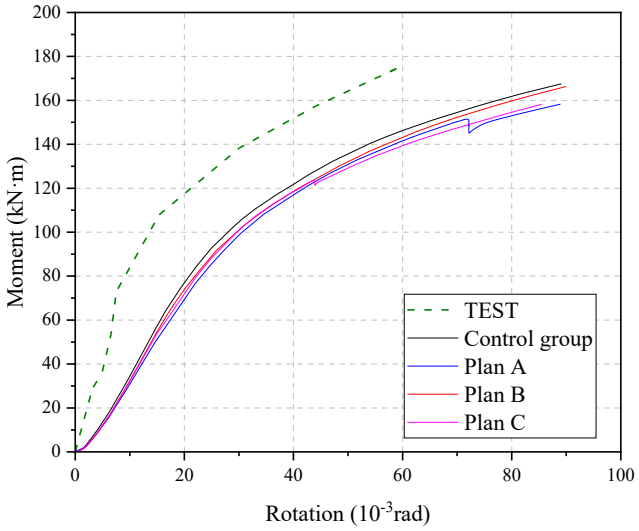

Fig. 18 Bending moment and angle curves under different bolt spacings

Table 4
Parameterization schemes for bolt spacing in the end plate node domain

Plan	Distance between the outer and inner center (mm)	Inner spacing (mm)	Inner moment arm (mm)
Control group	200	80	40
Plan A	240(+20%)	80(unchanged)	40(unchanged)
Plan B	200(unchanged)	60(-25%)	30(-25%)
Plan C	220(+10%)	70(-12.5%)	35(-12.5%)

TCR's modular framework accurately predicts responses for all configurations, as shown in Fig. 18, with deviations of ≤8% from the experimental data (TEST). The method's ability to accommodate local geometric adjustments is validated by the close match between the theoretical curves and FEA results, even for different bolt configurations (Fig. 18).

3.2.7. Failure mode analysis: bolt shear and flange buckling

Reasons for Neglecting the Bolt Shear Analysis

Parametric studies revealed that under pure bending or low-cycle reversed bending, the joint's load transfer is dominated by bending moments, inducing axial tension in bolts (via end-plate separation) rather than shear. Some key observations include the following:

(i) Moment-Driven Force Paths: Bolts in the tension zone resist tensile forces from end-plate rotation, while shear forces from beam shear are negligible.

(ii) Bolt Configuration: Symmetric bolt spacing (≤3d, where d is the bolt diameter) minimizes shear-induced slip, with stress distributions dominated by axial tension.

Flange Buckling in the Joint Domain

Stress distributions in the joint region confirm local buckling in column and beam flanges near the connection (Fig. 19), which arise from the following:

(i) Bending-shear coupling: The joint transfers combined bending and shear, inducing out-of-plane flexure in thin flanges (t_{cf}≤ 16 mm), consistent with stress concentration mechanisms discussed in Section 3.1.

(ii) Geometric discontinuity: The end plate connection creates stiffness transitions, concentrating stresses at the flange-end plate interface and triggering buckling, aligning with T-stub local buckling behavior in thin end plates.

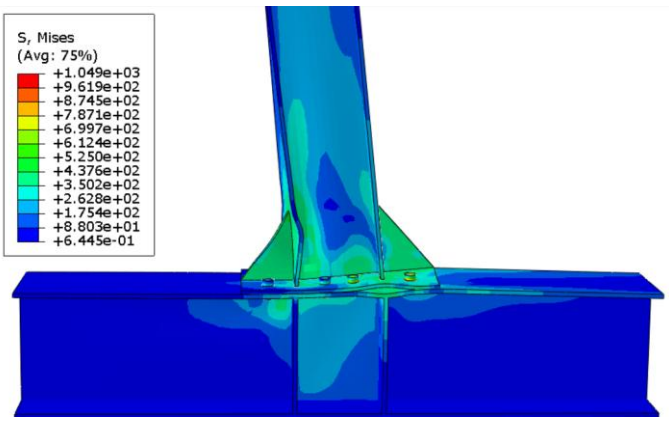

Fig. 19 Stress distribution revealing flange buckling in the joint region

3.3. Analysis of the entire bending process for end plates

To simplify the end plate-bolted connection failure analysis, previous researchers have proposed a method to simplify the end plate bending stress analysis by considering a T-shaped member composed of an end plate and a beam tension flange[24].

According to the Eurocode 3 standard [4], the failure of a T-shaped member can be divided into three types: plate yielding failure, bolt fracture failure, and plate-bolt combined failure. When the end plate thickness is small, plastic hinges may form at the end-plate-bolt and end-plate-beam tension flange connections, leading to end plate failure. This may result in plate yielding failure or plate-bolt combined failure, as shown in Figs. 20(a) and 20(c). When the end plate thickness is large, it may lead to bolt tensile failure, resulting in either bolt fracture or plate-bolt combined failure, as shown in Figs. 20(b) and 20(c). In this section, the analysis method for a T-shaped member is used to conduct theoretical research on the stress and deformation of the end plate and column flange under a bending moment load at the joint.

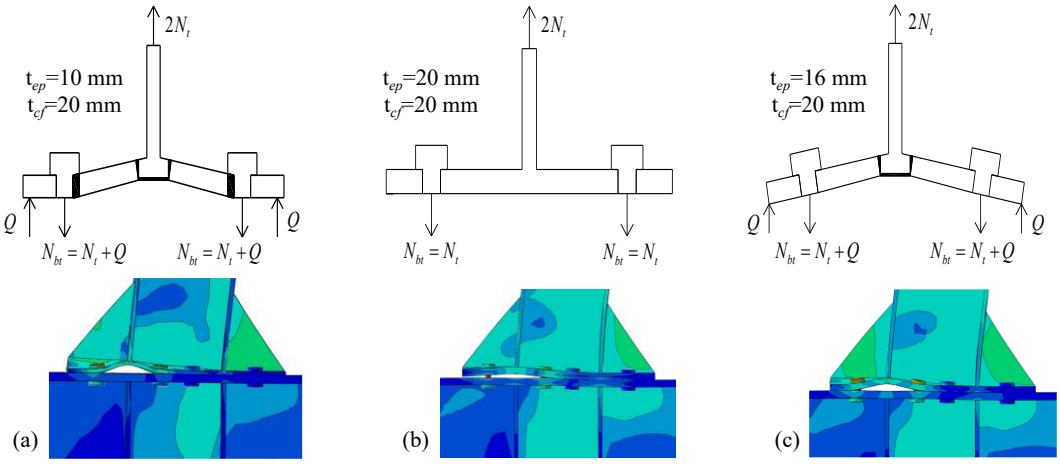

Fig. 20 Failure modes of the T-shaped component: (a) plate yielding; (b) bolt fracture; (c) plate-bolt simultaneous failure

To further illustrate the bending deformation and failure process of the end plate, we analyzed the plate buckling deformation through stagewise changes in the section load capacity. The specific analysis is as follows.

(1) Elastic stage

The mechanical model of the T-section used in this study is consistent with the EC3 simplification. However, for T-sections connected by high-strength bolts, the displacement due to the tensile force of the bolts was not considered. It was assumed that the restraint provided by the high-strength bolts acted as a fixed-end constraint. The theoretical calculation model of the T-section is shown in Fig. 21(a).

The theoretical initial flexural stiffness of the T-section is defined as the ratio of force N_t to the corresponding deformation in the elastic stage. According to structural mechanics principles, neglecting the shear deformation of the plates, the calculation of the corresponding deformation under the action of tensile force N_t can be determined using an equivalent simplified beam mechanical model, as follows:

$$\Delta=\frac{16N_t m^3}{192EI_T},\quad I_T=\frac{l_{eff}t_{ep}^{\ 3}}{12} \tag{24}$$

where I_T is the moment of inertia of the bent plate section of the T-section; I_{eff} can be calculated according to the provisions in EC3; and m is the distance from the center of the bolt hole to the intersection of the flange and web at the root.

The corresponding nodal rotation angle is calculated as follows:

$$\varphi=\frac{\Delta}{h_b} \tag{25}$$

where h_b is the beam height.

(2) Maximum elasticity in the elastic stage

The maximum elasticity-stage point is defined as the point at which the internal forces at the junction of the flange and end plates, as well as at the contact point of the bolt and end plate, reach the yield bending moment, as shown in Fig. 21(b). The yield bending moment at this point was calculated using the formulas defined in the EC3 specifications.

$$M_p=\frac{l_{eff}\times t_{ep}^{\ 2}\times f_y}{4} \tag{26}$$

where M_p is the plastic resistance moment of the equivalent T-section.

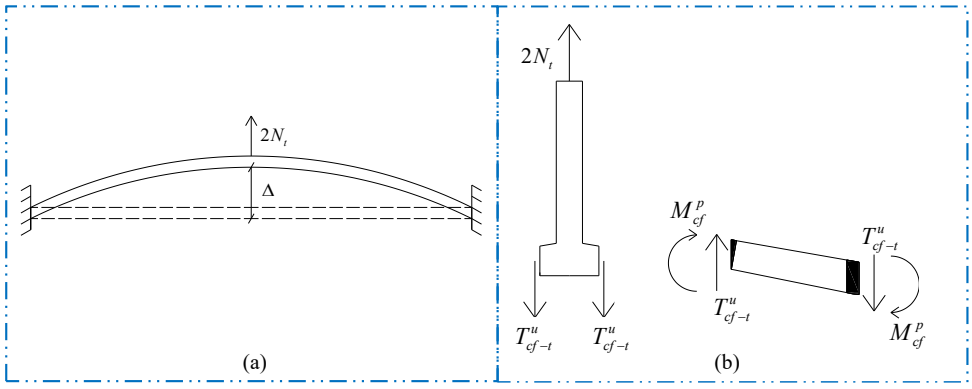

Fig. 21 T-section components: (a) Equivalent beam mechanical model; (b) Force diagram for yield deformation

The bearing capacity of the T-section flange segment under full flexural yield conditions was calculated as:

$$N_t=T_{cf-t}^u=\frac{M_p}{m} \tag{27}$$

Subsequently, the elastic stage of the end plate ends and enters the local plastic stage. For this stage, the stiffness change is defined as $10/t_{ep}$ multiplied by the initial stiffness, considering the influence of the end-plate thickness on the stiffness change in the local plastic stage.

(3) Point at which the entire cross-section of the end plate yields

The calculation of the end plate's bearing capacity according to the Chinese Technical Specification for Light Steel Structures of Portal Frame Buildings (GB 51022-2015)[25] was divided into the following four categories, with specific parameters as defined in the specification:

Category I: Extended Arm: $$N_{ut} = \frac{b_{ep} t_{ep}^2 f_y}{4e_f} \tag{28}$$

Category II: Ribless: $$N_{ut} = \frac{(0.5a + e_w) t_{ep}^2 f_y}{2e_w} \tag{29}$$

Category III: Both Sides Supported: $$N_{ut} = \frac{b_{ep} t_{ep}^2 f_y}{4e_f} + \frac{(e_f + e_w) t_{ep}^2 f_y}{2e_w} \tag{30}$$

Category IV: End-plate Section with Three-Sided Support:

$$N_{ut} = \frac{b_{ep} + 2b_s t_{ep}^2 f_y}{4e_f} + \frac{e_f t_{ep}^2 f_y}{e_w} \tag{31}$$

According to relevant literature, the stiffness changes to one-seventh of its original value until the plastic limit bending capacity is reached. In this study, for thin, medium, and thick plates, the plastic limit bending capacities were taken as 1.5, 1.5, and 1.1 times the plastic bending capacity, respectively. The change in stiffness after the yielding stage was calculated based on the stiffness variation in the joint domain.

(4) End plate moment-rotation curve

A comparison of the end plate moment-rotation models is depicted in Fig. 22. As can be seen, for thinner plates, there is a close agreement between the FEM results and the theoretical calculations. However, as the plate thickness increased, the discrepancies gradually increased. This may be because the simplification of T-shaped components ignores the spatial interaction between the end plate and the column flange, as well as the strain-hardening behavior of the steel in the post-yield stage. These factors result in insufficient representation of the actual load-bearing capacity of the end plate under complex stress states, highlighting the need for precise 3D modeling in future research.

Based on the aforementioned theoretical calculation methods, the results obtained from these methods (TCM) were compared with those from finite the FEA and tests (TEST) at different stages to validate the proposed theoretical model. The results of the moment and rotation models are presented in Fig. 23.

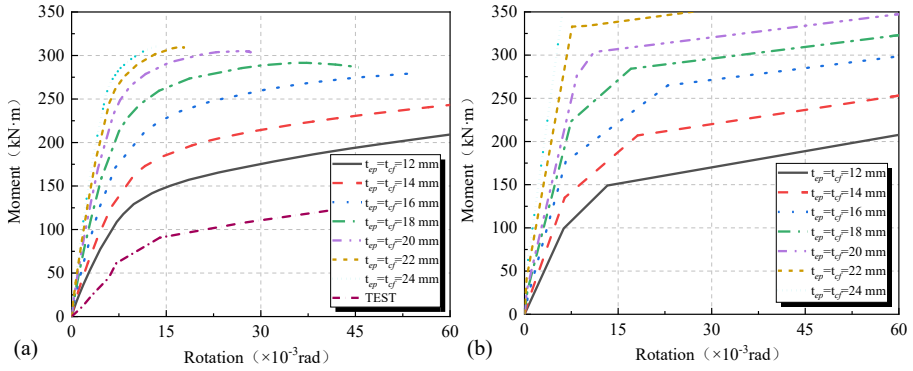

Fig. 22 Comparison of the end plate moment-rotation models: (a) finite-element and test results; (b) theoretical calculations

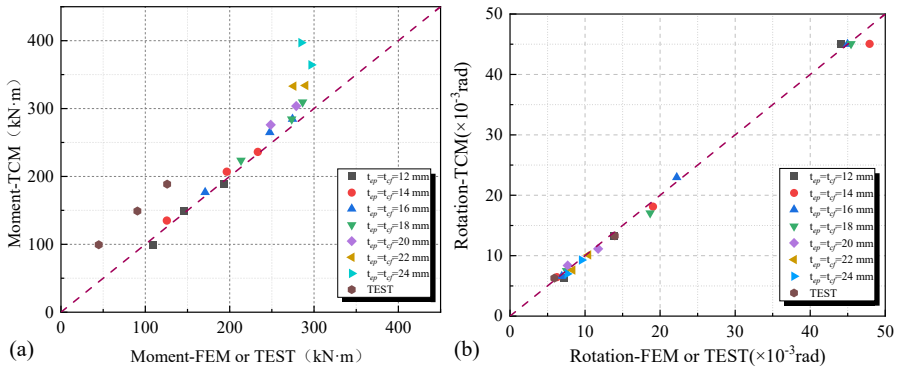

Fig. 23 End plate results for (a) moment and (b) rotation

3.4. Extended validation on end plate geometries

(1) Applicability to extended end-plate configurations

To validate the theoretical calculation method (TCR) across different end-plate geometries, ABAQUS simulations were conducted for four configurations: double-extended (DE), single-extended with tension on the extension side (SE-T), single-extended with compression on the extension side (SE-C), and flush (FLAT). Fig. 24 illustrates the geometric definitions of the DE, SE, and FLAT end-plate configurations, while Fig. 25 compares their moment-rotation curves. The simulation results reveal high consistency in the moment-rotation trends of the DE, SE-T, and SE-C configurations, indicating that TCR's subcomponent modeling framework, which focuses on the overall mechanical transmission of end plates, bolts, and panel zones, applies to extended end plate joints.

Notably, although SE-T and SE-C exhibit different force states on the extended side, the deformation coordination between the end plate and bolt system weakens the influence of single-side force differences, as evidenced by the overlapping curves in Fig. 25. This consistency confirms that TCR's modular approach, which decomposes the joint into independent subcomponents (end plate, bolts, panel zone), accurately captures the global mechanical behavior of extended configurations regardless of local force asymmetries. The subcomponent superposition principle allows TCR to maintain predictive accuracy by summing contributions from each element, as validated by the close alignment between the simulated and theoretical curves.

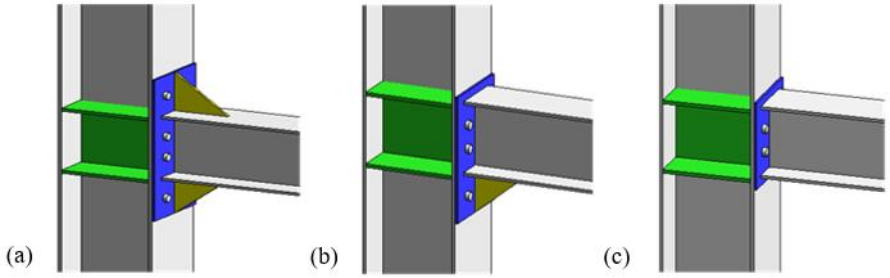

Fig. 24 Different end-plate geometries: (a) DE; (b) SE; (c) FLAT

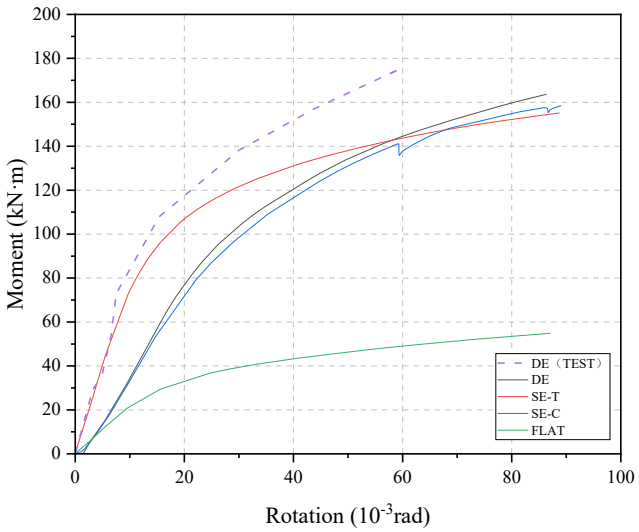

Fig. 25 Comparison between the bending moment and angle curves under different end-plate geometries

(2) Flush end plate load capacity decline mechanism

The FLAT end-plate configuration in Fig. 24 exhibits a significant decline in load-bearing capacity compared to the extended types, as shown by the abrupt stiffness degradation in Fig. 25. Unlike the DE and SE configurations, which use the extended segment to form a lever arm for dispersing bolt tension, the FLAT end plate relies on local bending near the bolts to resist moments. This leads to concentrated stress on the bolts and early local end-plate instability.

An analysis of the moment-rotation curves reveals that the FLAT end plate's rapid capacity decline stems from the absence of the lever effect present in the extended configurations. For approximate calculations using TCR, the effective bending length of the FLAT end plate is shorter, and local deformation is more pronounced. Therefore, the flexural stiffness of the end plate subcomponent can be adjusted by referencing the DE model: reducing the effective width coefficient to reflect the mechanical characteristics of FLAT configurations. This adjustment aligns the theoretical curve with the simulated response, leveraging TCR's modular framework to accommodate geometric variations by modifying subcomponent parameters without altering the overall modeling approach.

3.5. Stiffening rib-compression process analysis

After analyzing the stress variations in the rib-compression process based on multiple FEMs, the primary stress variations in the compressed region of the rib could be categorized into three stages: (i) initial yielding of one-third; (ii) two-thirds yielding in the second stage; and (iii) overall yielding in the third stage, as shown in Fig. 26.

As the applied bending moment increased and the joint gradually began to rotate, the rotation center of the beam end shifted. As shown in Fig. 27, the compressed region of the beam web (depicted in black) gradually moves from the middle position of the beam web towards the compressed flange of the beam (shown as the upper flange in Fig. 27) as the displacement load increases. Eventually, the compressed load was entirely borne by the compressed flange and ribs, with the black portion concentrated at the compressed flange. Therefore, the rotation center was defined as the compressed beam flange. In this section the stress distribution changes of the compressed ribs are analyzed. The compressed load distribution was determined based on the welded area ratio between the compressed beam flange and rib end plate.

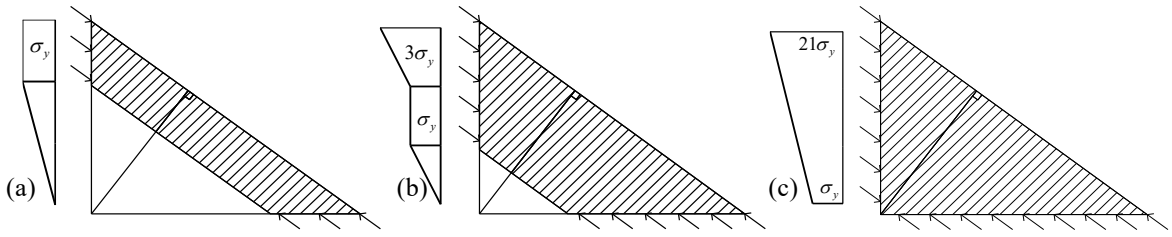

Fig. 26 (a) 1/3 stiffening rib compression yield; (b) 2/3 compression yield; (c) overall compression yield

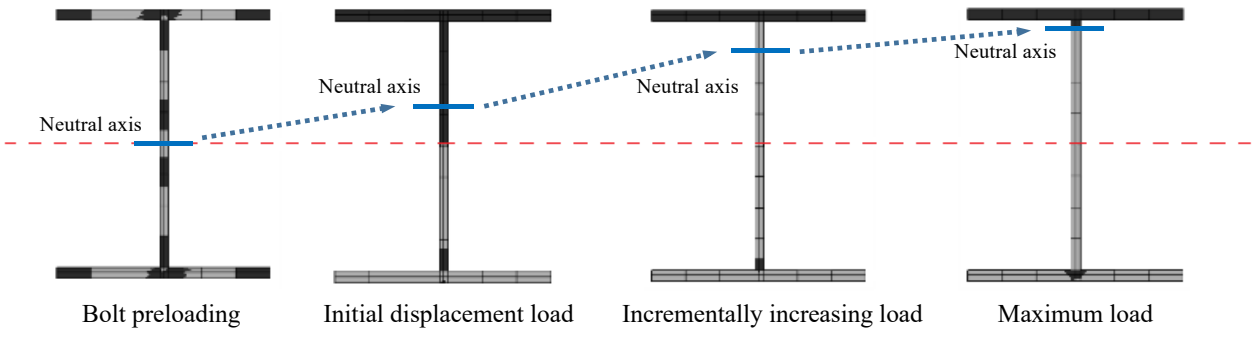

Fig. 27 Joint compression-zone variation diagrams

By combining the yielding states and stress development, the stress distribution along the diagonal of the stiffener can be calculated for the first two stages as follows:

$$P_{\mathrm{sy1x}} = \frac{1}{3} f_{\mathrm{psr,y}} h_{trangle} t_{\mathrm{psr}} \tag{32}$$

$$P_{\mathrm{sy2x}} = \frac{7}{6} f_{\mathrm{psr,y}} h_{trangle} t_{\mathrm{psr}} \tag{33}$$

where $h_{trangle}$ is the perpendicular distance from the intersection point on the right side to the diagonal.

In the third stage, the ultimate bearing capacity was calculated based on the cross-section of the triangular stiffener. Under bending moment loading, the contribution of the stiffener stress deformation to the rotation angle of the end-plate bolted connection of the beam-column joint can be calculated as follows:

$$\phi = \arctan\left(\frac{\varepsilon l_d}{l_{psr,s}}\right) \tag{34}$$

where ε is the oblique edge strain and l_d represents the length of the triangular stiffener diagonal. For the first, second, and third stages, ε was at maximum elastic strains of 1.5, 3, and calculated based on the calculated bearing capacity, respectively.

The stiffener bending moment-rotation model results are shown in Fig. 28, where the theoretical calculations based on the proposed method are compared with the FEM analysis results. As can be seen, for thinner plates, the FEM analysis results closely match the theoretical calculations; however, as the plate thickness increases, the discrepancies gradually become more significant.

Based on the theoretical calculation methods described above, the results (TCM) were compared with the FEM and test (TEST) results at different stages to validate the proposed theoretical model. The comparison results for the bending moment and rotation angle models are shown in Fig. 29.

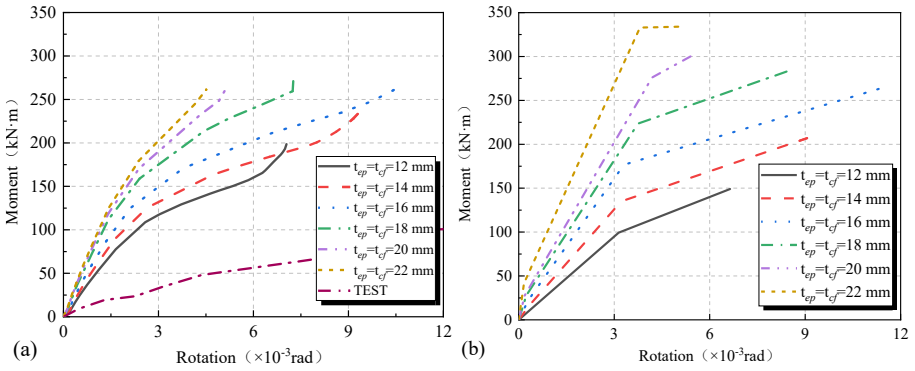

Fig. 28 Comparison between the stiffening rib moment-rotation models: (a) finite-element and test results; (b) theoretical calculations

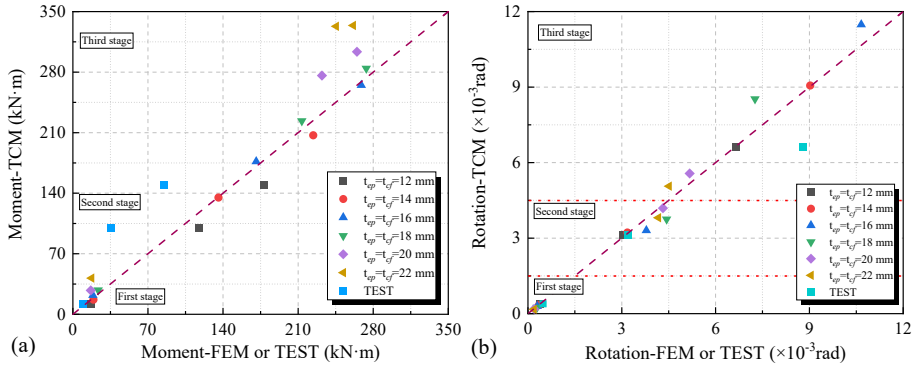

Fig. 29 Stiffening rib results for (a) moment and (b) rotation

3.6. Dynamic cyclic loading analysis: seismic applicability validation

To evaluate the proposed method's suitability for seismic design, dynamic (acceleration-driven) and quasi-static (displacement-controlled) cyclic loading simulations were conducted in ABAQUS. The simulations aimed to assess the joint behavior under inertial effects while maintaining consistent displacement amplitudes between loading types.

(1) Simulation setup

The quasi-static loading followed the JGJ/T101-2015 low-cycle reversed displacement protocol and serves as the baseline for static-mechanism validation. Meanwhile, for the dynamic loading, periodic acceleration histories were applied to induce inertial forces, mimicking seismic loading characteristics without direct seismic wave input. The loading frequency and amplitude were tuned to replicate earthquake-induced dynamic responses.

(2) Hysteresis curve comparison

In the quasi-static response, the hysteresis loops exhibited symmetric energy dissipation with stable stiffness degradation (Fig. 30(b)), aligning with the method's component-level superposition assumptions. In the dynamic response, the hysteresis loops exhibited pronounced pinching and scattering (Fig. 30(a)) due to inertial effects, but key mechanical features (e.g., yield displacement and post-peak deformation) remained consistent with the quasi-static trends. This confirms that core force-transfer mechanisms (e.g., bolt tension and end plate bending) are invariant under dynamic loading.

(3) Stress distribution and mechanistic robustness

Dynamic loading intensified the local stress gradients near bolt holes; however, primary stress concentrations at bolt interfaces and end plate-column junctions matched the static-mechanism predictions. The proposed method's applicability to seismic design is rooted in the following:

(i) Component-Level Invariance: Subcomponent superposition captures fundamental deformation mechanisms dominant in both static and dynamic scenarios.

(ii) Inertial Effect Integration: Treating dynamic inertial forces as equivalent static loads via D'Alembert's principle enables static-equivalent analyses, maintaining consistency with the FEA for key performance indicators (e.g., rotational stiffness trends).

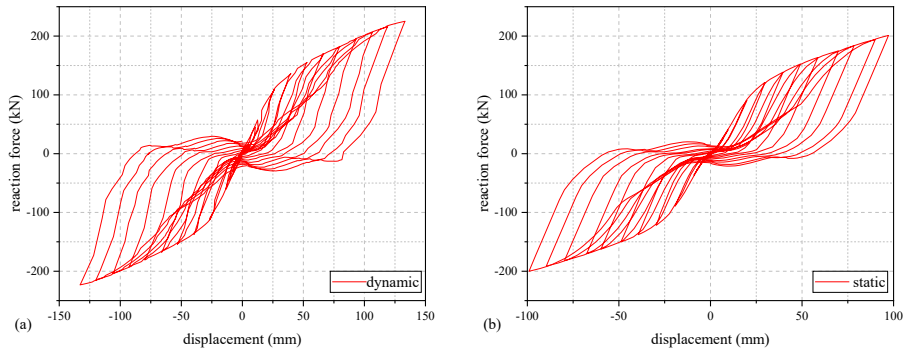

Fig. 30 Hysteresis curves: (a) Dynamic hysteresis curve (acceleration-driven); (b) Quasi-static (displacement - controlled)

3.7. Comparison with existing methods

Özkılıç et al. [5,6] focused on T-stub and end plate connection capacities but overlooked component-level deformation stages. Their models underpredict bolt tension in thin plates (40%-60% error) and oversimplify thick-plate stress states. To overcome these drawbacks, a full-process subcomponent approach is introduced in this paper, decomposing joint rotation into panel-zone, bolt, and end plate contributions. Additionally, Wang et al. [1] analyzed CFST column joints, but their study lacked generality for pure steel frames. In this study, the approach is generalized to steel joints, separating rotation into component contributions (panel zone: 30%-40%; bolts: 20%-30%), whereas Wang et al. [1] focused on concrete-confinement effects.

In conclusion, one of the main contributions of the proposed method lies in capturing component interactions and full deformation processes, unlike previous studies [1,5,6] that focused on isolated behaviors. This enables a systematic design; nevertheless, refinements for thick plates and CFST applications are still required.

4. Full bending moment-rotation angle curve validation

4.1. Validation of full-process bending moment-rotation curves of subcomponents via finite-element simulations

The theoretical calculation results of each component were synthesized to obtain the full-process subcomponent calculation results (TCM). These were then compared with the FEM results to validate the proposed theoretical model. The comparison results of the bending moment-rotation angle model are shown in Fig. 31.

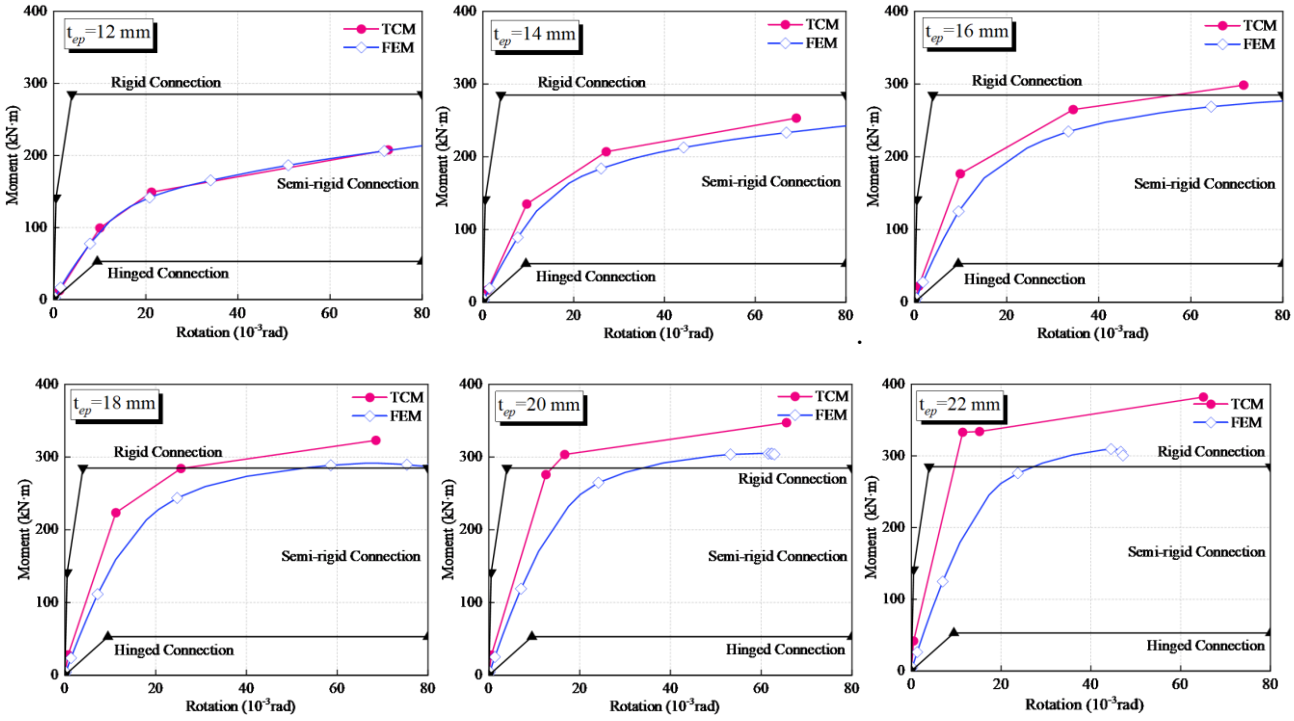

Fig. 31 Joint moment-rotation curve results

As can be observed in Fig. 31, the proposed method is more suitable for end plate connections of thin to medium thickness. However, for end plates with thicknesses greater than 20 mm, significant errors were observed in the calculations. This is attributed to the independent modeling of components without fully considering their synergistic effects—for example, the interaction between bolt tension and joint domain shear deformation. Experimental comparisons (Fig. 32) further indicate that the model's accuracy decreases with increasing loading complexity, highlighting the need for refined modeling of the contact nonlinearity and material ductility in future studies.

4.2. Validation of existing tests on end-plate-bolted beam-column joints

A comparison between the test results obtained by Sun et al. [25,26] and Zheng et al. [27,28] and those obtained with the proposed method is presented in Fig. 32. As can be seen, the theoretical values closely match the test data, indicating high accuracy and precision in terms of predicting the results of existing tests. This suggests that the proposed calculation method can accurately predict the full moment-rotation curve of the end-plate-bolted connection beam-column joints.

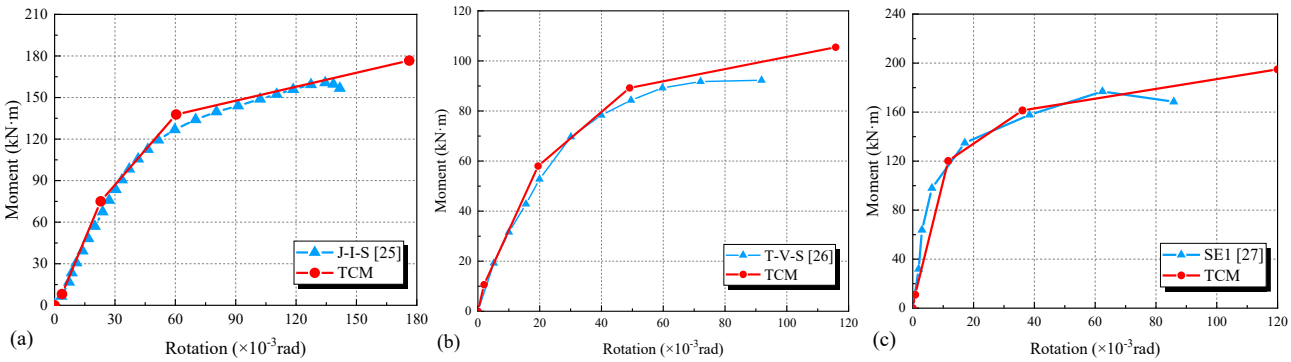

Fig. 32 Comparison between the proposed method and the other tests results from the literature: (a) J-I-S [25] ; (b) T-V-S [26] ;and (c) SE1 [27]

5. Engineering application and design guidelines

5.1. Design flowchart for subcomponent analysis

A systematic design flowchart (Fig. 33) is proposed to translate theoretical insights into practical engineering steps, outlining a modular approach to joint design. The proposed design flowchart involves the following:

(i) Decomposition: Joints are broken down into five subcomponents —joint domain, end plate, bolt group, column flange, and stiffeners.

(ii) Stage-wise analysis: Each component is evaluated through critical deformation stages (e.g., bolt tension from contact to full separation).

(iii) Superposition: Component rotations are synthesized to derive the joint's moment-rotation curve.

(iv) Validation: The results are cross-checked against design codes (e.g., EC3 and AISC) for compliance.

5.2. Key design guidelines for subcomponents

Table. 5 summarizes the actionable design rules for each joint subcomponent, validated via theoretical analysis and parametric studies.

5.3. Validation metrics for joint design

In this study, the key joint performance evaluation indicators were as follows:

(i) Inter-story drift angle: ≤1/500 under design seismic loads, ensuring structural integrity;

(ii) Joint rotational stiffness: Discrepancy of less than 10% between the theoretical and FEA results;

(iii) Plastic deformation capacity: End-plate rotation of ≥ 0.02 rad without rupture, enabling energy dissipation.

These guidelines provide a structured framework for engineers to optimize joint design, balancing computational efficiency with mechanical accuracy in prefabricated steel structures.

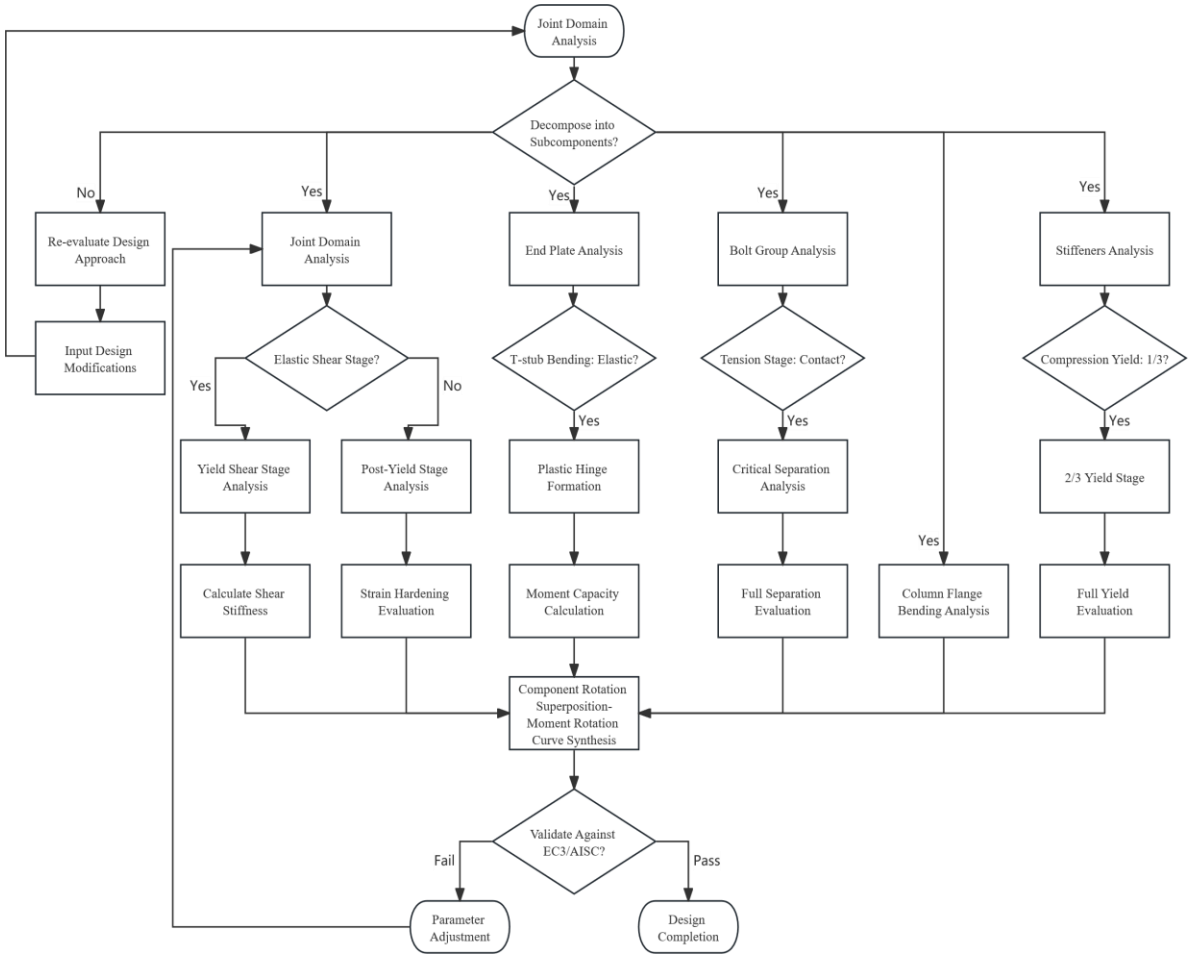

Fig. 33 Subcomponent-driven full-process design flow for beam-column joints

Table 5
Design rules and rationale for joint subcomponents

Subcomponent	Design Rule	Rationale
End plate	Use 12-16 mm for standard floors(plastic hinge development) ; 20-24 mm for seismic/critical floors (stiffness control).	Matches "strong-column/weak-joint" via thickness-dependent ductility.
Bolt group	Adopt 10.9-grade M20 bolts (pretension = 155 kN); symmetric double-row layout (spacing ≤ 3×bolt diameter).	Reduces lever effects (tested: >3d spacing increases bolt tension by over 15%).
Joint domain	Column web thickness ≥ 80% of end plate thickness.	Delays shear yielding to preserve initial stiffness (≥9×10³ kN·m/rad for seismic).
Column flange	Thickness matches end plate + 2 mm (e.g., 22 mm for 20 mm end plate).	Prevents flange failure before end plate/plastic hinges.
Stiffeners	Thickness ≥ 50% of end plate; mandatory in seismic zones.	Boosts compressive capacity (25% drop without stiffeners, per tests).

6. Conclusion

In this study, a theoretical analysis of the stress characteristics of an extended end plate bolted connection in steel frame beam-column joints was conducted. The theoretical calculation results were compared with FEM simulation results and existing studies. Based on the results, the main conclusions of this study can be summarized as follows:

1. The proposed full-process subcomponent analysis method effectively calculates the bearing capacity and deformation of individual components (joint domain, bolts, end plates, stiffeners) and synthesizes them to derive the joint's moment-rotation curve. This approach reduces reliance on complex FEM simulations, relying solely on component dimensions and material properties, making it suitable for engineering design - e.g., the Baoding Technician College steel frame project, where it guided the selection of end plate thickness (20 mm for ground floor; 16 mm for standard floors) and bolt configurations (symmetric double-row arrangements).

2. The thickness of end plates and column flanges significantly affects bolt internal forces: thinner plates (≤16 mm) amplify lever effects, leading to earlier end-plate plastic deformation, while thicker plates (≥20 mm) enhance the joint stiffness but require attention to the bolt tensile capacity. Three failure modes were identified: thin-plate yielding, medium-thick plate-bolt combined failure, and thick-plate bolt rupture.

3. Despite the fact that this study focused on the elastic and plastic stages, the proposed framework can be extended to include material-strengthening stages by incorporating strain-hardening parameters.

Acknowledgements

This work was financially supported by the Natural Science Foundation of Hebei Province (E2023208080).

References

[1] J Wang, L Han, et al. Hysteretic behaviour of flush end plate joints to concrete-filled steel tubular columns[J]. Journal of Constructional Steel Research, 2009, 65(8): 1644-1663.
[2] Yan S, Rasmussen K J R, Jiang L L, et al. Experimental evaluation of the full-range behaviour of steel beam-to-column connections[J]. Advanced Steel Construction, 2020, 16(1): 77-84.
[3] Shah S N R, Sulong N H R, Khan R, et al. Structural performance of boltless beam end connectors[J]. Advanced Steel Construction, 2017, 13(2): 144-159.
[4] ENV 1993-1-8:2005, Eurocode 3: Design of steel structures—Part 1.8: Design of joints.
[5] Y. O. Özkılıç. The capacities of unstiffened T-stubs with thin plates and large bolts. Journal of Constructional Steel research, 2021, 186:1-16.
[6] Y. O. Özkılıç, C. Topkaya. The plastic and the ultimate resistance of four-bolt extended end plate connections. Journal of Constructional Steel Research, 2021, 181: 106614.
[7] Zhang A L, Shangguan G H, Zhang Y X, et al. Experimental study of resilient prefabricated steel frame with all-bolted beam-to-column connections[J]. Advanced Steel Construction, 2020, 16(3): 255-271.
[8] JGJ/T 101-2015, Specification for test methods of seismic buildings, Architecture Industrial Press of China, Beijing, 2015.
[9] Gang Shi, Hao Fan, Yu Bai, et al. Improved measure of beam-to-column joint rotation in steel frames. Journal of Constructional Steel Research, 2012, 70: 298-307.
[10] Titoum M, Mazoz A, Benanane A, et al. Experimental study and finite element modelling of push-out tests on a new shear connector of I-shape[J]. Advanced Steel Construction, 2016, 12(4): 487-506.
[11] Lingli Pan, Yiyi Chen. Modified formula for calculating elastic stiffness of panel zone in H-shaped beam-column connections. Engineering Mechanics, 2016, 33(11): 68-74+94.
[12] GB 50017-2017, Steel Structure Design Standards. Architecture Industrial Press of China, Beijing, 2017.
[13] Ma H W, Zheng H, Zhang W, et al. Experimental and numerical study of mechanical properties for the double-ribbed reinforced beam-column connection[J]. Advanced Steel Construction, 2020, 16(4): 297-309.
[14] Sufang Wang, Yiyi Chen. Calculation of initial stiffness of beam-to-column end plate joint. Engineering Mechanics, 2008(08): 109-115.
[15] H. Krwinkler, V. M. Bertero, E. P. Popov. Shear Behavior of Steel Frame Joints. Journal of the Structural Division, 1975, 101(ST11).
[16] Torbaghan M K, Sohrabi M R, Kazemi H H. Investigating the behavior of specially pre-fabricated steel moment connection under cyclic loading[J]. Advanced Steel Construction, 2018, 14(3): 412-423.
[17] Bin Qin, Steel Structure Joint Design Manual. China Architecture & Building Press, Beijing, 2023.
[18] JGJ 82-2011, Technical specification for high strength bolt connection of steel structure, Architecture Industrial Press of China, Beijing, 2011.
[19] Macillo V, Shakeel S, Fiorino L, et al. Development and calibration of a hysteretic model for cfs strap braced stud walls[J]. Advanced Steel Construction, 2018, 14(3): 337-360.
[20] British Standards Institution, BS5950, Structural use of steelwork in building. British Constructional Steelwork Association, 2001.
[21] ANSI/ANSC 358-05, Prequalified Connections for Special and Intermediate Steel Moment Frames for Seismic Applications. American Institute of Steel Construction (AISC), Chicago, 2005.
[22] Patel V, Uy B, Pathirana S W, et al. Finite element analysis of demountable steel-concrete composite beams under static loading[J]. Advanced Steel Construction, 2018, 14(3): 392-411.
[23] GB51022-2015, Technical code for steel structure of light-weight building with gabled frames. Architecture Industrial Press of China, Beijing, 2015.
[24] Nouri K, Sulong N H R, Ibrahim Z, et al. Behaviour of novel stiffened angle shear connectors at ambient and elevated temperatures[J]. Advanced Steel Construction, 2021, 17(1): 28-38.
[25] Lele Sun, Xiaoxia Yang, Min Cai, et al. Monotonic bending behaviour of TOBs bolted beam to SHS column connection with stiffening component. Journal of Building Engineering 62 (2022) 105339.
[26] Lele Sun, Zeqi Liang, Qishuai Wang, et al. Seismic response on T-head square-neck one-side bolted endplate connection of beam to square tubular column. Engineering Structures 246 (2021) 113077.
[27] Baofeng Zheng, Dianhan Wu, Jiachang Wang, Ganping Shu. Test on seismic behaviors of stainless steel bolted extended end plate beam-column joints. Thin-Walled Structures 196 (2024) 111516.
[28] Li R, Jin J J, Xiao Z C, et al. Study on bending performance and load-carrying capacity of single-layer cylindrical reticulated shell with new sprayer joint[J]. Advanced Steel Construction, 2025, 21(1): 31-41.

Advanced Steel Construction – Vol. 22 No. 2 (2026) 198–207
DOI:10.18057/IJASC.2026.22.2.6

NUMERICAL STUDY ON STIFFENED CONCRETE-FILLED DOUBLE STEEL TUBE SQUARE COLUMNS BEHAVIOUR

Mohamed Ghannam [1, *] and Md Kamrul Hassan [2]

[1] *Associate professor in Structural Engineering Departement, Faculty of Engineering, Mansoura University, Mansoura, Dakahlia 35516, Egypt*
[2] *Seniour Lecturer in Fire Safety Engineering, School of Engineering, Design and Built Environment, Western Sydney University, Penrith, NSW 2751, Australia*
** (Corresponding author: E-mail: m.ghannam@mans.edu.eg)*

ABSTRACT

Nowadays, more research has been done to investigate the behaviour of concrete filled double steel tube (CFDT) columns owing to the numerous advantages over concrete-filled steel tube (CFST) columns. Very few studies have focused on the behaviour of stiffened CFDT columns. This research gap is aimed to be covered in this paper, by studying the behaviour of CFDT columns under axial loads using different stiffener profiles that are welded to the inner and outer tubes. The performance of square-stiffened CFDT columns is investigated using the finite element (FE) method. Three types of stiffeners were studied: rectangular, inclined, and tie stiffeners. The verified FE model is used to study the effect of different parameters on the behaviour of stiffened CFDT columns. The results show that using tie stiffeners give the most increase in the ultimate axial load capacity by more than 15%. A simplified analytical model is presented to predict the axial load capacity of stiffened CFDT columns using tie stiffeners.

ARTICLE HISTORY

Received: 25 June 2025
Revised: 2 January 2026
Accepted: 2 January 2026

KEYWORDS

Stiffened concrete filled double;
Steel tube columns;
Load capacity;
Stiffeners;
Finite element model;
Analytical model

1. Introduction

Concrete-filled double steel tube (CFDT) and concrete-filled double-skin tube (CFDST) columns represent advanced composite structural elements that are increasingly preferred in construction over conventional concrete-filled steel tube (CFST) columns due to their superior performance characteristics. A CFDST column comprises two concentrically placed steel tubes, with the annular space between them filled with concrete, leaving the central core void. This configuration yields lighter structures with enhanced ductility, strength, cyclic performance, and fire resistance [1-7]. The cross-sectional shapes of the inner and outer tubes can be varied, including circular-in-square, square-in-square, or circular-in-circular arrangements [8].

Initially, under loading, an interaction is formed between the inner steel tube and the concrete ring because the lateral expansion of the steel is greater than that of the concrete (a result of different Poisson's ratios) and inversely a gap is formed between outer steel tube and concrete. However, interaction between inner tube and concrete diminishes as the concrete enters the elasto-plastic stage. In the later loading stage and due to increasing strain in concrete interaction is formed between outer tube and concrete [2, 9].

The structural behavior of CFDST columns can be significantly improved by filling the central void core with concrete, resulting in a CFDT column. The solid concrete core not only substantially increases the cross-section's load capacity but also helps delay the outward and inward local buckling of the inner tube [10]. A key advantage of CFDT over CFDST columns is their superior fire resistance, primarily attributed to the heat sink effect provided by the concrete core, which can enhance fire resistance by up to 36% Romero et al. [1]

Interaction between the steel tube and the concrete core is a critical parameter influencing the overall behavior of CFST, CFDST, and CFDT composite columns. A primary strategy for enhancing structural performance is the incorporation of stiffeners welded to the steel tube, which promote confinement and bonding. The use of stiffeners in composite structures, particularly those utilized in offshore applications like wind turbine masts and steel towers, has been identified as a vital solution for mitigating problems associated with excessive weight and high cost [11, 12]

Stiffeners allow for the reduction of the steel tube thickness, leading directly to reductions in both structural weight and material cost. Numerous studies have demonstrated that employing binding bars or welding bars in CFST columns markedly enhances concrete confinement, increases axial load capacity, improves ductility, and delays elastic local buckling [13-16]

The application of rectangular rib stiffeners is also highly effective [17-21], with Tao et al. [18] and Tao et al. [19] showing they increase load capacity and postpone local buckling. These findings underscore that existing design codes may not accurately predict the load capacity of stiffened columns, a point further supported by the introduction of novel designs like the catty-cornered propped concrete-filled steel tube, which demonstrated increased ultimate load capacity. Singh et al. [22]. In fact, previous research indicates that most design codes overlook the beneficial effects of stiffeners, resulting in highly conservative predictions for CFST and CFDT columns [23-25]

Research specifically addressing the behavior of stiffened CFDST and CFDT columns remains limited, with most studies focusing on a single stiffener type without comprehensive comparisons [26]. Earlier work on stiffened hybrid CFDT columns (using FRP for the outer tube) concluded that stiffening the inner tube is preferable for preventing local buckling and that a greater number of thin ribs performs better than a few thick ribs, sometimes increasing axial load capacity by over 50% [27-29]. Zeng et al. [30] examined the seismic performance of similar stiffened columns, concluding that increasing the number of ribs enhances energy dissipation and seismic performance. Other work confirmed the viability of specific design models for FRP-replaced external steel tubes in CFDST columns as proposed by Zeng et al. [31] and Yu et al. [32] , others introduced novel stiffener types, such as stirrups welded to both tubes, which offered optimal confinement at a specific ratio Ding et al. [33]

Studies on stiffened cold-formed double steel tube columns have also proposed new design formulas to correct the underestimation of load capacity by current codes, showing enhancements in both ultimate load capacity and ductility [34-37]

Wang et al. [38] and Ghannam and Metwally [39] demonstrated that T-stiffeners could increase the axial load capacity of circular CFDT columns by more than 15%. Further research confirmed that stiffening the outer tube increases the ductility and energy dissipation of CFDST columns Wang et al. [40] and that welded reinforcement bars enhance capacity, stiffness, and ductility, with inner tube stiffening providing the greatest enhancement. Hasan and Ekmekyapar [41]

Finally, T-stiffeners were found to improve the fire resistance of circular CFDST columns more effectively than rib stiffeners, yielding up to a 70% increase in fire resistance Shekastehband et al. [42]

It is anticipated that the addition of stiffeners will yield a more significant enhancement in the performance and load capacity of square CFDT columns compared to their circular counterparts. This expectation is based on the fact that circular tubes provide inherent confinement to the concrete due to the hoop tensile stress generated by the concrete's lateral expansion, a phenomenon largely absent in square columns, which are more susceptible to local buckling and confine the concrete only at the rounded corners [43-47].

While numerous studies have been conducted on stiffened CFST columns [20]; research focusing on stiffened CFDST and CFDT columns is scarce. The novelty of this study lies in addressing this critical research gap and developing simplified design guidelines for square CFDT column. This paper continues the second part of the research previously published by Ghannam and Metwally [39] which investigated the behavior of stiffened circular CFDT columns. While this paper focuses on the square cross-section, , also this study directly compare the performance of three distinct stiffener profiles (rectangular, inclined and tie

stiffener) on the square CFDT columns under axila load. This comparison provides essential, previously unavailable design guidelines.

The objectives of this paper are achieved numerically using a Finite Element (FE) model developed in the ABAQUS program [48]. The FE model is verified against test results from [38], and subsequently employed to conduct a parametric analysis investigating the effect of various parameters on the behavior of stiffened square CFDT columns, which show the significant effect of tie stiffener in improves the performance of CFDT column compared to other studied stiffener types in this paper (Rectangular and incline stiffeners). Tie stiffeners can increase CFDT column ultimate strength by 15 %. Finally, a simplified analytical model is proposed to accurately predict the axial load capacity for these specific column types.

2. Finite element model

2.1. Description

2.1.1. Material models

Elastic-plastic stress-strain behaviour is used for square tubes, and multi-linear hardening is used for circular inner steel tubes similar to Tao et al. [49]. Concrete material is modelled using concrete-damaged plasticity [48]. The plasticity parameters are calculated as adopted by Tao et al. [49]. Ultimate tensile strength and corresponding fracture energy are used to simulate the tensile behaviour of concrete using ultimate tensile behaviour equal to 10% of compressive strength as proposed by Tao et al. [49],.

2.1.2. Interactions and constrains

Interaction between concrete and steel tubes is simulated by using surface-to-surface contact. The value of Coulomb friction is taken as 0.6. Tie constraints were used to model the contact between steel tubes and stiffeners which insure full attachment between both parts. Tie also are used between concrete and stiffeners, Ghannam and Metwally [39] compare between modeling the interaction between concrete and stiffeners as tie and as contact interaction and found that both gives similar results as stiffeners is completely embedded in the concrete.

2.1.3. Boundary conditions and element divisions

Solid element (C3D8R) was used to model concrete, while shell element (S4R) was used to model steel tubes and stiffeners. The top of the column was coupled with a reference point (using coupling constraint), where this point controls the column's top displacement and rotation. To save computational time and gain the benefits of model symmetry, a quarter model is used using half-length and half-section. The number of elements was determined after performing a sensitivity analysis.

The corner of the outer steel tube of the CFDT square column was modelled once as a sharp edge and another time as a curved edge. From Fig. 1, it can be seen that there was no significant effect. So, a sharp edge was chosen in order to simplify the model geometry. The column width is divided in to 12 elements, while the element size in the longitudinal direction is twice that within the cross-section [39]. Mesh size and division were obtained based on mesh sensitivity analysis. Several number of element divisions were used to show the optimum number of element that provide closer agreement with test result and also saving computational time. It was found that using smaller number of division provides less accuracy, using 12 elements division provide closer agreement to the test result without increasing the computational time, increasing number of elements more than this has minor effect on model accuracy.

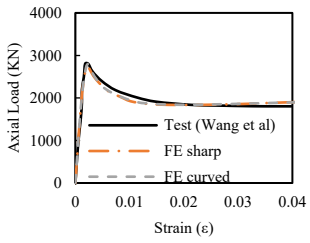

Fig. 1 Effect of square section corner shape

2.1.4. Initial imperfection and residual stress

Initial imperfection was included to the FE model through a separate buckling analysis where the first buckling mode with an amplitude equal to column length/1000, was implemented in the stress analysis as an initial state of the columns.

Previous researchs [50-53] shows that effect of residual stress can be ignored as they have minor effect on initial stiffness, ultimate load an overall performance. [52] shows that this is due to the presence of concrete which take part in carrying large portion of the columns load capacity.

2.2. Verification of the FE model

Due to limited research on stiffened square CFDT columns, the FE model was verified against test results that were performed by [38] for stiffened square double tube columns using four welded lipped angle (23 mm lip) for the outer steel tube and circular tube for inner steel, Also, [19, 54] were used for stiffened square CFST columns. Details of the specimens are presented in Table 1. The first column is the specimen ID and the references between square brackets; other column headings contain Do and to are the column's outer tube width and thickness, respectively, Di and ti are the column's inner tube width and thickness, respectively. fyo, fco', fyi, and fci are the outer steel tube yield strength, outer concrete ring cylinder compressive strength, inner steel tube yield strength and inner concrete core cylinder compressive strength, respectively. Specimens that do not have Di and ti and fyi, and fci' are CFST columns. Nu,test and Nu,FE are the ultimate loads obtained from the test and finite element (FE) model. L is the column's total length. The last column in the table contain cross-section shapes snd stiffeners.

Table 1
Test specimens details used in verification

Speci-mens [ref]	Do (mm)	to (mm)	Di (mm)	Ti (mm)	L (mm)	f_{yo} MPa	f_{co}' MPa	f_{yi} MPa	f_{ci}' MPa	Nu (KN) Test	Nu (KN) FE	Cross-section
SDS1-40a [38]	200	2.01	136.5	1.94	600	230	42.1	492.1	42.1	2450	2414.1	
SDS1-70a [38]	200	2.01	136.5	1.94	600	230	42.1	492.1	69.8	2806	2740.4	
SDS2-40a [38]	200	2.01	114.6	3.93	600	230	42.1	377.1	42.1	2463	2615	
SDS2-70a [38]	200	2.01	114.6	3.93	600	230	42.1	377.1	69.8	2765	2788.8	
SDS3-40a [38]	200	2.01	140.1	3.78	600	230	42.1	322.4	42.1	2505	2588.4	
SDS3-70a [38]	200	2.01	140.1	3.78	600	230	42.1	322.4	69.8	3100	2899.8	
SS-040-050~3 [54]	200	5	-	-	600	265.8	27.15	-	-	2728	2093.2	
SS-040-050~4 [54]	200	5	-	-	600	265.8	27.15	-	-	2903	2090.2	
SS-040-100~4 [54]	200	5	-	-	600	265.8	27.15	-	-	2463	2089.2	
SS-070-093~2 [54]	280	4	-	-	840	272.6	30.49	-	-	3744	3507.8	
SS-070-093-3 [54]	280	4	-	-	840	272.6	30.49	-	-	3855	3652.6	

Speci-mens [ref]	Do (mm)	to (mm)	Di (mm)	Ti (mm)	L (mm)	f_{yo} MPa	f_{co}' MPa	f_{yi} MPa	f_{ci}' MPa	Nu (KN) Test	Nu (KN) FE	Cross-section
SS-070-187-3 [54]	280	4	-	-	840	272.6	29.18	-	-	3457	3381.2	
SCFT 1-1 [19]	200	2.5	-	-	1190	270	49.3	-	-	2640	2398.8	
SCFT 2-1 [19]	200	2.5	-	-	2340	270	49.3	-	-	2455	2381.9	

Fig. 2 shows the comparison the test results and FE model in accordance to axial load and axial strain curve. It can be seen that there is a reasonable correlation between the test results and FE model results. The average value for axial load capacity obtained from the test result to that obtained from the FE model is 1.08 with COV = 0.12.

Fig. 3 shows the comparison between the failure mode obtained from the test and the FE model. All specimens fail due to local buckling of the steel tube. As can be seen from Fig. 3, the FE model tracks a similar failure mode as the test specimens.

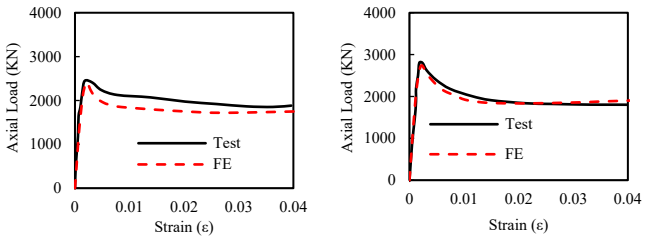

(a) SDS1-40 [38] (b) SDS1-70 [38]

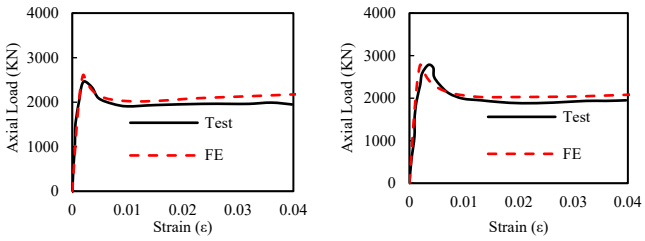

(c) SDS2-40 [38] (d) SDS2-70 [38]

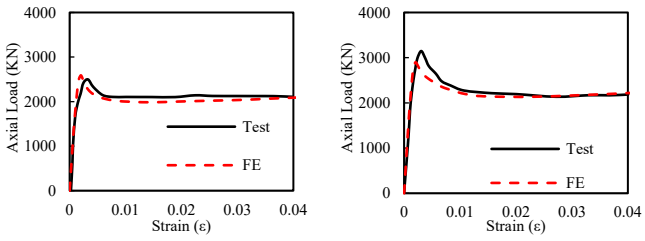

(e) SDS3-40 [38] (f) SDS3-70 [38]

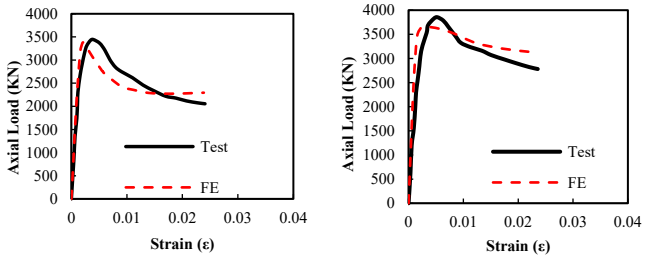

(g) SS-070-187 (3) [50] (h) SS-070-93 (3) [50]

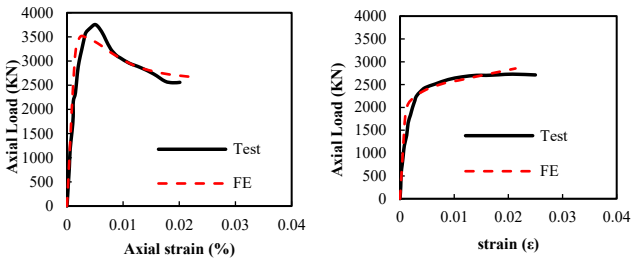

(i) SS-070-93 (2) [50] (j) SS-040-50 (3) [50]

Fig. 2 Comparison between test results and FE model

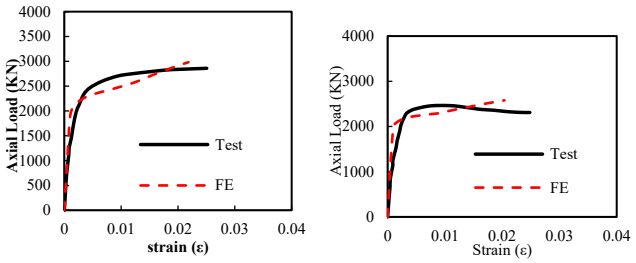

(k) SS-040-50 (4) [50] (l) SS-040-100 (3) [50]

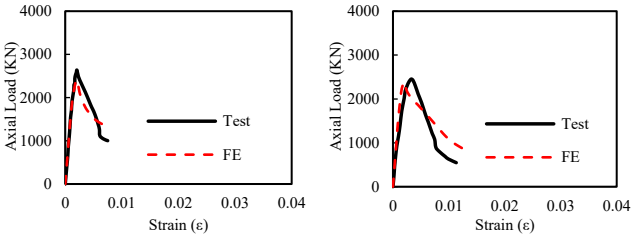

(m) SCFT1-1 [19] (n) SCFT2-1 [19]

Fig. 2 Comparison between test results and FE model (continue)

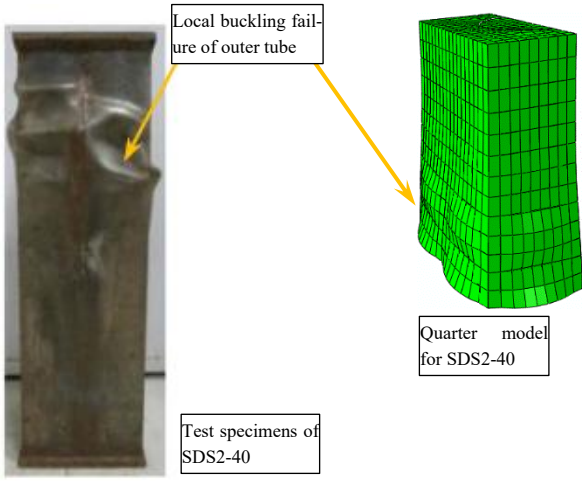

Fig. 3 Failure mode comparison between test specimens SDS2-40 and FE model

3. Analysis of different types of stiffeners

Three types of stiffeners, such as longitudinal rectangular plate (R), inclined plate (Inclined) and ties as shown in Fig. 4, are investigated in this paper. Their effects are compared with the control model with an outer diameter of 500 mm and a length of 8000 mm for slender columns, 1500 mm for stub columns, and 250 mm outer dimension of the inner tube. The D/t ratio is kept constant at 100.

The dimension of the rectangular stiffener was determined according to the research performed by Tao *et al.* [52], with stiffener length equal to 81 and 40.5 mm for outer and inner tube respectively, thickness for stiffener was kept the

same as the steel tube (5 and 2.5 mm for outer and inner tube respectively) .

For Inclined stiffeners the inclined length is equal to 464 and 232 mm attached to outer and inner tube respectively with 5 and 2.5 mm thickness attached to outer and inner tube respectively. No of inclined stiffener per meter is 3 for the outer tube and 6 for the inner tube.

The dimeter of Ties was 18 and 12 mm for outer and inner tube respectively and length of 230 and 115 for outer and inner tube respectively with keeping the number equal to 7 for both tubes.

Tie and inclined stiffeners were determined to maintain the same weight as the rectangular stiffener. This is to ensure that the weight and cost of different stiffening techniques are nearly the same.

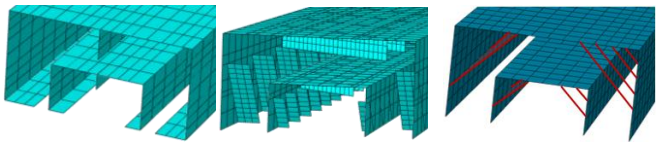

(a) Rectangular (b) Inclined (c) Tie

Fig. 4 Different types of stiffeners used in this study (half column section in abaqus)

It can be seen from Fig. 5 that the three types of stiffeners increase the ultimate load capacity for the columns for slender and stub columns. From the failure mode shown in Fig. 6a, it can be shown the half wavelength of the buckling of the unstiffened column is equal to the column width. For inclined stiffeners (Fig. 6b), the wavelength takes an inclined shape parallel to the inclined stiffeners. From Fig. 6c, half wavelength is equal to half column width as single rectangular stiffeners are placed in the middle of the column cross section, which helped in reducing the wavelength. In case ot Ties half wavelength for buckling is equal to one-third of the column width at the fixation point of ties. This explains the increased ultimate force in stiffened columns compared to unstiffened ones. Tie stiffeners provide less half wave length compared to other stiffners type which will delay local buckling of outer esteel tube providing more ultimate strength using Tie stiffeners.

Fig. 7 shows the contact pressure distribution over the outer and inner concrete core. It can be seen that the pressure in the unstiffened column is concentrated at corners with nearly zero at the middle, which explains the failure mode presented in Fig. 6a. Although contact pressure in stiffened columns has a lower maximum value than that of unstiffened columns, the pressure is distributed over a more concrete surface area than the unstiffened columns. In the case of inclined stiffened, pressure takes an inclined shape similar to the inclined stiffeners.

It can also be seen from Fig. 7 that contact pressure in rectangular stiffeners is concentrated at corners and at the location of rectangular stiffeners. A similar situation is presented in tie stiffeners where maximum pressure is located at corners and at the connection of ties with steel tubes. As a result of more contact pressure in Tie stiffened columns, more confinement pressure is provided to the concrete core (co mpared to other stiffeners) , which helps in increasing the load capacity of the columns, thanks to the tensile force formed in the ties due to the latteral expansion of concrete formed from axial froce. The formed tensile force will prevent outward buckling of steel tube and providing more contact between steel tube and concrete increasing interaction between both material. From the previous discussion, it can be concluded that the improvement in ultimate strength for stiffened columns over unstiffened columns is due to the reduction in steel tube buckling and concrete confinement.

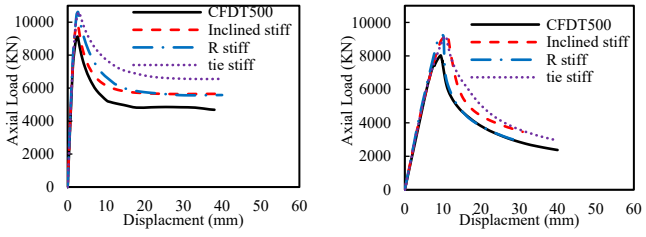

(a) Stub (b) Slender

Fig. 5 Effect of stiffeners on axial displacement curve

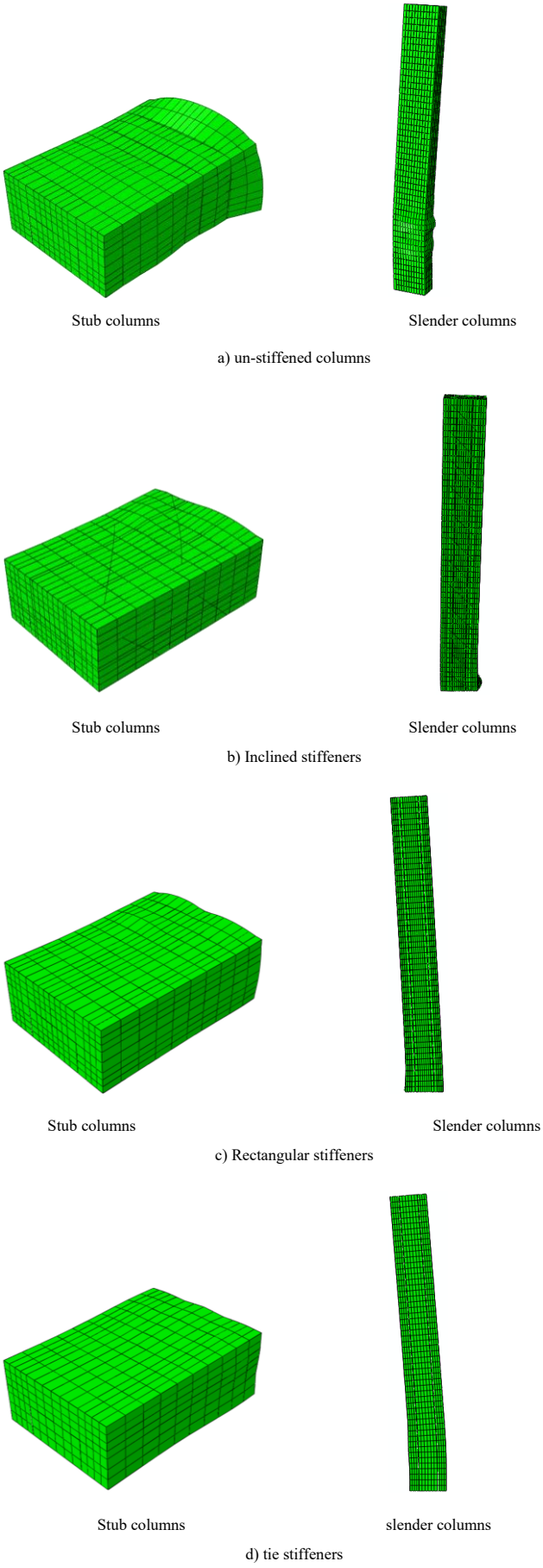

Fig. 6 Failure mode for different types of stiffeners

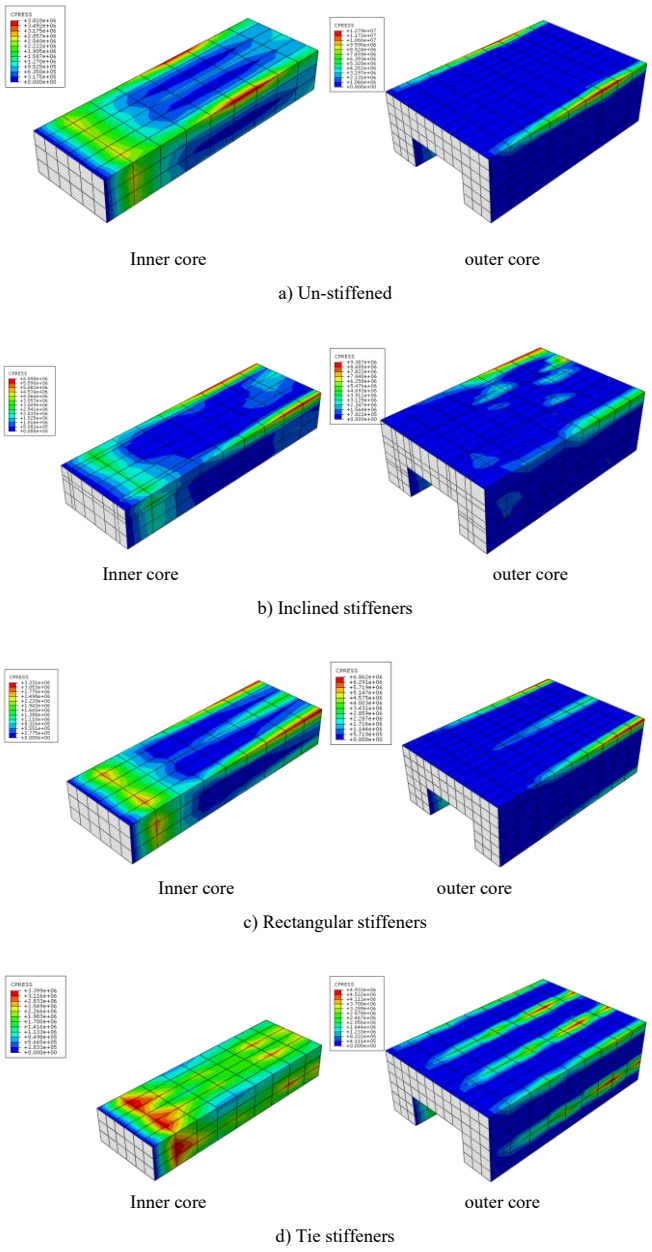

Fig. 7 Contact pressure in different stiffening profile

4. Parametric studies

This section presents a parametric study based on the finite element results. The analysis is performed on unstiffened and different stiffened column profiles (inclined, Rectangular and Tie stiffeners)

4.1. Effect of outer tube width to thickness ratio (Do/to)

Fig. 8 shows the effect of the outer tube width-to-thickness ratio on the ultimate load capacity and column behaviour. It can be seen that column strength and initial stiffness during the elastic zone increase significantly by increasing outer tube thickness as concrete is replaced with steel material since the outer tube dimension is kept constant, besides it decrease the local buckling of the outer tube.

4.2. Effect of inner tube width to thickness ratio (Di/ti)

The effect of the inner tube width-to-thickness ratio on column behaviour is shown in Fig. 9. It is found that the inner tube thickness is less significant than the outer tube thickness due to the larger steel area increase in the outer tube compared to the inner tube. Besides, the inner tube is more restrained against buckling compared to the outer tube as concrete in surrounds the inner tube from the inner and outer sides of the tube, unlike the outer tube where concrete is placed only from the inner side of the tube, providing less restraint to buckling. Increasing the outer tube thickness will have more effect in reducing tube buckling compared to the inner tube.

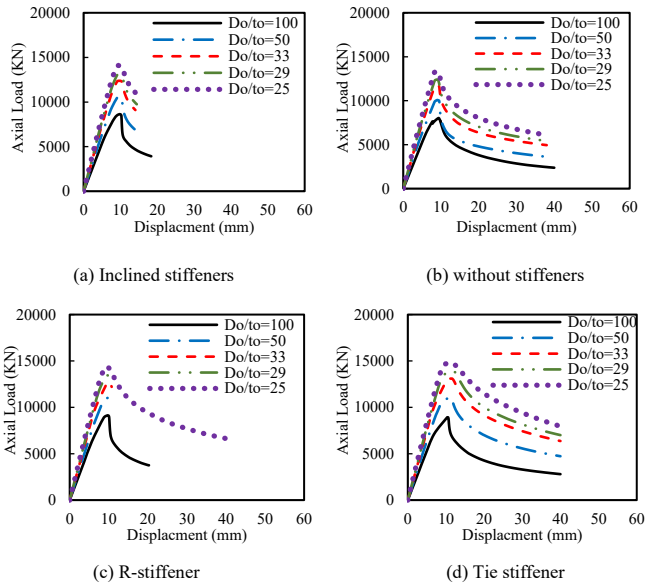

Fig. 8 Effect of outer tube width to thickness ratio (Do/to)

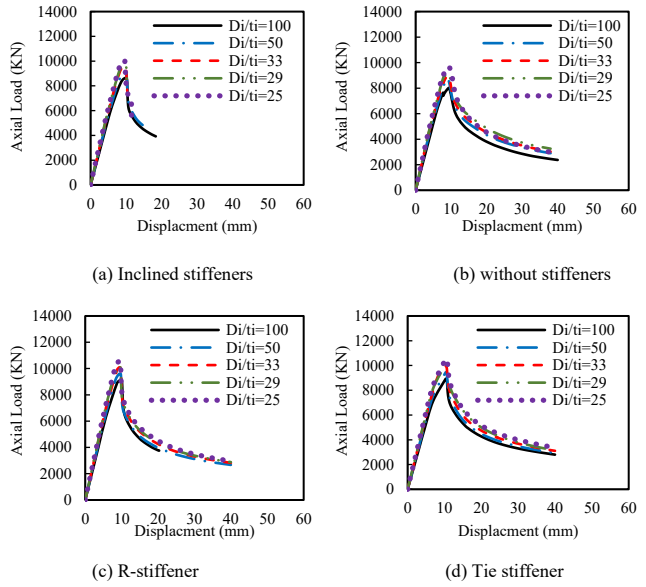

Fig. 9 Effect of inner tube width to thickness ratio (Di/ti)

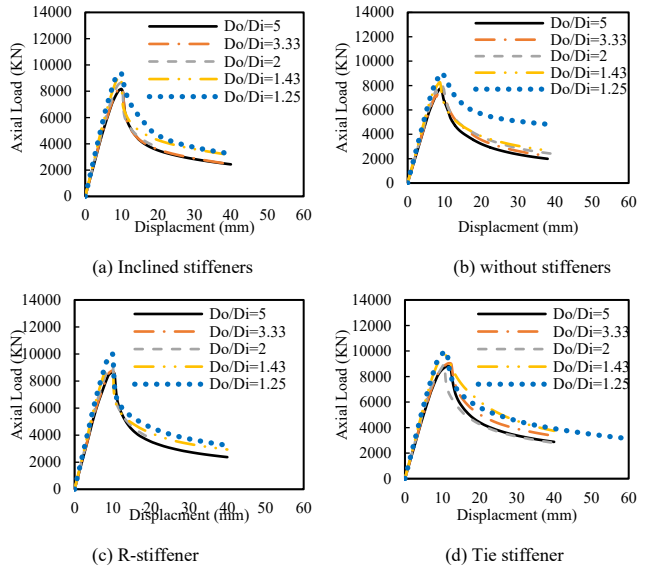

Fig. 10 Effect outer to inner tube width (Do/Di)

4.3. Effect outer to inner tube width (Do/Di)

In this case, the inner tube width is changed, and the outer tube width is kept constant. The effect of outer-to-inner tube diameter on ultimate column strength was not significant compared to the effect of Do/to ratio. The slender columns studied in this paper fail mainly due to a combination of outer tube local buckling and overall global buckling, as indicated previously in Fig. 6. Increasing the inner tube width will have minor effect in increasing column flexural stiffness (EI/L). This case is different from concrete-filled double skin tube columns where inner core is void so in this case increasing and decreasing column width will have a significant effect on column flexural stiffness.

4.4. Effect of concrete compressive strength (fc') and steel tube yield strength (fy)

Concrete strength has a significant effect on the ultimate strength of the CFDT column as the concrete area takes up a large portion of the column cross-section. So, increasing concrete strength will result directly in a significant increase in the column's ultimate strength. This is indicated in Fig. 11. Fig. 12 shows that steel tube yield strength significantly affects column ultimate strength, similar to the case of concrete compressive strength. Increasing yield strength leads to increasing column ultimate strength as a direct result of increasing axial load capacity of steel inner and outer tube. Besides, increasing steel yield strength will help increase the confinement of concrete provided by steel tubes. It can be seen that the effect of concrete strength is more effective compared to increasing column ultimate strength as the cross-sectional area of concrete is larger than that of steel tube.

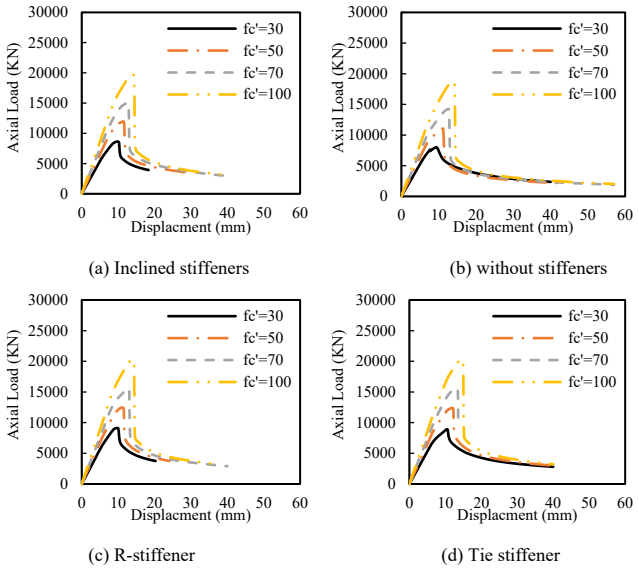

(a) Inclined stiffeners (b) without stiffeners

(c) R-stiffener (d) Tie stiffener

Fig. 11 Effect of concrete compressive strength (fc')

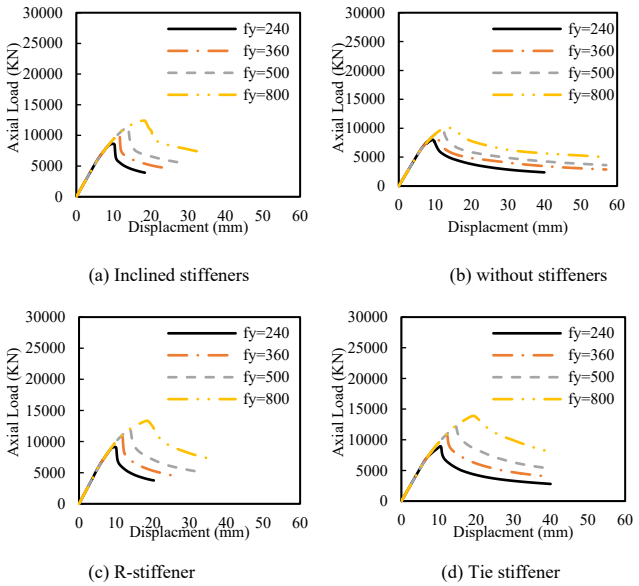

(a) Inclined stiffeners (b) without stiffeners

(c) R-stiffener (d) Tie stiffener

Fig. 12 Effect of steel tube yield strength (*fy*)

4.5. Effect of Slenderness ratio (λ)

Fig. 13 shows the effect of the column slenderness ratio on the column behaviour. It can be concluded that column slenderness has a negative significant effect on column ultimate strength. This is due to the reduction in the flexural stiffness of the column due to the increase in column length and slenderness. Besides, increasing column length will lead to an increase in the second-order effect provided by imperfection, which is taken equal to L/1000.

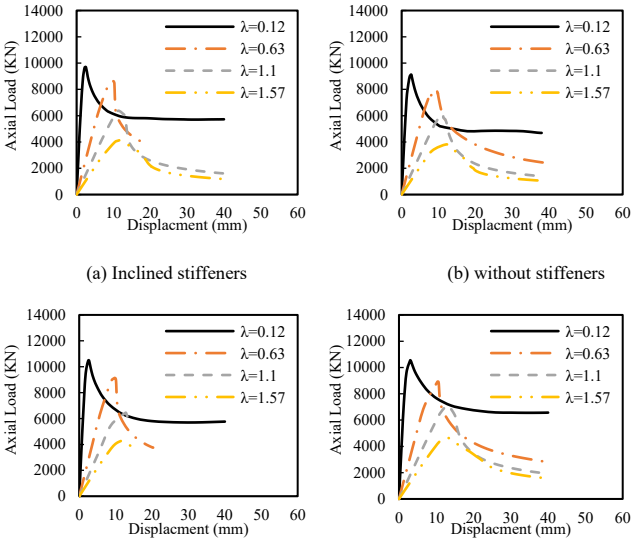

(a) Inclined stiffeners (b) without stiffeners

(c) R-stiffener (d) Tie stiffener

Fig. 13 Effect of Slenderness ratio (λ)

4.6. Effect of different stiffener profiles

From Figs. 8 to 13, it can be concluded that inclined, rectangular and tie stiffeners provided an increase in column ultimate strength with an average value (ultimate strength with stiffeners/ ultimate strength with no stiffeners) of 1.08, 1.14 and 1.15, respectively. This shows that rectangular and tie stiffeners increase ultimate strength the most.

This can be attributed to the profile of each stiffener. In the case of rectangular stiffeners, the local buckling occurred over half the column width due to the presence of stiffeners at the middle of the column width. While in tie stiffeners, buckling occurred at one-third of the tube width at the location of the tie fixation point with the tube, which will provide more contact area with concrete leading to more confinement, as presented in Fig. 7. Meanwhile, in inclined stiffeners, the local buckling occurs at the whole width of the inclined line parallel to the inclined stiffeners, providing the least confinement to concrete.

The ductility of each type of profile was determined according to the ductility index as presented by Tao *et al.* [52], which stated that the ductility index (DI) is equal to $\varepsilon_{(85\%)}/\varepsilon_y$ where $\varepsilon_{(85\%)}$ is the strain when the load fail to 85% of the ultimate load and $\varepsilon_y = \varepsilon_{(75\%)}/0.75$ where $\varepsilon_{(75\%)}$ is the ultimate strain when the load become 75 % of the ultimate load and before it reaches it. The average value of DI in the case of inclined, rectangular and Tie stiffeners is 1.34, 1.32 and 1.46, respectively. This shows that tie stiffeners provide more ductility compared to other stiffener types, owing to the delay in outer tube buckling due to the restraints provided by tie stiffeners to the steel tubes, as shown in Figs. 6 and 7. Further investigation is performed on tie stiffener as it provides the most increase in ultimate load value.

In Fig. 14, two parameters were investigated for tie stiffeners. Fig. 14a studied the effect of tie's diameter on colum behaviour. It was found that the diameter has an insignificant effect on ultimate load value while it provides a significant effect on post-ultimate load behaviour. Increasing ties diameter decreases the post failure deformation of the columns as increasing the tie diameter helps in increasing its axial stiffness, which will provide more restraint to the steel tube against buckling. However, it cannot eliminate buckling. Spacing between ties was investigated in Fig. 14b. It is found that decreasing tie's spacing will help in increasing column ultimate load and improve the post failure behaviour as a result of decreasing the steel tube buckling length in longitudinal direction.

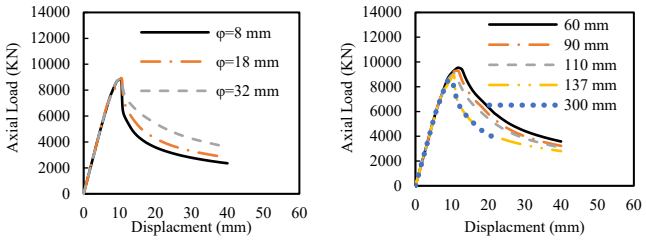

(a) Diameter of tie stiffeners (b) spacing between Tie stiffeners

Fig. 14 Parameters for Tie stiffeners

5. Proposed analytical model

In this section a simplified analytical model based on Eurocode 4 [55] is proposed to predict the ultimate strength of stiffened CFDT column using tie stiffeners. The design of composite columns in Eurocode 4 is applied for CFST column. However, it can be modified to fit CFDT columns as follows:

$$N_{\text{pl,Rd}} = A_{\text{so}} \times f_{\text{yo}} + A_{\text{si}} \times f_{\text{yi}} + A_{\text{co}} \times f'_{\text{co}} + A_{\text{ci}} \times f'_{\text{ci}} \quad (1)$$

Where $N_{\text{pl,Rd}}$ is the load-carrying capacity for the column based on cross-section capacity; A_{so} and A_{si} is the cross-sectional area for the outer and inner steel tube, respectively; $f_{\text{so,y}}$ and $f_{\text{si,y}}$ is the yield strength for the inner and outer steel tube, respectively; A_{co} and A_{ci} is the cross-sectional area of the outer concrete ring and inner concrete core, respectively ; f'_{co} and $f_{\text{ci}}{}'$ is the compressive strength of the outer concrete ring and inner concrete core, respectively.

$$N_{\text{b,Rd}} = \chi N_{\text{pl,Rd}} , \quad (2)$$

Where $N_{\text{b,Rd}}$ is the buckling load capacity for columns.

$$X = \frac{1}{\phi + \sqrt{\phi^2 - \lambda^{\ 2}}} \quad (3)$$

$\phi = 0.5\,(1 + \alpha\,(\lambda - 0.2) + \lambda^{2.4})$, α is the type of buckling curve used in calculation based on section type and equal to 0.21 if reinforcement in the cross-section is less than 3%. 0.34 is used if the reinforcement ratio is more than 3% can be used. In the CFDT columns, the area of the inner steel tube is used as an equivalent to the reinforcement ratio.

$$\lambda = \sqrt{N_{\text{pl,Rd}} / N_{\text{cr}}}$$

$$N_{\text{cr}} = \pi^2\,(E\,I)_{\text{eff}} / l_{\text{b}}^2 \quad (4)$$

$$EI_{\text{eff}} = E_{\text{so}} \times I_{\text{so}} + E_{\text{si}} \times I_{\text{si}} + 0.6\left(E_{\text{co}} \times I_{\text{co}} + E_{\text{ci}} \times I_{\text{ci}}\right) \quad (5)$$

E_{so} and E_{si} are the modulus of elasticity for outer and inner steel tubes, E_{co} and E_{ci} is the modulus of elasticity for outer and inner concrete, respectively concrete, I_{so} and I_{si} are the inertia for outer and inner steel tube, respectively. While I_{co} and I_{ci} are the inertia of outer and inner concrete respectively.

The ultimate load obtained from Eurocode 4 , AISC [56] and AIJ [57] are evaluated against the FE model ultimate load. The result is presented in Fig. 15 and Table 2. It can be seen that Eurocode 4, AISC [56] and AIJ [57] gives conservative results compared to the FE model results, with Eurocode closer to FE results, which mostly lead to an uneconomic design. This conclusion is similar to that obtained from previous researchers [23-25].

A new model is proposed, which predicts the ultimate load capacity of stiffened square CFDT columns using tie stiffeners. The proposed model is based on the Eurocode 4 model for unstiffened CFDT columns, as stated below:

$$N_{\text{pl,Rd}} = \beta_{so} \times A_{\text{so}} \times f_{\text{so,y}} + \beta_{si} \times A_{\text{si}} \times f_{\text{si,y}} + \beta_{co} \times A_{\text{co}} \times f'_{\text{co}} + \beta_{ci} \times A_{\text{ci}} \times f'_{\text{ci}} \quad (6)$$

Where: β_{so}, β_{si}, β_{co}, β_{ci} are the correction factors for outer steel tube, inner steel tube, outer concrete ring and inner concrete core, respectively. These factors consider the delay in local buckling of steel tube and concrete confinement formed due to the presence of tie stiffeners. The correction factors are obtained through nonlinear regression analysis as follows:

$$\beta_{so} = -3.674E^{-4}(b/t)^2 + 0.035(b/t) - 0.0107(S/t) - 3.370X^2 + 3.452X + 7.272E^{-4}\xi^{-2.202} - 0.0667 \quad (7)$$

$$\beta_{co} = 0.00218(b/to) + 4.803E^{-4}(S/t) + 0.0218X^2 - 0.265X + 18.188\xi^{0.00366} - 16.924 \quad (8)$$

$$\beta_{si} = 0.00179(b/to) - 2.299E^{-4}(S/t) - 0.538X^2 + 0.449X + 0.209(fyi/240) + 0.737 \quad (9)$$

$$\beta_{ci} = 0.0117(b/to) + 1.3515E^{-4}(S/t)^2 - 0.0112(S/t) - 0.317X^2 - 0.167X - 0.287\xi^2 + 0.627\xi + 0.986 \quad (10)$$

Where b is the longest unsupported length of outer steel tube width in horizontal direction and it is equal to tube outer width /3 if the ties support the tube at two intermediate points equally spaced, t is the thickness of outer steel tube and "S" is the spacing between tie in longitudinal direction of the columns X is the ratio between outer and concrete core width and equal Di/(Do-2to), fyi is the inner steel tube yield strength (Mpa) and ξ is confinement coefficient and equal to:

$\frac{A_{so} \cdot f_{yo}}{A_{co} \cdot f'_{co}}$.

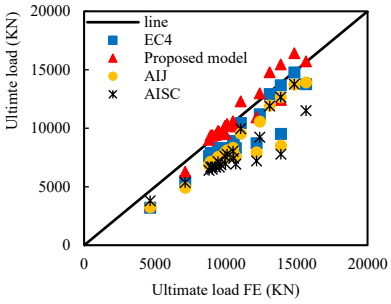

Fig. 15 Evaluation for Eurocode and proposed model

Table 2
Comparison between EC4 and proposed model

	N_ED (EC4)/N_FE	N_ED (AIJ)/N_FE	N_ED (AISC)/N_FE	N_ED(Pro-posed model)/N_FE
Avg	0.846	0.79	0.75	0.999
COV	0.095	0.104	0.118	0.086

The relation between β_{so} , β_{co} , β_{si} and β_{ci} and other significant parameters, such as unsupported steel tube horizontal width to thickness ratio, stiffener longitudinal spacing to tube thickness ratio, outer tube width to inner concrete width ratio, steel tube yield strength, and confinement ratio, are presented in Figs. 16 to 19. In Figs. 16 to 19, the terms $N_{\text{so\_no stiffener}}$, $N_{\text{co\_no stiffener}}$, $N_{\text{si\_no stiffener}}$ and $N_{\text{ci\_no stiffener}}$ are the axial load capacity for outer steel tube, outer concrete ring, inner steel tube and inner concrete core without the effect of any stiffeners respectively. At the same time, N_{so_tie}, $N_{\text{co\_tie}}$, $N_{\text{si\_tie}}$ and $N_{\text{ci\_tie}}$ are the axial load capacity for the outer steel tube, outer concrete ring, inner steel tube and inner concrete core using tie stiffener, respectively. The horizontal axis in these curves represents different parameters effect including unsupported steel tube horizontal width to thickness ratio (b/t), stiffener longitudinal spacing to tube thickness ratio (S/t), outer tube width to inner concrete width ratio (X), steel tube yield strength (f_{yi}/240) and confinement ratio (ξ).

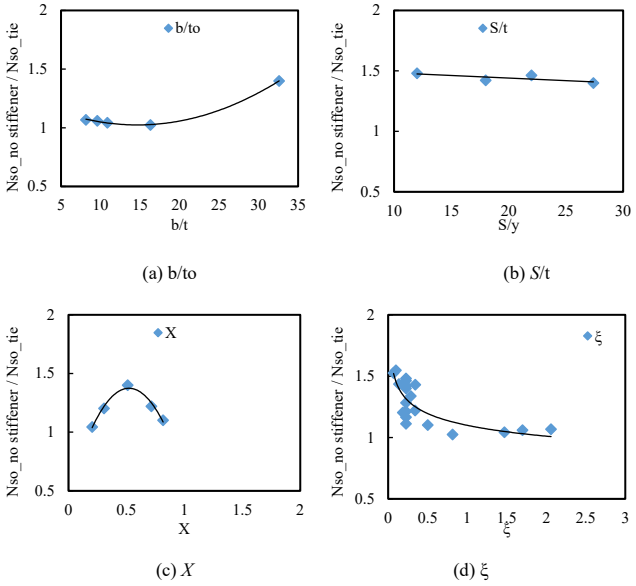

(a) b/to (b) *S*/t

(c) *X* (d) ξ

Fig. 16 Effect of different parameters on βso

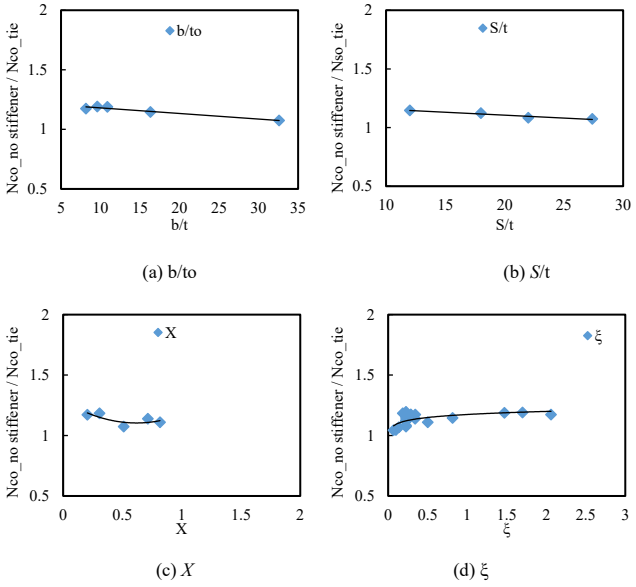

(a) b/to (b) *S*/t

(c) *X* (d) ξ

Fig. 17 Effect of different parameters on βco

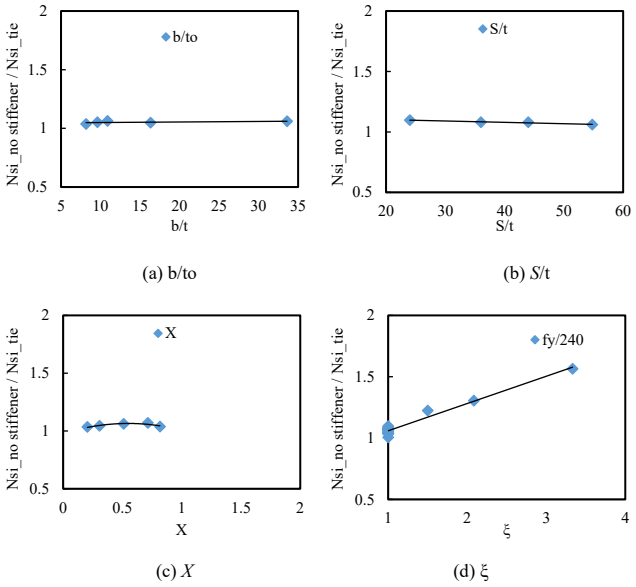

(a) b/to (b) *S*/t

(c) *X* (d) ξ

Fig. 18 Effect of different parameters on βsi

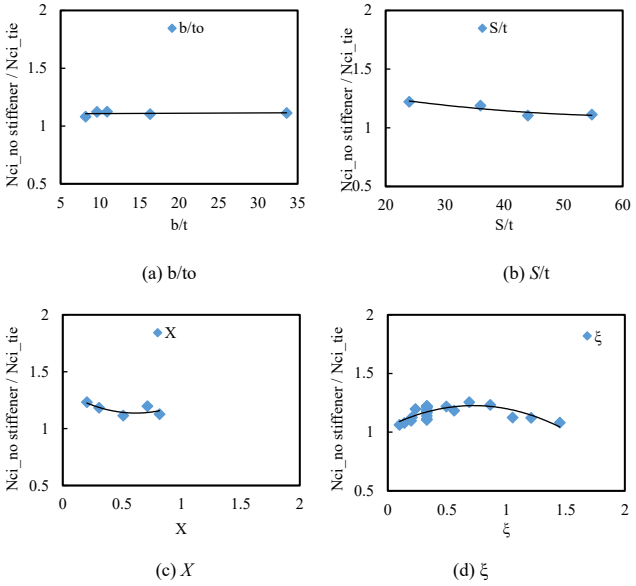

(a) b/to (b) *S*/t

(c) *X* (d) ξ

Fig. 19 Effect of different parameters on βci

The rest of the steps to calculate $N_{b,Rd}$ is similar to Eurocode 4. However, α is equal to 0.13. A comparison between the Eurocode buckling curve and the proposed buckling curve is shown in Fig. 20. The y-axis represents column slenderness (λ), and the x-axis represents the slenderness reduction factor (χ). N_FE represent the axial load of slender columns obtained from finite element (FE), while, Npl_Rd is the plastic resistance for cross-section as indicated in Equation (6), taking into account the effect of tie stiffener. Fig. 15 and Table 2 show the comparison between the proposed model and Eurocode 4, AISC and AIJ model. It can be found that the proposed mode gives better results compared to other standerds in terms of average value (avg) and coefficient of variance (COV) as indicated in Table 2.

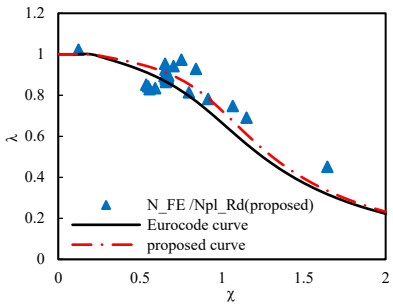

Fig. 20 Comparison between euro code buckling curve and proposed curve

6. Conclusions

This paper presented a numerical study on the behaviour of stiffened square CFDT columns. Three types of stiffeners were studied: inclined, rectangular and Tie stiffeners. A verified FE model was developed in order to give a better understanding for this type of column. The verified FE model was used in providing a parametric study and proposing a simplified analytical model. The following conclusion can be drawn based on the parametric study performed based on the FE model:

- The outer tube width-to-thickness ratio has a significant effect on ultimate strength and initial stiffness. Specifically, a reduction in the outer tube width-to-thickness ratio yields a substantial increase in the column's ultimate strength, dominating the effects of both the inner tube width-to-thickness ratio and the outer-to-inner tube width ratio. Decreasing outer tube width-to-thickness ratio will lead to a decrease in outer tube local buckling and as the outer dimension is kept constant decreasing outer tube width-to-thickness ratio leads to a decrease in concrete area and an increase in steel area, which will increase the capacity of the columns.
- Both the inner tube width-to-thickness ratio and the outer tube width-to-inner width ratio exhibit an inverse relationship with the ultimate compressive strength of the column.
- The use of Tie stiffeners provides a superior performance profile under axial loading, significantly enhancing both the ultimate load capacity and the ductility of the CFDT column. The ultimate load was observed to

increase by over 15% when incorporating Tie stiffeners compared to other configurations. This is due to the lower value of half wave length of the steel tube buckling compared to other stiffeners configurations and the higher confinement provided by the ties stiffeners to concrete thanks to the tensile fore formed in the ties preventing outward buckling of steel tube and providing more contact between steel tube and concrete

- The ultimate load of the CFDT column is inversely proportional to the longitudinal spacing of the Tie stiffeners; closer spacing leads to a higher ultimate capacity
- Increasing the diameter of the Tie stiffeners does not influence the column's ultimate strength; however, it demonstrably improves the structural performance during the post-ultimate load stage (enhancing residual capacity and stability).
- A simplified analytical model was successfully proposed to estimate the ultimate load capacity of CFDT columns utilizing Tie stiffeners. This model, which is fundamentally based on the principles of Eurocode 4, demonstrates strong agreement with the results generated by the detailed FE model.

Data availability

No data was used for the research described in the article

List of abbrevitaions

Symbol	Definition
Aci	the cross-sectional area of inner concrete core
Aco	the cross-sectional area of the outer concrete ring
Asi	the cross-sectional area for the inner steel tube
Aso	the cross-sectional area for the outer steel tube
b	longest unsupported length of outer steel tube width in horizontal direction
Di	column's inner tube width
Do	column's outer tube width
Eci	modulus of elasticity for inner concrete
Eco	modulus of elasticity for outer concrete
Esi	modulus of elasticity for inner steel tubes
Eso	modulus of elasticity for outer steel tubes
fci	inner concrete core cylinder compressive strength
fco’	outer concrete ring cylinder compressive strength
fyi	inner steel tube yield strength
fyo	outer steel tube yield strength
Ici	inertia of inner concrete
Ico	inertia of outer concrete
Isi	inertia for inner steel tube
Iso	inertia for outer steel tube
L	column's total length
Nb,Rd	the buckling load capacity for column
Nci_no stiffener	axial load capacity inner concrete core without using any stiffeners
Nci_tie	axial load capacity inner concrete core using tie stiffener
Nco_no stiffener	axial load capacity for outer concrete ring without using any stiffeners
Nco_tie	axial load capacity for outer concrete ring using tie stiffener
Nsi_no stiffener	axial load capacity for inner steel tube without using any stiffeners
Nsi_tie	axial load capacity for inner steel tube using tie stiffener
Nso_no stiffener	axial load capacity for outer steel tube without using any stiffeners
Nso_tie	axial load capacity for outer steel tube using tie stiffener
Nu,FE	ultimate loads obtained from the Finite elemnt (FE) model
Nu,test	ultimate loads obtained from the test
S	the spacing between tie in longitudinal direction of the columns
ti	column's inner tube thickness
to	column's outer tube thickness
X	ratio between outer and concrete core width and equal Di/(Do-2to)
β_ci	correction factors for inner concrete core
β_co	correction factors for outer concrete ring
β_si	correction factors for inner steel tube
β_so	correction factors for outer steel tube
ξ	confinement coefficient
χ	slenderness reduction factor

References

[1] Romero ML, Espinos A, Portolés JM, Hospitaler A, Ibañez C. Slender double-tube ultra-high strength concrete-filled tubular columns under ambient temperature and fire. Engineering Structures. 2015;99:536-45.

[2] Tao Z, Han L-H, Zhao X-L. Behaviour of concrete-filled double skin (CHS inner and CHS outer) steel tubular stub columns and beam-columns. Journal of Constructional Steel Research. 2004;60:1129-58.

[3] Tao Z, Han L-H. Behaviour of concrete-filled double skin rectangular steel tubular beam–columns. Journal of Constructional Steel Research. 2006;62:631-46.

[4] Han L-H, Huang H, Tao Z, Zhao X-L. Concrete-filled double skin steel tubular (CFDST) beam–columns subjected to cyclic bending. Engineering Structures. 2006;28:1698-714.

[5] Mohan AP, S A. Non-Linear Analysis of Concrete Filled Double Skin Circular Steel Column. International Journal of Engineering Research & Technology (IJERT). 2016;5:204-6.

[6] Elchalakani M, Hassanein MF, Karrech A, Yang B. Experimental investigation of rubberised concrete-filled double skin square tubular columns under axial compression. Engineering Structures. 2018;171:730-46.

[7] Hassanein MF, Elchalakani M, Karrech A, Patel VI, Daher E. Finite element modelling of concrete-filled double-skin short compression members with CHS outer and SHS inner tubes. Marine Structures. 2018;61:85-99.

[8] Zhao X-L, Han L-H. Double skin composite construction. Progress in Structural Engineering and Materials. 2006;8:93-102.

[9] Huang H, Han L-H, Tao Z, Zhao X-L. Analytical behaviour of concrete-filled double skin steel tubular (CFDST) stub columns. Journal of Constructional Steel Research. 2010;66:542-55.

[10] Ekmekyapar T, Al-Eliwi BJM. Concrete filled double circular steel tube (CFDCST) stub columns. Engineering Structures. 2017;135:68-80.

[11] Jin K-Y, Zhou X-H, Wen H, Deng R, Li R-F, Wang Y-H. Compressive behaviour of stiffened thin-walled CFDST columns with large hollow ratio. Journal of Constructional Steel Research. 2023;205:107886.

[12] Li B-F, Wang X-T, Xie C-D, Yan X-F, Wang S. Compressive behaviour and design of tapered lightweight concrete-filled double-skin stiffened steel tubular short columns with large hollow ratio. Structures. 2024;64:106527.

[13] Cai J, He Z-Q. Axial load behavior of square CFT stub column with binding bars. Journal of Constructional Steel Research. 2006;62:472-83.

[14] Younes SM, Ramadan HM, Mourad SA. Stiffening of short small-size circular composite steel–concrete columns with shear connectors. Journal of Advanced Research. 2016;7:525-38.

[15] Lai MH, Ho JCM. Uni-axial Compression Test of Concrete-filled-steel-tube Columns Confined by Tie Bars. Procedia Engineering. 2013;57:662-9.

[16] Huang CS, Yeh Y-K, Liu G-Y, Hu H-T, Tsai KC, Weng YT et al. Axial Load Behavior of Stiffened Concrete-Filled Steel Columns. Journal of Structural Engineering. 2002;128:1222-30.

[17] Tao Z, Han L-H, Wang Z-B. Experimental behaviour of stiffened concrete-filled thin-walled hollow steel structural (HSS) stub columns. Journal of Constructional Steel Research. 2005;61:962-83.

[18] Tao Z, Han L-H, Wang D-Y. Strength and ductility of stiffened thin-walled hollow steel structural stub columns filled with concrete. Thin-Walled Structures. 2008;46:1113-28.

[19] Tao Z, Han L-H, Wang D-Y. Experimental behaviour of concrete-filled stiffened thin-walled steel tubular columns. Thin-Walled Structures. 2007;45:517-27.

[20] Alatshan F, Osman SA, Hamid R, Mashiri F. Stiffened concrete-filled steel tubes: A systematic review. Thin-Walled Structures. 2020;148:106590.

[21] Zheng M, Nie X, Ding R. Experimental and numerical research on the uniaxial behavior of the stiffened circular concrete-filled steel tube stub columns. Engineering Structures. 2024;306:117785.

[22] Singh H, Tiwary AK, Eldin SM, Ilyas RA. Behavior of stiffened concrete-filled steel tube columns infilled with nanomaterial-based concrete subjected to axial compression. Journal of Materials Research and Technology. 2023;24:9580-93.

[23] Zhou Z, Denavit MD, Zhou X. New cross-sectional slenderness limits for stiffened rectangular concrete-filled steel tubes. Engineering Structures. 2023;280:115689.

[24] Hassanein MF, Huang W-F, Shao Y-B, Cashell KA, Elsisy AR. Confinement-based design and behaviour of concrete-filled stiffened steel tubular square slender columns. Ocean Engineering. 2024;304:117845.

[25] Huang W-F, Shao Y-B, Hassanein MF, Hadzima-Nyarko M, Radu D, Cashell KA. Experimental and numerical investigation of square concrete-filled double-skin steel stiffened tubular stub columns with CHS inner tubes under axial compression. Thin-Walled Structures. 2024;199:111792.

[26] Zhou Z, Zhou X, Gan D, Liu Y. Comparison and design of stiffened rectangular concrete-filled steel tubular members. Journal of Constructional Steel Research. 2023;208:108037.

[27] Peng K, Yu T, Hadi MNS, Huang L. Compressive behavior of hybrid double-skin tubular columns with a rib-stiffened steel inner tube. Composite Structures. 2018;204:634-44.

[28] Zakir M, Sofi FA, Naqash JA. Experimentally verified behavior and confinement model for concrete in circular stiffened FRP-concrete-steel double-skin tubular columns. Structures. 2021;33:1144-57.

[29] Zakir M, Sofi FA, Naqash JA. Compressive testing and finite element analysis-based confined concrete model for stiffened square FRP-concrete-steel double-skin tubular columns. Journal of Building Engineering. 2021;44:103267.

[30] Zeng J-J, Liang S-D, Zhuge Y, Zhou J-K, Liao J. Seismic behavior of FRP-concrete-steel double skin tubular columns with a rib-stiffened Q690 steel tube and high-strength concrete.

Thin-Walled Structures. 2022;175:109127.
[31] Zeng J-J, Zheng Y-Z, Long Y-L. Axial compressive behavior of FRP-concrete-steel double skin tubular columns with a rib-stiffened Q690 steel tube and ultra-high strength concrete. Composite Structures. 2021;268:113912.
[32] Yu T, Teng JG, Wong YL. Stress-Strain Behavior of Concrete in Hybrid FRP-Concrete-Steel Double-Skin Tubular Columns. Journal of Structural Engineering. 2010;136:379-89.
[33] Ding F, Lu D, Lai Z, Liu X. Study on restraint coefficient of the stirrups-stiffened square concrete filled double-skin steel tube axial compression stub columns. Structures. 2024;60:105847.
[34] Zhang J-H, Hassanein MF, Cashell KA, Hadzima-Nyarko M, Xu Y, Shao Y-B. Experimental and numerical investigation on the behaviour of square concrete-filled cold-formed double-skin steel stiffened tubular short columns. Engineering Structures. 2024;303:117560.
[35] Zhang J-H, Shao Y-B, Hassanein MF, Cashell KA, Hadzima-Nyarko M. Behaviour of ultra-high strength concrete-filled dual-stiffened steel tubular slender columns. Engineering Structures. 2024;300:117204.
[36] Zhang J-H, Shao Y-B, Hassanein MF, Patel VI. Axial compressive performance of ultra-high strength concrete-filled dual steel tubular short columns with outer stiffened tubes and inner circular tubes. Journal of Constructional Steel Research. 2023;203:107848.
[37] Zhang J-H, Shao Y-B, Hassanein MF, Cashell KA, Hadzima-Nyarko M. Behaviour of cold-formed concrete-filled dual steel stiffened tubular short columns. Journal of Constructional Steel Research. 2024;213:108381.
[38] Wang Z-B, Tao Z, Yu Q. Axial compressive behaviour of concrete-filled double-tube stub columns with stiffeners. Thin-Walled Structures. 2017;120:91-104.
[39] Ghannam M, Metwally IM. Numerical investigation for the behaviour of stiffened circular concrete filled double tube columns. Structures. 2020;25:901-19.
[40] Wang Z-B, Zhang J-B, Li W, Wu H-J. Seismic performance of stiffened concrete-filled double skin steel tubes. Journal of Constructional Steel Research. 2020;169:106020.
[41] Hasan HG, Ekmekyapar T. Mechanical Performance of Stiffened Concrete Filled Double Skin Steel Tubular Stub Columns under Axial Compression. KSCE Journal of Civil Engineering. 2019;23:2281-92.
[42] Shekastehband B, Taromi A, Abedi K. Fire performance of stiffened concrete filled double skin steel tubular columns. Fire Safety Journal. 2017;88:13-25.
[43] Ghannam M, Song TY. Fire Resistance Design of Concrete-Filled Steel Tube Stub Columns. Fire Technology. 2021;57:911-42.
[44] Benzaid R, Mesbah HA. Circular and Square Concrete Columns Externally Confined by CFRP Composite: Experimental Investigation and Effective Strength Models. In: Intech, editor. Fiber Reinforced Polymers - The Technology Applied for Concrete Repair: INTECH; 2013. p. 167-201.
[45] Song X, Gu X, Li Y, Chen T, Zhang W. Mechanical Behavior of FRP-Strengthened Concrete Columns Subjected to Concentric and Eccentric Compression Loading. Journal of Composites for Construction. 2013;17:336-46.
[46] Campione G, Miraglia N, Papia M. Strength and strain enhancements of concrete columns confined with FRP sheets. Structural Engineering and Mechanics. 2004;18.
[47] Tabsh SW. Stress-Strain Model for High-Strength Concrete Confined by Welded Wire Fabric. Journal of Materials in Civil Engineering. 2007;19:286-94.
[48] ABAQUS. ABAQUS standard user's manual, Version 6.12. USA: Dassault Systèmes Corp., Providence, RI; 2012.
[49] Tao Z, Wang Z-B, Yu Q. Finite element modelling of concrete-filled steel stub columns under axial compression. Journal of Constructional Steel Research. 2013;89:121-31.
[50] Gardner L, Nethercot DA. Numerical Modeling of Stainless Steel Structural Components—A Consistent Approach. Journal of Structural Engineering. 2004;130:1586-601.
[51] Ellobody E, Young B. Structural performance of cold-formed high strength stainless steel columns. Journal of Constructional Steel Research. 2005;61:1631-49.
[52] Tao Z, Uy B, Han L-H, Wang Z-B. Analysis and design of concrete-filled stiffened thin-walled steel tubular columns under axial compression. Thin-Walled Structures. 2009;47:1544-56.
[53] Ayough P. Experimental and Numerical Investigations of the Compressive Behavior of Concrete-Filled Steel Tubular Columns [Ph.D.]. Malaysia: University of Malaya (Malaysia); 2022.
[54] Huang CS, Yeh YK, Liu GY, Hu HT, Tsai KC, Weng YT et al. Axial Load Behavior of Stiffened Concrete-Filled Steel Columns. Journal of Structural Engineering. 2002;128:1222-30.
[55] Eurocode-4_part1.1. Design of composite steel and concrete structures, Part 1-1: General rules and rules for buildings. London: BS EN 1994-1-1:2004. British Standards Institution; 2005.
[56] AISC-360-22. American Institute of Steel Construction: Specification for Structural Steel Buildings. 2022.
[57] AIJ. Architectural Institute of Japan (AIJ) Standard for Structural Calculation of Steel Reinforced Concrete Structures, 5th Ed. 2001.

Advanced Steel Construction – Vol. 22 No. 2 (2026) 208–221
DOI:10.18057/IJASC.2026.22.2.7

EXPERIMENTAL STUDY ON SEISMIC BEHAVIOR OF DOUBLE-SKIN COMPOSITE WALL WITH REBAR TRUSSES

Li-Ping Zhang [1, 4], Yan-Sheng Huang [1], Chun Yang [1, *], Chi-Yu Luo [2], Xing-Long Luo [3], Bing-Qiang Sui [3] and Jian Cai [1]

[1] *South China University of Technology, Guangzhou, 510641, China*
[2] *Guang Dong Architectural Design and Research Institute Corporation Limted, Guangzhou, 510010, China*
[3] *MCC Shanghai Steel Structure Technology Corporation Limted, Shanghai 201908, China*
[4] *CCCC-FHDI Engineering Corporation Limted, Guangzhou 510000，China*
** (Corresponding author: E-mail: 13392631280@189.cn)*

ABSTRACT

This paper introduces a novel double-skin composite wall (DSCW) system reinforced with horizontal rebar trusses. The seismic performance of five double-skin composite wall specimens with rebar trusses and one specimen without rebar trusses was investigated under low cyclic lateral loading. The test results demonstrate that all specimens reached a flexure-dominated ultimate state, accompanied by local buckling of the faceplates in the shear wall and the boundary columns of the concrete-filled steel tube (CFST). The five specimens reinforced with rebar trusses exhibited excellent ductile behavior, with ductility coefficients ranging from 1.86 to 2.78. Comparative analysis among the specimens revealed that the inclusion of rebar trusses effectively stabilized the faceplates and improved the overall performance of the composite walls. Closer spacing of the rebar trusses, such as 100 mm, proved to be more effective. Specimens with vertical and horizontal rebar trusses demonstrated similar peak load capacities; however, the specimen with vertical rebar trusses achieved a 6.0% higher ductility coefficient, indicating improved deformation capacity. Furthermore, the use of a discontinuous inner steel plate in the CFST boundary column was found to reduce both lateral load-carrying capacity and ductility, rendering it an unsuitable design choice for this system.

ARTICLE HISTORY

Received: 22 February 2025
Revised: 16 July 2025
Accepted: 18 July 2025

KEYWORDS

Double-skin steel-concrete composite wall;
Rebar trusses;
Quasi-static test;
Seismic performance

1. Introduction

The shear wall is a critical load-bearing and lateral force-resisting component in high-rise buildings. Existing prefabricated shear walls primarily include precast reinforced concrete walls, precast double-superimposed walls, pure steel plate walls, and double-skin steel-concrete composite walls. Precast reinforced concrete shear walls are heavy and challenging to install [1]. Precast double-superimposed walls have certain drawbacks, such as complex splicing construction, high installation precision requirements, and low reliability [2–5]. Pure steel plate walls, while effective for lateral resistance, have limited vertical load-carrying capacity [6]. As a novel type of composite component, the double-skin steel-concrete composite wall (DSCW) consists of concrete filled between two steel faceplates, which are connected by shear connectors. The steel plates and concrete work together compatibly throughout the entire loading process, significantly enhancing the wall's compressive, tensile, and shear capacities, as well as its energy dissipation performance.

In the 1980s, PF Adams, Hassinen, and Stephen [7–9] initiated research on DSCWs. Their studies primarily focused on the performance and failure mechanisms of DSCWs under the impact of ice and sea waves, demonstrating that DSCWs provide high strength and ductility when subjected to out-of-plane loads. Wright et al. [10–12] investigated the axial compression and shear performance of DSCWs with profiled steel sheeting and developed design formulas for shear strength and stiffness. Link [13] employed a nonlinear finite element method to study the ultimate bearing capacity and post-peak behavior of DSCWs under transverse and longitudinal loads. Emori [14] conducted experimental research on concrete-filled steel box walls under compressive and shear loading. The results revealed that the wall elements exhibited both high strength and excellent ductility. Nie et al. [15–17] designed a series of DSCW test specimens equipped with studs and load-bearing steel bars, with axial compression ratios ranging from 0.15 to 0.4. The test results showed that the average ultimate displacement angle of the walls was 1.7%, and the average ductility coefficient was 3.2. In further research, Nie [18] designed another set of DSCW test specimens with short stiffeners and studs, with a higher axial compression ratio of 0.5. The results indicated that the average ultimate lateral displacement angle of these walls was 1.6%.

To further improve buckling capacity of the DSCWs, experimental researches on DSCW strengthened with batten plate [19-20], tie rod [21-24], steel tube bundles [25-26], corrugated plates[27] and hybrid connectors [28] were conducted, test results concluded that the specimens had good ductility and energy dissipation capacity, and the hysteretic curves were full and stable.

While Shi et al. [29] adopted vertical rebar trusses to stabilize the steel faceplate of DSCW, experimental results found that reducing the welding spot spacing-to-thickness ratio and opening slits on the steel plate could increase the buckling capacity of the DSCW. Han et al. [30] also investigated the seismic behavior of DSCW stiffened with vertical steel truss, and found that aspect ratio had the greatest impact on the failure mode and seismic performance of the specimen, while the axial compression ratio had little impact on the strength. The ductility and energy consumption of specimens with small axial compression ratios are good, however. The larger the spacing of the steel truss, the weaker the out of plane constraint on the steel plate, and the earlier the appearance of the specimen's buckling and failure.

Further parametic studies were carried out to investigate key parameters that affected the seismic performances of DSCW. Wei et al. [31] established the finite element model of DSCW and presented the effects of key parameters including the space of stud connectors, the thickness of both the steel plate and concrete core, the concrete strength, and the span-depth ratio of walls on the shear resistance of the walls. Results indicated that the thickness of both the steel plate and the concrete core, and the strength of concrete are the most critical factors affecting the shear resistance of the walls, and the spacing of stud connectors affects the failure mode of the walls. The influence of various parameters on the hysteretic behavior of the DSCW was studied by Luo et al. [32] through numerical analysis. Numerical evaluation reveals a substantive impact exerted by all three parameters upon the mechanical attributes of the wall. Of particular note, the axial compression ratio emerges as the predominant determinant influencing the wall's loading capacity, framed within this context. Furthermore, it becomes evident that the aspect ratio, characterized by its considerable elongation relative to width, coupled with the ratio of width-to-thickness, manifests as pivotal determinants dictating the initial stiffness attributable to the wall structure.

The studies mentioned above have significantly contributed to the advancement of the mechanical behavior and design theory of the DSCW structure. However, the structural forms of the wall studied are complex, and the construction process needs to be improved. The welding workload of steel plate wall in the form of batten plate is large, the welding deformation of thin steel plate is easy to form and difficult to rectify, the batten plate is limited by the width-thickness ratio of steel plate and the welding operation, the vertical joint should be added for long steel plate wall, which further increase the welding workload and the difficulty of correction. The requirement for reserve holes on the steel plate of the wall in the form of a restraining rod weakens the steel plate section. Additionally, additional stiffness strengthening measures are required to meet the deformation and site alignment requirements during the transportation and hoisting of high flexible steel plate walls, which is challenging to do during the actual construction of high-rise buildings. While the DSCW reinforced with vertical rebar trusses avoids some defects above, it provides weak transverse stiffness during construction.

Inspired by various designs of DSCW, this study proposes a novel DSCW system reinforced with horizontal rebar trusses. The proposed DSCW consists of concrete-filled square steel tubes (CFSTs) and a concrete-filled steel plate shear wall body, reinforced with horizontal rebar trusses, as illustrated in Fig. 1. Previous research [33] has shown that CFSTs significantly enhance the in-plane flexural capacity and out-of-plane flexural rigidity of walls, enabling them to meet maximum compressive demands more effectively.

The shear wall web is composed of concrete, rebar trusses, and two steel faceplates welded to the CFST. Each rebar truss comprises one longitudinal bar (acting as the chord member) and diagonal bars. The diagonal bars are spot-welded to the steel faceplates. Under compression, the synergy between the diagonal bars, chord bar, and steel faceplates effectively constrains the infilled concrete, while also stabilizing the steel faceplates during transportation and hoisting. Before the infilled concrete sets, the horizontal rebar trusses enhance the wall's out-of-plane flexural capacity and rigidity. In addition to improving rigidity, the horizontal rebar trusses, in conjunction with the steel faceplates, serve as the primary shear reinforcement to resist in-plane shear forces. They also act as formwork, enabling convenient and rapid construction without the need for additional construction aids. Furthermore, the rebar trusses are arranged separately, meaning they are independently welded to the steel faceplates. This eliminates the need for welding in enclosed spaces during the production of the steel plate wall, facilitating factory-based manufacturing of the composite wall.

Experimental research on the mechanical properties of six DSCW specimens with fixed axial compression ratio and span ratio under low cycle reciprocating loads was conducted in this paper. The key parameters considered include the spacing and direction of the steel truss, as well as the continuity of the steel plates in the shear wall adjacent to the CFST. The influence of each parameter on the seismic performance of the new composite wall, such as bearing capacity, ductility, stiffness and strength degradation, and energy dissipation capacity, was studied.

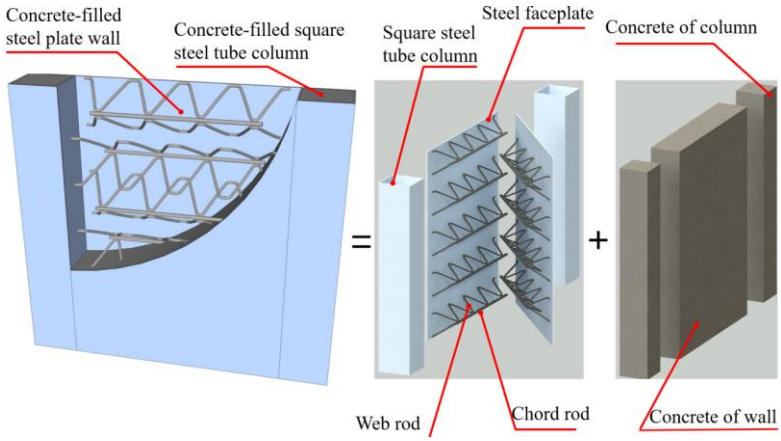

Fig. 1 Proposed DSCW with horizontal rebar trusses

2. Experimental program

2.1. Test specimens

Six specimens were designed and constructed for this study, including five DSCWs with rebar trusses and one DSCW without rebar trusses for comparison. The DSCWs with rebar trusses consisted of concrete-filled square steel tubes (CFSTs) and a concrete-filled steel plate wall body reinforced with separately arranged rebar trusses. To ensure direct comparison, all specimens had identical dimensions, with a net height of 1300 mm, a width of 650 mm, and a thickness of 100 mm. The specimens were embedded into rigid foundation beams and caps at both ends. The square steel tubes had a wall thickness of 4 mm, while the steel faceplates of the shear wall were 3 mm thick. The diameters of the web and chord bars in the rebar trusses were 6 mm and 8 mm, respectively. Notably, no additional shear connectors were incorporated into the DSCW specimens.

Two key parameters were investigated in this study. First, the spacing of the rebar trusses was identified as a critical factor influencing the bearing capacity and failure mode, particularly the local buckling behavior. Second, the orientation of the rebar trusses, whether embedded horizontally or longitudinally in the shear wall, was examined for its impact on the flexural and shear capacity as well as the rigidity of the wall.

Additionally, a trial parameter was introduced to explore construction feasibility. Since the CFST serves as the edge component, welding the inner steel plate of the square steel tube becomes challenging when connecting walls between floors. To address this issue, one specimen was designed with a discontinuous inner steel plate in the CFST, achieved by cutting the inner steel plate below the top of the beam. This modification was a preliminary attempt to determine whether this structural form could be viable for practical applications.

To isolate the effects of the aforementioned parameters on the mechanical behavior of the specimens, other key factors, such as the axial compression ratio and the height-to-width ratio, were held constant. In this study, the height-to-width ratio of all specimens was set to 2.0 to ensure the preferred flexural limit state [34], while the axial compression ratio was maintained at 0.40, consistent with values commonly used in engineering applications. Future experimental studies will further explore the effects of axial compression ratio and height-to-width ratio on the mechanical behavior of the newly designed DSCWs.

The structural details of all specimens are shown in Table 1 and Fig. 2. The axial compression ratio of the specimen was calculated using Eq. (1) as below:

$$n_t = N/(f_{ck}A_c + f_yA_a) \quad (1)$$

where n_t is the test axial compression ratio applied to the specimen, N is the test value of axial compression, f_{ck} is the material compressive strength of concrete infill, f_y is the yield strength of steel faceplate and steel tubes, A_c is the area of concrete wall, A_a is the sum of cross-sectional areas of steel tube and steel plate.

Table 1
Demensions and configurations of six test specimens

Specimen	$H \times h_w \times b_w$/mm	n_t	λ	Rebar trusses		Continuity of the CFST inner steel plate
				Spacing/mm	Direction	
SCW-1	1300x650x100	0.40	2.0	(without rebar trusses)		Continuous
SCW-2	1300x650x100	0.40	2.0	100	Horizontal	Continuous
SCW-3	1300x650x100	0.40	2.0	140	Horizontal	Continuous
SCW-4	1300x650x100	0.40	2.0	200	Horizontal	Continuous
SCW-5	1300x650x100	0.40	2.0	100	Vertically	Continuous
SCW-6	1300x650x100	0.40	2.0	100	Horizontal	Discontinuity

Note: H is the height from the loading point to the bottom of the wall, h_W and b_W are the height and thickness of the cross section respectively, n_t is the test axial compression ratio, and λ is the aspect ratio.

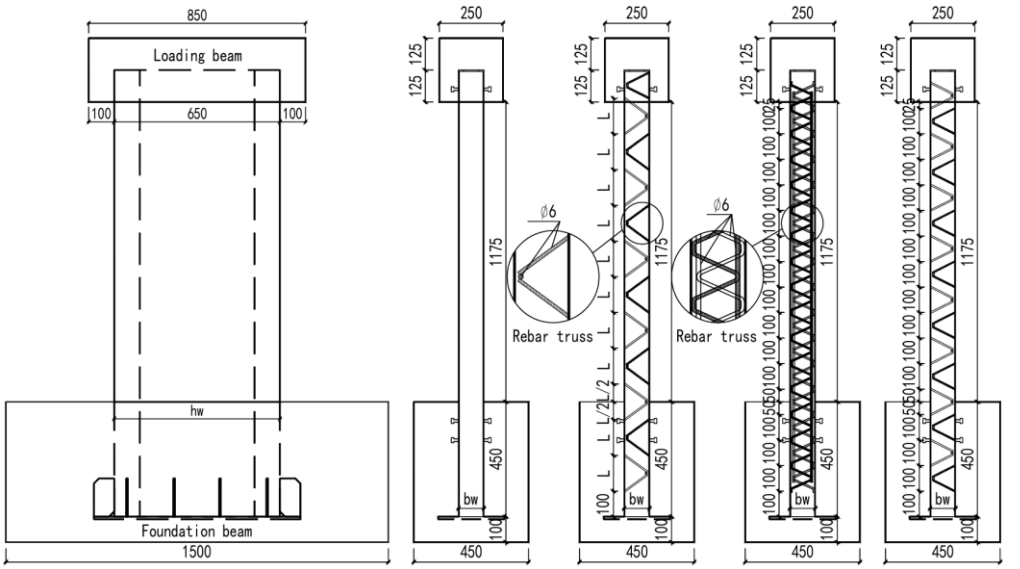

Fig. 2 Layout of the test specimens (mm)

The material properties of the steel plates and rebars were determined through monotonic tensile tests conducted on standard coupons. The measured values are summarized in Table 2. All specimens were cast using the same batch of concrete, and the average compressive strength of the concrete, measured using standard cube specimens (150 mm × 150 mm × 150 mm), was 55.35 MPa.

Table 2
Material properties of steel plate and steel bar

Material type	f_y/MPa	f_u/MPa	E_s/GPa
Steel plate	366.50	468.00	196.91
Steel bar	404.11	470.74	242.09

2.2. Test setup and loading protocol

The test was carried out in the structural laboratory of State Key Laboratory of Subtropical Building Science, South China University of Technology. All specimens were tested as walls with the fixed-end condition using the test setup shown in Fig.3. As illustrated, a concrete loading beam with a section of 250 x 250 mm was set on the top of the specimen. The bottom of each specimen was fixed to a foundation beam. The rigid foundation beam was poured at the bottom of the specimen to ensure that the bottom of the wall met the boundary conditions of fixed constraints. Both ends of the foundation beam were fixed on a rigid base plate with ground anchor bolts, and horizontal jacks were set at both ends of the foundation beam to prevent horizontal sliding of the foundation beam during loading. The horizontal reciprocating load was applied by a 1000 kN MTS hydraulic servo actuator connected to a rigid loading beam, and they were loaded at the center of the loading beam. The actuator and the loading beam were fixed by the loading head, and the rear end of the actuator was fixed to the reaction wall.

The vertical load was applied by a vertical inverted hydraulic jack, a sliding support was installed between the jack and the reaction frame to ensure that the loading point of the vertical load was always along the centerline of the wall, and to synchronize with the deformation of the specimen during loading process. A steel beam was set between the vertical jack and specimen to evenly apply vertical load on the wall. During the test, lateral support was set outside the plane of the specimen to avoid instability outside the plane. The device was a rigid beam with horizontal sliding bearing, which was fixed on the reaction base plate by rigid support to achieve in-plane working conditions of the specimens.

During the experiment, the vertical load was constant, and the MTS hydraulic servo actuator was used to apply the horizontal cycling load. The drift angle of the wall was considered as the control value during the entire loading process. At the beginning of loading, the displacement scheme was cycled only once until the steel plate at the bottom of CFST yielded, then the lateral displacement was imposed on the specimens with three cycles of loading at each step. The loading history is shown in Fig. 4. The test terminated when the specimen could not maintain the applied axial load or the horizontal peak load degraded 15% or more.

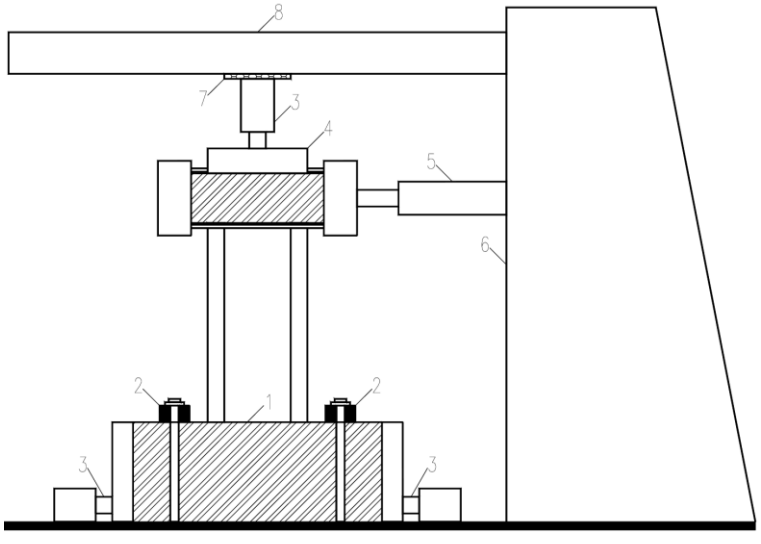

1. Foundation beam; 2. Beam; 3. Jack; 4. Distribution beam; 5. Actuator; 6. Reaction wall; 7. Sliding support; 8. Reaction frame
(a) Sketch of test setup

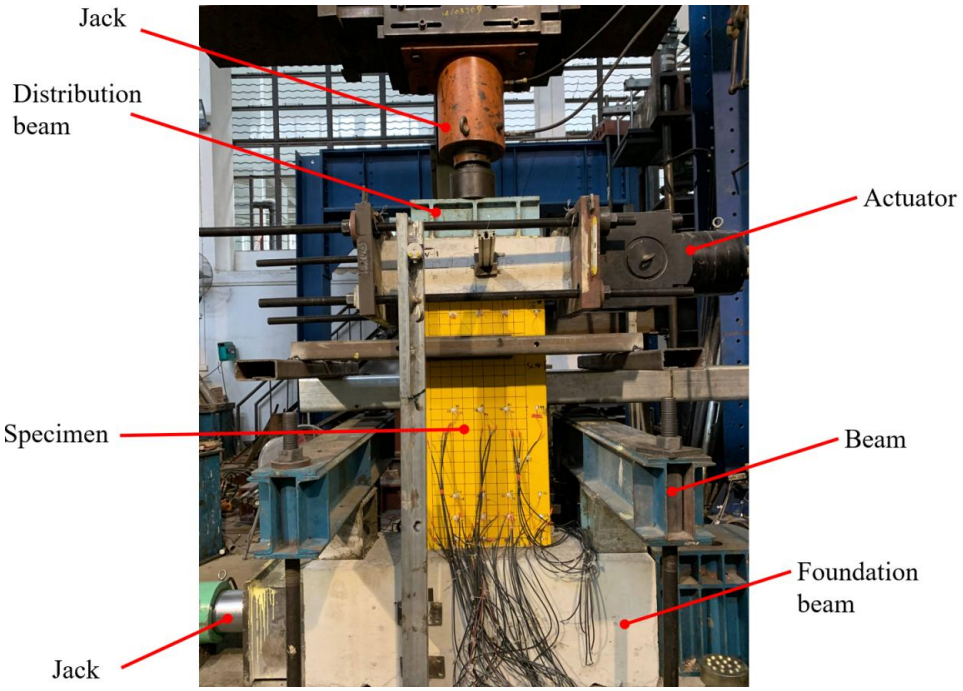

(b) Test setup in SCUT's lab

Fig. 3 Test setup

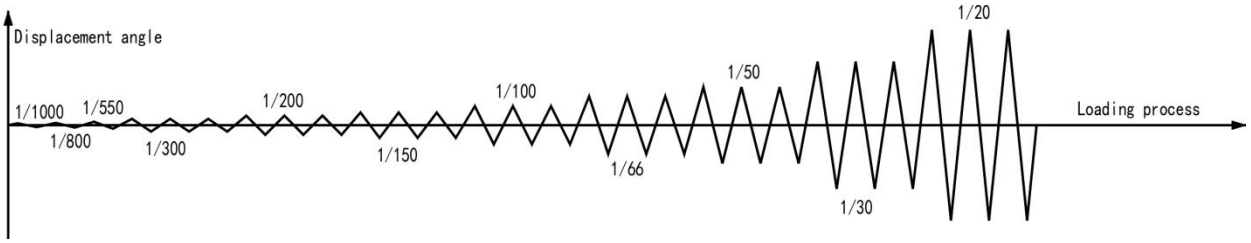

Fig. 4 Loading protocol

The experimental test setup used in this study is illustrated in Fig. 3, consisting of eight key components: the foundation beam, steel beam, test specimen, jack, distribution beam, actuator, reaction wall, sliding support, and reaction frame. The foundation beam and reaction frame were designed to provide a rigid base and structural support for the test specimens, while the jack and actuator applied lateral loading to simulate in-plane forces. The distribution beam ensured uniform load transfer to the specimen, and a sliding support was incorporated to allow for controlled movement during testing. The entire setup was constructed in SCUT's laboratory, as shown in Fig. 3(b), to facilitate accurate measurement of the mechanical behavior of the shear wall specimens under cyclic loading conditions. The corresponding loading protocol is depicted in Fig. 4.

2.3. Measurement method

Five displacement meters and fifty-three strain gauges were employed to record the displacement and strain responses of each specimen. The horizontal load was automatically measured using the MTS servo-hydraulic actuator's built-in measuring system. Displacement meters No. 1 to 3 were positioned to measure the in-plane lateral displacement at three key locations along the wall height: the center of the cap, the midpoint, and 150 mm above the footing. Additionally, two wire-type displacement meters were arranged diagonally on the wall to capture its shear deformation.

A total of fifty-three strain gauges were strategically placed along the CFST and the steel faceplates to monitor strain responses at critical locations. The detailed arrangement of the instrumentation is illustrated in Figs. 5 and 6.

3. Test results and discussion

3.1. Damage progression and failure modes

Upon the application of an axial compression load of 1700 kN, no visible overall or local displacement was observed in the specimens. As lateral loading was progressively applied to a peak drift angle of 1/550, only the outer steel plate of SCW-1's CFST reached its yield point. When the peak drift angle increased to the first cycle of 1/300, a slight "rustling" sound was detected, indicating local bonding failure at the interface between the steel faceplate and the infill concrete of SCW-1. At this stage, the outer steel plates of the CFST in all newly developed DSCW specimens (SCW-2 to SCW-6) began to yield. After three cycles of loading, all specimens produced a similar "rustling" sound.

The first instance of local buckling was observed in specimen SCW-1 during the first cycle at a peak drift angle of 1/200, where a bulge of approximately 5–10 mm appeared on the front and back steel faceplates, located 100 mm above the foundation beam. In specimen SCW-3, which featured horizontal rebar trusses with a spacing of 140 mm, local buckling occurred at the end of the 1/200 drift angle loading, resulting in a 3–5 mm bulge at a height of 250 mm. Similarly, in specimen SCW-4, local buckling appeared as a 2–3 mm bulge on the left side of the front steel faceplate at a height of 200 mm during loading to a drift angle of 1/150. After three loading cycles, the local buckling in SCW-3 expanded slightly, and the right side of the front plate in SCW-4's wall body developed minor local buckling at the same height of 200 mm.

No local buckling or visible damage was observed in the other specimens. These results suggest that the newly developed composite shear walls are prone to local buckling when the spacing of the rebar trusses is relatively wide, as seen in specimens SCW-3 and SCW-4, with spacings of 140 mm and 200 mm, respectively.

The local buckling of specimen SCW-1 continued to develop with the progression of loading, and at the first cycle of a peak drift angle of 1/100, the steel faceplates continued to bulge 10-15 mm. However, the steel faceplates of specimens SCW-3 and SCW-4 developed high-mode local buckling, slight 2-5 mm local buckling was observed on the left side of the front steel faceplates approximately 50 mm away from the wall ends, and 5-7 mm local buckling was also observed at the height of 200 mm from the faceplates of specimen SCW-4, which easily provides high plate compression strength.

Steel faceplates of specimens SCW-2, SCW-5 and SCW-6 did not develop local buckling until the end of loading cycles with the peak value of 1/100. About 2-3 mm bulge can be observed on the right side of front faceplate, located 100

mm above the wall ends, as shown in Fig.7(a).

At the same loading step, some new local buckling occurred in the specimen SCW-3. A 15 mm bulge was observed on the front steel faceplate at the height of 250 mm, and a 3-5 mm bulge appeared on the right side of the steel faceplate at the height of 50 mm. Additionally, the outer side steel plate of CFST began to develop slight local buckling with about 3-5 mm bulge. For specimen SCW-4, "bang bang" sound was heard around the welding point between the rebar trusses and the steel faceplates, indicating that the welding point began to break and the constraint of the rebar trusses to the steel faceplates began to fail, the bulging increased to 10-15 mm at the height of 200 mm on the front wall.

When the peak value reached 1/66, all specimens reached the peak load at the first cycle of loading. Cracking sounds of concrete were heard through the loading step for specimen SCW-1, where local buckling continued to deteriorate at the steel faceplate and outer steel plate of CFST, the bulging was about 25-30 mm at the end of this loading step. During this loading step, specimens SCW-2, SCW-5 and SCW-6 also degraded with the further development of local buckling of steel faceplates, along with local buckling of CFST, as depicted in Fig. 7 (b), and "bang bang" sound indicated that the rebar trusses and the steel plate started to break during the process. As for specimens SCW-3 and SCW-4, high-mode buckling developed along the steel faceplate and outer steel plate of CFST, the local buckling range enlarged to about 50-300 mm, and the height of the bulges reached 30-40 mm at the end of loading step, accompanied by the crack sound of concrete and intermittent 'Bang Bang' breaking sound of the welding point.

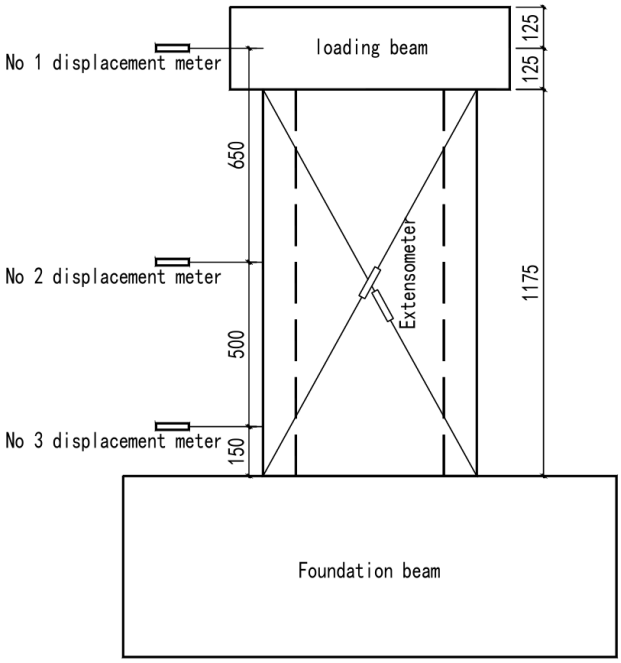

Fig. 5 Configuration of displacement meters

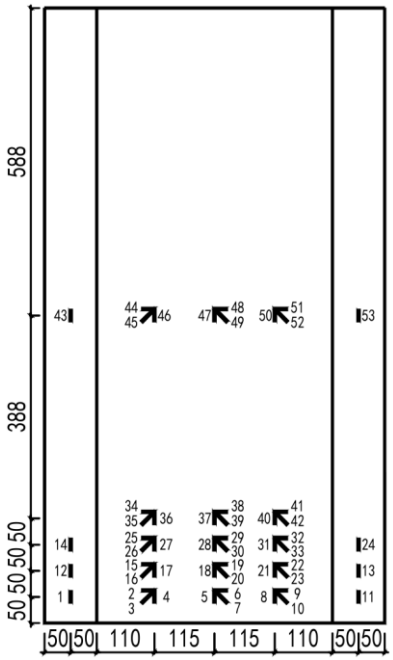

Fig. 6 Arrangement of strain gauges on steel plates

(a) Drift angle of 1/100 (b) Drift angle of 1/66

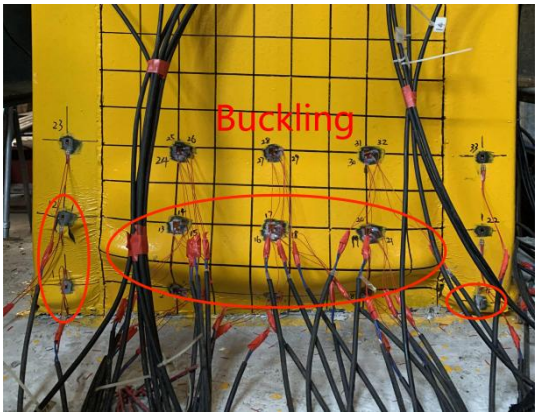

(c) Drift angle of 1/50

Fig. 7 Damage progression of the specimen SCW-2

Table 3
Drift angle of each specimen corresponding to key damage characteristics

Specimen	θ_1	θ_2	θ_3	θ_4	θ_5	θ_6
SCW-1	1/550(1)	1/300(1)	1/200(1)	——	1/55(1)	1/55(1)
SCW-2	1/300(1)	1/300(3)	1/100(3)	1/66(3)	1/30(1)	1/20(2)
SCW-3	1/300(1)	1/300(3)	1/200(3)	1/66(1)	1/50(3)	1/30(3)
SCW-4	1/300(1)	1/300(3)	1/150(1)	1/100(3)	1/30(1)	1/30(1)
SCW-5	1/300(1)	1/300(3)	1/100(3)	1/66(3)	1/50(3)	1/20(2)
SCW-6	1/300(1)	1/300(3)	1/100(3)	1/50(3)	1/50(3)	1/30(3)

Note: The number in brackets indicates loading cycle in each loading step. θ_1 is the yield displacement angle of CFST's outer steel plate, θ_2 is the displacement angle of local bond slip between steel faceplate and infill concrete, θ_3 is the displacement angle during local buckling of steel faceplate, θ_4 is the displacement angle when the welding point between rebar trusses and the steel faceplate breaks, θ_5 is the displacement angle when steel plate cracking or concrete crushing occurs in CFST, θ_6 is the displacement angle at the end of the experiment.

In cyclic loading with the peak drift angle of 1/55, specimen SCW-1 could not maintain the applied axial load due to serious buckling of the steel faceplate and outer steel plate of CFST. Additionally, with the crushing of the infill concrete, the lateral load decreased to 54% of the peak load, leading to the conclusion of the test.

At the peak drift angle of 1/50, with the further development of local buckling of the steel faceplate and outer steel plate of CFST (shown in Fig. 7(c)), the lateral loads of specimens SCW-2 to SCW-6 declined to 70%, 64%, 61%, 82% and 71% of the peak load, respectively. However, the specimens still exhibited considerable bearing capacity.

When the load was applied to the drift angle of 1/30, fracture occurred at the welding seam near the bottom of CFST after three loading cycles, the infill concrete was crushed out, and the lateral loads of specimens SCW-2 to SCW-6 degraded to 63%, 57%, 62%, 74% and 64%, respectively. Among all the specimens, specimen SCW-6 suffered the most serious damage, the welding seam between CFST and the steel faceplate of shear wall body was torn open, and the infill concrete was crushed into pieces. At the end of this loading step, the specimen could not maintain the applied axial load, and it suffered serious out-of-plane instability, therefore the test was concluded. It can be concluded that the discontinuity of the steel plate on the inner side of CFST exacerbates the degree of damage to the specimen. This is because the steel plate inside the concealed column is continuous, and the concealed column is a complete rectangular steel pipe. If the steel plate inside the concealed column is disconnected, the concealed column is a C-shaped channel steel. The bending stiffness and bearing capacity of the rectangular steel pipe are much stronger than those of the channel steel of the same section. Therefore, the stability of the wall outside the plane after the steel plate inside the concealed column is disconnected is weaker than that of the wall with continuous steel plate inside the concealed column.

Specimens SCW-2 and SCW-5 experienced similar damage when loaded to drift angel of 1/20. The lateral load decreased to 25% and 23% of the peak load, respectively. As a result, the specimens were unable to maintain the applied axial load, leading to the termination of the tests.

Fig. 7 illustrates the main damage progression of specimen SCW-2, Fig. 8 depicts the final failure state of each specimen, Fig. 9 shows the failure condition of the infill concrete after the steel faceplate was removed, and Table 3 summarizes the drift angles of each specimen corresponding to key damage characteristics.

The damage progression of the specimens demonstrates that the newly developed composite shear wall achieved the desired flexural failure mode. The failure process followed a consistent sequence: (1)Yielding of the outer steel plate of the CFST; (2) Bonding failure at the interface between the steel faceplate and the infill concrete; (3) Local buckling in the bottom part of the wall, approximately 250 mm above the foundation beam; (4) Disconnection of welding points between the rebar trusses and the steel faceplate; (5) Crushing of the concrete and fracture of the CFST's steel plate.

The following conclusions can be drawn by comparing the damage progression and failure modes of each specimen with those of SCW-2:

(1) From specimens SCW-1 and SCW-2, it is evident that rebar trusses effectively restrain local buckling of the steel faceplate, reducing the extent of buckling under the same loading drift angle.

(2) Specimens SCW-2, SCW-3, and SCW-4 had rebar truss spacings of 100 mm, 140 mm, and 200 mm, respectively. It was observed that denser truss spacing delayed the onset of buckling and reduced the severity of buckling in the steel faceplate under the same drift angle. Therefore, closer spacing of rebar trusses is strongly recommended to enhance the performance of the shear wall.

(3) The rebar trusses in specimens SCW-2 and SCW-5 were arranged horizontally and vertically, respectively. Both specimens exhibited similar damage progression and failure modes; however, SCW-5 experienced less severe damage. This improvement can be attributed to the vertical rebar trusses, which enhanced the global stability of the shear wall.

(4) Specimen SCW-2 featured a continuous CFST inner steel plate, whereas SCW-6 had a discontinuous configuration. Both specimens performed similarly up to a drift angle of 1/50. However, SCW-6 experienced earlier failure due to inadequate out-of-plane restraint on the steel faceplate caused by the discontinuity of the CFST's inner steel plate. Therefore, for ease of construction, this structural form is not recommended due to its adverse impact on wall performance.

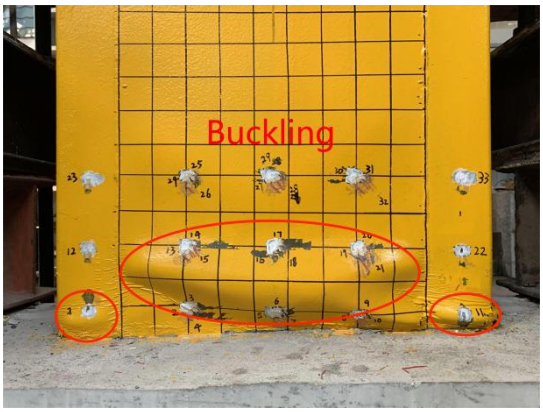

(a) Failure mode of steel plate in SCW-1

(b) Failure mode of steel plate in SCW-2

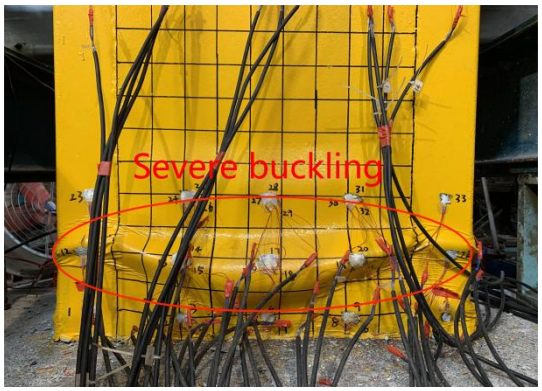

(c) Failure mode of steel plate in SCW-3

(d) Failure mode of steel plate in SCW-4

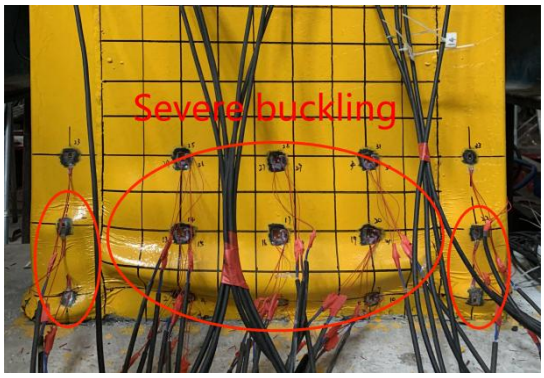

(e) Failure mode of steel plate in SCW-5

(f) Failure mode of steel plate in SCW-6

Fig. 8 Failure mode of steel plate in specimens

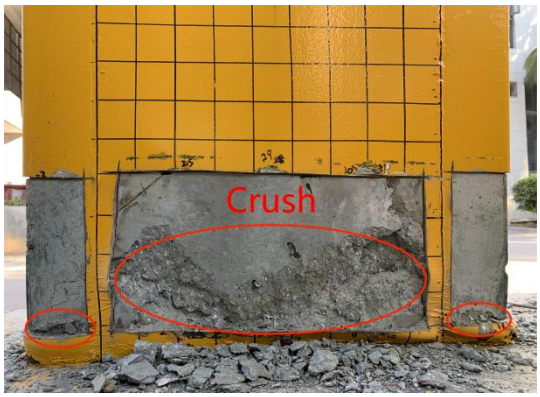

(a) Failure mode of internal concrete in SCW-1

(b) Failure mode of internal concrete in SCW-2

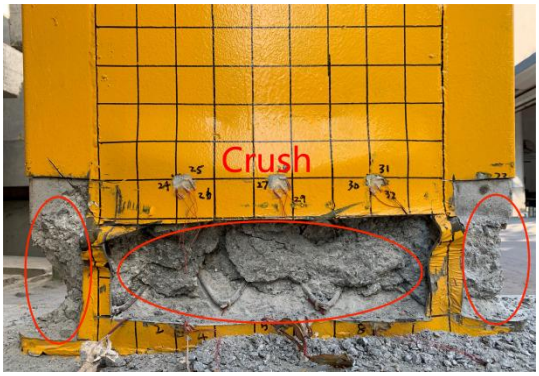

(c) Failure mode of internal concrete in SCW-3

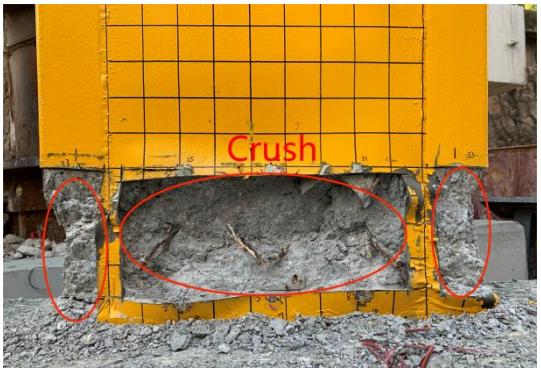

(d) Failure mode of internal concrete in SCW-4

(e) Failure mode of internal concrete in SCW-5

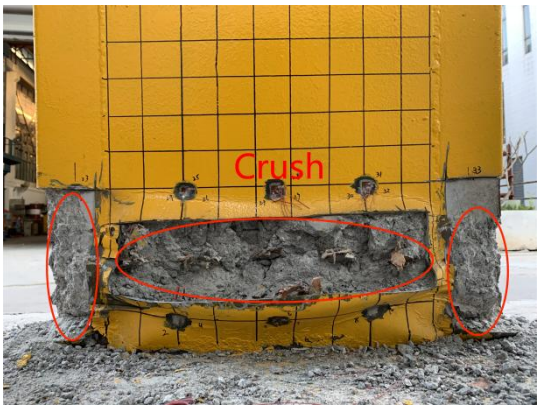

(f) Failure mode of internal concrete in SCW-6

Fig. 9 Failure mode of internal concrete in specimens

3.2. Hysteresis and skeleton curves

Figs. 10 and 11 illustrate the hysteretic and backbone curves of each specimen, derived from the lateral load and lateral displacement data. It is evident that, with the exception of specimen SCW-1, all the newly developed DSCWs exhibited significantly more stable hysteretic behavior up to a drift angle of 1/50. The initial lateral stiffness of the specimens with rebar trusses was found to be nearly identical, indicating that the spacing and orientation of the rebar trusses have minimal influence on the initial lateral stiffness.

The proposed shear walls reached their peak load at a drift angle of 1/66. Although the lateral bearing capacity dropped below 85% of the peak load at a drift angle of 1/50, the shear walls still demonstrated favorable hysteretic behavior. However, during subsequent loading phases, the strength and stiffness of the specimens deteriorated significantly due to progressive local damage. A comparative analysis of the specimens provides valuable insights into their performance:

(1) The new shear wall with closer spacing of rebar trusses exhibited a much more stable hysteretic response, deformation capacity, and energy dissipation capacity, as shown in Fig. 10(b) and Fig. 11(b). When comparing specimens SCW-2, SCW-3, and SCW-4, the peak loads were 622.2 kN, 582.5 kN, and 576.2 kN, respectively, as listed in Table 4. The bearing capacity of SCW-2 was 7% higher than SCW-3 and SCW-4, but the peak loads for SCW-3 and SCW-4, with rebar truss spacings of 140 mm and 200 mm, respectively, were essentially the same. These results suggest that rebar truss spacing has a notable effect on the specimen's strength when the spacing is less than 140 mm. Moreover, closer rebar truss spacing is a critical parameter influencing the post-peak strength, stiffness, and ductility, which deteriorated more slowly with tighter spacing.

(2) A comparison of SCW-2 and SCW-5, which featured horizontal and vertical rebar trusses respectively, revealed similar behavior throughout the entire loading process. The peak loads of these specimens were 622.2 kN and 614.8 kN, respectively. However, the vertical rebar trusses in SCW-5 contributed to maintaining more stable strength and stiffness after the peak load, as clearly illustrated in Fig. 11(c).

(3) Despite the discontinuity of the CFST's inner steel plate, specimen SCW-6 exhibited nearly the same initial stiffness, peak load, and strength and stiffness degradation up to a drift angle of 1/30. However, the discontinuity of the CFST's inner steel plate compromised the ductility of the shear wall, reducing its ability to sustain deformation under large loading cycles.

(4) Specimen SCW-1, which lacked rebar trusses, exhibited significantly worse hysteretic responses, with notably reduced hysteretic loops. In contrast, the peak loads of the new shear walls were 132%, 124%, 123%, 131%, and 129% of SCW-1, respectively. Furthermore, the new shear walls demonstrated much more stable deformation capacity and energy dissipation capacity after reaching their peak load, highlighting the improvements achieved with the new design.

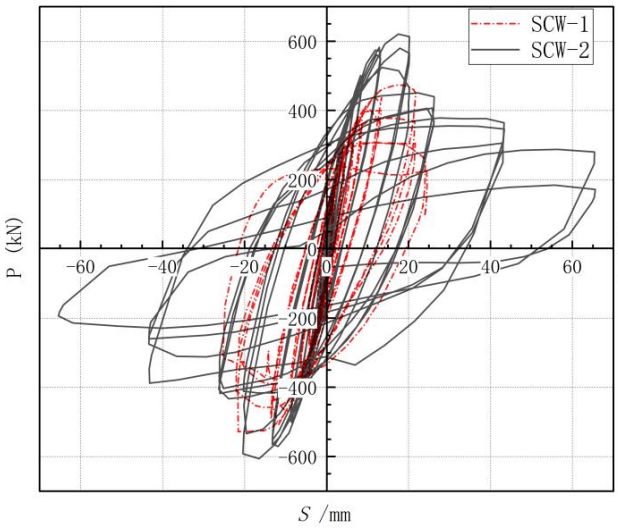

(a) With or without rebar trusses

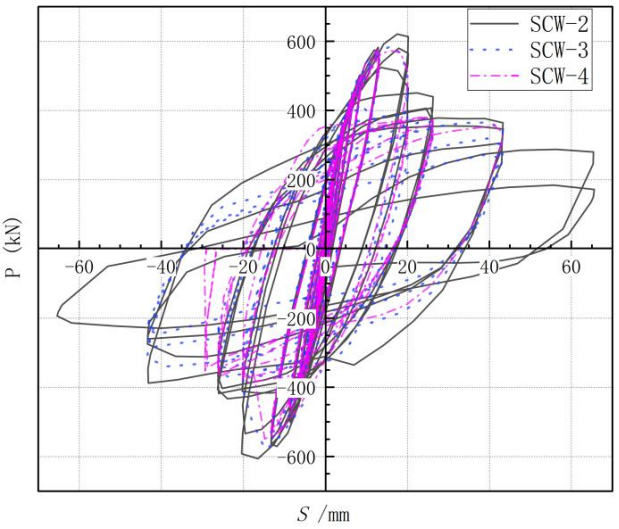

(b) Rebar truss spacing

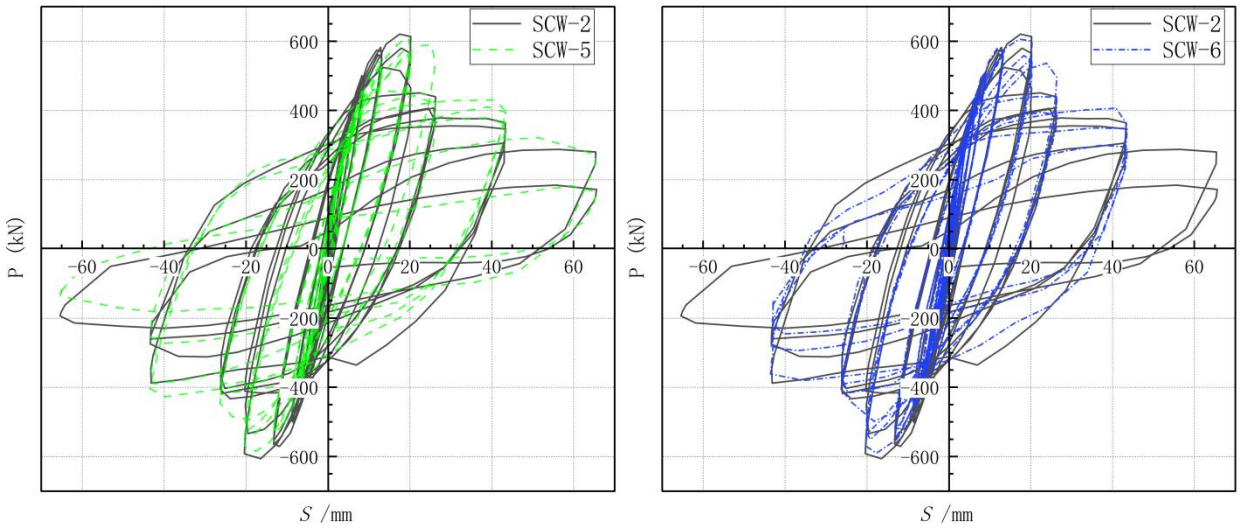

(c) Horizontal and vertical rebar trusses (d) Discontinuity of CFST' inner steel plate

Fig. 10 Comparison of hysteretic behavior of specimens

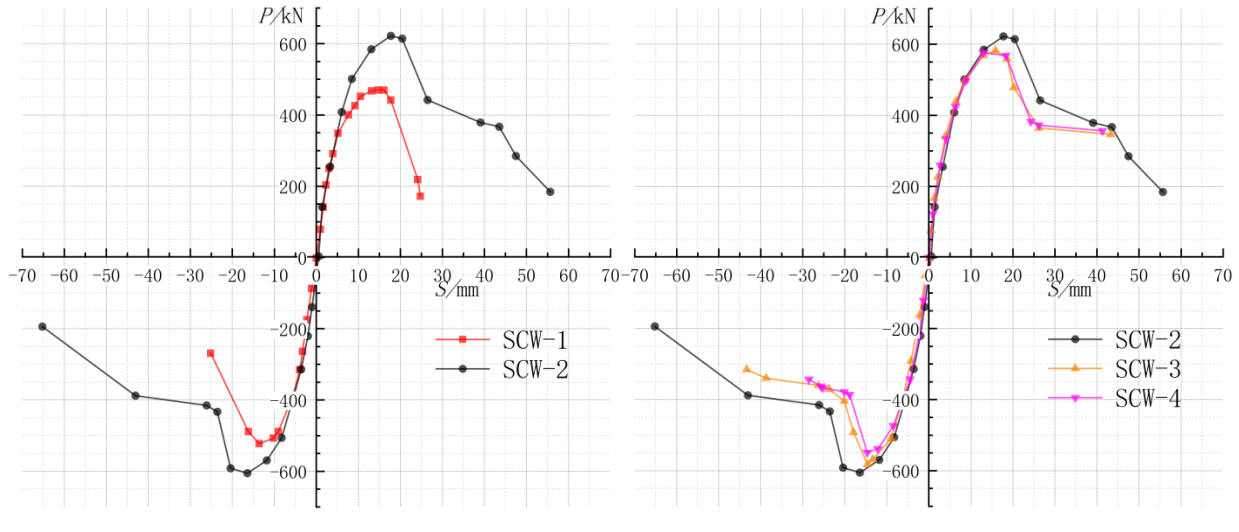

(a) With or without rebar trusses (b) Rebar truss spacing

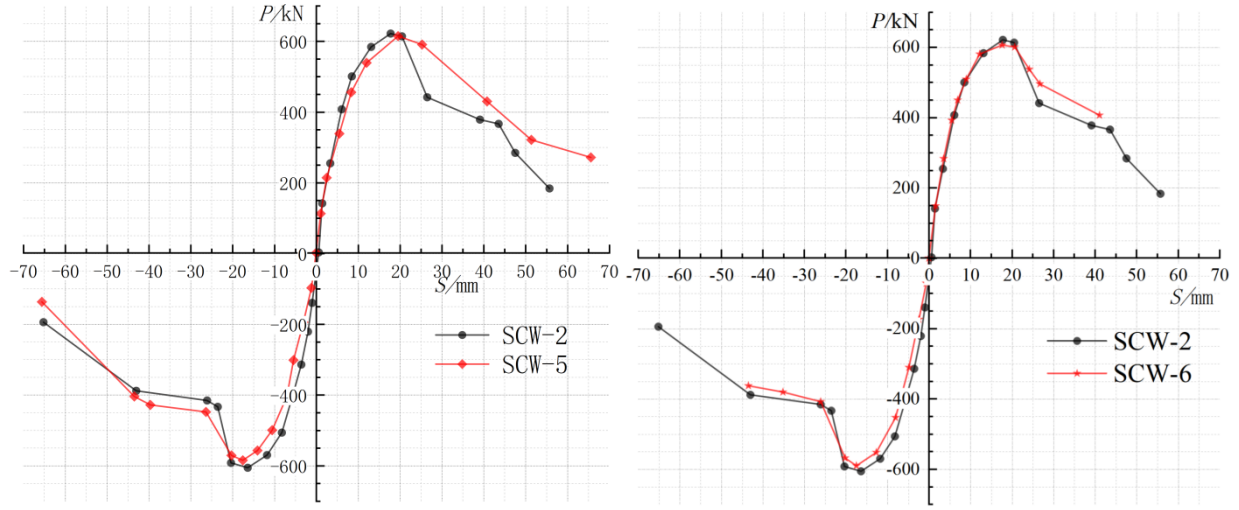

(c) Horizontal and vertical rebar trusses (d) Discontinuity of CFST' inner steel plate

Fig. 11 Skeleton curves of horizontal load-displacement at the top of specimen

3.3. Characteristic values of the specimens

To further analyze the effects of various parameters on the seismic performance of the new composite shear wall, the yield load and yield displacement are defined as the load and drift angle corresponding to the intersection of the secant stiffness at 75% of the specimen's peak bearing capacity and the elastic-plastic line, as illustrated in Fig. 12. Similarly, the failure load and failure displacement are determined as the load and drift angle corresponding to the point on the descending section of the skeleton curve where the load drops to 85% of the peak load [35], as summarized in Table 4.

Key characteristic values, including critical loads, corresponding drift angles, and ductility coefficients for each specimen, are provided in Table 4. The displacement ductility coefficient is calculated as the ratio of the failure displacement to the yield displacement. This coefficient ranges from 1.86 to 2.78,

with an average value of 2.30, indicating that DSCWs with rebar trusses exhibit good deformation capacity under an axial compression ratio of 0.40. This suggests their suitability for widespread application in real engineering projects.

The limit drift angle ranges from 1/77 to 1/41, with an average value of 1/59, exceeding the specified limit of 1/120 for shear wall structures as stipulated in the Chinese seismic code [36].

A comparison of the yield point, peak load, and failure load demonstrates that rebar trusses significantly enhance the lateral bearing capacity of the shear walls. However, variations in the spacing and orientation of the rebar trusses have minimal influence on the key load values, with the maximum observed difference being less than 7.4%.

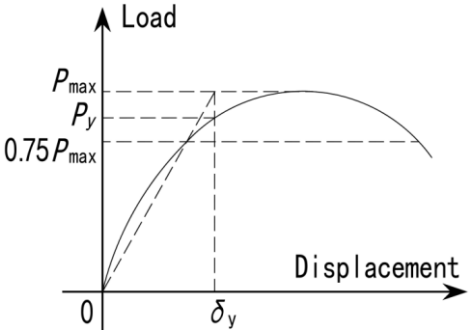

Fig. 12 Definition of yield displacement

Table 4
Key loads, drift angles and ductility coefficients of specimens

Specimen number	Loading direction	Yield point		Peak load point		Failure point		Displacement ductility coefficient
		$F_{y,EXP}$/kN	$\theta_{y,EXP}$	$F_{p,EXP}$/kN	$\theta_{p,EXP}$	$F_{u,EXP}$/kN	$\theta_{u,EXP}$	
SCW-1	positive	390.3	1/182	470.4	1/81	399.8	1/69	2.64
	negative	447.2	1/170	522.3	1/96	444.0	1/72	2.36
SCW-2	positive	530.4	1/129	622.2	1/73	528.9	1/56	2.30
	negative	524.4	1/140	605.1	1/79	514.3	1/59	2.37
SCW-3	positive	496.7	1/153	582.5	1/82	495.1	1/65	2.35
	negative	517.0	1/136	581.8	1/89	494.5	1/73	1.86
SCW-4	positive	498.9	1/146	576.2	1/101	489.8	1/62	2.35
	negative	478.6	1/148	548.5	1/89	466.2	1/77	1.92
SCW-5	positive	525.7	1/114	614.8	1/67	522.6	1/41	2.78
	negative	507.7	1/117	584.2	1/74	496.6	1/54	2.17
SCW-6	positive	519.7	1/139	607.4	1/74	516.3	1/51	2.73
	negative	503.4	1/124	589.2	1/74	500.8	1/57	2.18

Note: $F_{y,EXP}$ indicates yield load, $\theta_{y,EXP}$ is the yield drift angle, $F_{p,EXP}$ is the peak load, $\theta_{p,EXP}$ is the peak drift angle, $F_{u,EXP}$ is the failure load, $\theta_{u,EXP}$ is the failure drift angle.

Another important parameter for assessing the seismic performance of shear walls is loop stiffness [37], which reflects the stiffness degradation of the specimen. Fig. 13 illustrates the loop stiffness-lateral displacement curves of the specimens under various configurations. As shown, the loop stiffness of specimens with rebar trusses is 8.7%–34.7% higher than that of specimens without rebar trusses. Reducing the spacing of rebar trusses marginally enhances the loop stiffness and delays stiffness degradation. The loop stiffness curves of specimens SCW-2 and SCW-5 are almost identical, indicating that the orientation of the rebar trusses has minimal impact on stiffness degradation. For specimen SCW-6, which has a discontinuous steel plate inside the CFST, the loop stiffness is slightly lower than that of SCW-2 with a continuous steel plate. Additionally, the stiffness degradation of SCW-6 becomes more significant in the later stages of loading.

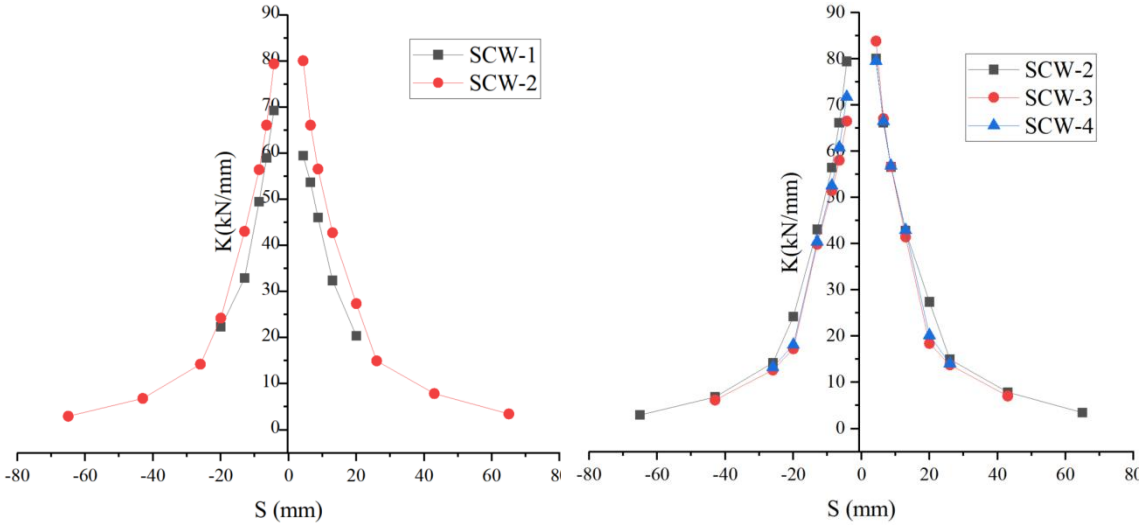

(a) With and without rebar trusses

(b) Different rebar trusses spacing

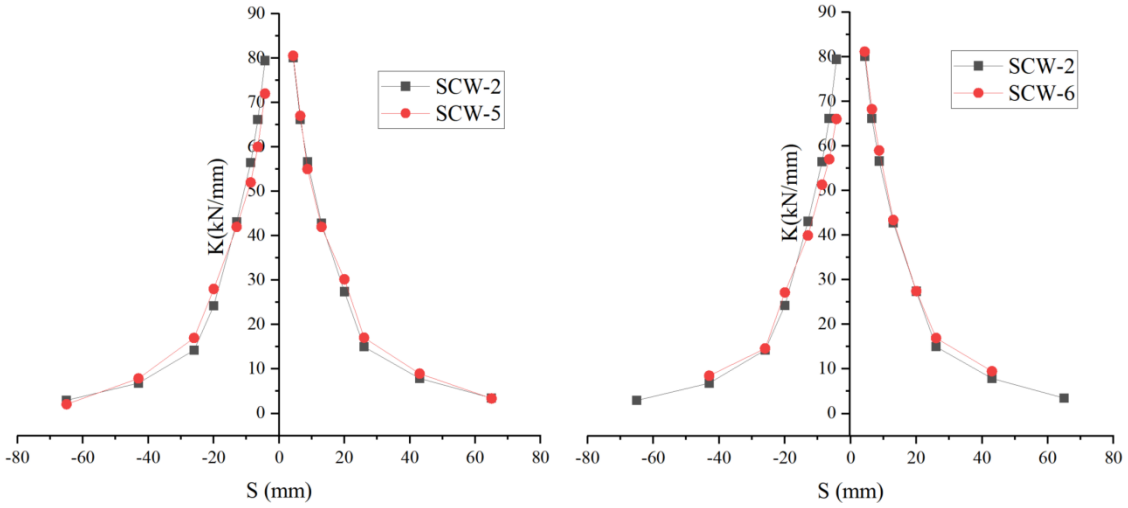

(c) Different arrangement direction of rebar trusses (d) Continuous and disconnected steel plate inside CFST

Fig. 13 Comparison of stiffness degradation curves of specimens under different parameters

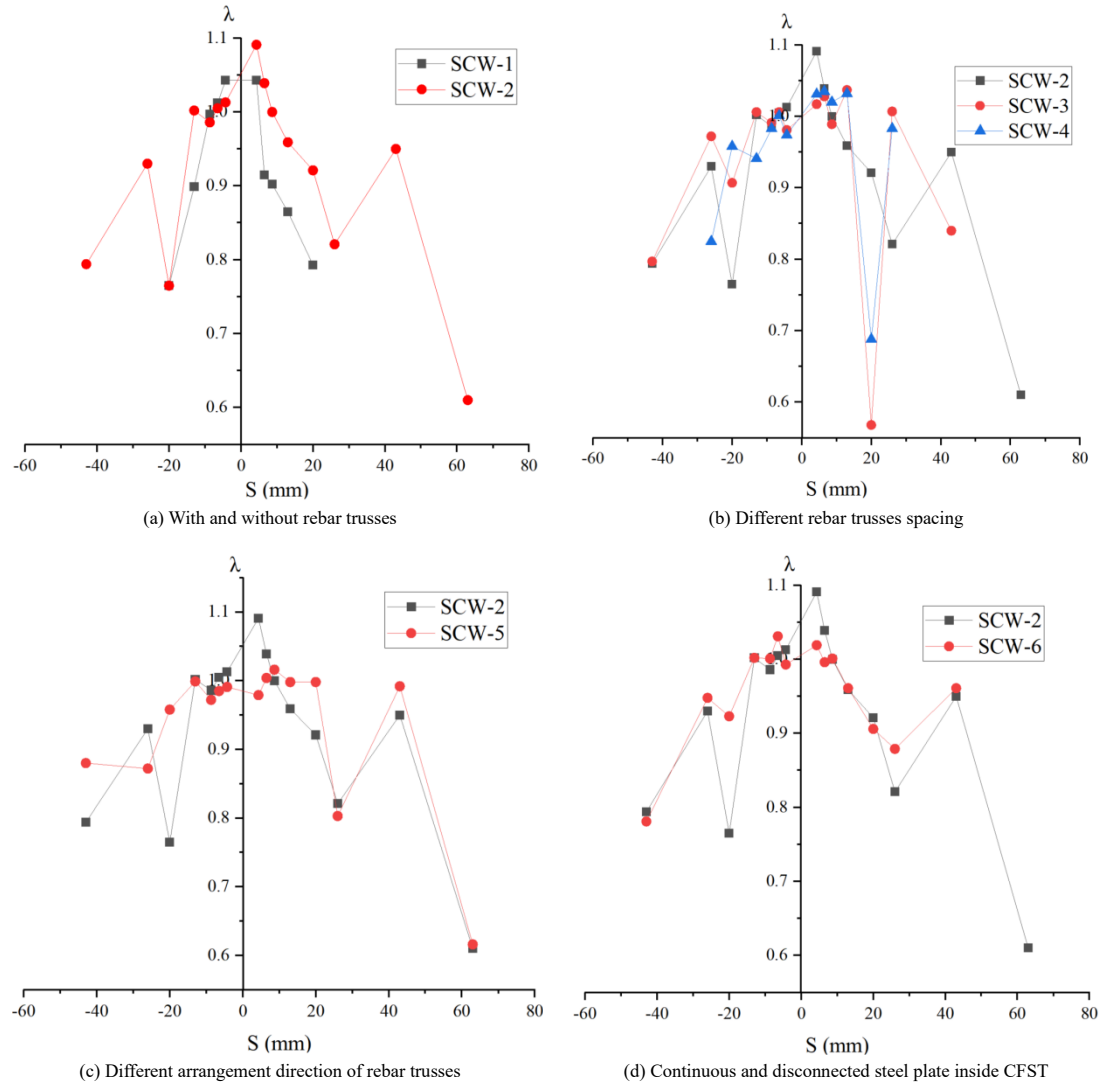

(a) With and without rebar trusses (b) Different rebar trusses spacing

(c) Different arrangement direction of rebar trusses (d) Continuous and disconnected steel plate inside CFST

Fig. 14 Second cycle strength degradation curves of each specimen under different parameters

Strength degradation is another critical parameter for evaluating shear wall performance. The strength degradation coefficient (λi) is used to quantify the ratio of the peak load of the i-th cycle to that of the first cycle at a given loading amplitude [37]. Fig. 14 shows the second-cycle strength degradation curves of the specimens under various configurations. As illustrated, the strength degradation coefficient decreases as the loading drift angle increases. The arrangement and denser spacing of rebar trusses significantly help the shear wall maintain stable strength, especially during the later loading stages when major damage occurs. Although specimens SCW-2 and SCW-5 exhibit a similar strength degradation process, the shear wall with vertical rebar trusses (SCW-5) demonstrates more stable strength retention. Additionally, the discontinuity of the CFST's inner steel plate in specimen SCW-6 does not compromise its overall strength capacity. Fig. 14(d) shows that SCW-6 maintains stable strength capacity even during the very late stages of loading when major damage occurs.

To further evaluate the energy dissipation capacity, energy consumption-half cycle curves, cumulative energy consumption-half cycle curves and equivalent viscous damping coefficient versus number of cycles were analyzed, as show in Fig. 15 to Fig. 17. In general, the energy consumption of the

specimens increases continuously with the number of loading cycles. Compared with SCW-1, the energy dissipation capacity of DSCWs is significantly enhanced by the inclusion of rebar trusses. The cumulative energy consumption of specimens with rebar trusses is 4.38–8.68 times that of specimen SCW-1.

When comparing specimens SCW-2, SCW-3, and SCW-4, reducing the spacing of rebar trusses significantly improves energy dissipation capacity. The cumulative energy consumption of SCW-2 is 1.37 times and 1.84 times that of SCW-3 and SCW-4, respectively. Comparing SCW-2 and SCW-6, the energy consumption of specimens with continuous and discontinuous steel plates inside the concealed column is similar under the same half-cycle number. However, due to its stronger stiffness at later stages, the cumulative energy consumption of SCW-2 is higher than that of SCW-6.

When comparing SCW-2 and SCW-5, both specimens exhibit nearly identical energy dissipation capacity. However, during the later loading stages, the shear wall with vertical rebar trusses (SCW-5) demonstrates better deformation capability, enabling it to consume more energy.

Fig. 17 shows the equivalent viscous damping coefficient energy dissipation cycle curve, where the equivalent viscous damping coefficients are all greater than the 0.05 value specified in the Chinese seismic code. The equivalent viscous damping coefficient shows a curve of first decreasing and then increasing with the number of energy dissipation cycles, and the turning point occurs at the 5th cycle, which is 1/300 displacement angle. This is a direct reflection of the evolution of internal material damage and the periodic activation of energy dissipation mechanism. When the displacement angle is less than 1/300, concrete cracking and interface slip cause stiffness collapse degradation, and energy dissipation growth lags behind. When the displacement angle is greater than 1/300, an efficient synergistic energy dissipation mechanism is formed by steel plate yielding, concrete crack friction, steel reinforcement plasticity, and interface slip.

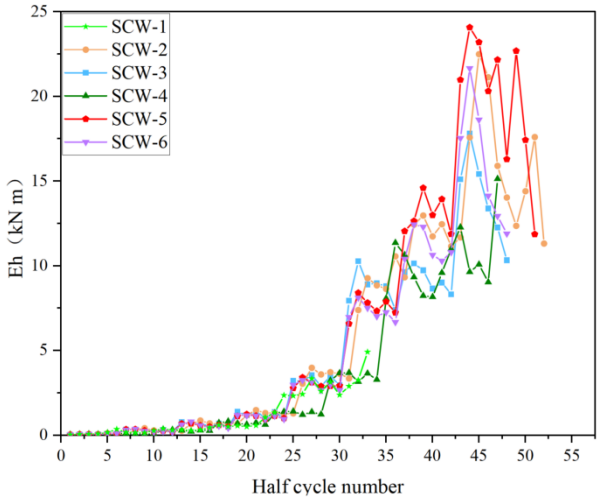

Fig. 15 Energy consumption-half cycle curves

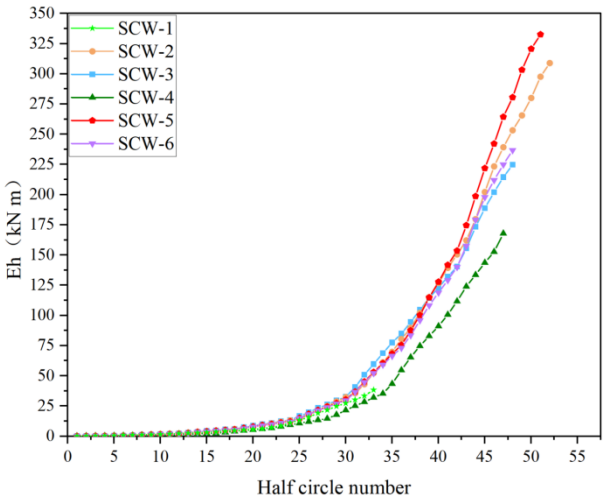

Fig. 16 Cumulative energy consumption-half cycle curves

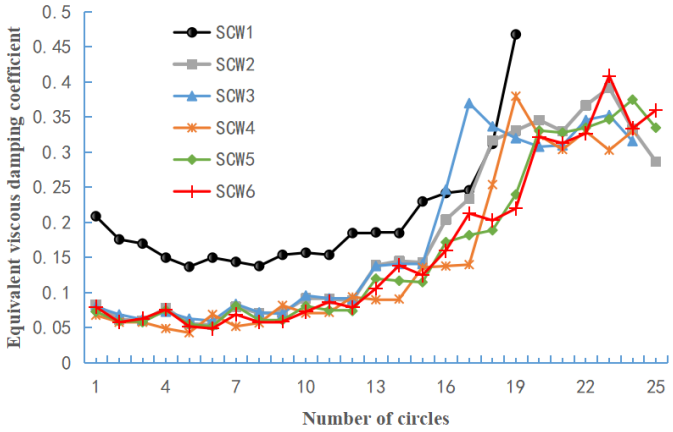

Fig. 17 Equivalent viscous damping coefficient versus number of cycles

4. Compressive and bending bearing capacity of DSCW

To evaluate the compressive and bending bearing capacities of the newly developed DSCW, the European Code Eurocode 4 [38] and the Chinese Code CECS: 546-2018 [39] were used for calculation and comparison.

4.1. European code - Eurocode 4 (2004)

Eurocode 4 adopts the full-section plastic method for calculating the compressive and bending bearing capacities of composite components. This method considers the influence of shear force while ignoring the tensile strength of concrete. The calculation formulas are as follows:

$$M_{Ed} = \alpha_M M_{Pl,N,Rd} \tag{2}$$

$$M_{pl,N,Rd} = f_{cd} A_c d_c + f_y A_{sc} d_{sc} + (1-\rho) f_y A_{swc} d_{swc} + f_y A_{st} d_{st} + (1-\rho) f_y A_{swt} d_{swt} \tag{3}$$

$$N_{Ed} = f_{cd} A_c + f_y A_{sc} + (1-\rho) f_y A_{swc} - f_y A_{st} - (1-\rho) f_y A_{swt} \tag{4}$$

$$\rho = \left(2V_{Ed} / V_{Rd} - 1\right)^2 \tag{5}$$

In the formula, M_{Ed} is the flexural bearing capacity of the composite shear wall, $M_{Pl,N,Rd}$ is the flexural bearing capacities of the composite shear wall without considering reduction, α_M is the steel grade adjustment factor, f_{cd} is the compressive strength of the concrete cylinder, A_c is the area of the concrete in the compression zone, d_c is the distance from the compressive concrete to the center of the composite wall, f_y is the yield strength of steel plate, A_{sc} and A_{st} are the areas of the compressive and tensile flange steel plates from the center of the composite wall, d_{sc} and d_{st} are the distances of the compressive and tensile flange

steel plates from the center of the composite wall, A_{swc} and A_{swt} are the areas of the compressive and tensile steel web plates, d_{swc} and d_{swt} are the distances of the compressive and tensile steel web plates from the center of the composite wall, and ρ is the reduction factor of steel plate strength considering the affection of shear force, where V_{Ed} is the design shear force and V_{Rd} is the shear bearing capacity.

4.2. Chinese code - CECS: 546 (2018)

The "Technical Standard for Steel Tube Concrete Bundle Composite Structures" (CECS: 546-2018) is based on the ultimate state theory and provides simplified N-M relationship formulas for composite shear walls under combined compression and bending. For practical design purposes, the following formulas are used:

$$\frac{N}{N_{\mathrm{u}}}+\left(1-\alpha_{\mathrm{c}}\right)\frac{M_x}{M_{ux}}\le 1 \tag{6}$$

$$\alpha_c = f_c A_{c0} / N_u \tag{7}$$

$$N_u = f_y A_{s0} + f_c A_{c0} \tag{8}$$

$$M_{ux} = \left[0.5A_{s0}\left(h-2t_s-d_{nx}\right)+bt_s\left(t_s+d_{nx}\right)\right]f_y \tag{9}$$

$$d_{nx} = \left(A_{s0}-2bt_s\right)/\left[\left(b-2t_s\right)f_c/f_y+4t_s\right] \tag{10}$$

In the formula, N is the axial compressive force of the composite wall, N_u is the axial compressive bearing capacity of the composite wall, α_c is the concrete working bearing coefficient, M_x is the bending bearing capacity of the composite wall, M_{ux} is the bending bearing capacity of the composite wall when only bending moment is applied, f_c is the compressive strength of the concrete, A_{c0} is the cross-sectional area of the concrete, f_y is the yield strength of the steel plate, A_{s0} is the cross-sectional area of the steel plate, t_s is the thickness of the steel plate, b and h are the thickness and width of the composite wall, and d_{nx} is the height of the concrete compression zone.

4.3. Comparison between Eurocde 4 and CECS:546

Using the two theoretical models provided by Eurocode 4 and CECS: 546, the compressive and bending bearing capacities of specimens SCW-2 to SCW-6 were calculated, and the results are presented in Table 5.

From Table 5, it can be observed that the calculated values for all five specimens with rebar trusses are lower than the experimental results. Specifically, the European standard (Eurocode 4) underestimates the experimental values by approximately 20%; while the Chinese standard (CECS: 546-2018) provides more accurate results, with deviations averaging only 8%.

These findings indicate that, for the DSCWs with rebar trusses proposed in this study, under a given axial pressure, the theoretical model from the Chinese standard CECS: 546-2018 is more accurate for calculating the bending bearing capacity.

Table 5
Comparison of theoretical values from two standards with experimental results

Number	Test Value / kN	Eurocode 4 / kN	Ratio	CECS: 546-2018 / kN	Ratio
SWC-2	527.4	422.1	1.25	471.6	1.12
SWC-3	506.9		1.20		1.07
SWC-4	488.8		1.16		1.04
SWC-5	516.7		1.22		1.10
SWC-6	511.6		1.21		1.08

5. Conclusions

This study investigated the seismic performance of a novel double-skin composite wall (DSCW) system reinforced with rebar trusses. A series of experimental tests and analytical comparisons were conducted based on an axial compression ratio of 0.4 and a shear span ratio of 2.0 to evaluate the mechanical behavior of the proposed DSCW under low-cycle lateral loading. The following conclusions can be drawn based on the findings:

(1) The inclusion of rebar trusses significantly improves the seismic performance of DSCWs compared to conventional designs. The rebar trusses effectively constrain the steel faceplates, delaying local buckling and enhancing overall stability. As a result, the bearing capacity of the DSCWs was increased by approximately 7%–36%, and the energy dissipation capacity was improved by 3 to 7 times compared to specimens without rebar trusses.

(2) All tested specimens exhibited a flexure-dominated failure mode. The progression of damage followed a consistent sequence: (1) bonding failure between the steel faceplates and the concrete core, (2) local buckling of the steel faceplates, (3) disconnection of the welding points between the rebar trusses and steel faceplates, (4) local buckling of the outer steel plate of the CFST boundary columns, and (5) crushing of the infill concrete and fracture of the CFST steel plate.

(3) The mechanical properties of DSCWs are only marginally influenced by the orientation of the rebar trusses (horizontal or vertical). However, walls with vertical rebar trusses demonstrated approximately 9.1% higher flexural bearing capacity at later loading stages due to enhanced global stability provided by the vertical truss configuration.

(4) Reducing the spacing of rebar trusses effectively delays stiffness and strength degradation, improving the ductility and energy dissipation capacity of the wall. Specimens with closer truss spacing (e.g., 100 mm) exhibited more stable hysteretic behavior and slower post-peak deterioration compared to specimens with larger spacings.

(5) While introducing a discontinuous inner steel plate in the CFST boundary column can facilitate construction, it compromises the deformation capacity and out-of-plane stability of the wall after reaching peak load. This structural form is therefore not recommended for practical applications where high deformation capacity is required.

(6) The displacement ductility coefficients of the specimens ranged from 1.86 to 2.78, with an average value of 2.30, indicating excellent deformation capacity. The ultimate drift angles varied from 1/77 to 1/41, with an average of 1/59, exceeding the seismic design limit of 1/120 specified in the Code for Seismic Design of Buildings. This demonstrates that the proposed DSCWs can sustain substantial deformations before failure, making them suitable for seismic applications.

(7) The theoretical model provided by the Chinese Code CECS: 546-2018 more accurately predicts the bending bearing capacities of the DSCWs, with deviations averaging only 8% compared to experimental results. In contrast, the European Code Eurocode 4 underestimates the bearing capacities by about 20%, highlighting the suitability of the Chinese code for designing DSCWs with rebar trusses.

(8) Considering the small number of specimens in this article, further in-depth research will be conducted on the seismic performance of this component under the variation parameters of axial compression ratio and shear span ratio, combining experiments and finite element analysis.

Declaration of competing interest

Financial and personal entanglements, either with entities or individuals bearing potential sway over our scholarly endeavors, are categorically nonexistent, it is declablue. Absent from the ambit of our professional lives are interests—both tangible and intangible—that might be perceived as exerting influence upon the stance articulated within, or critiqued in, a discourse designated: "Experimental Investigation into the Seismic Response of Double-Skin Composite Walls Reinforced by Rebar Trusses," demonstrably shown thus.

Acknowledgements

This work was supported by the National Natural Science Foundation of China (Grant No.52178139) and the Natural Science Foundation of Guangdong Province (Grant No. 2021B1111610009).

References

[1] Wu Gang, Feng Decheng, Xu Zhao, et al. Research developments in precast concrete structural systems [J]. Journal of Civil Engineering and Management, 38 (2021) 41−51.(in Chinese).
[2] Salmon D C, Tadros M K, Culp T. A New Structurally and Thermally Efficient Precast Sandwich Panel System [J]. PCI Journal, 1994,39(4): 90-101.
[3] Chu Mingjin, Liu Jiliang, Cui Huichen, et al. Experimental study on seismic behaviors of assembled monolithic concrete shear walls built with precast two-way hollow slabs with various details[J]. Journal of Building Structures, 2014, 35(1):93-102.(in Chinese).
[4] Zhi Q, Guo Z. Experimental evaluation of precast concrete sandwich wall panels with steel–glass fiber–reinforced polymer shear connectors[J].Advances in Structural Engineering, 2017, 20(10):136943321668319.
[5] Yang Lianping, Yu Shaole, Zhang Qilin, et al. Research status quo and key issues in superimposed shear wall structure [J]. Building Structure, 2017,47(12):78-88. (in Chinese).

[6] Liu Wei, Wang Chao. Research and development of steel plate shear wall[J]. Journal of Jilin Jianzhu University, 2017(3):26-30. (in Chinese).
[7] Adams P F , Zimmerman T , Macgregor J G . Design and Behavior of Composite Ice-Resisting Walls[J]. Aci Special Publication, 87 (1988) 23-40.
[8] Hassinen P, Kouhi J , Zimmerman T , et al. Static and cyclic load tests of a composite ice-resisting wall. 1989.
[9] Stephen M J, Zimmerman T. The Strength Of Composite Ice-Resisting Walls Subjected To Combined Loads[J]. Aztex Corp, 1990.
[10] Wright H D, Gallocher S C. The behaviour of composite walling under construction and service loading[J]. Journal of Constructional Steel Research, 35(3)(1995)257-273.
[11] Wright H . The axial load behaviour of composite walling[J]. Journal of Constructional Steel Research, 45(3) (1998) 353-375.
[12] Hossain K, Wright H D. Experimental and theoretical behaviour of composite walling under in-plane shear[J]. Journal of Constructional Steel Research, 60(1) (2004) 59-83.
[13] RA Link, A. E. Elwi. Composite Concrete-Steel Plate Walls: Analysis and Behavior. [J]. J. Struct. Eng., 121(2) (1995) 260-271.
[14] Emori K . Compressive and Shear Strength of Concrete Filled Steel Box Wall[J]. International Journal of Steel Structures, 26(2) (2002) 29-40.
[15] NIE Jianguo，BU Fanmin，FAN Jiansheng． Quasi-static test on low shear-span ratio composite shear wall with double steel plates and infill concrete under high axial compression ratio [J]. Engineering Mechanics, 2013,30 (6) : 60-66. (in Chinese).
[16] BU Fanmin, NIE Jianguo, FAN Jiansheng. Experimental study on seismic behavior of medium and high shear-span ratio composite shear wall with double steel plates and infill concrete under high axial compression ratio [J]. Journal of Building Structures, 2013,34 (4) 91-98. (in Chinese).
[17] Nie Jianguo, Bu Fanmin, Fan Jiansheng. Experimental research on seismic behavior of low shear-span ratio composite shear wall with double steel plates and infill concrete [J]. Journal of Building Structures, 2011,32 (11) 74−81. (in Chinese).
[18] Jian-Guo Nie, hong-Song Hu, Jian-Sheng Fan, Mu-Xuan Tao, Sheng-Yong Li, Fu-Jun Liu. Experimental study on seismic behavior of high-strength concrete filled double-steel-plate composite walls [J]. Journal of Constructural Steel Research. 88 (2013) 206-219.
[19] Tang Xulin, Ding Changyin, Zuo Zhiliang, et al. Experimental research on seismic behavior of composite shear wall with double steel plates and infill concrete with stiffeners [J]. Journal of Building structures, 2017,38 (5) 85−91. (in Chinese).
[20] Wu Xiaodong, Tong Lewei. Experimental study on seismic behavior of steel-concrete-steel composite shear walls with CFST boundary columns and partitioning steel plates [J]. Journal of Building structures, 2019,40 (12) 41 −50. (in Chinese).
[21] Tae-Sung Eom, Hong-Gun Park, Cheol-Ho Lee, Jin-Ho Kim, In-Hwa Chang. Behavior of Double Skin Composite Wall Subjected to In-Plane Cyclic Loading [J]. Struct. Eng. 135(10) (2009) 1239-1249.
[22] Liu Hongliang, Cai Jian, Yang Chun, et al. Experimental study on seismic behavior of composite shear wall with double steel plates and infill concrete with binding bars [J]. Journal of Building Structures, 2013,34 (6) 84 −92.(in Chinese)
[23] Cai Jian, Duan Weining, Tang Xuning, et al. Influence of axial compression ratios and shear-span ratios on seismic behavior of composite shear wall with double steel plates and infill concrete with binding bars [J]. Journal of Building Structures, 2018,39 (2) 37−43.(in Chinese).
[24] JI Xiaodong, JIANG Feiming, QIAN Jiaru, et al. Experimental study on seismic behavior of steel tube-double steel plateconcrete composite shear walls [J]. Journal of Building Structures, 2013,34 (6) 75-83.(in Chinese).
[25] Zhang X M, Qin Y, Chen Z H. Experimental seismic behavior of innovative composite shear walls [J]. Journal of Constructional Steel Research, 116 (2016) 218–232.
[26] Chen Zhihua, Jiang Yuting, Zhang Xiaomeng, et al. Research on resilience model of steel tube bundle composite shear wall [J]. Earthquake Engineering and Engineering Dynamics, 2017,37 (1) 115–122. (in Chinese)
[27] Chen Zongping, Zhou Ji, Mo Linlin, et al. Experimental study on seismic behavior of double-skin corrugated plates and concrete composite shear wall [J]. Journal of Building Structures, 2022, 43(10) 75-83.(in Chinese)
[28] Zhang Zhuangnan, Li Shanshan, Wang Chungang, et al. Seismic performance of double steel plate concrete composite
shear wall with hybrid connectors [J]. Journal of Building Structures, 2023, 44(S1) 92-100.(in Chinese)
[29] Jun Shi, Shan Gao, Lanhui Guo, et al., Compressive behaviour of double skin conposite shear walls stiffened with rebar trusseses, J. Constr. Steel Res. 2021,180(5):106581.
[30] Jianhong Han, Ganping Shu, Ying Qin, et al. Experimental seismic behavior of double skin composite wall with rebar trusses, J. Constr. Steel Res 2021,180: 106569.
[31] Wei fangfang, Zhu youhua, Yu jun. Numerical analysis of shear resistance of concrete filled double-steel-plate composite walls with shear stud connectors. [J]. Journal of Civil and Environmental Engineering, 2021,43(1):96-106.(in Chinese) .
[32] Luo yongfeng, Li jian, Guo xiaonong. Numerical Analysis of hysteretic performance of double-steel-layer-concrete composite shear wall. [J]. Journal of Hunan University, 2013,41(11)57-62.(in Chinese)
[33] Cai Jian, Xie Xiaofeng, Yang Chun, et al. An Experimental Research on the Composite Column with Core of High-Strength Concrete Filled Steel Tube under Axial Compression Loading [J]. Journal of South China University of Technology (Natural Science Edition),2002, 30(6) 81-85. (in Chinese).
[34] Alzeni Y, Bruneau M. In-plane cyclic testing of concrete-filled sandwich steel panel walls with and without boundary elements. J Struct Eng 2017,143(9):04017115.
[35] Ductility of prestressed concrete piles subjected to situlated seismic loading: Park, R and Falconer T JJ. Prestressed Concr. Inst. Vol 28 No 5 (September–October 1983) 112−144.
[36] Ministry of Housing and Urban-Rural Development of the People's Republic of China.Code for seismic design of buildings:GB 500112010 [S].Beijing:China Architecture & Building Press,2016.
[37] Tang Jiuru.Seismic performance of reinforced-concrete beam-column connections[M].Nanjing:Southeast University Press,1989: 312-316 (in Chinese).
[38] BS EN 1994-1-1: 2004, Eurocode 4: Design of Composite Steel and Concrete Structures [S]. Brussels: European committee for Standardization, 2004.
[39] CECS: 546−2018, Technical Standard for Structures with Concrete-Filled Multicellular Steel Tube Walls [S]. Beijing: China Planning Press, 2018. (in Chinese)

Advanced Steel Construction – Vol. 22 No. 2 (2026) 222–236
DOI:10.18057/IJASC.2026.22.2.8

STUDY ON BAND GAP CHARACTERISTICS OF PERIODIC GRID STRUCTURE AND SHOCK WAVE ATTENUATION IN IT

Hai-Xiang Zhao [1], Bai-Qian Sun [1], En Zhang [2], Zhi-Xing Wang [3], Li-Gang Zheng [3], Qian Yang [3], Peng-Cheng Chen [1, *] and Guo-Yun Lu [1]

[1] *College of Civil Engineering, Taiyuan University of Technology, Taiyuan 030024, Shanxi, China*
[2] *Department of Architecture and Environmental Engineering, Taiyuan University, Taiyuan 030032, Shanxi, China*
[3] *Shanxi Xiaohe Construction Industry Co., Ltd, Taiyuan 030032, Shanxi, China*
** (Corresponding author: E-mail: chenpengcheng@tyut.edu.cn)*

ABSTRACT

The unique band gap characteristics of periodic structures result in varying degrees of attenuation of elastic wave propagation across different frequency ranges. With the increasing demand for periodic grid structures, particularly long-span grids, in various sectors of industry and daily life, the issues of vibration reduction and isolation in such structures have become increasingly prominent. Inspired by the periodic properties of phononic crystals, this study conducts a mechanical analysis of grid rod elements, derives the corresponding periodic equations, and investigates their underlying periodic mechanisms. Numerical simulations confirm the existence of band gaps in steel and aluminum hybrid grid rods and examine the effects of the rod's Elastic modulus, density, and inner radius on these band gap characteristics. Finally, the impact attenuation performance of the steel–aluminum hybrid grid rod is compared with that of pure steel and pure aluminum grid rods. The results show that: (1) with increasing Elastic modulus, the starting frequency, end frequency, and width of the widest band gap all increase, while the starting frequency, end frequency, and width of the 13th-order band gap first increase and then disappear; (2) with increasing density, the width of the widest band gap decreases, and the starting frequency, end frequency, and width of the 16th-order band gap all decrease until it disappears; (3) with increasing inner radius, the width of the widest band gap increases, and the starting frequency, end frequency, and width of the 19th-order band gap all increase, with low-frequency band gaps gradually emerging; and (4) compared to steel and aluminum grid rods, the steel and aluminum hybrid grid rod exhibits superior impact wave attenuation performance, with the band gap characteristics of single-rod elements playing a critical role in suppressing vibrations throughout the entire grid structure.

ARTICLE HISTORY

Received: 11 March 2025
Revised: 4 July 2025
Accepted: 18 July 2025

KEYWORDS

Periodic structures;
Grid structure;
Band gap;
Vibration reduction and isolation;
Steel structure

1. Introduction

Grid structures exhibit excellent performance under extreme loads, such as large earthquakes. Therefore, large-scale buildings employing this structural form are often designated by the state as disaster shelters, highlighting the importance of evaluating their resilience under extreme conditions[1-4]. The safety of these structures is crucial for protecting public lives and ensuring social stability. As a result, progressive collapse in large-span structures has become a significant research focus, aiming to understand their sequential failure processes and anti-collapse mechanisms under sudden extreme loads. Given the waveguide properties inherent to periodic grid structures, stress waves generated by dynamic loads or group failures propagate within the structure. Due to the dispersive properties of periodic structures[5-8], phenomena such as wave blockage or localized resonance may occur[9], potentially leading to the localized storage of energy, causing member vibration buckling, pulse buckling, or even node fractures.

According to stress wave theory, stress and strain caused by vibrations primarily propagate through structures in the form of waves[10]. Periodic structures have attracted significant attention from researchers due to their desirable vibration-damping properties, which can block the propagation of stress waves. Effectively enhancing and leveraging the periodic properties of structures to achieve vibration damping is a current research hotspot. In 1992, M.M. Sigalas theoretically demonstrated the existence of elastic wave band gaps in three-dimensional periodic lattice structures made of composite materials, wherein elastic waves with frequencies within these gaps cannot propagate[11]. This concept evolved from the Bragg scattering mechanism to the localized resonance band gap mechanism, significantly broadening the range of wavelengths corresponding to band gap frequencies. Today, periodic structures find extensive applications in defense, aerospace[12], marine[13], and other fields. Michele Brun introduced the concept of phononic band gaps in structural mechanics, using waveguide properties to address vibration problems in slender bridges and extending this application to vibration reduction in high-rise structures[14].

The inherent wave conversion and frequency band gap characteristics of periodic structures lead to the suppression of elastic wave transmission within certain frequency ranges[15-16]. This underscores how innovative design and optimization based on structural periodicity can achieve effective vibration isolation. Muhammad et al. proposed sinusoidal connecting elements in two-dimensional periodic structures and found that certain geometric parameters influence the transmission and blocking characteristics of these structures[17]. Several scholars have conducted studies on concrete metamaterials, impact mitigation, vibration resistance, and blast resistance[18-22]. Feng[23] studied a two dimensional tunable acoustic crystal based on square rods. In this structure, 1.6 mm wide steel rods are arranged in air. By introducing variations in the scattering interface through symmetry breaking, achieved by simply rotating the square rods, the scattering cross section corresponding to different geometric factors changes from positive to negative refraction. This enables control over wave propagation and achieves tunable refraction of acoustic waves. Shen et al.[24] applied phononic crystal theory to guide the design of periodic structures in seawater pipeline systems. The designed structure can regulate the propagation characteristics of vibroacoustic waves within specific frequency bands, thereby achieving vibration reduction in the pipeline system. However, limited research has been carried out on the periodic properties of large-scale grid structures, which are most similar to crystal lattice structures, from the perspective of wave propagation and dispersion. This research gap is partly due to the conventional belief among engineers that the instantaneous nature of wave propagation does not significantly affect structural collapse[25], and partly due to the requirement that periodic dimensions must be approximately half the wavelength of elastic waves to realize Bragg band gaps[26-27]. Consequently, flat grid structures are often not considered to exhibit band gap properties. In reality, the concept of localized resonance has greatly extended these wavelength conditions. Previous discussions also indicate that the condition of matching half-wavelengths to member lengths is achievable. Numerical simulations of real structures have shown that grid structures exhibit characteristics of periodic structural responses. However, due to their three-dimensional forms and the coupling of bending and axial longitudinal waves, the analysis becomes more complex, resulting in narrower band gaps that are harder to detect. An, et al.[28] fabricated a three-dimensional acoustic metamaterial featuring a truss lattice structure using additive manufacturing techniques. Employing finite element analysis and numerical simulations, they systematically investigated the band structure of the proposed lattice and identified band gaps arising from local resonance and wave mode conversion. Zuo, et al. optimized the design of periodic rigid grid structures by altering unit shapes and geometric parameters, identifying factors that influence band gap characteristics[29]. Meruane, et al. proposed a new design of sandwich panels with cellular truss cores, aimed to harness these band gaps to achieve pronounced wave suppression within specific frequency ranges[30]. Modern

materials with complex architectures show higher structural efficiency when compared to traditional materials, Quinteros, et al. designed two-dimensional truss-like cellular structures to find best frequency range of each truss element[31]. By designing the structural parameters of periodic structures effectively, vibration isolation performance can be optimized.

Applications of periodic characteristic analysis in large bridge structures[32-33] and foundations[34] have demonstrated that macro-scale periodic structures also possess inherent band gap and dispersion properties. Some literature suggests that structural collapse may be caused by failure waves propagating within large structures[35]. Therefore, studying wave propagation characteristics in grid structures is essential for predicting structural health and providing theoretical explanations for certain failure causes. Using grid structures as research targets for wave dynamics within periodic structures offers advantages not found in lattice materials. This will promote the development of periodic structure research and help explain grid structure collapse incidents, guiding anti-collapse design through waveguide properties.

2. Mechanical Modeling Analysis of grid structure rod unit

2.1. grid structure rod unit

A large-scale grid structure consists of fundamental units connected in a periodic configuration, forming a highly redundant spatial system through the systematic arrangement of multiple members joined at nodes in a defined repeating pattern. The intersecting members and nodes provide mutual support in three dimensions, while the inherent vibration isolation characteristics of periodic structures further enhance their performance. As a result, grid structures possess wider applicability compared to planar trusses, which predominantly carry unidirectional loads. An illustrative example is the double-layer grid structure with a quadrangular pyramid configuration, as shown in Fig. 1.

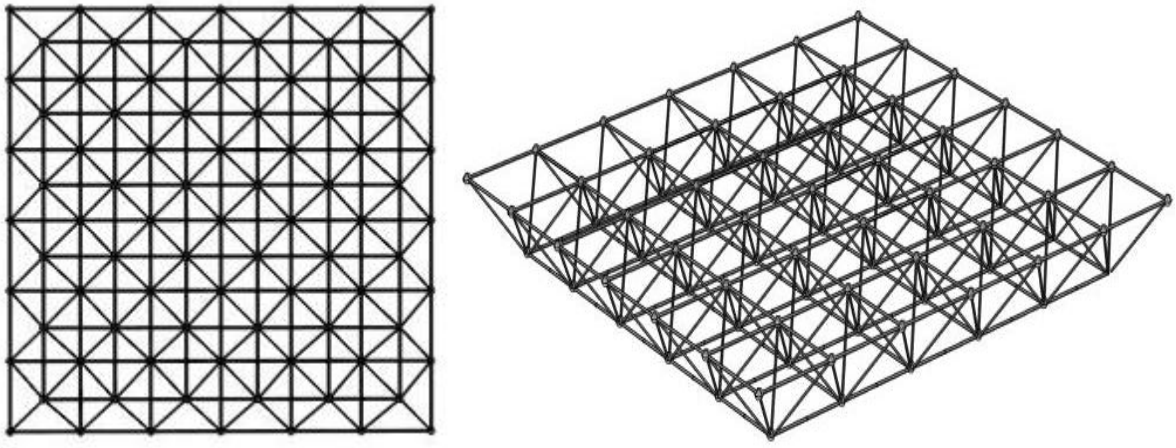

(a) Planar periodic grid structure (b)Three-dimensional diagram of periodic grid structure

Fig. 1 Periodic quadrangular pyramid grid

Grid structures are a type of periodic structure formed by the periodic arrangement of joints and members. This structure is created by repeating a minimal unit in a topological pattern, which allows for the analysis of the dynamic characteristics of grid structures to begin with a simplified dynamic analysis of the minimal unit and then extend to the entire structure. A quadrangular pyramid grid structure can be viewed as being composed of several quadrangular pyramids, as shown in Fig. 2.

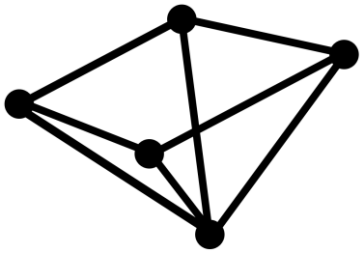

Fig. 2 Four-sided pyramid unit

Each quadrangular pyramid grid unit consists of several spherical nodes and members. When studying periodic structures, it is common practice to select the smallest periodic unit. Therefore, research into the band gap characteristics of periodic grid structures should begin with the member units, as illustrated in Fig. 3.

Fig. 3 grid structure rod unit

2.2. Periodical analysis of grid structures

When analyzing the band gap characteristics of periodic structures, it is essential to select a computational method appropriate to the specific features of the structure. The choice of method influences both the computational efficiency and the accuracy of the results. Over the years, through the research of many scholars, various methods for solving the bandgap have emerged, including the Plane Wave Expansion method (PWE)[36-38] and the Transfer Matrix method (TM)[39-41], et al. For the simplified mechanical analysis of grid structures, this section presents the transfer equation for the vibration response of member units within the grid structure. Since the grid structure exhibits periodicity, its analysis can be effectively carried out by examining the smallest repeating unit, applying appropriate boundary conditions, and solving accordingly. This section focuses on the dynamic analysis of the grid structure's member units. While members are typically idealized as axially loaded elements in conventional analyses, dynamic loading can excite a variety of vibration modes. As a result, members may display complex wave behavior beyond simple longitudinal compression and tension, including bending, torsional, and shear waves. Therefore, the member units are modeled as bending beam elements, as depicted in Fig. 4, with each unit characterized by two translational degrees of freedom and one rotational degree of freedom.

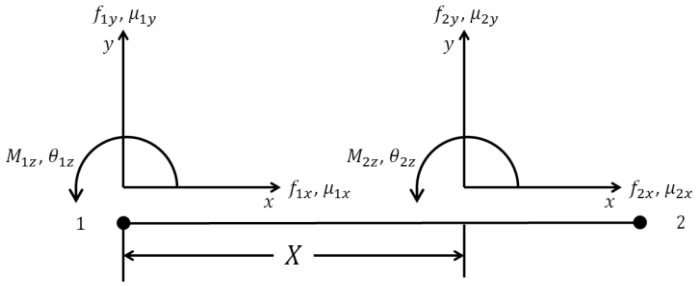

Fig. 4 Analysis model of single rod vibration

The input and output parameters of the rod cell vector in the smallest unit body of the grid structure in the local coordinate system are represented as follows:

$$S_1 = \{f_{1x}, f_{1y}, M_{1z}, u_{1x}, u_{1y}, \theta_{1z}\} \tag{1}$$

$$S_2 = \{f_{2x}, f_{2y}, M_{2z}, u_{2x}, u_{2y}, \theta_{2z}\} \tag{2}$$

Where f is the external load of the rod, M is the torque, u is the displacement value of the vibration response, θ is the angular displacement value of the torsional response, the subscripts x, y, z of each equation represent the axial, transverse and longitudinal directions of the coordinate system, respectively, and 1, 2 are the two end point marks. S_1 and S_2 represent the state vectors at the two end points.

The bending moment vibration equation is:

$$\frac{\partial f_y}{\partial x} + \frac{\partial f_x}{\partial R_m} = \rho h \ddot{u}_y \tag{3}$$

$$\frac{\partial f_x}{\partial x} + \frac{\partial f_y}{\partial R_m} = \rho h \ddot{u}_x \tag{4}$$

Where ρ for the material density, h for the equivalent height of beam section, R_m for the bending beam radius of curvature.

For the bending vibration equation, f_x, f_y, M_z can be solved using the equations from strength of materials.

According to the bending theory in mechanics of materials, for a curved beam with a radius of curvature R_m:

$$\varepsilon_x = \varepsilon_0 + y\kappa_z = \left(\frac{\partial u_x}{\partial x} - \frac{u_y}{R_m}\right) + y\kappa_z \tag{5}$$

Taking into account the effect of curvature on the elongation of any fiber within the curved beam, the resulting force is given by:

$$f_x = \int_A \sigma_x dA = E\int_{-\frac{h}{2}}^{\frac{h}{2}} \frac{\varepsilon_x + y\kappa_z}{1 + \frac{y}{R_m}} h dy = Eh\int_{-\frac{h}{2}}^{\frac{h}{2}} \frac{\varepsilon_x + y\kappa_z}{1 + \frac{y}{R_m}} dy \tag{6}$$

Since the rod is simplified as a curved beam, the axial strain distribution differs from the linear pattern observed in straight beams. Due to geometric nonlinear effects, the fiber length varies with the position Y, and therefore a correction term $1 + \frac{y}{R_m}$ is introduced.

According to shear deformation theory, the shear strain is given by:

$$\gamma_{xy} = \frac{\partial u_y}{\partial x} + \frac{u_x}{R_m} - \theta_z \tag{7}$$

Shear deformation is not merely a simple geometric slope variation; it also involves a combined effect of curvature and rotation. Therefore, the shear force can be expressed as:

$$f_y = \kappa G h \gamma_{xy} = \kappa G h \left(\frac{\partial u_y}{\partial x} + \frac{u_x}{R_m} - \theta_z\right) \tag{8}$$

The bending moment of the structure about the neutral axis z is expressed as:

$$M_z = \int_A y\sigma_x dA \tag{9}$$

Assuming a linear strain distribution and still using Eq.(5) as the axial strain, we obtain:

$$M_z = E\int_{-h/2}^{h/2} y\left(\left(\frac{\partial u_x}{\partial x} - \frac{u_y}{R_m}\right) + y\kappa_z\right) dy \tag{10}$$

The symmetric integral of the first term is zero, yielding:

$$M_z = EZ_2\left(\frac{\partial u_x}{\partial x} - \frac{u_y}{R_m} - R_m\frac{\partial \theta_z}{\partial x}\right) \tag{11}$$

According to planar bending theory, $\frac{\partial u_x}{\partial x} - \frac{u_y}{R_m} - R_m\frac{\partial \theta_z}{\partial x}$ represents the actual state of neutral bending and distortion under the applied loads.

In Eq.(6), $\varepsilon_x = \frac{\partial u_x}{\partial x} - \frac{u_y}{R_m}$, which is the longitudinal strain induced by longitudinal expansion combined with transverse bending, $\kappa_z = \frac{\partial \theta_z}{\partial x}$, which is the axial strain induced by torsion, and $Z_2 = -R_m h Z^*$, $Z^* = \frac{R_m}{h} ln\left(\frac{h}{R_m} + 1\right) - 1$, where G is the shear stiffness and κ is the shear constant. The expressions for ε_x and κ_z are substituted into Eq.(6) for simplification to obtain the following equation:

$$f_x = Eh\left(\frac{\partial u_x}{\partial x} - \frac{u_y}{R_m}\right)\int_h \frac{1}{1+\frac{y}{R_m}} dy + Eh\frac{\partial \theta_z}{\partial x}\int_h \frac{y}{1+\frac{y}{R_m}} dy \tag{12}$$

The integral term in Eq.(12) can be simplified, and the equation is as follows:

$$\int_h \frac{1}{1+\frac{y}{R_m}} dy = R_m ln\left(\frac{h}{R_m} + 1\right) = R_m h - R_m^2 ln\left(\frac{h}{R_m} + 1\right) \tag{13}$$

By substituting the simplified integral term into the original equation, the following expression is obtained:

$$f_x = EhZ_1\left(\frac{\partial u_x}{\partial x} - \frac{u_y}{R_m}\right) + EhZ_2\frac{\partial \theta_z}{\partial x} \tag{14}$$

where $Z_1 = h(1 + Z^*)$, and then by simultaneously solving Eqs.(3), (4), (6), (8), (11) and (14), we obtain the solution for the vector $S = \{f_x, f_y, M_z, u_x, u_y, \theta_z\}$, where differential matrix equation of each parameter is as follows:

$$B\frac{\partial S}{\partial x} = AS \tag{15}$$

$$A = \begin{bmatrix} 0 & \frac{1}{R_m} & 0 & -\rho h\omega^2 & 0 & 0 \\ -\frac{1}{R_m} & 0 & 0 & 0 & -\rho h\omega^2 & 0 \\ 0 & -1 & 0 & 0 & 0 & \frac{-\rho h^3\omega^2}{12} \\ \frac{1}{EhZ_1} & 0 & 0 & 0 & \frac{1}{R_m} & 0 \\ 0 & \frac{1}{\kappa Gh} & 0 & -\frac{1}{R_m} & 0 & 1 \\ 0 & 0 & -\frac{1}{EZ_2R_m} & 0 & -\frac{1}{R_m^2} & 0 \end{bmatrix} \tag{16}$$

$$B = \begin{bmatrix} 1 & 0 & 0 & 0 & 0 & 0 \\ 0 & 1 & 0 & 0 & 0 & 0 \\ 0 & 0 & 1 & 0 & 0 & 0 \\ 0 & 0 & 0 & 1 & 0 & -\frac{Z_2}{Z_1} \\ 0 & 0 & 0 & 0 & 1 & 0 \\ 0 & 0 & 0 & 0 & \frac{1}{R_m} & 1 \end{bmatrix} \tag{17}$$

where ω is the angular frequency.

The structure model is solved under harmonic excitation, and the solution to the equation is:

$$S(x) = B_0 e^{\lambda x} \tag{18}$$

Substituting Eq.(18) into the matrix equation and solving, we obtain the following expression:

$$[B^{-1}A - \lambda I]B_0 = 0 \tag{19}$$

Since the necessary and sufficient condition for a nonzero solution in matrix equations is that the determinant of the coefficient matrix must be zero, the following system of equations is obtained:

$$det[B^{-1}A - \lambda I] = 0 \tag{20}$$

Solving this matrix equation gives the characteristic root λ_i:

$$S(x) = B_0 \begin{pmatrix} e^{\lambda_1 x} & \cdots & 0 \\ \vdots & \ddots & \vdots \\ 0 & \cdots & e^{\lambda_i x} \end{pmatrix} C \tag{21}$$

where C is the coefficient matrix associated with the loading conditions.

Let the length of the smallest rod unit in the grid structure model be l. The vibration response from the left endpoint 1 to the right endpoint 2 is described by the transmission matrix equation:

$$S(x_2) = t(l)S(x_1) \tag{22}$$

where $t(l)$ is expressed as follows:

$$t(l) = B_0 \begin{pmatrix} e^{\lambda_1 l} & \cdots & 0 \\ \vdots & \ddots & \vdots \\ 0 & \cdots & e^{\lambda_i l} \end{pmatrix} B_0^{-1} \tag{23}$$

Eq.(22) describes the vibration transmission matrix relationship for a one-dimensional single-beam element. The next step is to extend this formulation to the grid structure. As shown in Fig. 5, the grid structure consists of multiple nodes and interconnected members, with each member unit featuring four input-output points at its ends. This configuration introduces greater complexity compared to a one-dimensional grid structure. For simplification, three degrees of freedom are considered at each point.

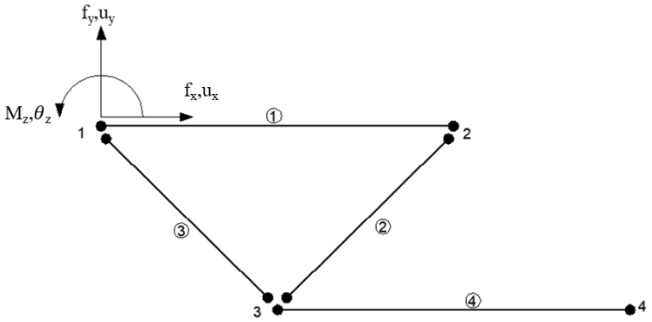

Fig. 5 Vibration analysis model of the smallest unit of grid structure

The relationship between the force and the vibration response is expressed as follows:

$$\{f, g\}_i = \{f_x, f_y, M_z, u_x, u_y, \theta_z\}_i^T \tag{24}$$

where $\{f\}_i$ represents the input force at the i-th interaction point of the selected subunit, and g denotes the vibration velocity response. The vibration response transfer relationship between points i and j at the ends of a rod is expressed in matrix form as follows:

$$\{f, g\}_i = T_{ij}\{f, g\}_j \tag{25}$$

where i and j are from the set (1, 2, 3, 4). The transfer matrix is given as:

$$T_{ij} = \begin{bmatrix} t_{11} & t_{12} \\ t_{21} & t_{22} \end{bmatrix} \tag{26}$$

Using the finite element method, the admittance matrix relationship between points i and j for the grid beam element is obtained as:

$$\{\{g\}_i, \{g\}_j\}^T = H_{ij}\{\{f\}_i, \{f\}_j\}^T \tag{27}$$

In Eq.(27), H is the admittance matrix as follows:

$$H_{ij} = \begin{bmatrix} H_{11} & H_{12} \\ H_{21} & H_{22} \end{bmatrix} \tag{28}$$

In the above equation, H_{11} is the admittance matrix of point i, H_{22} is the admittance matrix of point j, H_{12} and H_{21} are the transfer admittance responses between points i and j. From the admittance matrix equation, the transfer matrix from the input vibration response at point i to the output vibration response at point j is given by:

$$T_{ij} = \begin{bmatrix} -H_{21}^{-1}H_{22} & -H_{21}^{-1} \\ -H_{12}H_{11}H_{21}^{-1}H_{22} & H_{11}H_{21}^{-1} \end{bmatrix} \tag{29}$$

When applied to grid structures, each nodal point within the grid possesses three degrees of freedom, and interactions occur between the degrees of freedom of different connected members. Accordingly, Eq. (26) is modified to become:

$$[T] = \begin{bmatrix} T_{3m\times 3m} & T_{3m\times 3n} \\ T_{3n\times 3m} & T_{3n\times 3n} \end{bmatrix} \tag{30}$$

Since the grid structure is formed by periodic arrangement of the smallest unit cells, the transfer matrix for the grid structure can be derived as:

$$[T] = [T]_1[T]_2[T]_3 \cdots [T]_k \tag{31}$$

According to the theory of elastic dynamics, the elastic wave of simple harmonic vibration can be described by the following equation:

$$\nabla \cdot \big(C(r) : \nabla u(r)\big) + \rho(r)\omega^2 u(r) = 0 \tag{32}$$

Where $\nabla = \left(\partial/\partial x, \partial/\partial y, \partial/\partial z\right)$ is the differential operator, ":" is the double dot product, $u(r)$ is the displacement vector, $r = (x, y, z)$ is the position vector, $\rho(r)$ is the density of the material, and $C(r)$ is the elastic tensor of the material.

In the low-frequency range or near the dominant band gap, the dynamic behavior of the structural unit cell is primarily governed by a finite number of degrees of freedom, represented by its effective mass and equivalent stiffness. Based on the previous derivations, the dynamic transfer matrix of the unit cell is obtained and applied to periodic boundary conditions to derive the dispersion relation. This low-order approximation, rigorously derived from the transfer matrix method, enables accurate prediction of the dynamic characteristics within the primary band gap.

According to Bloch's theorem, the displacement field of a periodic structure can be expressed as:

$$u(r) = e^{i(k\cdot r)}u_k(r) \tag{33}$$

where $i = \sqrt{(-1)}$, $u(r)$ is the displacement field within a unit cell , which shares the same periodicity as the phononic crystal structure. The wave vector $K = (k_x, k_y)$ is constrained to the first Brillouin zone.

When the periodic boundary conditions are applied to the finite element eigenvalue equation for free vibration, it becomes:

$$(K - \omega^2 M)U = 0 \tag{34}$$

This generalized eigenvalue problem with respect to ω^2 is solved by traversing the wave vector k within the irreducible Brillouin zone to obtain the dispersion relationship between the eigenfrequency ω and the wave vector k, thus determining the band gap characteristics of the periodic grid structure.

For the rod- sphere assembly, compared to the sphere, the rod has both relatively smaller mass and stiffness, it can be considered as a unit cell of a phononic crystal, which can be roughly simplified into a spring-mass-spring structure, as illustrated in the Fig. 6.

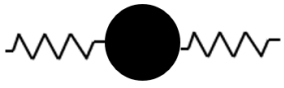

Fig. 6 Spring-mass-spring model

Then, the expression for the starting frequency of the band gap in the simplified model can be given as:

$$f_1 = \frac{1}{2\pi}\sqrt{\frac{k}{M}} \tag{35}$$

where k is the equivalent stiffness of the spring, and M is the equivalent mass.

The derivation of k and M is more complex than that for a two-dimensional phononic crystal unit cell or a metamaterial concrete unit cell. Eq.(35) is intended to reveal the general mechanism and trends of band gap formation rather than to provide precise quantitative predictions.

3. Vibration characteristic of periodic grid rod structures

3.1. Verification of the presence of band gaps in periodic grid rod structures

In order to verify the accuracy of the model in this paper, the calculation results in this paper are compared with the results in the literature[29]. The material parameters and geometric dimensions of the model used in the checking calculation are all from the literature[29]. The model in the text was constructed using COMSOL, as shown in Fig. 7.

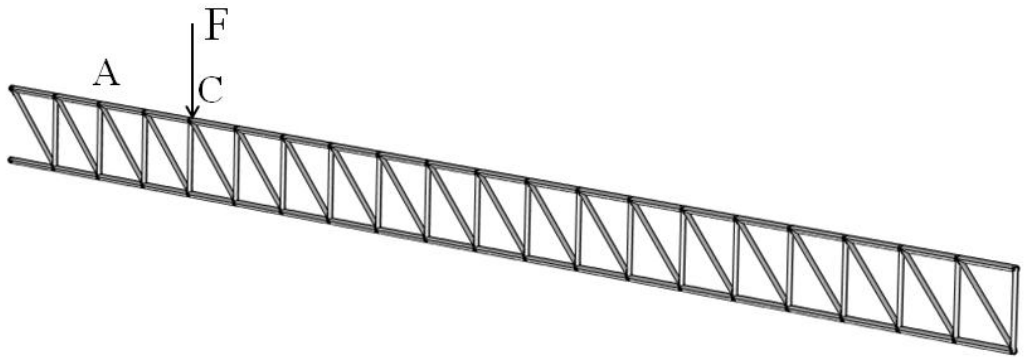

Fig. 7 Truss model in the reference

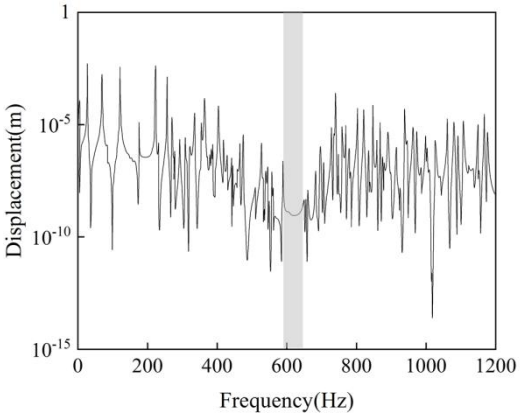

Fig. 8 Frequency-domain calculation results

Fixed constraints are applied at the upper and lower ends on the left side of the structure. A force F of 10 N is applied at point C, and point A is set as the receiving point. The displacement-frequency curve is obtained through frequency-domain analysis, as shown in Fig. 8.

By comparing the stop-band region from the reference literature with the results in Fig. 8, it can be seen that the stop-band obtained from the COMSOL calculation is 585 Hz to 641 Hz, while the reference literature reports a range of 590 Hz to 646 Hz. The value obtained by the finite element calculation is very closed to that found in the literature, so it is thought that the finite calculation is suitable for the calculation of band gap in this paper.

By intentionally altering the material properties of the rods within the grid structure, it is possible to induce distinct band gap characteristics in the system. In this study, a numerical model of the rod elements in a four-sided pyramid grid structure, as illustrated in Fig. 9, was developed using the commercial finite element software COMSOL Multiphysics. In the model, all rods have a uniform length of 4 meters, an outer radius of 0.066 meters, and a wall thickness of 0.006 meters. The spherical nodes possess an outer radius of 0.15 meters and a wall thickness of 0.01 meters.

Fig. 9 Schematic diagram of material grouping of gird rod

As shown in Fig. 9, the single-rod elements of the grid structure are divided into two groups, with the rod on the left named as rod A and the blue rod on the right named as rod B. The material for rod A is selected as steel, while the material for rod B is aluminum. The spherical nodes are all made of steel. The specific material parameters are provided in Table 1.

Table 1
Material parameters of grid rod unit

Material	Density（kg/m^3）	Elastic modulus(GPa)	Poisson's ratio
Steel	7800	200	0.3
Aluminium	2700	70	0.3

From the data in the table 1, it can be observed that the density and Elastic modulus of steel and aluminum differ significantly, resulting in considerable mass and stiffness differences between adjacent rods. This variation facilitates the development of band gap characteristics in the rod elements.

Periodic boundary conditions are applied to both sides of the grid rod elements, restricting displacement along the x-axis. To verify the mesh sensitivity of the rod structure calculations, different mesh sizes were set and analyzed. In this study, a relatively fine mesh was used for the rod calculations, with a maximum element size of 0.44 m and a minimum element size of 0.032 m. For the validation model, an ultra-fine mesh was applied, with a maximum element size of 0.337 m and a minimum element size of 0.0144 m. Both models were then computed separately for comparison. The model is automatically meshed using tetrahedral elements and subjected to a parametric scan for characteristic frequencies, with the first 20 characteristic frequencies obtained. The resulting characteristic frequency graph is shown in Fig. 10.

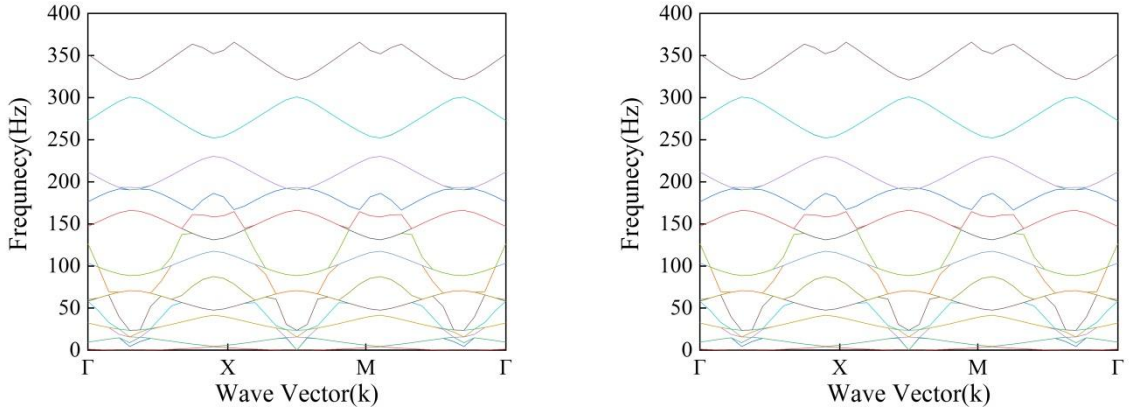

(a) The mesh size is relatively fine (b) The mesh size is ultra-fine

Fig. 10 Grid structure rod unit band gap diagram

As shown in Fig. 10, the calculation results of the model under the two mesh conditions are completely consistent. Therefore, under the mesh conditions used in this study, mesh sensitivity does not affect the model calculations, and the results obtained with this mesh configuration are accurate.

From Fig. 10, it can be observed that the rod structure exhibits two band gaps. The first band gap starts at 230.45 Hz and ends at 252.29 Hz, with a width of 21.84 Hz; the second band gap starts at 300.65 Hz and ends at 321.50 Hz, with a width of 20.85 Hz. This demonstrates that by artificially altering the materials of adjacent rods in the grid structure element, the four-sided pyramid grid structure can achieve its band gap characteristics.

3.2. Analysis of the parameters affecting the band gap of gird structure rod units

According to Eq.(35), the equivalent stiffness influences the value of the band gap. Based on the existing equivalent stiffness calculation equation [42], it is evident that the Elastic modulus of the rods, the cross-sectional dimensions, and the density of the spherical nodes play a crucial role in affecting the starting frequency of the band gap.

To investigate the factors affecting the start frequency, end frequency, and the width of the band gap in grid rod units, an analysis is conducted by varying the material parameters and geometric dimensions to understand their impact on the band gap characteristics of the grid rod units.

3.2.1. Difference in Elastic modulus of adjacent rod materials

Without changing other material parameters and geometric dimensions, only the Elastic modulus of the B rod material is varied. The specific values for the Elastic modulus are provided in Table 2.

Table 2
Elastic modulus of group B

	Elastic modulus（GPa）
Condition 1	0.07
Condition 2	0.7
Condition 3	7
Condition 4	70

The band gap characteristics of the grid rod units under four operating conditions are obtained through calculations, as shown in Fig. 11. The first band gap under different operating conditions is selected for analysis, with its start frequency, end frequency, and width of band gap listed separately for analysis, as shown in Fig. 12.

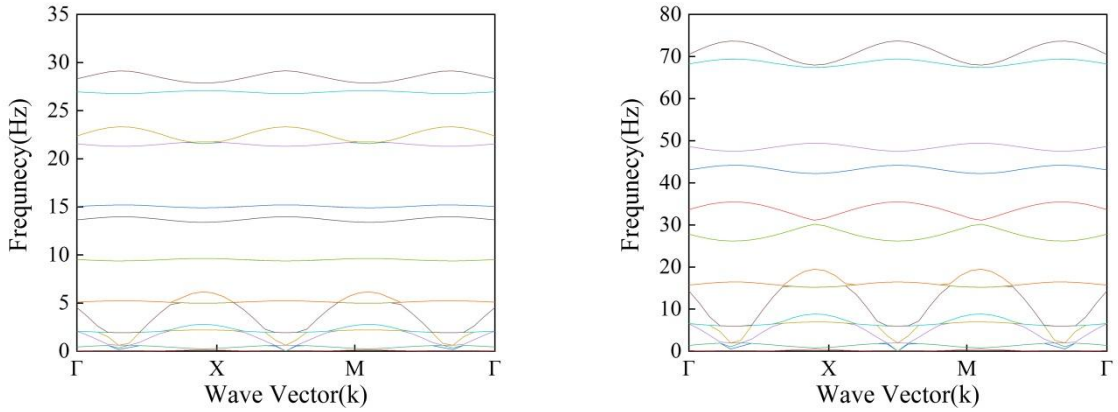

(a) The Elastic modulus of group B is 0.07GPa (b) The Elastic modulus of group B is 0.7GPa

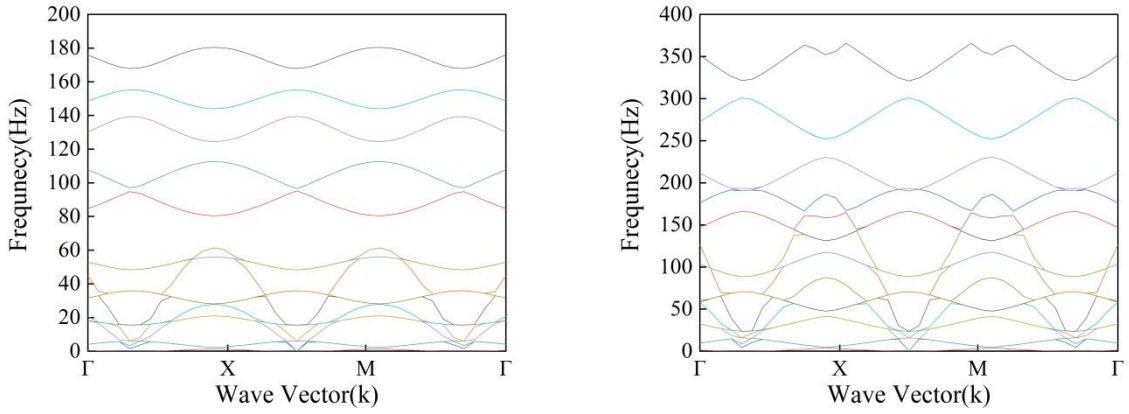

(c) The Elastic modulus of group B is 7GPa (d) The Elastic modulus of group B is 70GPa

Fig. 11 Effect of Elastic modulus of group B on the band gap diagram of grid rod unit

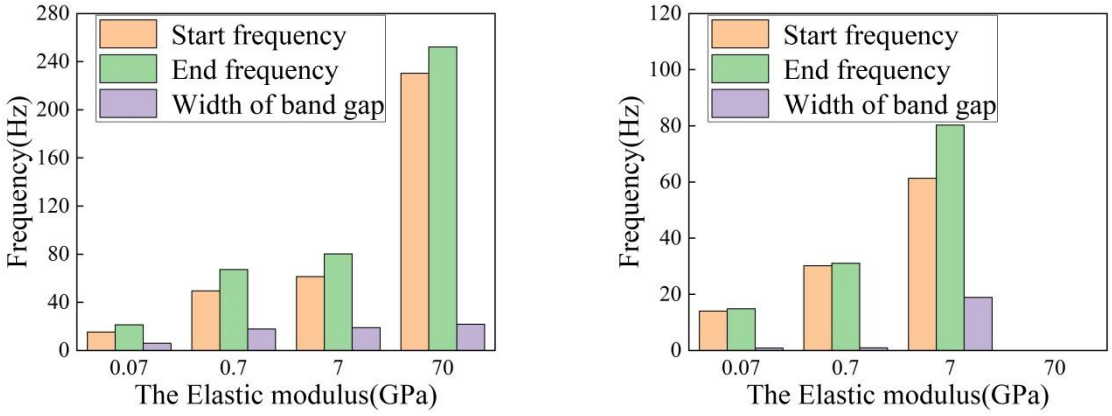

(a) The maximum width band gap (b) The 13th-order band gap

Fig. 12 The variation of band gap diagram under different Elastic modulus conditions for Group B

As shown in Fig. 11 and Fig. 12, when the Elastic modulus of the Group B material is 0.07GPa, four distinct band gaps are observed. The first band gap has a start frequency of 6.16 Hz, an end frequency of 9.40 Hz, and a width of 3.24 Hz. The second band gap starts at 9.73 Hz and ends at 13.36 Hz, with a width of 3.63 Hz. The third band gap, which has the largest width at this modulus, ranges from 15.25 Hz to 21.27 Hz with a width of 6.02 Hz. The fourth band gap spans from 23.34 Hz to 26.71 Hz, with a width of 3.37 Hz. When the Elastic modulus is increased to 0.7GPa, four clear band gaps also appear. The first band gap starts at 19.42 Hz and ends at 26.10 Hz, with a width of 6.68 Hz. The second ranges from 35.56 Hz to 42.11 Hz (width 6.55 Hz), the third from 44.32 Hz to 47.43 Hz (width 3.11 Hz), and the fourth, which has the largest width at this modulus, extends from 49.51 Hz to 66.30 Hz with a width of 17.79 Hz. When the Elastic modulus is 7GPa, four band gaps are again evident. The first band gap, with the largest width at this modulus, ranges from 61.35 Hz to 80.25 Hz, with a width of 18.90 Hz. The second band gap spans 112.79–124.40 Hz (width 11.61 Hz), the third 139.44–144.20 Hz (width 4.76 Hz), and the fourth 155.41–168.02 Hz (width 12.61 Hz). When the Elastic modulus is increased to 70GPa, only two prominent band gaps are observed. The first, which has the largest width across all cases, starts at 230.45 Hz and ends at 252.29 Hz, with a width of 21.84 Hz. The second ranges from 300.96 Hz to 320.98 Hz with a width of 20.02 Hz. If all other material properties and geometric dimensions are held constant, increasing the elastic modulus of Group B raises the natural frequencies of the quadrangular pyramid grid structure. Analysis of the widest band gaps indicates that band gap width generally increases with the elastic modulus of Group B. Given the large number of band gaps present, only one representative band gap is selected for detailed analysis.

By comparing the band gap between the 13th and 14th characteristic frequencies under different conditions of Elastic modulus, it can be observed that when the Elastic modulus of the Group B rods increases, the equivalent stiffness also increases. Consequently, the start frequency, end frequency and the width of band gap for the grid rod unit both increase, however, when the Elastic modulus reaches 70GPa, the 13th-order band gap disappears. This is because as the Elastic modulus of the group B rods increases to 70GPa, the difference in equivalent stiffness between the rods and the spherical nodes decreases, making it difficult for band gaps to form in the low-frequency range. As the natural frequencies of the structure increase, the band gap regions gradually shift toward higher frequencies. For the low-frequency range, when the Elastic modulus of the Group B rods is 7GPa, the value falls within the peak band gap width region; however, for the high-frequency range, 70GPa has not yet reached the peak band gap width region.

3.2.2. Difference in density of adjacent rod materials

Assuming that other material parameters and geometric dimensions remain unchanged, if only the density of the group B material is varied, the specific density values can be found in Table 3.

Table 3
Density values for group B

	Density（kg/m^3）
Condition 1	1000
Condition 2	2700
Condition 3	6000
Condition 4	10000

The band gap characteristics of the quadrangular cone grid structure under four different operating conditions were calculated and are displayed in Fig. 13. The band gap with the largest width under each condition was selected for analysis, with its start frequency, end frequency, and width of band gap presented separately for further examination, as shown in Fig. 14.

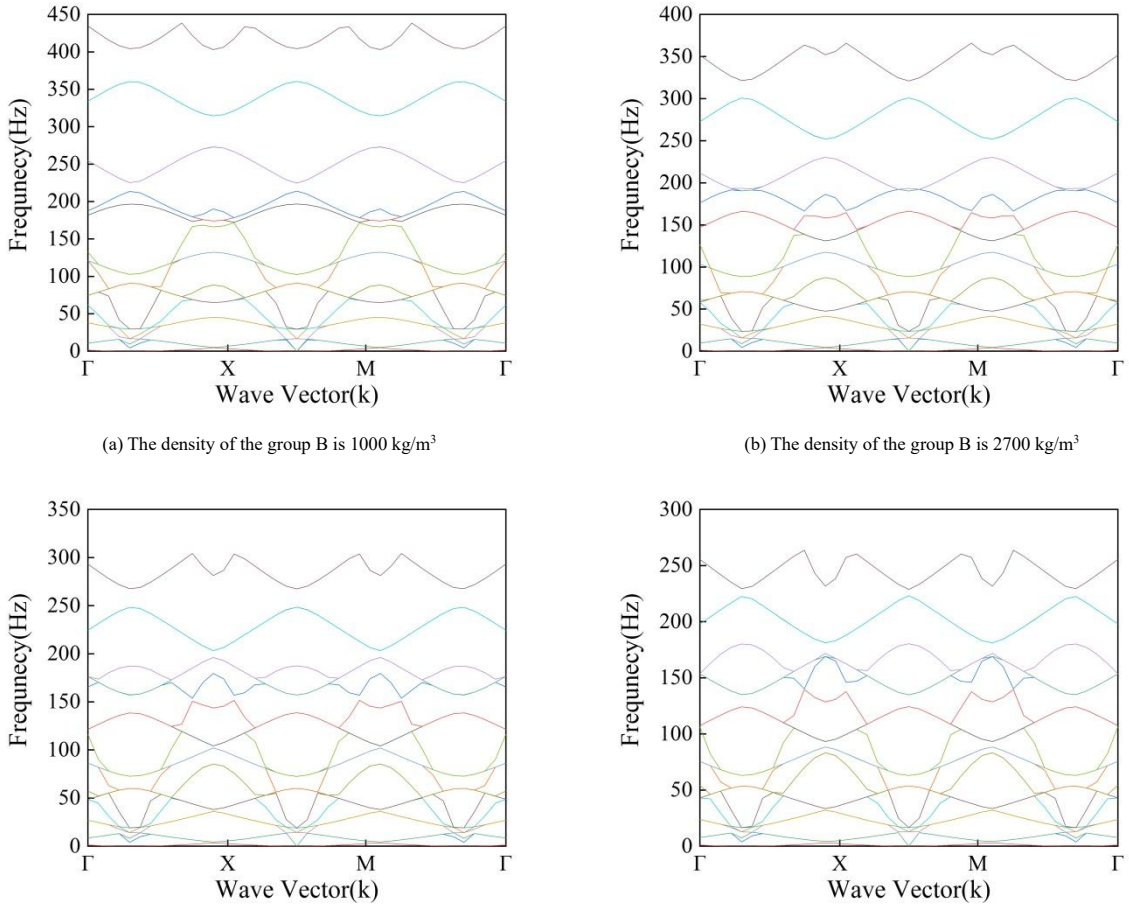

(a) The density of the group B is 1000 kg/m³

(b) The density of the group B is 2700 kg/m³

(c) The density of the group B is 6000 kg/m³

(d) The density of the group B is 10000 kg/m³

Fig. 13 Effect of material density of group B on the band gap diagram of grid rod unit

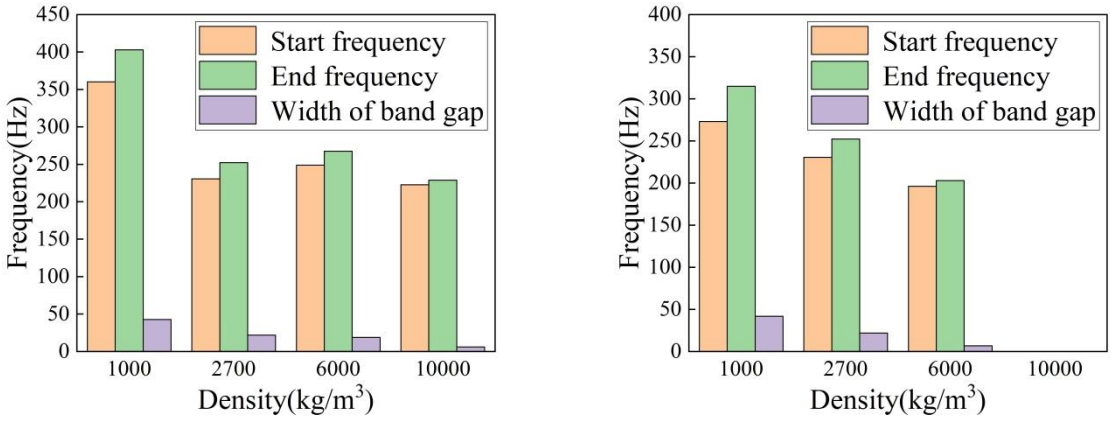

(a) The maximum width band gap

(b) The 16th-order band gap

Fig. 14 The variation of band gap diagram under different density conditions for Group B

As illustrated in Fig. 13 and Fig. 14, when the density of the Group B material is 1000 kg/m³, three distinct band gaps are observed. The first band gap begins at 213.67 Hz and ends at 225.38 Hz, with a width of 11.71 Hz. The second band gap spans from 273.70 Hz to 314.64 Hz, with a width of 40.94 Hz. The third band gap, which has the largest width at this density, extends from 360.10 Hz to 402.89 Hz, with a width of 42.79 Hz. When the density of the Group B material increases to 2700 kg/m³, two clear band gaps emerge. The first band gap, with the largest width, ranges from 230.45 Hz to 252.29 Hz (width 21.84 Hz), and the second spans from 300.96 Hz to 320.98 Hz (width 20.02 Hz). At a density of 6000 kg/m³, two band gaps are also identified. The first starts at 196.10 Hz and ends at 203.81 Hz, with a width of 7.71 Hz. The second, having the larger width, extends from 248.75 Hz to 267.40 Hz, yielding a band gap width of 18.65 Hz. When the density is further increased to 10,000 kg/m³, only a single band gap is present, ranging from 222.75 Hz to 228.86 Hz, with a width of 6.11 Hz. If other material parameters and geometric dimensions remain constant, increasing the density of the Group B material results in a decrease in the self-oscillation frequency of the quadrangular cone grid structure. Moreover, The maximum band gap width initially decreases, then increases, and decreases again with the increase of the density of the Group B rods. This behavior occurs because, as the density of the Group B rods increases, the rate at which the low-frequency band gap width decreases first slows down and then accelerates, while the high-frequency band gap width decrease rate initially accelerates and then slows down. Therefore, at a density of 2700 kg/m³, the low-frequency band gap width surpasses that of the high-frequency band gap region. However, as the density continues to increase, the rate of decrease of the low-frequency band gap width rapidly grows, and the high-frequency band gap width decrease rate diminishes. At a density of 10000 kg/m³, the low-frequency band gap disappears entirely, leaving only the high-frequency band gap present.

By comparing the band gap between the 16th and 17th characteristic

frequencies under different density conditions, it can be observed that as the density of the Group B rods increases, the mass of the rods also increases. Consequently, the start frequency and end frequency of the band gap for the grid rod unit decrease, resulting in a reduction in the width of band gap, until the density reaches 10,000 kg/m³, the 16th-order band gap in the low-frequency range no longer exists. As the density of the rods increases, the density of the Group B rods gradually approaches that of the adjacent rods, reducing the acoustic impedance contrast between neighboring materials. This leads to a decrease in the interface reflection coefficient and an increase in the transmissibility between rods, thereby disrupting the periodic impedance contrast necessary for band gap formation and resulting in the inability to form band gaps.

3.2.3. Difference in inner radius of group B rods

Without changing other material parameters and geometric dimensions, only the density of the Group B material is changed and the specific density values are taken from Table 4.

Table 4
Inner radius of group B

	Inner radius（m）
Condition 1	0.051
Condition 2	0.054
Condition 3	0.057
Condition 4	0.060

The band gap characteristics of the grid rods under four conditions have been calculated and are illustrated in Fig. 15. A band gap with the maximum width under various operating conditions has been selected for analysis, with its start frequency, end frequency, and width of band gap separately listed for examination, as shown in Fig. 16.

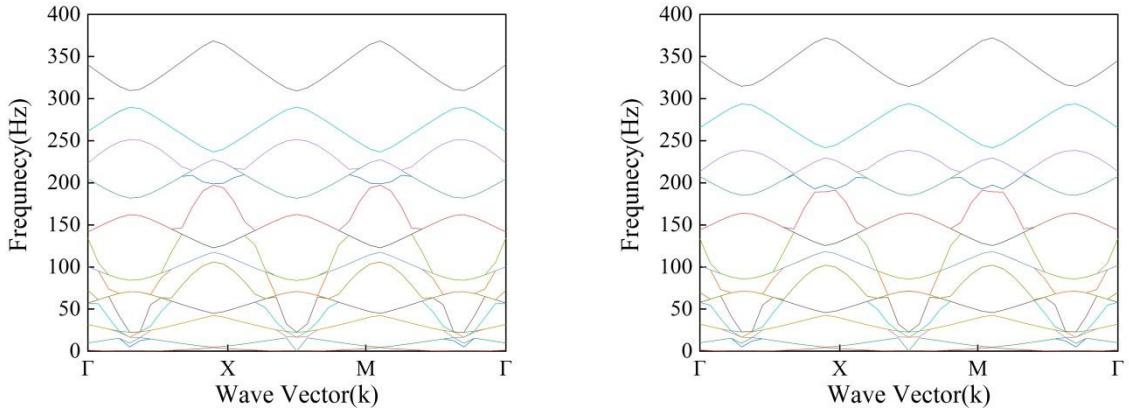

(a) The inner radius of the rod is 0.051 m

(b) The inner radius of the rod is 0.054 m

(c) The inner radius of the rod is 0.057 m

(d) The inner radius of the rod is 0.06 m

Fig. 15 Effect of material density of group B on the band gap diagram of grid rod unit

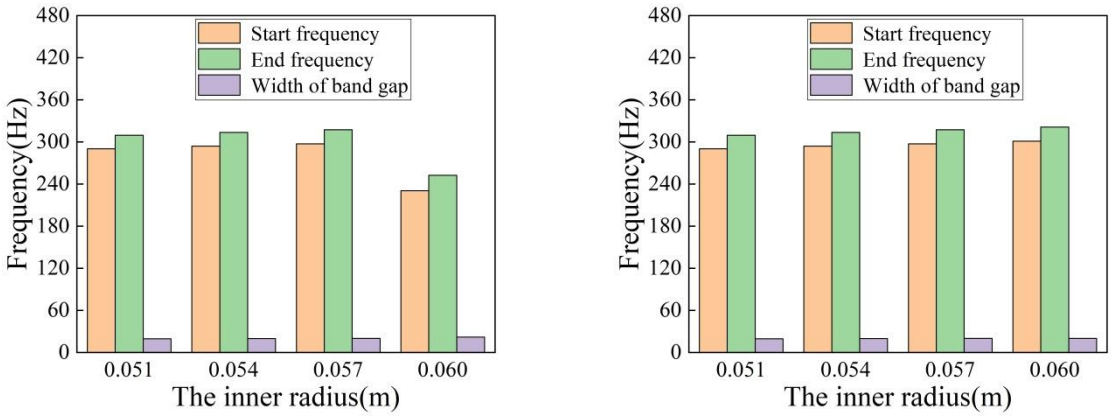

(a) The maximum width band gap

(b) The 19th-order band gap

Fig. 16 The variation of band gap diagram under different inner radius conditions for Group B

As shown in Fig. 15 and Fig. 16, when the inner radius of the Group B rod is 0.051 m, a pronounced band gap is observed, with a start frequency of 290.10 Hz, an end frequency of 309.56 Hz, and a band gap width of 19.46 Hz. When the inner radius is increased to 0.054 m, a similarly clear band gap appears, starting at 294.00 Hz and ending at 313.64 Hz, with a width of 19.64 Hz. When the inner radius reaches 0.057 m, two distinct band gaps are present. The first band gap occurs in the lower frequency range, starting at 231.15 Hz and ending at 246.86 Hz, with a width of 15.71 Hz. The second band gap spans from 297.34 Hz to 317.26 Hz, with a width of 19.92 Hz. When the inner radius is further increased to 0.06 m, two clear band gaps are again observed. The first band gap has the largest width, starting at 230.45 Hz and ending at 252.29 Hz, with a width of 21.84 Hz. The second band gap begins at 300.96 Hz and ends at 320.98 Hz, with a width of 20.02 Hz. If other material parameters and geometric dimensions remain unchanged, by analyzing the largest width of band gap, it can be concluded that the largest width of band gap increases as the inner radius of the Group B rods increases. By comparing the band gap between the 19th and 20th frequencies under different inner radius conditions, it can be seen that as the inner radius increases, both the start frequency, end frequency and width of the band gap increase. As the inner radius gradually increases, high-frequency band gaps gradually decreases. However, the band gap in the low-frequency range appears and gradually widens. This is because as the inner radius of the hollow rods increases, the wall thickness decreases and stiffness reduces. Consequently, the ratio of the bending or longitudinal wave wavelength to the unit cell scale increases, weakening localization effects in the high-frequency range. As a result, high-frequency short waves tend to propagate as nearly continuous waves at the unit cell scale, making it difficult to form high-frequency band gaps.

3.3. Multifactor Analysis

In order to compare the changes in the band gap characteristics of the grid structure rod elements under multiple parameter conditions, the three parameter conditions are calculated for analysis, and the largest width of band gap is selected for further analysis. Table 5 provides a detailed listing of the values for each parameter and their corresponding band gap values.

Table 5
Parameter combinations and their corresponding band gap values

Elastic modulus(GPa)	Inner radius(m)	Density(kg/m^3)	Start frequency(Hz)	End frequency(Hz)	Width of band gap(Hz)
0.07	0.051	1000	23.40	32.00	8.60
	0.051	2700	14.50	20.20	5.70
	0.051	6000	10.20	13.75	3.55
	0.051	10000	8.35	10.78	2.43
	0.054	1000	23.90	32.20	8.30
	0.054	2700	14.75	20.57	5.82
	0.054	6000	10.22	13.95	3.73
	0.054	10000	8.26	10.94	2.68
	0.057	1000	24.20	32.30	8.10
	0.057	2700	15.00	20.90	5.90
	0.057	6000	10.30	14.20	3.90
	0.057	10000	8.20	11.10	2.90
	0.06	1000	24.60	32.40	7.80
	0.06	2700	15.25	21.27	6.02
	0.06	6000	10.43	14.48	4.05
	0.06	10000	8.25	11.25	3.00
0.7	0.051	1000	74.80	94.80	20.00
	0.051	2700	48.83	64.00	15.17
	0.051	6000	37.90	44.28	6.38
	0.051	10000	32.80	35.08	2.28
	0.054	1000	76.00	95.50	19.50
	0.054	2700	49.20	65.12	15.92
	0.054	6000	38.90	44.85	5.95
	0.054	10000	19.04	21.70	2.66
	0.057	1000	77.00	95.70	18.70
	0.057	2700	49.38	66.30	16.92
	0.057	6000	37.62	45.60	7.98
	0.057	10000	18.58	21.92	3.34
	0.06	1000	78.20	96.10	17.90
	0.06	2700	49.51	66.30	17.79
	0.06	6000	36.83	45.60	8.77
	0.06	10000	17.71	21.92	4.21
7	0.051	1000	151.90	185.15	33.25
	0.051	2700	151.50	174.90	23.40
	0.051	6000	117.00	133.27	16.27
	0.051	10000	60.75	66.90	6.15
	0.054	1000	153.80	187.80	34.00

Elastic modulus(GPa)	Inner radius(m)	Density(kg/m^3)	Start frequency(Hz)	End frequency(Hz)	Width of band gap(Hz)
	0.054	2700	153.15	178.10	24.95
	0.054	6000	117.80	135.80	18.00
	0.054	10000	59.90	66.87	6.97
	0.057	1000	108.90	143.46	34.56
	0.057	2700	154.45	181.10	26.65
	0.057	6000	118.00	137.70	19.70
	0.057	10000	58.50	66.83	8.33
	0.06	1000	106.50	146.72	40.22
	0.06	2700	61.35	80.25	18.90
	0.06	6000	68.75	83.50	14.75
	0.06	10000	56.82	66.78	9.96
70	0.051	1000	266.50	304.20	37.70
	0.051	2700	290.10	309.56	19.46
	0.051	6000	241.63	252.80	11.17
	0.051	10000	0.00	0.00	0.00
	0.054	1000	269.00	309.00	40.00
	0.054	2700	294.00	313.64	19.64
	0.054	6000	245.12	257.63	12.51
	0.054	10000	217.50	221.90	4.40
	0.057	1000	271.35	313.17	41.82
	0.057	2700	297.34	317.26	19.92
	0.057	6000	247.50	262.80	15.30
	0.057	10000	220.78	225.50	4.72
	0.06	1000	360.10	402.89	42.79
	0.06	2700	230.45	252.29	21.84
	0.06	6000	248.75	267.40	18.65
	0.06	10000	222.75	228.86	6.11

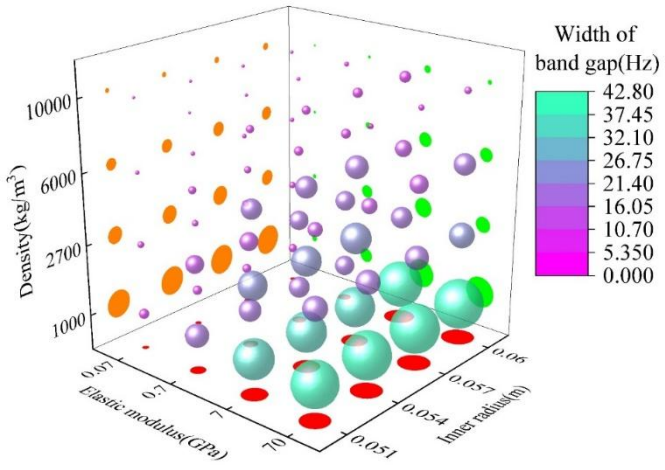

Fig. 17 3D scatter plot of the maximum band gap width under the combined effects of three factors

Based on Table 5 and Fig. 17, for the same density and inner radius conditions, the maximum band gap width increases with the Elastic modulus of the Group B rods. Under high-density and large inner radius conditions, the band gap width is relatively low because the impedance difference between rods decreases, weakening interface scattering effects. A smaller inner radius leads to reduced rod stiffness, which suppresses the formation of high-frequency band gaps. When the Elastic modulus is 0.07GPa or 0.7GPa, for the same Elastic modulus and density, the maximum band gap width decreases as the inner radius of the Group B rods increases. However, when the elastic modulus is 7GPa or 70GPa, under the same Elastic modulus and density, the maximum band gap width increases with increasing inner radius. When both Elastic modulus and density increase simultaneously, the equivalent stiffness difference between rods decreases, and the acoustic impedance contrast reduces, making it difficult to form wide band gaps. For the same Elastic modulus and inner radius, the maximum band gap width decreases as the density of the Group B rods increases. As the rod inner radius increases, wall thickness decreases and stiffness reduces, while the ratio of bending or longitudinal wave wavelength to unit cell scale increases. Additionally, the stiffness difference between adjacent rods diminishes, weakening localization effects in the high-frequency range. Consequently, high-frequency short waves tend to propagate as nearly continuous waves at the unit cell scale, hindering the formation of high-frequency band gaps.

Among the four selected values for each factor, the Elastic modulus undoubtedly has the greatest and most direct influence because it directly affects the equivalent stiffness of the structure. Considering that the Elastic modulus values span orders of magnitude, its impact on band gap values is greater than that of density, which also increases by an order of magnitude. Therefore, the effect of Elastic modulus is more significant than that of density. Compared to the rod inner radius, since the rod volume is proportional to the square of the rod radius, an equivalent numerical change in inner radius has the largest impact on band gap values. However, the range of inner radius variation studied here is very small (on the order of 10^{-3}m), and in practical engineering applications, changing the Elastic modulus through material selection is much easier than drastically altering structural dimensions. Thus, under the conditions studied in this paper, the Elastic modulus has the greatest influence on the structural band gap values, followed by density, with inner radius having the least impact.

4. Attenuation effects of periodic grid structures on shock waves

In order to study the damping effect of the periodic grid structure on vibration loads, the band gap range of the grid structure is determined through simulation calculations. The self-oscillation characteristics and damping effects on shock waves are investigated by applying shocks with different initial frequencies. Specifically, the self-oscillation characteristics of the grid structure and its attenuation effect on the shock wave are examined.

To illustrate the damping effect of the periodic grid structure on the shock wave, the periodic grid structure model shown in Fig. 18 is created by COMSOL Multiphysics software. The model consists of three rod units arranged in a linear direction. To eliminate the influence of boundary effects, a fixed constraint is applied at the rightmost side of the grid structure. An initial excitation is applied to the left side of the model, while a receiver is placed on the right side of the model, as shown in Fig. 18. A total of three conditions are set up for the simulation. In all conditions, the material of the ball nodes is steel. In Condition 1, all rod materials are selected as steel; in Condition 2, all rod materials are selected as aluminium; and in Condition 3, the rod materials are selected according to the material grouping shown in Fig. 9. All material parameters are chosen based on the data provided in Table 1.

A frequency excitation of 240 Hz and 150 Hz was applied separately to the rod structure, with both excitation durations set to 1 second. The chosen excitation frequency of 240 Hz lies within this band gap range (230.45–252.29 Hz), where the structure is expected to suppress the propagation of vibrational waves. In theory, as long as the selected excitation frequency falls within this band gap range, the hybrid rod is expected to provide better attenuation of vibrational wave propagation compared to pure steel and pure aluminum rods. However, in practical engineering and experimental settings, manufacturing tolerances, assembly inaccuracies, and measurement errors can cause discrepancies between the actual band gap range and the simulation results. To facilitate future experimental validation and comparison, it is advisable in simulations to choose an excitation frequency near the midpoint of the band gap range. Therefore, 240 Hz was selected. The expressions are as follows:

$$D_1 = 0.001\,sin(2\pi \times 240t) \tag{36}$$

$$D_2 = 0.001\,sin(2\pi \times 150t) \tag{37}$$

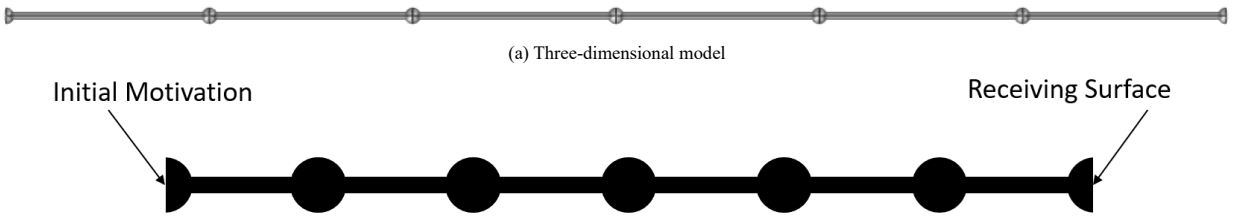

(a) Three-dimensional model

(b) Two-dimensional diagram

Fig. 18 Schematic diagram of grid structure calculation

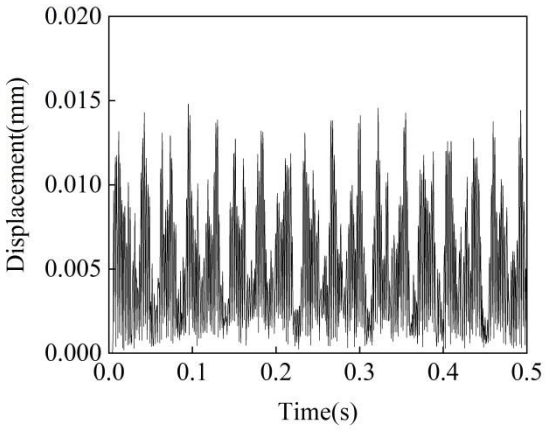

(a)Steel grid structure rods

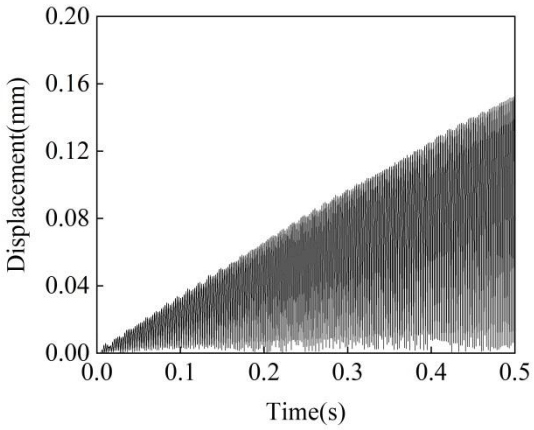

(b)Aluminium grid structure rods

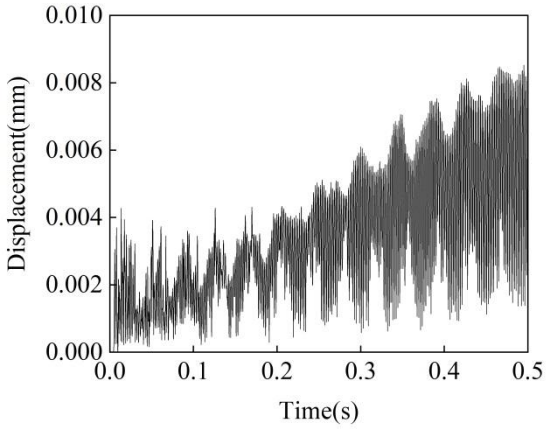

(c)Steel and aluminium hybrid grid structure rods

Fig. 19 Displacement-Time curve of grid rods under D_1

First, the lattice rod structure was subjected to the D_1 excitation, and the displacement time-history curves under different material components were obtained, as shown in Fig. 19. The displacement time histories for the three conditions obtained by transient analysis are shown in Fig. 20. For the steel

grid structure, the peak displacement at the measurement point is 0.0148mm; for the aluminum grid structure, the peak displacement at the measurement point is 0.1526mm; for the steel-aluminum hybrid grid structure, the peak displacement is 0.0085mm. Using the peak displacement of the steel-aluminum hybrid lattice rod as the reference, the peak displacement of the pure steel lattice rod is 174.12% of the reference value, while that of the pure aluminum lattice rod is 1795.29% of the reference value, which proves that the steel-aluminium grid structure rods have better shock wave attenuation than the traditional steel structure grid structure rods.

By applying the Fast Fourier Transform (FFT), the displacement time-history curve in Fig. 19(c) was converted into the displacement frequency-domain curve, yielding displacement responses at different frequencies. Using the Eq.(38), the transmission loss at each frequency was then calculated.

$$\eta = 20lg\left(\mu_{out}/\mu_{in}\right) \tag{38}$$

where μ_{out} refers to the response at the receiving, and μ_{in} refers to the response at the input end.

The calculation results are shown in Fig. 20. As observed from the figure, the transmission curve exhibits significant attenuation within the band gap region of the rod unit, reaching a minimum value of -15.10 dB. This demonstrates that the structure has an effective attenuation capability when subjected to external impacts within the band gap frequency range.

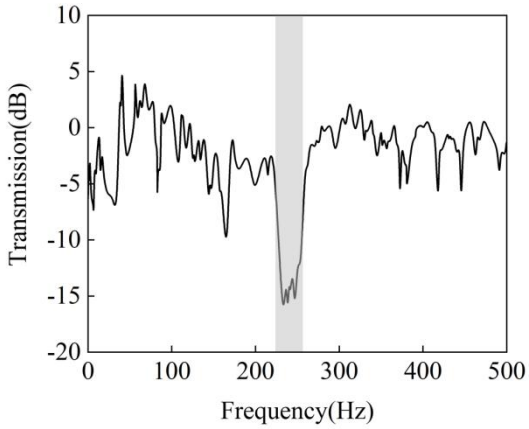

Fig. 20 Transmission loss of the lattice rod structure

For comparison, an D_2 excitation was applied to the lattice rod structure, and the displacement time-history curves for different material components were obtained, as shown in Fig. 21.

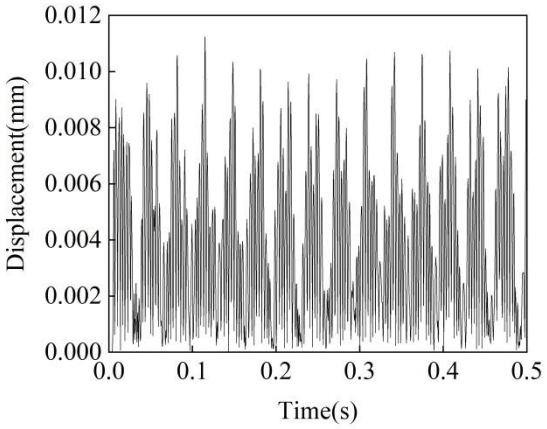

(a) Steel grid structure rods

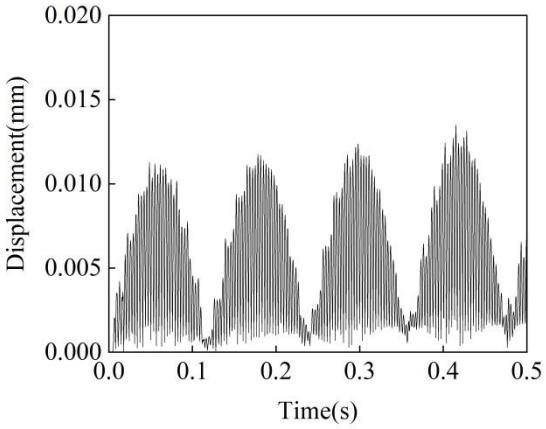

(b) Aluminium grid structure rods

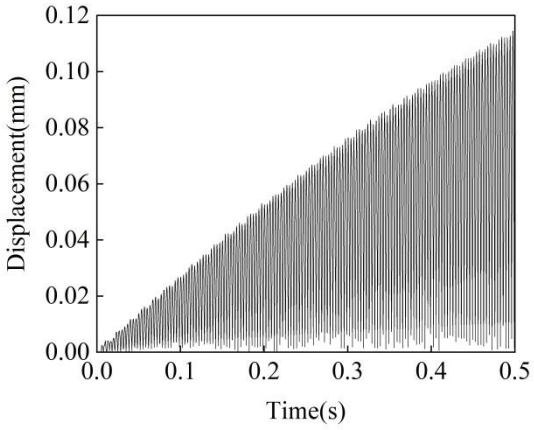

(c) Steel and aluminium hybrid grid structure rods

Fig. 21 Displacement-Time curve of grid rods under D_2

The displacement time histories for the three conditions obtained by transient analysis are shown in Fig. 21. For the steel grid structure, the peak displacement at the measurement point is 0.0112mm; for the aluminum grid structure, the peak displacement at the measurement point is 0.0135mm; for the steel-aluminum hybrid grid structure, the peak displacement is 0.1141mm. Using the peak displacement of the steel-aluminum hybrid lattice rod as the reference, the peak displacement of the pure steel lattice rod is 9.82% of the reference value, and that of the pure aluminum lattice rod is 11.83%. This indicates that when subjected to impacts at frequencies outside the band gap range, the steel-aluminum hybrid rod structure no longer exhibits attenuation. On the contrary, due to its unique material composition, the steel-aluminum hybrid lattice shows poorer attenuation performance against external impacts

compared to the traditional all-steel lattice.

Compared to hybrid rods, steel–aluminum hybrid rods exhibit superior impact wave attenuation not only due to the band gap effect, which filters specific frequency components, but also because the acoustic impedance mismatch at material interfaces leads to multiple wave scatterings and partial reflections. In an ideal periodic structure, conceived as an infinite repetition of unit cells, the cumulative effect of interface scattering gives rise to the formation of band gaps. However, in practical scenarios, the size of a periodic structure is finite. The actual attenuation effect arises from the combined action of energy suppression within the band gap frequency range and multiple interface scatterings outside the band gap range. The band gap effect and wave scattering are interrelated and jointly operative mechanisms: interface scattering is the physical basis for band gap formation, while in finite structures it also independently contributes to broadband impact energy dissipation.

Although steel–aluminum hybrid rods can effectively suppress impact waves and vibrations through band gap effects and impedance scattering, several challenges exist in practical engineering applications. First, due to the significant difference in thermal expansion coefficients between steel and aluminum, the interface is prone to residual stresses and potential cracking under thermal cycling, requiring specialized joining techniques to ensure interface integrity. Second, the formation of galvanic couples between the two metals can lead to electrochemical corrosion in humid or saline environments, necessitating effective isolation coatings or cathodic protection measures, which increase manufacturing and maintenance costs. Additionally, achieving standardized and modular structural designs is more complex.

In order to further understand the attenuation mechanism, A frequency sweep analysis was conducted on the structure shown in Fig. 18 under the following conditions: an initial prescribed displacement of 10^{-6} m was applied to the leftmost end of the structure, a receiving surface was positioned at the rightmost end, and low-reflection boundary conditions were imposed on both the left and right ends. The frequency sweep spanned from 10Hz to 300Hz with a 1Hz interval. In Condition 1, all rod materials are selected as steel; in Condition 2, all rod materials are selected as aluminium; and in Condition 3, the rod materials are selected according to the material grouping shown in Fig. 9. All material parameters are chosen based on the data provided in Table 1.

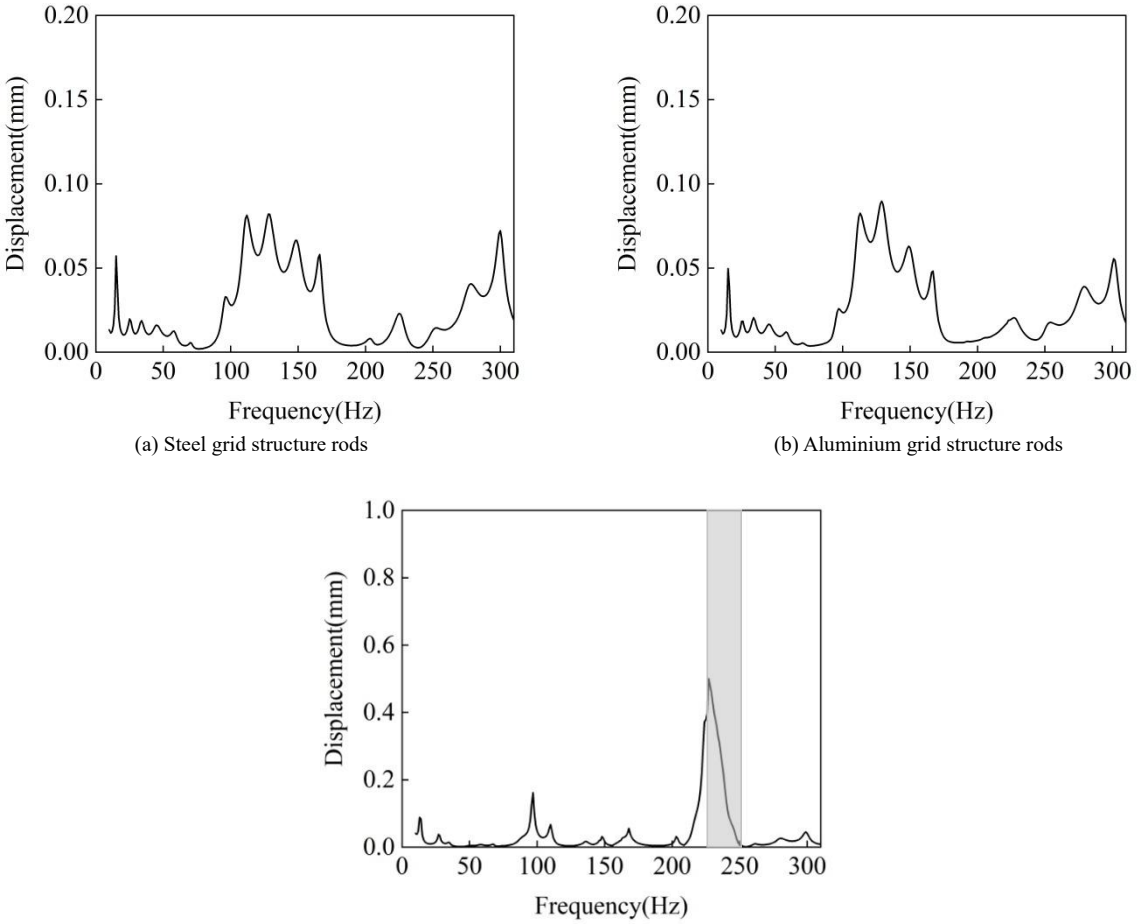

(a) Steel grid structure rods

(b) Aluminium grid structure rods

(c) Steel and aluminium hybrid grid structure rods

Fig. 22 Frequency-Displacement curve of grid rods

Fig. 22 shows that for the steel grid and aluminum grid structures, the displacement at the measurement point exhibits no significant attenuation across the 10Hz–300Hz frequency range. However, for the steel-aluminum hybrid grid structure, a prescribed displacement attenuation is observed within the frequency range of 225.53Hz to 253.74Hz, where the displacement decreases from 0.56mm to 0.003mm. As shown in Fig. 9, the band gap of the steel-aluminum hybrid single-bar structure spans 230.45Hz to 252.29Hz, which lies entirely within the displacement attenuation frequency range. This confirms that the steel-aluminum hybrid grid structure exhibits significant attenuation for waves within the band gap frequency range. Furthermore, this result demonstrates that the band gap characteristics of the single-bar structure play a critical role in suppressing vibrations across the entire grid structure.

5. Conclusion

In order to study the vibration reduction and isolation effects of periodic grid structures, this paper analyzes the band gap characteristics of the grid rod units and their shock wave attenuation effects, and draws the following conclusions:

(1) The grid structure is a typical periodic structure, and the analysis methods for periodic structures can be applied to the grid structure. The grid rod unit can be roughly simplified into a spring-mass spring mechanical model, and its band gap calculation equation can reflect the variation of parameters. By intentionally modifying the grid structure, its band gap characteristics can be achieved.

(2) Rods with low Elastic modulus can form low-frequency band gaps, but the width of band gap is narrow, with the increase of the Elastic modulus of the group B, the start frequency, end frequency, and width of the 13th-order band gap and the largest width band gap all increase, however, when the Elastic modulus reaches 70GPa, the 13th-order band gap disappears, meaning the low-frequency band gap vanishes, while the high-frequency band gap width continues to increase. Rods with lower density can form wider band gaps, with

the increase of the density of the group B, the largest width of band gap gradually decreases, The starting frequency, end frequency, and bandwidth of the 16th-order band gap all decrease, and the 16th-order band gap disappears when the density reaches 10,000 kg/m³. As the inner radius of the group B increases, the starting frequency, end frequency, and bandwidth of the 19th-order band gap all increase. When the inner radius of the group B reaches 0.057 m, a low-frequency band gap appears, and its bandwidth continues to increase with the inner radius.

(3) Compared to steel grid structure rods and aluminium grid structure rods, the steel-aluminium hybrid grid structure rods exhibit stronger attenuation effects on shock waves, the band gap characteristics of the single-bar structure play a critical role in suppressing vibrations across the entire grid structure.

(4) Compared to traditional dampers, the hybrid rod solution offers inherent broadband vibration suppression potential within the structure itself, without relying on external power or maintenance, providing better life cycle cost advantages in enclosed and temperature controlled environments. However, under conditions of high corrosion or significant temperature variations, conventional viscous or friction dampers, due to their mature manufacturing processes, simple maintenance, and flexible design, may be more competitive in terms of cost and reliability. Therefore, the design and application of steel and aluminum hybrid rods require a comprehensive life cycle cost benefit analysis tailored to specific operating conditions.

Acknowledgement

This research was funded by National Natural Science Foundation of China, grant number (12172244).

Declaration

The authors declare that they have no known competing financial interests or personal relationships that could have appeared to influence the work reported in this paper.

Appendix

S_1: State vector at endpoint 1;
S_2: State vector at endpoint 2;
f: the external load of the rod;
M: the torque;
u: the displacement value of the vibration response;
θ: the angular displacement value of the torsional response;
ρ: the material density;
h: the equivalent height of beam section;
R_m: the bending beam radius of curvature;
G: the shear stiffness;
κ: the shear constant;
ω: angular frequency;
C: the coefficient matrix associated with the loading conditions;
$\{f\}_i$: the input force at the i-th interaction point of the selected subunit;
g: the vibration velocity response;
H: the admittance matrix;
∇: the differential operator;
$u(r)$: the displacement vector;
$r = (x, y, z)$: the position vector;
$\rho(r)$: the density of the material;
$C(r)$: the elastic tensor of the material;
$u_1(r)$: the displacement field within a unit cell;
K: the wave vector;
k: the equivalent stiffness of the spring;
M_1: the equivalent mass;
μ_{in}: input response;
μ_{out}: output response.

Reference

[1] Li H W. Planning and Design of Urban Disaster Earthquake Shelters and Disaster Relief Strongholds[M]. China Architecture and Building Press, 2013.
[2] Ding B D, Lv H L, Li X, et al. Tests for dynamical progressive collapse of a grid structure based on key member failure[J]. Journal of Vibration and Shock. 2015, 34(23):106-114.
[3] Adam J M, Parisi F, Sagaseta J, et al. Research and practice on progressive collapse and robustness of building structures in the 21st century[J]. Engineering Structures, 2018, 173(OCT.15):122-149.
[4] Xue H, Wang H, Liu X G. Effects of supporting-substructure lateral stiffness on the internal forces of grid structures[J]. Journal of Constructional Steel Research, 2025, volume 224, part A, 109155.
[5] Lord rayleigh, On the maintenance of vibrations by forces of double frequency and on the propagation of waves through a medium endowed with a periodic structure, Philosophical Magazine XXIV, 1887, 145-159.
[6] Floquet G. Sur les équations différentielles linéaires à coefficients périodiques[J]. Annales Scientifiques de l'Éolecole Normale Supérieure, 1883, 12: 47-88.
[7] Bloch F. Über die quantenmechanik der electronen in kristallgittern[J]. Zeitschrift Für Physik AHadrons & Nuclei, 1929, 52:555-600.
[8] Mead D M. Wave propagation in continuous periodic structures: research contributions from Southampton[J]. Journal of Sound and Vibration, 1996, 190(3):495-524.
[9] Zhu X, Li T Y, Zhao Y. Vibration energy flow characteristics and damage identification of crack damaged structures[M], Huazhong University of Science and Technology Press, 2017.
[10] Zhao X Z, Yan S, Chen Y Y. Comparison of progressive collapse resistance of single-layer latticed domes under different loadings[J]. Journal of Constructional Steel Research, 2017, 129(Complete):204-214.
[11] Sigalas M M, Economou E N. Elastic and Acoustic wave band structure[J]. Journal of Sound and Vibration, 1992, 158(2):377-382.
[12] Wang D Z, Zhi X D, Fan F, et al. The energy-based failure mechanism of reticulated domes subjected to impact[J]. Thin Walled Structures, 2017, 119:356-370.
[13] Lin L. Refined study on impact response and failure of reticulated shells[D]. Harbin Institute of Technology, 2015.
[14] Brun M, Movchan A B, Jones I S. Phononic band gap systems in structural mechanics: finite slender elastic structures and infinite periodic waveguides [J].Journal of Vibration and Acoustics, 2013, 135(4):041013.1-041013.9.6.
[15] Gao M, Kong X L, Zhao L Z, et al. Study on band gap characteristics of periodic structural wave impeding block[J]. China Civil Engineering Journal, 2022:11.
[16] Xiong Y H, Li F M. Optimization of Band-gap Characteristics of Hierarchical Periodic Beam[J]. Chinese Journal of Solid Mechanics, 2021, 42 (06)：634-641.
[17] MUHAMMAD, LIM C W, YAW Z, et al. Periodic and a-periodic 3-D composite metastructures with ultrawideband gap for vibration and noise control[J]. Composite structures, 2022, 287: 115324.
[18] Liu Y, An X Y, Chen H L, et al. Vibration attenuation of finite-size meta-concrete: Mechanism, prediction and verification[J]. Composites Part A: Applied Science and Manufacturing, 2021, Volume 143,106294.
[19] Zhang E, Lu G Y, Yang H W et al. Band gap characteristics of metamaterial concrete and its attenuation effect on shock wave[J]. Explosion and Shock. 2020,40(6):66-74.
[20] Han J, Lu G Y. A study of undamped free vibration characteristics on a metaconcrete unit cell[J]. Vibration and Shock, 2021, 40(08), 173-178+215.
[21] Xu C, Chen W S, Hao H. The influence of design parameters of engineered aggregate in metaconcrete on band gap region[J]. Journal of the Mechanics and Physics of Solids, 2020, 139:103929.
[22] Akintoye O. Oyelade *, Yetunde. O. Abiodun , Mufutau O. Sadiq. Dynamic behaviour of concrete containing aggregate resonant frequency[J]. JCAMECH, 2018.269048.339.
[23] Feng L, Liu X P, Lu M H, et al. Refraction control of acoustic waves in a square-rod constructed tunable sonic crystal[J]. Physical Review B, 2006, 73(19):193101.
[24] Shen H J. Control of Sound and Vibration for Seawater Pipe System Based on Phononic Ctrystal Theory [D]. National University of Defense Technology, 2015.
[25] Zhao X Z, Yan S. Mechanisms of Continuous Collapse of Space Structures and Design Countermeasures[M]. China Architecture and Building Press, 2018.
[26] Wen X S, Wen J H, Yu D L, et al. Phononic Crystals[M]. National Defense Industry Press, 2008.
[27] Wen J H, Yu D L, Zhao H G, et al. Elastic wave propagation in artificial periodic structures: vibrational and acoustic properties [M]. China Science Publishing & media Ltd., 2016.
[28] An X Y, Lai C L, He W P, et al. Three-dimensional meta-truss lattice composite structures with vibration isolation performance[J]. Extreme Mechanics Letters, 2019, 33.
[29] ZUO S L, LI F M, ZHANG C Z. Numerical and experimental investigations on the vibration band-gap properties of periodic rigid frame structures[J]. Acta mechanica, 2016, 227(6): 1653-1669.
[30] Meruane V, Puiggros I, Fernandez R, et al. Efficient design of sandwich panels with cellular truss cores and large phononic band gaps using surrogate modeling and global optimization[J]. Frontiers in Mechanical Engineering, 2024, volume 10.
[31] Quinteros L, Meruane V, Cardoso E L. Phononic band gap optimization in truss-like cellular structures using smooth P-norm approximations[J]. Structural and Multidisciplinary Optimization, 2021, volume 64, pages 113-124.
[32] Brun M, Movchan A B, Jones I S. Phononic band gap systems in structural mechanics: finite slender elastic structures and infinite periodic waveguides[J]. Journal of Vibration and Acoustics, 2013, 135(4):041013.1-041013.9.
[33] Michele B, Felice G G, Movchan A B, et al. Transition Wave in the Collapse of the San Saba Bridge[J]. Frontiers in Materials, 2014, 1.
[34] Meng Q J, Shi Z F. Ambient vibration attenuation by periodic pile barriers using periodic theory and COMSOL PDE method [J]. Rock and Soil Mechanics, 2018, 39(11):343-352.
[35] Cherepanov G P. Mechanics of the WTC collapse[J]. International Journal of Fracture, 2006, 141(1-2):287-289.
[36] Dal Poggetto V F, Serpa A L. Flexural wave band gaps in a ternary periodic metamaterial plate using the plane wave expansion method[J]. Journal of Sound and Vibration, 2021, 495.
[37] V. F D P, Alberto L S. Elastic wave band gaps in a three-dimensional periodic metamaterial using the plane wave expansion method[J]. International Journal of Mechanical Sciences, 2020, 184.
[38] Hong X, Guo W J, Dai C X. Effect of Hysteresis Damping on Vertical Vibration Band Gap Characteristics of Periodic Track Structure[J]. Journal of East China Jiaotong University, 2023, 40(01):82-91.
[39] S. K A. Multichannel tunable polarizing filter properties of one-dimensional ternary photonic crystal containing single-negative materials[J]. Indian Journal of Physics, 2021: 1-11.
[40] Shahsavari H, Talebitooti R, Kornokar M. Analysis of wave propagation through functionally graded porous cylindrical structures considering the transfer matrix method[J]. Thin-Walled Structures, 2021, 159.
[41] Threetanya P, Puttharaksa C, Plaipichit S, et al. Recursive transfer-matrix method for second-harmonic generation in a one-dimensional nonlinear photonic crystal at arbitrary incidence angle[J]. Journal of Physics: Conference Series, 2021, 1719(1).
[42] Zhao H X, Zhang E, Lu G Y. Study on the equivalent stiffness of a local resonance metamaterial concrete unit cell[J]. Buildings, 2024, (14):1035.

Advanced Steel Construction – Vol. 22 No. 2 (2026) 237–243
DOI:10.18057/IJASC.2026.22.2.9

EXPERIMENTAL STUDY ON MECHANICAL PROPERTIES OF PREFABRICATED BEAM AND SLAB UNITS OF NEW ASSEMBLED RAFT FOUNDATION

Ji-Zhi Su [1], Chen-Lei Wang [2], Wen-Tao Qiao [2, 3, *], Wu-Chen Zhang [1] and Li-Huan Wang [1]

[1] *Economic and Technological Research Institute, State Grid Hebei Electric Power Co., Ltd, Shijiazhuang, China*
[2] *School of Civil Engineering, Shijiazhuang Tiedao University, Shijiazhuang, China*
[3] *Key Laboratory of Roads and Railway Engineering Safety Control (Shijiazhuang Tiedao University), Ministry of Education, Shijiazhuang, China*
** (Corresponding author: E-mail: qwt@stdu.edu.cn)*

ABSTRACT

Prefabricated foundations offer numerous advantages such as convenient construction, high bearing capacity, energy efficiency, environmental friendliness, and less wet work on-site. Accordingly, this study introduces a novel structural system based on an assembled beam-slab foundation. To further explore the mechanical properties of the precast beam slab units in the modular beam-slab foundation, experimental research and numerical simulation were conducted. Test findings indicate that the structure primarily undergoes bending-type failure. From the yielding of the specimen to the attainment of the ultimate load, the specimen undergoes significant displacement changes, indicating that the structure possesses good bending resistance and ductility. Based on the experimental results, an accurate finite element model was established for parametric analysis. The findings indicate that the bearing capacity of the foundation slab is significantly influenced by parameters such as reinforcement ratio and slab thickness, with the reinforcement ratio having the most pronounced effect. The ultimate load-carrying capacity increases with the reinforcement ratio, composite slab thickness, and concrete strength. In contrast, the thickness of the C-section steel has the least effect on the bearing capacity, with the foundation slab's bearing capacity remaining virtually unchanged.

ARTICLE HISTORY

Received: 19 January 2025
Revised: 23 July 2025
Accepted: 2 August 2025

KEYWORDS

Assembled raft foundation;
Prefabricated beam and slab units;
Static loading test;
Numerical simulation

1. Introduction

With rapid urbanization, the number of high-rise buildings in China has been steadily increasing, leading to greater loads transferred from superstructures to foundations. When the superstructure is subjected to heavy loads and the foundation exhibits limited bearing capacity, conventional independent or strip foundations often fail to satisfy deformation control requirements. Under such circumstances, raft foundations have been widely applied. Raft foundations not only meet the requirements of different foundation bearing capacities but also make more effective use of underground space, thus having broad application prospects and promotional value[1, 2].

At present, numerous scholars have conducted extensive experimental research and theoretical analysis on raft foundations. Among them, Wang[3] conducted experimental studies on single-span and multi-span beam-slab raft foundations with different slab thicknesses, revealing the distribution pattern of foundation reaction under various load conditions. Yu et al.[4]conducted full-scale experimental studies on two groups of beam-slab raft foundation specimens. During the loading process, the foundation exhibited overall positive bending, while the internal slab grid areas showed characteristics of negative bending. Akash et al.[5] investigated the influence of factors such as pile length, number of piles, and diameter on the load distribution of pile-raft foundations. Xi et al.[6] carried out experimental research on the load-bearing behavior of pile-raft foundations, and the study demonstrated that pile-raft slab foundations outperform conventional pipe pile foundations. Hoang et al.[7] investigated the long-term performance of three pile-raft foundations with different numbers of piles, revealing that load magnitude significantly impacts the distribution of loads between the raft and piles over time. Anuj et al.[8] conducted an analysis on pile-raft foundations revealing that their bearing capacity is considerably higher than raft foundations, with pile length, spacing, and soil density showing strong positive correlations with load-bearing performance. Overall, these studies highlight the structural advantages and performance improvements of raft and pile-raft foundations under various loading and soil conditions, but there remains a need for further exploration of more efficient structural forms tailored for prefabrication and assembly.

With the development of prefabricated buildings, the feasibility of adopting reasonable prefabricated foundation forms has attracted increasing attention. Several scholars have conducted in-depth research on this topic. Rasmussen[9] proposed a prefabricated strip foundation made of EPS, which is only suitable for small buildings with no more than two floors. Adams[10] introduced a prefabricated concrete block foundation component that connects to the superstructure by arranging rebar and casting concrete on-site. Dae Hong Kim et al.[11] designed a micropile foundation for transmission towers, where each foundation component is connected by bolts. Catalano[12] proposed a detachable prefabricated foundation component suitable for temporary buildings with relatively small upper loads, where the foundation components are bolted to the foundation beams. Li et al.[13] proposed a novel prefabricated foundation structure for transmission lines and conducted numerical simulation analysis. The results indicate that the structure satisfactorily fulfills the functional demands. In summary, current prefabricated foundations are mostly used in structures with small upper loads, and related research is relatively limited. Therefore, studying a prefabricated foundation structure with better bearing capacity and a wider range of applications is of great significance.

In recent years, a large number of scholars have carried out comprehensive research on composite slabs. Ranzi et al.[14] conducted experiments to evaluate the flexural performance of composite slabs with steel strand, proposing a theoretical calculation model suitable for prestressed composite slabs. Crisinel et al.[15] introduced an analytical approach for calculating the load-bearing capacity of composite slabs. Qiao et al.[16] proposed a novel cold-formed thin-walled steel-concrete composite slab and conducted experimental studies on its flexural performance, the test results revealed that this structure exhibits good mechanical performance. Vainiūnas et al.[17] investigated the shear performance of profiled steel sheet-concrete composite slabs and developed a calculation method for their horizontal cross-sectional strength. Mistakidis et al.[18] conducted experimental studies on the flexural performance of embossed steel-concrete composite slabs, with results indicating that the embossing on the steel significantly improves the flexural performance of the slabs. Rios et al.[19] proposed a computational approach to analyze the shear bond behavior in steel-concrete composite slabs. Zhang et al.[20] carried out experimental research on a novel thin-walled steel-wood composite panel, demonstrating its excellent bending performance. Xiang et al.[21] proposed a calculation method for the vertical shear resistance of ribbed steel-concrete composite slabs.

It can be observed that current research on composite slabs primarily focuses on unidirectional composite slabs, with relatively few studies on bidirectional composite slabs. Additionally, the application of composite slabs in foundation structures is also relatively limited. In response to this situation, this paper proposes a prefabricated beam-slab foundation structural system, composed of multiple standardized prefabricated beam-slab units. This structure has advantages in easy construction, energy saving, material saving, and high bearing capacity. The mechanical performance between prefabricated beam-slab units in prefabricated foundations directly influences the overall behavior of the structure. Therefore, this paper focuses on certain prefabricated beam-slab units within the prefabricated beam-slab foundation. Through static load tests, the mechanical performance of the foundation bottom slab and the slab connectors was investigated, revealing the failure characteristics and load-bearing mechanisms of the specimens under vertical loads. Additionally, numerical simulation analysis utilizing the experimental data was conducted to validate the correctness of the finite element model. Based on the experimental and finite element verification, a parametric analysis was performed to explore

the impact of factors such as concrete strength, reinforcement ratio, composite slab thickness, and C-shaped steel thickness on the static performance of the foundation base slab.

2. The structure system

The new prefabricated beam-slab foundation system presented in this paper is depicted in Fig. 1. The structure mainly consists of foundation beams, foundation bottom plates, and various connection nodes. In the prefabricated raft foundation, the foundation slab primarily bears the bending moment. Considering the span requirements for the raft foundation, the foundation slab adopts grooved slab, which consists of prefabricated beam-slab units with ribbed edges, as shown in Fig. 1(b). This structure is grooved along the thickness direction of the slab, not only reducing material usage but also effectively lightening the weight of the structure. Meanwhile, the surrounding ribbed beams significantly enhance the global stiffness and load-bearing capacity of the structure. The prefabricated beam-slab units are composed of C-shaped steel, reinforcement, and concrete. The C-shaped steel is placed in the ribbed beam section of the prefabricated beam-slab unit. The internal reinforcement is connected to the surrounding C-shaped steel by welding, while bolt holes are pre-formed in the web section to enable linkage with inter-panel connectors. The connectors between the prefabricated beam-slab units consist of inner and outer sleeves, with the inner and outer sleeves locking together to join the prefabricated beam-slab units.

The structure of the foundation beams and their connection nodes is shown in Fig. 1(c). When designing the structure, it was considered that the large cross-section of the profile steel and its good continuity could effectively disperse and transfer loads, providing better local shear and punching shear resistance. Therefore, T-shaped steel is embedded in the foundation beams, with a single layer of reinforcement arranged at the top. In the process of making the precast foundation beam, the concrete is not poured at the joint, and the exposed profile steel and reinforcement are used for the node connections. When designing the connection nodes between the foundation beams, the node is divided into upper, middle, and lower parts, as shown in Fig. 1(c). This connection node consists of three steel tubes of different sizes: the upper square steel tube has slots for fixing the rebar inside the composite beam, the middle square steel tube has bolt holes in the extended end plate, which connect to the web of the extended T-shaped steel of the composite beam via bolts, and the lower square steel tube has an upward opening to support the flange of the extended T-shaped steel of the composite beam.

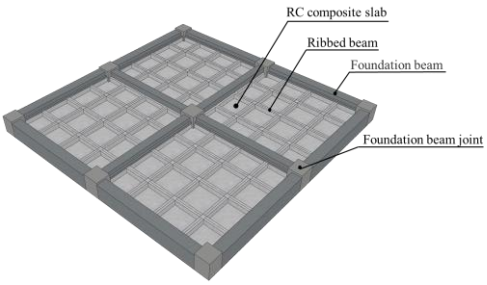

(a) assembled raft foundation

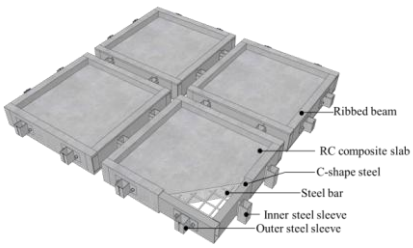

(b) prefabricated beam and slab units

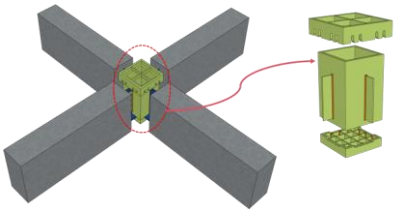

(c) foundation beam joint

Fig. 1 structural diagram of assembled raft foundation

3. Experiment investigation

3.1. Specimen details

To study the mechanical performance of the prefabricated beam and slab units and its connectors in this structure, a full-scale foundation slab specimen was fabricated. The specimen consists of four prefabricated beam-slab units and four prefabricated foundation beams, as shown in Fig. 2 Each prefabricated beam-slab unit includes steel-reinforced concrete slab and ribbed beams. The reinforced concrete (RC) composite slab is 200 mm thick, and the ribbed beam section dimensions are 100×300 mm. Inside the RC composite slab, a single layer of rebar with a diameter of 12 mm is arranged, with a spacing of 100 mm. The concrete used for the specimen is C30, and the rebar is HRB400 grade steel. The C-shaped steel is Q235 grade, with dimensions of 250×80×9 mm. The connectors between the slabs are prefabricated square steel tubes, available in two models: 110×110×5 mm and 100×100×6 mm. The composite beam dimensions are 400×500 mm, with internal T-shaped steel made of Q235 grade steel, model dimensions of 250×200×10×16 mm. All bolts used in the specimen are grade 8.8 high-strength bolts, with a diameter of M20 and a hole diameter of d_0=22 mm. The detailed dimensions of the prefabricated beam-slab units are shown in Fig. 3.

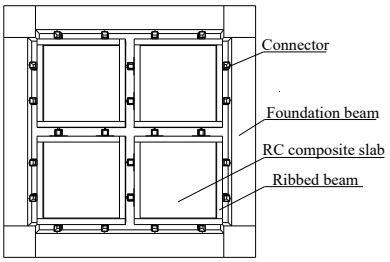

Fig. 2 Installation completion diagram

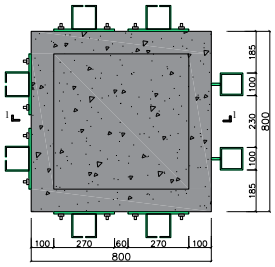

(a) Plan drawing

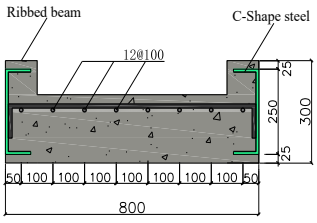

(b) 1-1 cross-section drawing

Fig. 3 Detail of prefabricated beam and slab units (mm)

3.2. Material properties

In accordance with GB/T 228.1-2010[22] and GB/T 2975-2018[23], tensile tests were employed to characterize the mechanical properties of the experimental steel. Three specimens each were taken from the C-shape steel and T-shape steel used in the experiment, and tensile tests were performed on a universal testing machine. The mechanical characteristics of the tested steel are shown in Table 1. The prefabricated beam-slab units used reinforcement with a diameter of 12 mm. To measure the mechanical properties of this reinforcement, three 500 mm long samples were selected for tensile tests. The mechanical properties of the tested reinforcement are shown in Table 2.

C30 grade concrete served as the material for all test specimens. To measure the compressive performance of concrete, three sets of 150 × 150 ×

150 mm concrete cubes were reserved when pouring the concrete for the specimens. Compressive strength tests were conducted on these reserved concrete cubes according to the Chinese standard GB/T 50081-2002[24]. The measured material properties of the concrete are listed in Table 3.

Table 1
Material property of section steel

Specimen number	Yield strength /MPa	Ultimate strength /MPa	Elastic modulus /10^5 MPa	Elongation /%
T-1	306.0	390.1	2.02	32.1
T-2	302.3	394.2	2.07	33.5
T-3	310.2	390.7	2.04	35.1
Average	306.2	391.7	2.04	33.5
C-1	305.5	390.3	2.03	30.1
C-2	302.5	392.3	2.02	30.6
C-3	309.5	396.2	2.04	30.2
Average	301.6	394.3	2.07	30.3

Note: T-1 is the steel specimen for the slab connector, and C-1 is the steel specimen for the web of the C-shaped steel.

Table 2
Material property of rebar

Specimen number	Rebar diameter /mm	Yield load /kN	Yield strength /MPa	Maximum tension /kN	Ultimate strength /MPa
G-1	12	46.52	411.3	69.25	612.3
G-2	12	46.78	413.6	69.94	618.3
G-2	12	47.46	419.6	69.59	615.2
Average	12	46.92	414.8	69.59	615.3

Table 3
Material property of concrete

Concrete grade	Axial compressive strength /MPa	Average /MPa	Elastic modulus /104 MPa	Average /10^4 MPa
C30	32.7	32.1	3.16	3.12
	30.2		3.08	
	33.5		3.12	

3.3. Testing program

3.3.1. Loading protocol

The experiment used a 1000-ton multifunctional testing machine to apply vertical loads. In order to simulate the loads experienced by the specimen during actual service conditions, the specimen was inverted during installation, with the bottom of the base plate facing upward for load application. During loading, a secondary distribution beam was used to achieve four-point loading, with the load points located at the center of the prefabricated beam-slab units. The specimen is a two-way slab, and the support system consists of four steel beams and four steel columns. When installing the specimen, it was placed on the steel frame, with the steel beams supporting the bottom of the composite beam. This support configuration restricted vertical displacement while allowing rotation along all four slab edges, and is therefore classified as a simply supported boundary condition. The loading setup is shown in Fig. 4.

3.3.2. Loading steps

Displacement-controlled loading was applied during the test. Prior to the formal loading process, a preload of 10 kN was applied to the specimen and maintained for 5 minutes to ensure the proper functioning of all systems and to eliminate any gaps between the specimen and the support system. The displacement-controlled loading in the formal testing stage was performed at 3 mm/min, with a 3-minute hold at each increment. This loading rate was selected with reference to the Chinese standard GB/T 50152-2012[25], which recommends a loading speed within the range of 0.5–5 mm/min for quasi-static testing. During the test, the specimen was monitored using force sensors, and its deformation under different loading stages was carefully observed.

Fig. 4 Example of a figure

3.3.3. Layout of measuring points

During the loading process, the deflection change, crack development, inter-plate connector strain and steel bar strain of the specimen were mainly observed. Fig. 5 illustrates the layout of the displacement and strain gauges. A total of four displacement gauges were used in the experiment. Gauge W1 was placed at the center of the specimen, gauges W2 and W3 were placed at the 1/4 points of the specimen's centerline, and gauge W4 was placed at the center of the composite beam to observe changes in specimen deflection. Strain gauges were distributed on the slab connectors, rebar, and C-shaped steel.

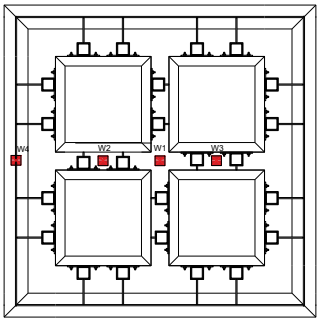

(a) Layout of Displacement meter

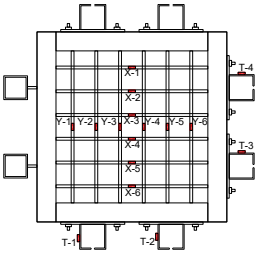

(b) Layout of Strain gauges

Fig. 5 Layout of measurement points

4. Failure process

During the early loading stage, the specimen remained in the elastic range without significant deformation. A progressive increase in deflection was observed as the applied load increased. At approximately 35% of the peak load, fine cracks appeared at the center of the bottom of the specimen along the diagonal direction, but there was no noticeable flexural deformation. With the gradual increase of applied load, crack propagation was observed at the specimen's central region, accompanied by the initiation of 45° diagonal cracks at the mid-span of the bottom surface of the RC composite slab. When the load reached 51% of the peak load, minor cracking appeared in the concrete at the ribbed beam node connection area, and the number of cracks at the RC composite slab increased. As the load increased to 62% of the peak, slight sounds were heard from within the specimen, indicating it had reached the yield state, with a mid-span deflection of 6.72 mm, and more cracks appeared at the RC composite slab. At peak load, the crack width at the RC composite slab increased, more cracks appeared in the ribbed beam node connection area, and the rebar inside the RC composite slab had yielded. As shown in Fig. 6, at the end of the test, large cracks developed in the tensile zone of the concrete, and

the maximum deflection reached 18 mm, approximately 1/160 of the structure's span, which is considered as the failure criterion of the structure.

(a) The cracks of ribbed beam

(b) The cracks of composite slab

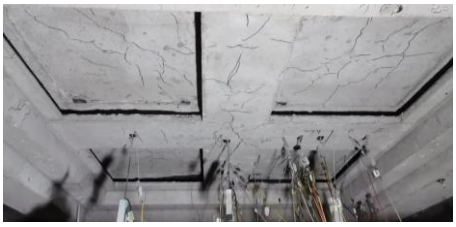

(c) The cracks of the whole structure

Fig. 6 The failure of structure

5. Analysis of test results

5.1. Bearing capacity and ductility

As shown in Fig. 7, the load-displacement curve can be segmented into three phases, with the specimen exhibiting elastic behavior during the initial loading at low loads. The curve exhibits a nearly linear relationship, indicating good synergy between the section steel, rebar, and concrete within the prefabricated beam-slab unit. As loading progresses, cracks begin to develop in the tensile zone of the concrete, and the curve enters the elastoplastic phase. Due to the cracking of the concrete, the section steel and rebar inside the RC composite slab bear the load and also provide some constraint on the development of concrete cracks. With the progressive growth in both the quantity and width of cracks, the synergy between the section steel, rebar, and concrete weakens. The rate of load increase diminishes while the rate of displacement increase becomes more pronounced. When the load reaches its peak, the curve enters the failure stage. At this point, the rebar within the specimen yields, the deformation of the specimen increases, and the load gradually decreases until the specimen is destroyed and the test ends.

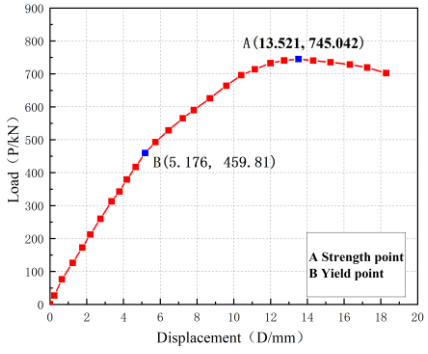

Fig. 7 Load-displacement curves

An essential metric for evaluating structural deformation capacity is the ductility coefficient of the component. The test results are illustrated in Table 4, indicating that the ductility coefficient of this specimen is 3.53, which demonstrates that the structure has good ductility.

Table 4
Ductility coefficient of the specimens

Specimen number	Δ_y / mm	*Ny* /kN	Δ_u / mm	*Nu* /kN	DI
Specimen 1	5.176	459.81	18.29	757.19	3.53

Note： Δ_y is the yield displacement， Δ_u is the ultimate displacement，*Ny* is the yield strength，Nu is the ultimate strength，DI is the ductility coefficient

5.2. The analysis of concrete deflection variation

In order to better observe the deflection variation of the two-way slab specimen, displacement gauges were installed at the specimen's mid-span, quarter-span, and support regions. The deflection variation at the centerline of the specimen during the test was monitored, as illustrated in Fig. 8. The curve exhibits an approximately sinusoidal pattern. When the load is less than $0.6N_u$, the specimen remains in the elastic phase, with deflection increasing linearly and at a relatively slow rate. When the load exceeds $0.6N_u$, the specimen transitions into the elastic-plastic phase, and the rate of deflection change accelerates. Additionally, the general pattern of the curve demonstrates that the mid-span undergoes a more pronounced change in deflection compared to the quarter-span regions.

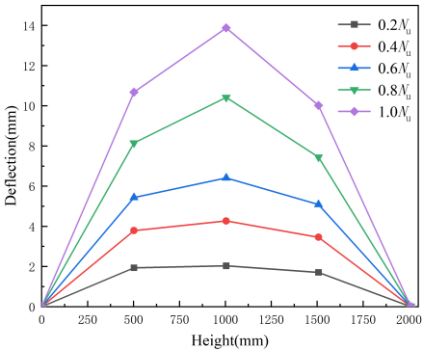

Fig. 8 Deflection curve of concrete

5.3. Strain analysis of rebar

Fig. 9 presents the strain distributions of the reinforcement along the X and Y directions within the composite slab. It can be observed that under vertical loading, the rebars are all in a tensile state. The strain patterns of the reinforcement in both X and Y directions exhibit similar behavior: strain increases more rapidly as the location approaches the mid-span. In the initial loading phase, the specimen is in the elastic phase, and the strain growth of the rebars is slow. As the load increases, the concrete begins to crack, and the rebars bear more load, leading to a rapid increase in strain until the specimen fails.

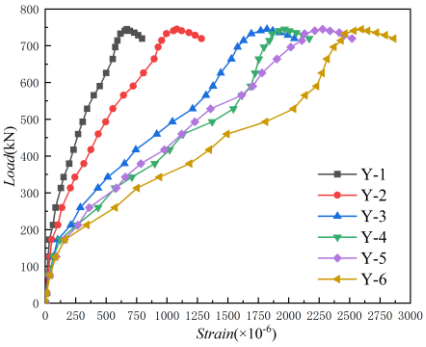

(a) Reinforcement strain of Y-direction

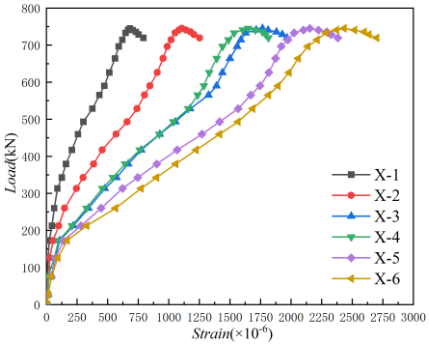

(b) Reinforcement strain of X-direction

Fig. 9 Load-strain curve of reinforcement

5.4. Strain analysis of connector

The load-strain curves of the inter-slab connectors reflect the stress and deformation characteristics of the connection nodes under vertical loads. The load-strain curves of the node connectors obtained from the experiment are illustrated in Fig. 10. It can be observed that the strain values of the curves are all positive, indicating that all the connectors are in a tensile state. The strain development trends of the connectors in different regions are essentially consistent. In the initial loading phase, the curves display linear growth. As loading progresses, concrete cracks develop continuously, and the strain of the connectors gradually increases. According to the material property test data, the yield strain of the connectors is 1.5×10^3. It can be seen that connectors have not reached yield stress. At the ultimate load stage, the T-4 connector at mid-span exhibits the highest tensile strain, aligning well with the experimental findings.

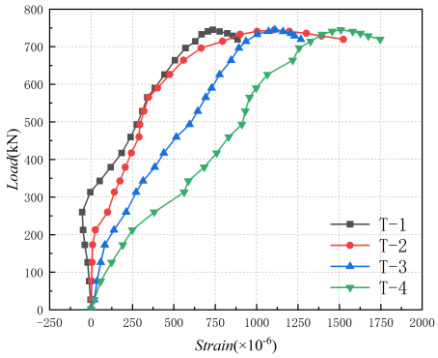

Fig. 10 Load-strain curve of connectors

6. Finite element modeling investigation

6.1. Finite element model

6.1.1. General

To analyze the mechanical characteristics of the prefabricated beam-slab units in the novel foundation system, finite element modeling (FEM) was performed in ABAQUS. The model dimensions were consistent with the experimental specimens. Both concrete and internal section steel were modeled using C3D8R elements, while the reinforcement was simulated using 3D two-node truss elements. The material constitutive relationships were based on material property tests: concrete elements utilized a plastic damage model with a concrete strength grade of C30 and an elastic modulus of E=31200 MPa; the section steel and reinforcing bars were simplified into bilinear models based on relevant test data. During the mesh generation process, a sensitivity analysis was performed by simulating models with different mesh sizes to determine the optimal mesh size for each material element. The final mesh sizes were 50 mm for concrete elements, 35 mm for section steel, and 15 mm for reinforcing bar truss elements. An illustration of the FEM is provided in Fig. 11.

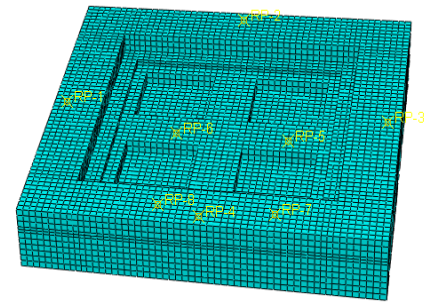

(a) Concrete

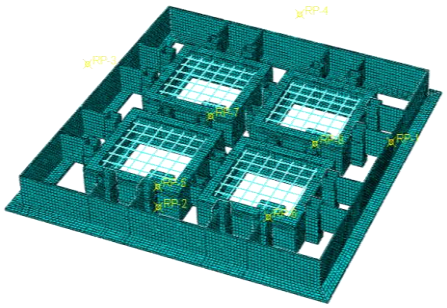

(b) Steel frame

Fig. 11 Finite element model

6.1.2. Interactions

Surface-to-surface contact constraints were employed to simulate the interaction between the connectors and the section steel. The normal contact was modeled as hard contact, while tangential behavior adhered to Coulomb friction with a coefficient of 0.15. The rebars and the C-shaped section steel were constrained using TIE constraints, with the Embedded method employed to embed the steel framework formed by the C-shaped steel and the rebars into the concrete. Additionally, steel pads were placed at the loading points of the model. The pads were tied to the model, ensuring that they remained tightly connected throughout the loading process without any relative sliding.

6.1.3. Boundary conditions

The FEM uses identical boundary conditions and loading procedures as those applied in the experiment. In applying boundary conditions, only the translational degrees of freedom along U1, U2, and U3 are restricted, whereas the rotational degrees of freedom around the X, Y, and Z axes remain free. Four-point loading is employed during the loading process. Four rigid pads are placed at the loading points, which are bonded to the model. The loading surface is coupled at one point, and the loading is applied using displacement control.

6.2. Numerical simulation results and analysis

6.2.1. Comparison of failure modes

The cracking condition of the specimen can be clearly seen through the tensile damage of the concrete. As illustrated in Fig. 12, the FEM failure modes align well with the experimental observations. Cracking primarily occurs in the composite slab region and the central part of the ribbed beams. The cracks within the composite slab are symmetrically arranged under vertical loads. The crack distribution in the FEM closely matches the experimental results.

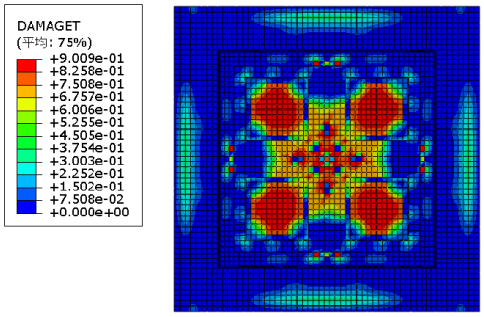

(a) Tensile damage of FEM

(b) Cracks and failure in test

Fig. 12 Comparison of damage characteristics

6.2.2. Comparison of load-displacement curves

The load-displacement curves from both the FEM analysis and the experimental tests are compared in Fig. 13. The finite element simulation results closely match the experimental data, particularly in the elastic range where discrepancies are negligible. However, as the curve enters the elastoplastic stage, the simulation results exhibit some discrepancy compared to the experimental findings. Compared to experimental data, the FEM slightly overestimated the load capacity, which can be attributed to the simplified model's exclusion of concrete–steel bond-slip interactions. Overall, the error between the two results is within 15%. The consistency between the experimental and FEM curves indicates that the simulation results are reliable.

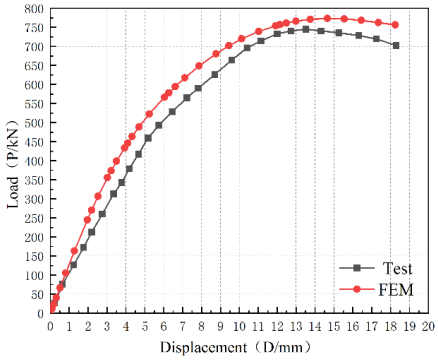

Fig. 13 Comparison of FEM and tested Load-Displacement curves

7. Parameter analysis

The effects of different parameters on the load-bearing behavior and failure characteristics of foundation slab units are investigated through parametric analysis, based on the established and validated FEM. In conjunction with the load-bearing characteristics and capacity variation patterns of the test specimens, four key influencing factors, namely concrete strength, rebar diameter, composite slab thickness, and C-shaped steel thickness, were selected as the focus of the research.

7.1. Concrete strength

Based on the commonly used concrete strength grades in current engineering practice, the concrete strength in the FEM models was set sequentially as C20, C30, C40, and C50. Load-displacement responses obtained from FEM simulations for concrete grades C20 through C50 are illustrated in Fig. 14. The results indicate increases in flexural capacity of 11.58%, 8.04%, and 6.11% as the grade progresses from C20 to C30, C30 to C40, and C40 to C50, respectively. Under different concrete strength grades, the specimens exhibited distinct elastoplastic behavior. As the concrete strength grade increased, the specimens exhibited a notable improvement in bending load capacity, indicating that concrete strength is a key factor affecting the static behavior of prefabricated beam-slab units. Moreover, as the concrete strength increased, the failure mode tended to become more brittle, and the plastic deformation capacity was slightly reduced. Additionally, the contribution of concrete strength to further enhancement of bearing capacity became progressively less significant. Therefore, in practical applications, a suitable concrete grade can be selected based on engineering requirements and economic considerations.

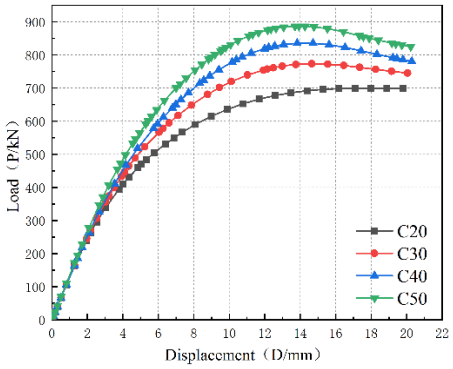

Fig. 14 Load displacement curve of different concrete strength

7.2. Reinforcement ratio

According to the requirements for reinforcement ratio in GB 50010-2010, the reinforcement diameters in the model were set sequentially as 10 mm, 12 mm, 14 mm, and 16 mm. Specimens with various reinforcement ratios in the composite slab exhibit distinct load-displacement curves, as shown in Fig. 15. It can be observed that as the reinforcement ratio in the slab increases from 0.44% (corresponding to a rebar diameter of 10 mm) to 1.06% (corresponding to a rebar diameter of 16 mm), the bending load-bearing capacity increases by 50.5%. The ultimate load-bearing capacity corresponding to adjacent rebar diameters differs by 12.7%, 16.1%, and 15.2%, respectively. This indicates that the bending load-bearing capacity of the foundation slab is strongly affected by the reinforcement ratio in the composite slab. With an increase in reinforcement ratio, the tensile capacity contributed by the reinforcement is improved, resulting in a significant enhancement of the foundation slab's bending load-bearing capacity. Additionally, the increment in load-bearing capacity between successive reinforcement ratios diminishes as the reinforcement ratio increases, indicating a trend of diminishing returns within a certain range. Therefore, considering structural design codes and experimental findings, a rebar diameter ranging from 10 mm to 14 mm is recommended for the composite slab.

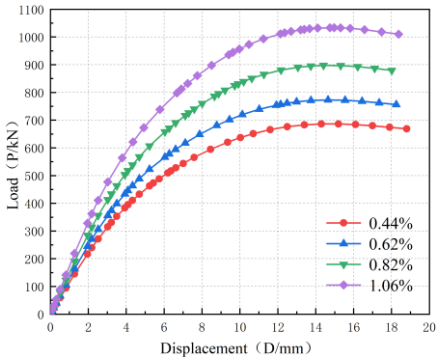

Fig. 15 Load displacement curve of different reinforcement ratio

7.3. Thickness of composite slab

This section focuses on the influence of composite slab thickness on the mechanical performance of prefabricated beam-slab units. To this end, when establishing the FEM, only the thickness of the composite slab was varied while the height of the rib beam remained constant. As shown in Fig. 16, the FEM results indicated a 16.3% increase in ultimate load-bearing capacity when the slab thickness was raised from 200 mm to 220 mm, followed by an additional 16.1% increase as it reached 240 mm. The findings indicate that changes in slab thickness substantially impact the structural capacity of the foundation base slab. Additionally, from the figure, it can be seen that as the slab thickness increases, the mid-span displacement at the peak load also gradually increases, suggesting that within a certain range, increasing the slab thickness helps improve the overall structural ductility, allowing the foundation base slab to withstand larger deformations.

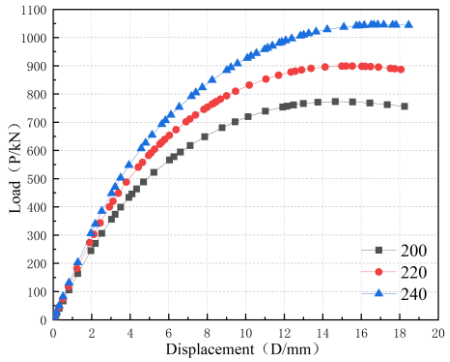

Fig. 16 Load displacement curve of different slab thickness

7.4. Thickness of C-shaped steel

C-shaped steel is an important component of the steel framework in prefabricated beam-slab units. This part investigates the influence of C-shaped steel thickness on bending capacity by varying its thickness while maintaining all other variables constant. The FEM assigns C-shaped steel thicknesses of 5 mm, 7 mm, 9 mm, and 12 mm sequentially. and finite element numerical simulations are conducted. As illustrated in Fig. 17, the load-displacement behavior of the foundation base slab is depicted. It can be observed that as the thickness increases from 5 mm to 12 mm, the ultimate load-bearing capacity of the foundation base slab shows a slight increase. Specifically, the bending load-bearing capacity increases by 4.6% when the C-shaped steel thickness is raised from 5 mm to 12 mm. It can be concluded that variations in the thickness of the C-shaped steel have limited effect on the load-bearing capacity of the foundation slab. During structural design, smaller dimensions of C-shaped steel may be considered, providing a reference for optimizing both the economy and performance of the section steel.

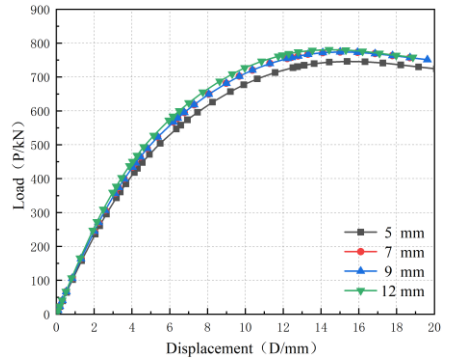

Fig. 17 Load displacement curve of different C-Section Steel thickness

8. Conclusions

This paper conducted an experimental study on the mechanical performance of foundation slabs and inter-slab connectors under vertical loads in prefabricated beam-slab foundations. The study analyzed the failure characteristics, bearing capacity, ductility, and strain patterns of reinforcement and connectors of the test specimens under static load tests. Additionally, a numerical simulation analysis of the test specimens was conducted using the finite element software ABAQUS. The conclusions drawn are as follows:

(1) Under vertical loading, the specimen exhibited overall bending failure characteristics. During failure, multiple cracks appeared in the tensile zone of the composite slab concrete, while no significant damage was observed in the node core area. This satisfies the design principle of "strong node, weak component," indicating that the structure possesses good bending load-bearing capacity.

(2) The load-displacement curve showed distinct elastic, elastoplastic, and failure stages. The curve experienced significant displacement changes from the specimen's yield point to the ultimate load, indicating good ductility performance of the structure.

(3) The failure characteristics of the FEM are in good agreement with the experimental results. The load-displacement curve obtained from the numerical simulation matches closely with the experimental curve, indicating that the FEM effectively simulates the real behavior of the test specimen. Thus, the FEM is reliable.

(4) A parametric analysis was conducted considering four influencing factors: concrete strength, reinforcement ratio, composite slab thickness, and C-shaped steel thickness. The results indicate that the bending load-bearing capacity of the foundation base plate is positively correlated with concrete strength, reinforcement ratio, and composite slab thickness, with reinforcement ratio having the most significant impact on load-bearing capacity. Conversely, the thickness of the C-shaped steel has negligible influence on the bending capacity of the foundation base plate.

Acknowledgments

This research was supported by Natural Science Foundation of Hebei Province for Distinguished Young Scholars (Grant No. E2022210084).

References

[1] Weidong Kang, Huang Bei, Gu Hao. Application of Raft Foundation in Transmission Line Engineering[J]. Academic Journal of Engineering and Technology Science,2020,3.0(8.0): 61-69.
[2] Teng L, Yamin W, Linjie C, et al. Research on design of the prefabricated foundation in substations[J]. Journal of Physics: Conference Series,2021,1904(1): 1-20.
[3] Shuguang W. Experimental study on failure behavior of beam-slab raft foundation under uniform column load [J]. Journal of Civil Engineering, 2006, (10): 97-101.
[4] Yu D, Gong J, Jiang S, etc. Experimental study on reaction deformation and failure characteristics of beam-slab raft foundation under column under uniform and non-uniform loads [J]. Building Science, 2015,31 (05): 29-35.
[5] Priyadarshee A, Kumar V, Sharma K, et al. Study on the load sharing in piled raft foundation[J]. Multiscale and Multidisciplinary Modeling, Experiments and Design,2024,7(3):3005-3015.
[6] Xi X, Wentao G, Tatsunori M, et al. Bearing characteristics of model piled raft foundations supported by sheet piles[J]. International Journal of Physical Modelling in Geotechnics,2023,24(1):38-53.
[7] Hoang T L, Xiong X, Matsumoto T. Effect of pile arrangement on long-term settlement and load distribution in piled raft foundation models supported by jacked-in piles in saturated clay[J]. Soils and Foundations,2024,64(2):101426-.
[8] Anuj C, Sandip V. Experimental investigation of inclined compressive loading on a piled raft foundation[J]. Ocean Engineering,2023,287(P1):1-9.
[9] Rasmussen T V Ø. Integrated Strip Foundation Systems for Small Residential Buildings[J]. The Open Construction & Building Technology Journal, 2010, 4: 39-53.
[10] Adams F H. Concrete footer block and foundation system formed therefrom[P]. U.S. Patent 4903450,1989-5-2.
[11] Kim, D. H., Pyo, W. S., Kim, J. G., et al. Base body of electric transmission tower using micropile[P]. U.S. Patent 20170191239A1,2017-7-6.
[12] Catalano S F R. Precast foundation assembly for mobile homes[P]. U.S. Patent 3879905,1975-4-29.
[13] Guanhua L, Rui L, Xu D, et al. Design of prefabricated foundation for 66kV tower assembly and simulation of mechanical properties and grounding current density distribution[J]. Journal of Physics: Conference Series,2022,2296(1): 1-6.
[14] Ranzi G, Ostinelli A. Ultimate behaviour and design of post-tensioned composite slabs[J]. Engineering Structures,2017,150: 711-718.
[15] Crisinel M, Marimon F. A new simplified method for the design of composite slabs[J]. Journal of Constructional Steel Research,2004,60(3):481-491.
[16] Qiao W, Yan X, Zhu R, et al. Flexural properties of new cold-formed thin-walled steel and concrete composite slabs[J]. Journal of Building Engineering,2020,31:1-13.
[17] Vainiūnas P, Valivonis J, Marčiukaitis G, et al. Analysis of longitudinal shear behaviour for composite steel and concrete slabs[J]. Journal of Constructional Steel Research,2006,62(12):1264-1269.
[18] Mistakidis S E, Dimitriadis G K. Bending resistance of composite slabs made with thin-walled steel sheeting with indentations or embossments[J]. Thin-Walled structures,2008,46(2):192-206.
[19] Ríos, J. D, Cifuentes, H, Concha, A. M.-D. L, et al. Numerical modelling of the shear-bond behaviour of composite slabs in four and six-point bending tests[J]. Engineering Structures, 2017,133:91-104.
[20] Zhang A, Chen Z, Liu J. Flexural performance of innovative thin-walled steel–timber composite floor slabs[J]. Engineering Structures,2024,318:118676-118676.
[21] Da X, Yuqing L, Yichi S, et al. Vertical shear capacity of steel-concrete composite deck slabs with steel ribs[J]. Engineering Structures,2022,262:114396.
[22] Metallic Materials - Tensile Testing - Part 1: Method of Test at Room Temperature GB/T 228.1-2010 [S]. Beijing: Standards Press of China, 2010.
[23] Steel and Steel Products - Location and Preparation of Test Pieces for Mechanical Testing GB/T 2975-2018 [S]. Beijing: Standards Press of China, 2018.
[24]Standard for Test Methods of Mechanical Properties of Concrete GB 50081-2002 [S]. Beijing: China Architecture & Building Press, 2002.
[25] Standard Test Methods for Concrete Structures GB/T 50152-2012 [S]. Beijing: China Architecture & Building Press, 2016.

Advanced Steel Construction – Vol. 22 No. 2 (2026) 244–254
DOI:10.18057/IJASC.2026.22.2.10

A DATA-CENTRIC STRATEGY TO MITIGATE OVERFITTING OF ML MODELS FOR PREDICTING TORSIONAL CAPACITY FOR CFST COLUMNS

Ming-Xia Dang [1], Meng-Xue Guo [2, *], Ying Li [1], Hua Li [1] and Shi-Lin Yang [3]

[1] *School of Intelligent Construction and Environment, Xi'an Jiaotong University City College, Xi'an, 710018, China*

[2] *School of Civil & Architecture Engineering, Xi'an technological university, Xi'an 710021, China*

[3] *Shaanxi Construction Engineering Group Corporation Limited, Xi'an 710003, China*

** (Corresponding author: E-mail: 18792602146@163.com)*

ABSTRACT

This study investigates the effectiveness of both model-centric and data-centric strategies in addressing the overfitting issue in machine learning (ML) models for predicting the torsional capacity of concrete-filled steel tubular (CFST) columns under combined loading. While prior work has largely focused on optimizing model architectures, our findings reveal that model-centric approaches offer limited improvement when training data is scarce. To address this, we propose a data-centric framework that enhances both the quantity and quality of training data. Specifically, we augment the dataset with synthetic data generated by Conditional Generative Adversarial Networks (CGANs) and finite element analysis (FEA) results. To ensure reliability, we introduce a filtering mechanism that selects high-quality simulated data for model training. Our results reveal that directly incorporating unfiltered synthetic or FEA data into model training can degrade test performance due to the presence of noisy or unreliable samples. In contrast, when high-quality FEA data is carefully filtered and selectively combined with experimental data, the model exhibits a substantial improvement in generalization, reflected by a 5% increase in R^2 with only a marginal 0.45% rise in MAPE. The proposed data selection strategy consistently reduces performance variance across multiple test splits, indicating strong robustness and resistance to overfitting.

ARTICLE HISTORY

Received: 31 March 2025
Revised: 7 July 2025
Accepted: 2 August 2025

KEYWORDS

Data-centric;
Overfitting;
Machine learning;
CTGAN;
CFST columns

1. Introduction

The recent proliferation of machine learning technologies has sparked a paradigm shift in structural engineering research, ushering in a new era of innovative approaches to tackle intricate challenges that were previously intractable using traditional mechanical models[1-4]. Traditionally, engineering practices have been grounded in limit state design criteria, reliant on rigorous experimental validation, intricate finite element modeling, or a synthesis of parameter regression analysis and strength theory derivations to formulate predictive frameworks[5-7]. However, these methodologies are constrained by inherent limitations, notably model dispersion and biases stemming from modeling inaccuracies or the imposition of overly simplistic assumptions. The exponential growth in computational power, coupled with the pressing need for efficient solutions in the engineering sector, has catalyzed significant advancements in machine learning algorithms.

The core of machine learning is inherently data-driven, especially data-centric, with model accuracy and generalization power intimately tied to the diversity and quality of datasets. Suboptimal sample quality can exacerbate model biases by incorporating low-fidelity instances, while limited sample diversity undermines the surrogate models' capacity for generalization[8]. Consequently, the utilization of machine learning in civil engineering has sparked significant concerns within the engineering community, particularly regarding the adequacy and quality of data, along with the risk of overfitting[9]. Models trained on inadequate data are unreliable and prone to overfitting, yielding spurious predictions that undermine their credibility. To address this challenge, the cornerstone lies in constructing comprehensive datasets comprising multi-source, high-quality samples. In civil engineering, where machine learning models operate as black boxes, their reliance on extensive and unbiased physical experimental data for training is paramount. This data must be comprehensively representative, devoid of biases, and encompass a broad range of conditions. However, experimental uncertainties and equipment malfunctions inevitably introduce noisy samples and outliers during testing, limiting the availability of training data in structural engineering and further hindering the acquisition of high-quality data. Consequently, relying solely on data from physical experiments to train machine learning models can be fraught with errors, as limited training data often precipitates overfitting, potentially misleading evolutionary search processes and compromising the models' predictive performance.

The scarcity of experimental samples, insufficient for training robust machine learning models, poses a significant challenge. This limitation underscores the paramount importance of critically evaluating data sources' appropriateness and reliability when designing and deploying machine learning models for civil engineering applications. To address this issue, FEA data are frequently utilized as a complementary resource to experimental data[10]. However, a fundamental gap exists due to the inherent constraints of simulation methods. Despite significant advancements, these methods struggle to fully capture the intricate and dynamic interactions inherent in real-world systems. Factors such as variations in material constitutive laws, mesh discretization techniques, and solution strategies contribute to this discrepancy, rendering it challenging to achieve alignment between simulated and experimental outcomes. To bridge this gap, researchers engage in rigorous validation and calibration of finite element models, striving to develop more precise and generalized machine learning solutions[11]. It is imperative to acknowledge that the inherent discrepancy between non-physical experimental data and real-world data remains an inescapable reality.

In the pursuit of mitigating model biases arising from the limited training data, researchers across disciplines have intensified their focus on tackling data-centric challenges within machine learning[12, 13]. This heightened awareness is particularly pronounced in the realms of medicine and materials science, where the collection, cleansing, and evaluation of data have become paramount. Within structural engineering, scholars have likewise embarked on addressing the dual challenges of data quantity and quality. Notably, Li et al.[14] have employed Gaussian regression to devise a machine learning model that achieves remarkable precision in measuring deformations of reinforced concrete columns, effectively demonstrating its resilience across a broad spectrum of data quality. Additionally, Luo et al.[15] have introduced a pioneering dual-weighted support vector transfer regression methodology, which aims to bolster prediction performance by effectively countering the detrimental effects of limited sample sizes. Moreover, Marani et al.[16] have taken an approach by leveraging physical experimental data to train a Generative Adversarial Network (GAN), enabling the synthesis of novel data that supplements the existing experimental corpus. This technique has facilitated the successful training of machine learning models on a combined dataset, revealing that the utilization of synthetic data significantly reduces the reliance on scarce real-world data during the model training phase. These findings underscore the potential of synthetic data in streamlining and augmenting the machine learning process within structural engineering, thereby enhancing the efficiency and accuracy of predictive models[17].

The advent of existing methodologies has undoubtedly alleviated the burden of data scarcity to a certain degree. Nevertheless, a pivotal yet underexplored challenge looms large: the biases inherent in models fueled by the limited and low-quality data. The difference between physical experimental data, and non-experimental counterparts, including finite element simulations and synthetic data, continues to pose a formidable obstacle. This not only complicates the predictive accuracy of models but also undermines their credibility in real-world applications. Synthetic data, a promising avenue for augmenting data availability, holds the key to bridging the data gap[18]. However, the divide between synthetic and experimental data, albeit narrowing, remains a significant hurdle

that must be overcome. Current endeavors, focused on refining finite element models for heightened realism in simulations and advancing generative models to mirror real-world complexity[19,20]. However, the quest for parity between these data sources and their experimental counterparts persists, emphasizing the need for a more nuanced approach.

This study explores the effect of the model design and data on mitigating overfitting in machine learning models, respectively, i.e., the model-centric and the data-centric training strategy. And, two strategies were used and analyzed in the context of predicting the composite torsional capacity of concrete-filled steel tubular (CFST) columns. Drawing upon two prevalent data augmentation techniques: Conditional Generative Adversarial Network (CTGAN)-based synthetic data[21] and finite element analysis data (FEA). Our approach distinguishes itself from existing research by not focusing on the refinement or development of new models, but rather on devising an efficient strategy for leveraging multiple data sources. Applying this training strategy to the prediction of CFST columns' torsional behavior, we embark on a comprehensive investigation that spans from models to data, with the overarching goal of addressing the issue of overfitting in machine learning models, especially for the predictions of CFST torsional performance. Specifically, our research endeavors encompass:

1) Explore the impact of diverse model-centric strategies on mitigating overfitting in machine learning contexts, shedding light on the effectiveness of various approaches, including model replacement and reduction of non-critical input parameters.

2) Investigate the influence of data-centric strategies including GAN-generated synthetic Data and FE simulation data in training processes, assess their respective contributions to reducing overfitting and enhancing model generalization.

3) Develop and evaluate sample selection and training strategies based on the error minimization, to mitigate overfitting, thereby refine the overall predictive capabilities of the models.

2. Workflow to mitigate overfitting in ML prediction models

Fig. 1 outlines the approach devised in this research to address the challenge of overfitting in data-driven predictive models for assessing the torsional capacity of concrete-filled steel tubular (CFST) columns. This framework encompasses four key stages: data compilation, model evaluation, model-centric optimizations, and data-centric enhancements.

(1) Data Compilation: A comprehensive dataset, initially comprising 243 experimental observations curated from the scientific literature[22-34], serves as the cornerstone for model development. To augment this dataset and enable a deeper exploration of overfitting mitigation strategies, we incorporate 561 FEA data[35-41], and 1670 synthetic samples generated based on CTGAN. This enriched dataset encompasses a wide range of features, including cross-sectional geometries, steel tube dimensions, and loading conditions.

(2) Model-Centric Strategy: A rigorous evaluation framework was established, wherein the initial 243 experimental data points were meticulously partitioned into training (70%) and testing (30%) subsets. Ten state-of-the-art machine learning algorithms were systematically employed for model training and subsequent performance assessment, with the selection of the optimal model being guided by metrics such as the coefficient of determination (R^2). Two model-centric approaches are employed to address overfitting. Firstly, a selection and subsequent substitution of distinct, well-established machine learning algorithms are undertaken, for evaluating their efficacy in extrapolating knowledge from the training samples to unseen data. Secondly, the impact of varying input feature subsets on overfitting was then quantitatively assessed. The elimination of non-critical variables was aligned with the physical insights derived from traditional engineering models.

(3) Data-Centric Strategy: Leveraging the augmented dataset, two distinct strategies (CTGAN- and FEA) are devised to harness the potential of synthetic and FEA data. For these non-experimental data, there was two training strategies was applied, recorded as S1 and S2. For S1, the synthetic and FEA data are directly integrated for model training. In contrast, S2 introduces a sample selection phase. Based on prediction errors, a selective filtering process is applied, the data with the lowest errors at different proportions was utilized for training resulting in datasets. These datasets are then utilized for surrogate model training, aimed at achieving a more robust and generalized model with reduced overfitting tendencies.

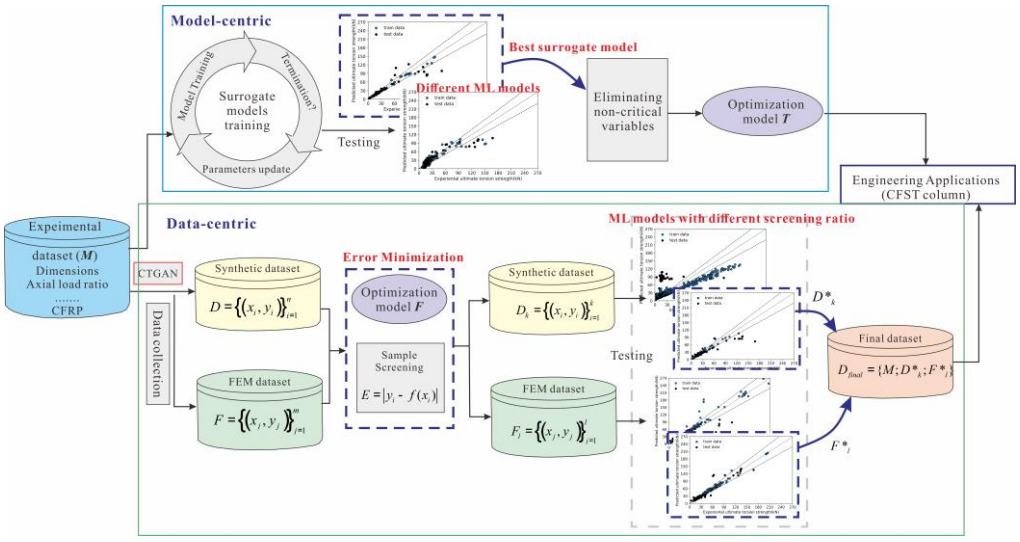

Fig. 1 Workflow to mitigate overfitting in ML prediction model

3. Evaluating model-centric strategies for effective overfitting mitigation

3.1. Update surrogate models

3.1.1. Data collection

The comprehensive dataset employed in this research endeavor comprises 243 rigorously curated experimental data points. The feature parameters intricately woven into this dataset encompass crucial structural design elements alongside the various loading scenarios. These structural design parameters meticulously detail aspects such as cross-sectional shape, steel tube diameter (D), wall thickness (t), steel yield strength (f_y), concrete strength (f_c), longitudinal-bending-torsion ratio (M/T), and axial compression ratio. Table 1 offered a comprehensive statistical summary of the key parameters within the dataset.

3.1.2. Preliminary assessment of traditional ML models

Out of the 243 experimental samples, 167 data points were randomly selected to serve as the training set for the model, while the remaining 76 samples constituted the test set. This strategic partitioning ensures that the test set encapsulates a diverse range of data pertaining to CFST columns under various load combinations, encompassing compression, bending, and torsion. Drawing upon the experimental dataset comprising 243 unique sets of data, we embarked on an initial predictive analysis of the torsional capacity of CFST columns. This endeavor leveraged five well-established machine learning paradigms: Support Vector Regression (SVR), Decision Tree Regression, Random Forest Regression, Linear Regression, and Extreme Gradient Boosting (XGBoost). By establishing predictive models to each of these methodologies, we conducted a comparative analysis to evaluate the corresponding performance. Table 2 provided a comprehensive overview of the prediction results achieved by these models under their hyperparameters configurations.

Upon rigorous validation using 76 genuine experimental data points from the test set, which encompasses both bending-torsion and compression-bending-torsion scenarios, it becomes strikingly apparent that the linear regression model

falls short, demonstrating the intricate nonlinearity inherent in the torsional behavior of reinforced concrete columns under combined loading conditions. This underscores the inadequacy of simplistic linear approaches in capturing complex dynamics. In contrast, the decision tree regression model displays a pronounced overfitting tendency, achieving an impeccable fit with an R^2 of 0.99 on the training dataset, accompanied by remarkably high RMSE, MAE, and MAPE values. However, as Fig. 2 illustrates, this training performance is mirrored by a dramatic deterioration in accuracy and predictive power on the test set, with an MAPE of 43.77%, reflecting a staggering 42.71% drop from its training performance. This phenomenon underscores the model's susceptibility to overfitting noise and nuances within the training data.

Among the myriad of evaluated models, XGBoost emerges as the best performance model, surpassing Adaboost, RF, Linear Regression, and SVM in terms of predictive accuracy. This is due to XGBoost capture the intricacies of the torsional capacity of reinforced concrete columns under pure torsion and compression-torsion loading, a testament to the adequacy of the training samples.

Despite the commendable performance of all five models in predicting structural bearing capacity, as evidenced by their respective performance metrics evaluated on the test set. However, Fig.2 prominently reveals a proportion of samples exhibiting errors exceeding the 15% threshold. This observation underscores the models' struggle to adequately capture specific subsets of data, indicating a limitation in their ability to generalize. The outliers with substantial errors were identified as originating from experimental data pertaining to CFST columns subjected the combined loading of bending and torsion. Even for the model XGBoost, encounters significant challenges when confronted with the 67 test samples encompassing bending-torsion and compression-bending-torsion. This indicated that the models encounter difficulties in learning the intricate and complex interplay between compression, bending and torsion, with a limited availability of bending-torsion experimental data for CFST columns. In other words, the models exhibited pronounced signs of overfitting when confronted with bending-torsion samples, highlighting the need for further refinement and augmentation of the training dataset to better encompass these challenging loading conditions.

Table 1
Statistical information of parameters included 243 experimental data

Variable	Count	Mean	Std	Min	25%	50%	75%	Max
Sectional Shape	243	0.71	0.46	0	0	1	1	1
Loading method	243	0.74	0.43	0	1	1	1	1
M/T ratio	243	0.31	0.80	0	0	0	0	4
Axial force rate	243	0.23	0.30	0	0	0	0.3	0.85
Aspect ratio	243	7.23	4.85	1.29	3.00	4	7	20
Wall thickness of steel tube	243	3.40	1.42	1.6	2.1	3.5	4.5	6.5
Yield strength of steel	243	355.3	68.21	242.3	312.8	342.41	397.35	466
Concrete strength	243	32.84	0.10	17.15	24.15	33.10	38.62	54.20
Diameter of steel tube	243	134.4	34.21	90	114	120	160	230
CFRP transverse layers	243	0.57	0.86	0	0	0	0	6
CFRP longitudinal layers	243	0.32	0.68	0	0	0	0	3
Ultimate torsion strength	243	32.86	30.85	3.32	16.8	21.34	28.15	173.5

Table 2
Performance measures for the machine learning models

Regression models	Sets	R^2	RMSE(KN)	MAE(KN)	MAPE(%)
Random forest	Test	0.78	17.95	5.25	13.96
	Train	0.99	1.08	0.78	3.97
AdaBoost	Test	0.75	19.85	8.78	13.89
	Train	0.99	0.83	0.40	1.90
XGboost	Test	0.81	16.92	7.60	12.37
	Train	0.98	3.17	1.51	5.05
SVM	Test	0.76	18.95	10.08	26.87
	Train	0.97	4.94	3.93	26.16
LinearRegression	Test	0.81	16.65	10.08	36.07
	Train	0.74	12.80	8.54	42.88

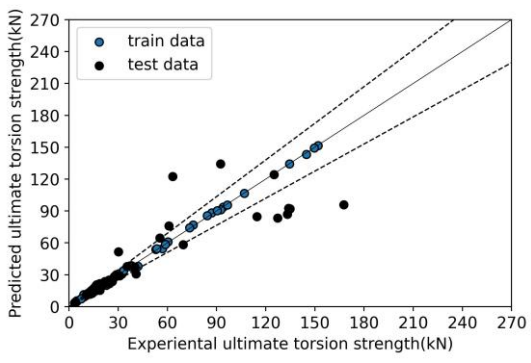

(a) Random forest

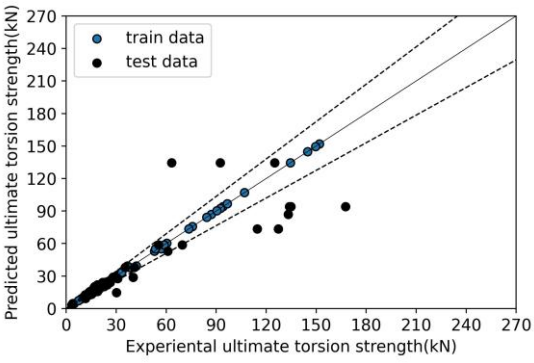

(b) AdaBoost

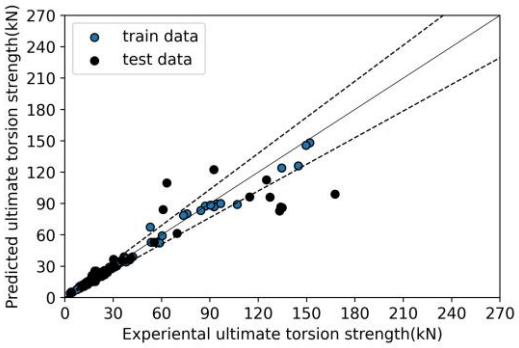

(c) XGboost

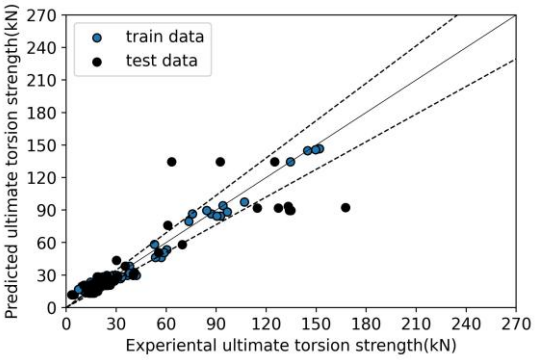

(d) SVM

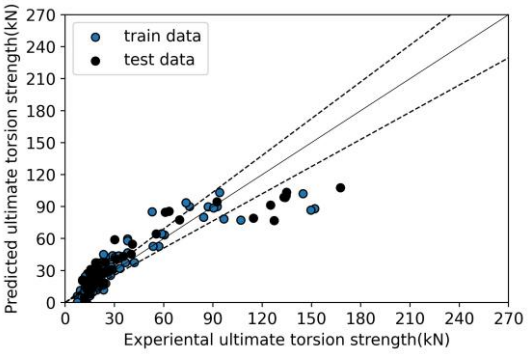

(e) Linear Regression

Fig. 2 Predicted performance of the machine learning models

3.2. Eliminating non-critical variables

To further explore the potential of mitigating overfitting by reducing model inputs, we implemented a strategy of eliminating non-critical variables. This involved the removal of variables deemed less significant, such as cross-section form and loading method. Table 3 provides a direct comparison of the model's performance under varying numbers of excluded input variables[41]. Based on the 11 characteristic parameters in Table 1, delete the CFRP longitudinal layers, CFRP transverse layers, and loading method in sequence, corresponding to the 10, 9, and 8 characteristic parameters input in Table 3, respectively[41]. Although the removal of non-essential variables exhibited an alleviation of overfitting issues compared to the contrast model with all inputs included, the effect was not pronounced. We concluded that solely optimizing the model, through strategies such as change machine learning models or eliminating non-important variables, proves insufficient to effectively and significantly reduce the model's overfitting problem.

Consequently, we shift our focus from the model itself to the data dimension, intending to adopt a data-centric approach. We aim to achieve fundamental improvements in addressing the model's overfitting phenomenon.

Table 3
Performance measures by reducing model input parameters

Regression models	Sets	R^2	RMSE(KN)	MAE(KN)	MAPE(%)
11	Test	0.81	16.92	7.60	12.37
	Train	0.98	3.17	1.51	5.05
10	Test	0.82	19.85	8.78	11.98
	Train	0.99	2.83	1.42	4.55
9	Test	0.82	16.36	7.60	12.64
	Train	0.99	3.26	1.60	5.10
8	Test	0.83	15.82	7.21	11.91
	Train	0.99	2.88	1.45	4.67

4. Evaluating data-centric strategies for effective overfitting mitigation

4.1. CTGAN-based synthetic data strategy

4.1.1. Establishment of CTGAN

This paper aimed to explore the potential of the non-experimental data in enhancing the availability and quality of data for analysis and modeling, for enhancing prediction accuracy for torsional tests on reinforced concrete columns. The dataset comprises 167 experimental samples meticulously curated from published literature, ensuring the absence of any missing values. It should be noted that, in order to avoid data leakage in the model test set, the generated data based on CTGAN for training the model must only come from the training data. The records are comprehensive, encompassing well-documented information on cross-sectional dimensions, concrete strength, and reinforcement configurations. Utilizing parameters such as concrete strength, steel yield strength, and cross-sectional dimensions as inputs, and the ultimate torsional capacity of reinforced concrete columns as the output, we aim to establish a machine learning model. This approach facilitates the development of predictive capabilities grounded in a robust and comprehensive dataset. To address the potential overfitting issue in machine learning models for predicting the torsional capacity of reinforced concrete columns, arising from data scarcity, we employed the CTGAN methodology to generate 1670 synthetic samples at a ratio of 1:10.

In the pursuit of validating the hypothesis that incorporating additional data, be it synthetic or derived from finite element simulations, into the training process can elevate model performance, it is imperative to emphasize that for all experiments conducted in this study, the test set exclusively comprises authentic experimental data. The selection of model parameters has a significant impact on model performance. In this study, hyperparameter optimization was conducted using the grid search method to identify the optimal parameter combination. Grid search systematically examines all possible combinations of user-defined hyperparameters and selects the configuration that yields the best validation performance. To ensure the reliability of the model and address potential overfitting, external validation was performed using a K-fold cross-validation strategy[42]. In this method, the dataset is divided into K equally sized subsets. In our study, K was set to 10, corresponding to 10-fold cross-validation, as illustrated in Fig. 4.

Table 4 presented the hyperparameter configurations employed for the CTGAN model in this study. CTGAN utilizes fully connected multilayer perceptrons (MLPs) for both the generator and discriminator, consistent with the original architecture proposed by Xu et al [43]. Fig. 3 showed the network structure of CTGAN. The CTGAN model was trained on an Intel i7-13700K CPU (16 cores, 24 threads). Training for 1,000 epochs with a batch size of 16 took approximately 20 minutes, indicating a relatively efficient computation process even without GPU acceleration.

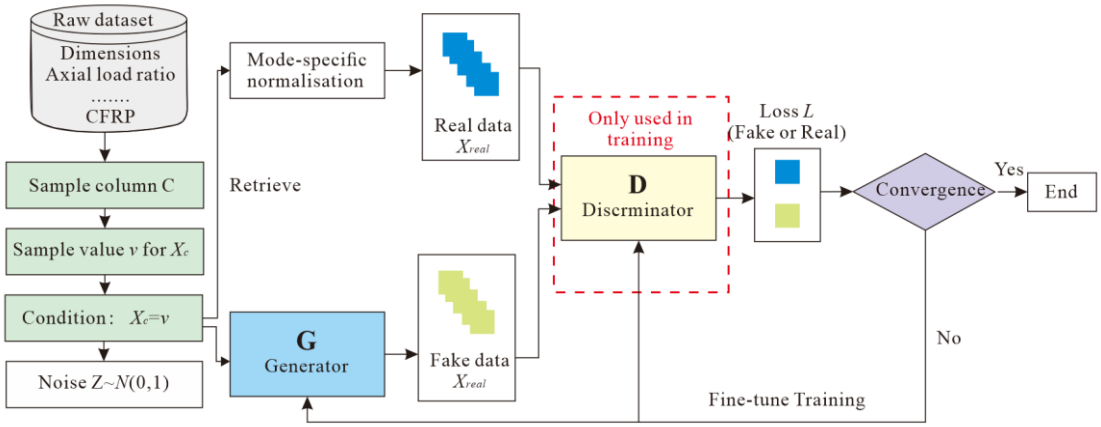

Fig. 3 CTGAN Network Structure

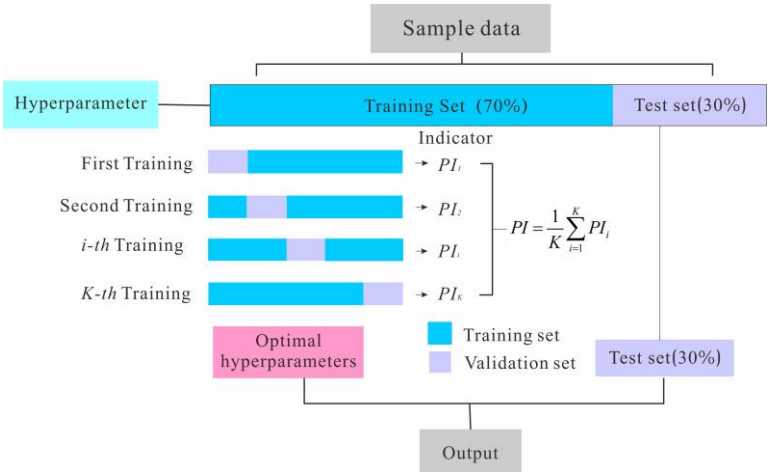

Fig. 4 10-fold cross-validation

Table 4
CTGAN model hyper-parameters settings

Hyper-parameters	Set Value
RNN cell's units in generator	400
Fully connected layer in generator	100
Layers in discriminator	2
Number of units per layer in discriminator	200
Optimizer	Adam
Learning rate	0.001

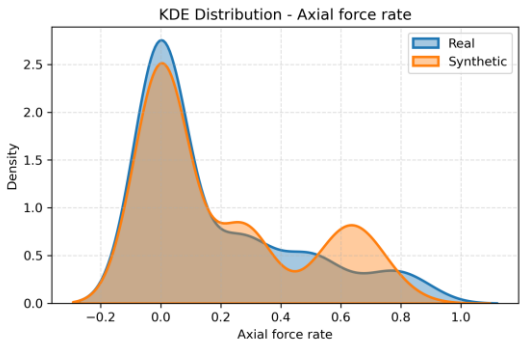

(a) Axial force rate

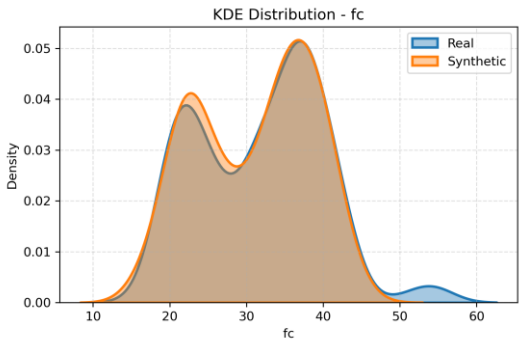

(b) Concrete strength

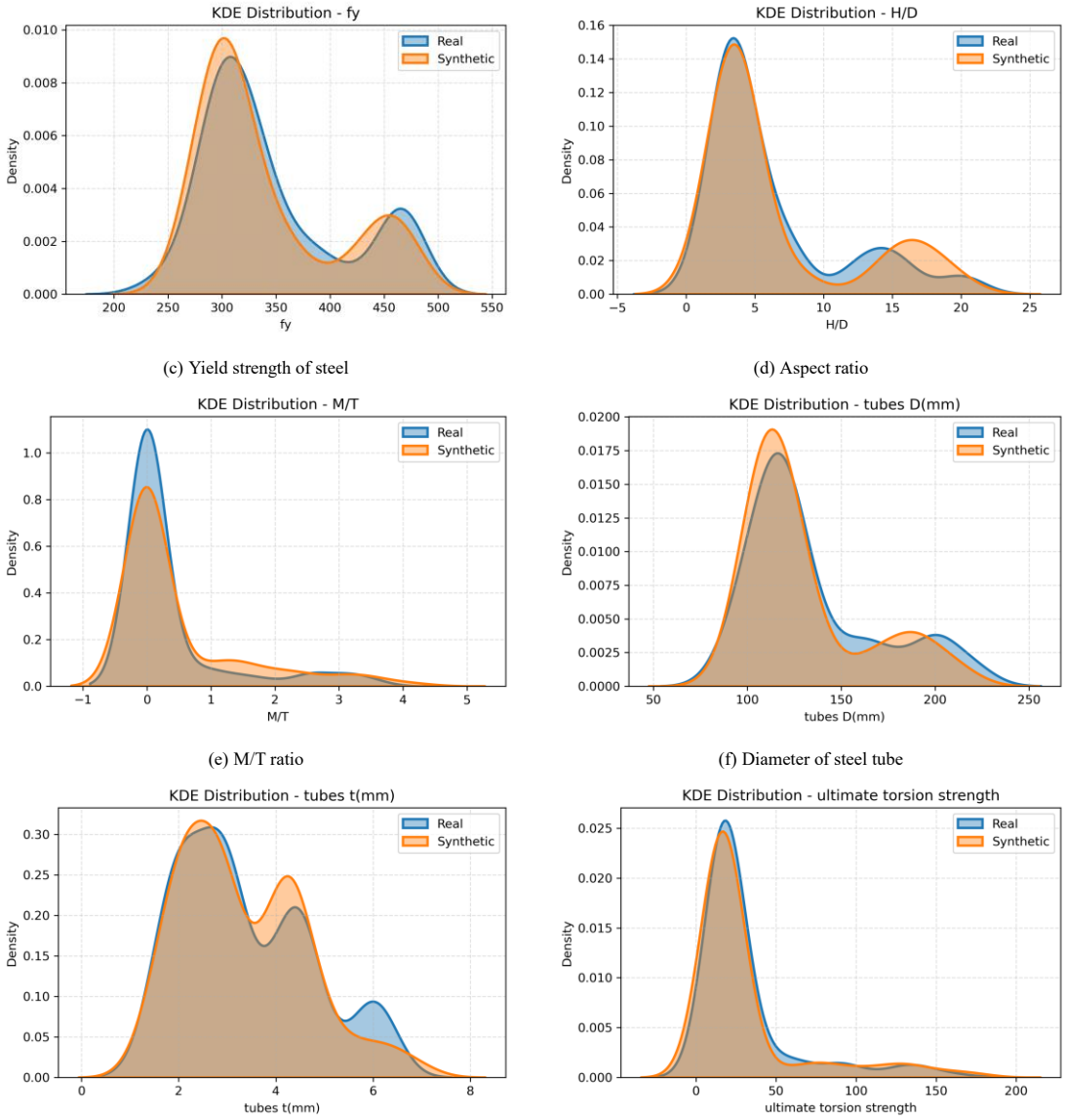

(c) Yield strength of steel

(d) Aspect ratio

(e) M/T ratio

(f) Diameter of steel tube

(g) Wall thickness of steel tube

(h) Ultimate torsion strength

Fig. 5 Comparison of Synthetic and Real Data Distributions for Key Structural Parameters (KDE Analysis)

To evaluate the quality of the synthetic dataset generated by CTGAN, a kernel density estimation (KDE)-based comparison was carried out between the synthetic and experimental datasets. Several key structural parameters, such as concrete compressive strength, steel yield strength, and aspect ratio, were selected for distributional analysis. As shown in Fig. 5, the marginal distributions of these parameters demonstrate close agreement between the two datasets. These results suggest that the synthetic data can effectively replicate the statistical characteristics of the original experimental samples, thereby validating their representativeness for subsequent structural performance modeling.

4.1.2. Establishment of CTGAN-based synthetic data training strategy

Table 5 illustrated the predictive performance of the ML model trained directly on the entire dataset. However, due to the inherent instability of the generative model, employing the entire sample set (100%) directly for training has resulted in significant bias within the model, ultimately leading to the failure of the training process.

Addressing the issue of model performance collapse caused by directly utilizing vast amounts of synthetic data for training, this study introduces a simple sample screening strategy. The core of the strategy is quantifies the error between predictions generated by a machine learning model, specifically XGBoost (due to its demonstrated superiority in predicting the torsional behavior of CFST columns in this research), and the labels of synthetic data produced by a CTGAN. Subsequently, a subset of samples with the smallest errors is selected for model training.

The error minimization-based sample screening strategy is as follows:

1. Initialization and Model Construction Framework: This study initiates by setting a series of key parameters. Utilizing a comprehensive dataset of CFST columns sets (*M*), XGBoost is chosen to obtain an initial predictive ML model (*F*) through preliminary training.

2. Data Preprocessing and GAN Sample Generation: Following data preprocessing to ensure quality, GAN model parameters are configured, and the number of generated samples is specified. The trained GAN model $G(x)$ then produces a synthetic dataset $D = \{(x_i, y_i)\}_{i=1}^{n}$, where n is the total number of generated samples.

3. Error Evaluation and Sample Ranking: Each synthetic sample is fed into the preliminary predictive model T to obtain a predicted value $f(x_i)$, considered a pseudo-truth in this context. The error between the value y_i and the value $f(x_i)$ is calculated, serving as a critical metric for assessing sample quality. All synthetic samples are then ranked based on their error, ensuring that samples with the smallest errors are prioritized.

4. Sample Screening Based on Error Minimization: Building upon the ranking, a proportional screening strategy is implemented, selecting the k% samples with the smallest errors to form a new training set $D_k = \{(x_i, y_i)\}_{i=1}^{k}$, where $k \in [0,100]$.

4.1.3. Analysis of CTGAN-based synthetic data training strategy

In pursuit of enhancing model performance, we embarked on an experiment involving a sample selection strategy applied to synthetic data. Specially, the prediction errors of synthetic samples against their true counterparts were calculated,

The top of 10%, 25%, 50%, and 70% data with the lowest errors was categorized and retained resulting in datasets,and subsequent utilized for model

training respectively, shown in Fig. 6. As shown in Table 5, an intriguing trend emerged: as the proportion of retained samples increased, the model exhibited a gradual amplification of bias. Comparative analysis with models trained solely on experimental data revealed a decline in accuracy, marked by a 10.71% reduction in R^2, highlighting the challenges posed by synthetic data. This behavior indicated that while the generative model effectively captures intricate bending-torsion relationships among samples, its inherent instability leads to the generation of samples with significant errors, which subsequently contribute to model bias.

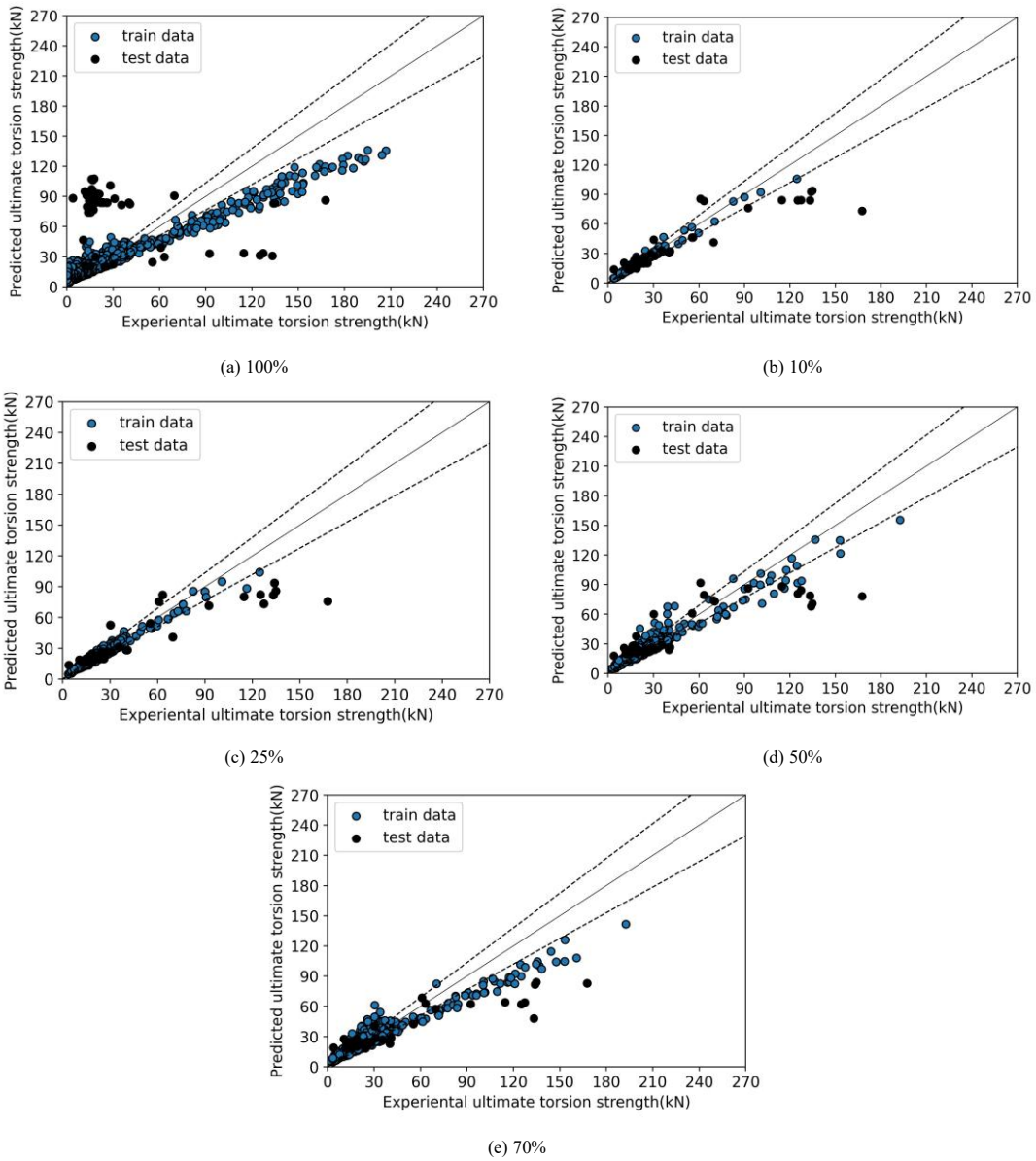

(a) 100%

(b) 10%

(c) 25%

(d) 50%

(e) 70%

Fig. 6 Predicted performance for CTGAN-based synthetic data training strategy

Table 5
Performance measures for CTGAN-based synthetic data training strategy

Regression models	Sets	R^2	RMSE(KN)	MAE(KN)	MAPE(%)
100%	Test	None	63.81	59.59	None
	Train	0.64	9.87	5.64	69.91
10%	Test	0.75	19.29	10.12	24.98
	Train	0.97	2.16	1.13	5.58
25%	Test	0.73	20.01	11.02	28.76
	Train	0.95	2.42	1.52	7.98
50%	Test	0.62	23.87	14.73	41.39
	Train	0.78	6.11	3.61	19.12
70%	Test	0.67	18.68	9.34	43.93
	Train	0.90	4.40	2.67	14.32

4.2. Analysis of FEA-based data training strategy

To mitigate these issues, the similar investigation was extended to FEA data. FEA data used in this paper was shown in Table 6. As shown in Fig. 7, when the entire set of FEA data was used for ML model training, an notable improvement in accuracy was achieved. The test set accuracy of 0.55 surpassed that of models trained solely on entire synthetic dataset. Similar FEA-data screening was conducted as mentioned in the error minimization-based sample screening strategy. Upon further scrutinizing the impact of sample selection based on error thresholds, we discovered that retaining simulation samples with errors below 70% achieved the highest model accuracy. When subjected to validation with genuine experimental data, both models trained exclusively on generated data and those utilizing FEA data exhibit a certain level of precision. Nevertheless, a discernible yet consistent gap in performance is observed when compared to models that are trained directly on experimental data. This phenomenon can be attributed to two pivotal factors: (1) the inherent bias in the synthetic data generation model, creating a non-negligible gap between the synthetic and authentic experimental data; (2) the complexity of material constitutive properties and limitations in model solution strategies, collectively impacting the stability of FE simulations, potentially introducing non-physical errors. Additionally, the potential erroneous information embedded within low-quality or non-standard experimental data undoubtedly exacerbates the risk of model overfitting, thereby reducing predictive accuracy.

Table 6
Statistical information of parameters included 561 FEM-based synthetic data

Variable	Count	Mean	Std	Min	25%	50%	75%	Max
Sectional Shape	561	0.96	0.17	0.00	1.00	1.00	1.00	1.00
Loading method	561	0.94	0.15	0.00	1.00	1.00	1.00	1.00
M/T ratio	561	0.70	1.49	0.00	0.00	0.00	1.03	10.25
Axial force rate	561	0.07	0.17	0.00	0.00	0.00	0.00	0.85
Aspect ratio	561	4.01	3.04	0.19	3.00	4.00	4.00	27.00
Wall thickness of steel tube	561	4.31	3.92	1.00	2.40	3.00	5.00	40.00
Yield strength of steel	561	306.1	56.11	234.00	229.00	335.0	345.0	420.0
Concrete strength	561	45.18	14.02	30.00	36.80	36.80	50.00	90.00
Diameter of steel tube	561	190.2	80.11	100.00	120.00	200.0	200.0	400.0
CFRP transverse layers	561	0.87	1.31	0.00	0.00	0.00	2.00	6.00
CFRP longitudinal layers	561	0.18	0.60	0.00	0.00	0.00	0.00	6.00

Table 7
Performance measures for FEM-based data training strategy

Regression models	Sets	R^2	RMSE(KN)	MAE(KN)	MAPE(%)
100%	Test	0.55	25.93	13.20	29.80
	Train	0.99	21.71	6.03	5.65
10%	Test	0.54	26.19	14.49	42.60
	Train	0.99	1.39	0.72	2.53
25%	Test	0.63	23.53	11.41	26.73
	Train	0.99	1.23	0.60	1.80
50%	Test	0.54	26.31	12.54	26.67
	Train	0.99	2.18	1.21	3.80
70%	Test	0.90	11.89	6.42	23.86
	Train	0.99	2.59	1.46	4.43
80%	Test	0.59	24.86	12.65	28.84
	Train	0.99	3.05	1.62	4.80

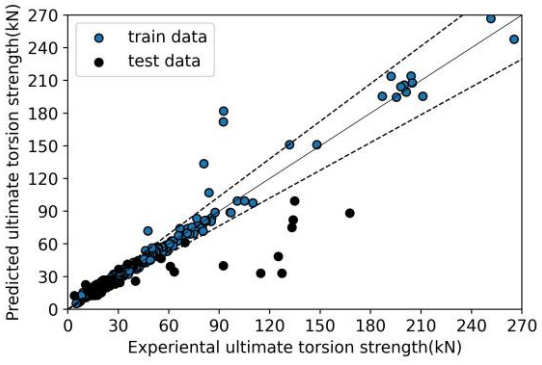

(a) 100%

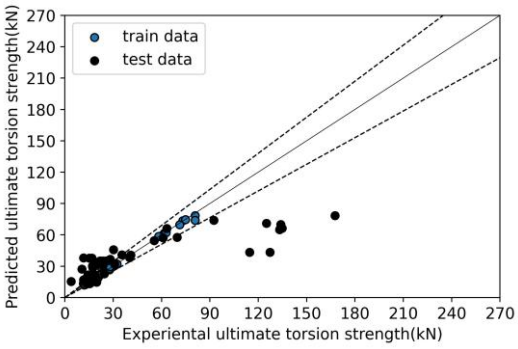

(b) 10%

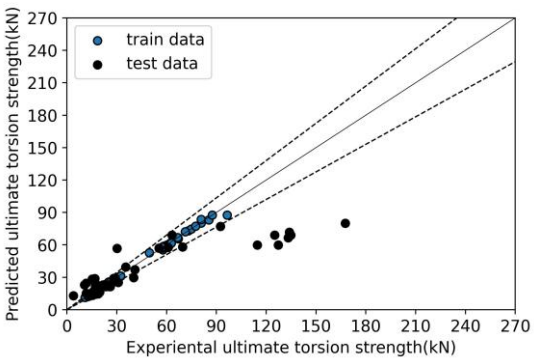

(c) 25%

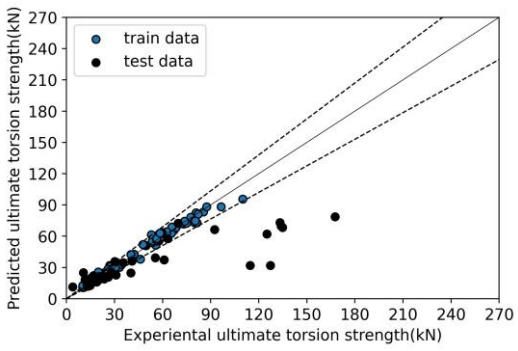

(d) 50%

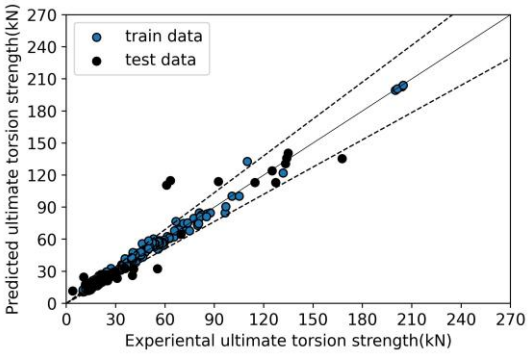

(e) 70%

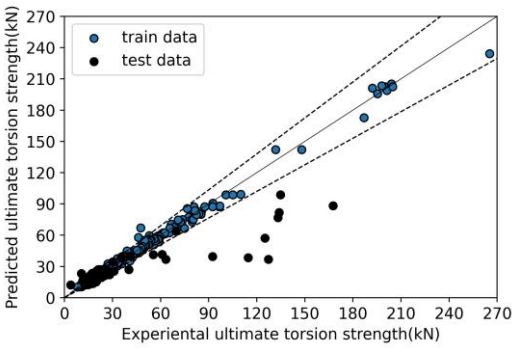

(f) 80%

Fig. 7 Predicted performance for FEM-based data training strategy

4.3. A optimal data-centric strategy to mitigate overfitting in ML models

This section aimed to propose an no-real sample screening strategy that aims to effectively mitigate model overfitting through data-centric preprocessing approaches. Specifically, the XGBoost model trained by the model-centric training strategy due to its exceptional performance was selected as the foundation for our research. Six comparative experimental setups were devised based on the above mentioned analysis results: *Experiment 1*, only the top 10% synthetic data with the lowest errors was utilized for training; *Experiment 2*, the top 70% FEM data with the lowest errors was utilized for training; *Experiment 3*, wherein only experimental data was utilized for training; *Experiment 4*, where a blend of experimental data and the top 10% synthetic data with the lowest errors was utilized for training; *Experiment 5*, where a blend of the top of 70% FEM data with the lowest errors and experimental data was utilized for training, and *Experiment 6*, a blend of experimental data, the top 10% synthetic data with the lowest errors , and the top 70% FEM data with lowest errors was utilized for training.

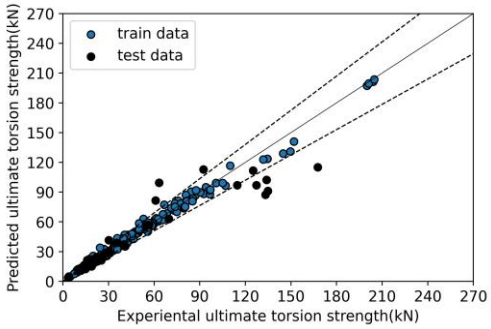

(a) 70% FEM data and test data

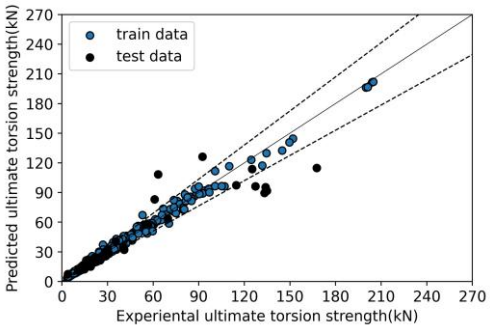

(b) 70% FEM data, 10% GAN-data, and test data

Fig. 8 Comparison of predicted performance of different training strategies

Table 8
Performance measures for data-centric training strategies

Experiment	Training data	Sets	R^2	RMSE(kN)	MAE(kN)	MAPE(%)
Experiment 1	10% GAN-data	Test	0.75	19.29	10.12	24.98
		Train	0.97	2.16	1.13	5.58
Experiment 2	70% FEM-data	Test	0.90	11.89	6.42	23.86
		Train	0.99	2.59	1.46	4.43
Experiment 3	Test data	Test	0.83	15.82	7.21	11.91
		Train	0.99	2.88	1.45	4.67
Experiment 4	10% GAN-data+Test data	Test	0.84	18.73	8.01	17.24
		Train	0.99	2.94	1.71	5.15
Experiment 5	**70% FEM-data+Test data**	**Test**	**0.88**	**16.93**	**7.59**	**12.39**
		Train	**0.99**	**2.55**	**1.42**	**4.46**
Experiment 6	70%FEM-data+10%GAN-data+Test data	Test	0.85	14.93	7.07	12.92
		Train	0.99	2.19	1.25	4.63

The performance metrics and validity assessments for *Experiments 1-6* are presented in Table 8. It can be found that, compared with the accuracy to those based exclusively on experimental data of R^2=0.83, the accuracy of the model solely relying on either the top 10% synthetic data with the lowest errors or the 70% FEM data with the lowest errors were 0.75 and 0.90, respectively. However, an enlargement in the RMSE, MAE(kN), and MAPE is observed for the former two experiments when evaluated on the test set.

Furthermore, when the experimental data was introduced to the synthetic or FEM data for model training (as demonstrated in *Experiments 4 and 5*), the accuracy of model with 10% GAN-based data and experimental data increased from 0.75 to 0.84, and there is a marginal decline in the aforementioned error metrics on the test set. The improvement in R^2 signifies an enhancement in the

model's stability and robustness, indicating that the integration of diverse data sources can lead to more resilient predictive models. This can be attributed to the fact that while synthetic data successfully captures the statistical features of real data, its generation relies solely on the currently available physical experiments, which inherently suffer from uneven distributions of certain parameters. Consequently, incorporating synthetic data into training, when directly compared to using solely physical experiments, naturally leads to a slight decrease in test set accuracy, as the synthetic data merely approximates the real data distribution rather than fully capturing its intricacies. CTGAN emerges as an effective approach for generating synthetic data for heterogeneous features and structured tabular datasets; however, it is not without limitations.

Fig. 8 given the prediction performance of the *Experiment 5* and *Experiment 6*. Upon conducting *Experiment 6*, involved integrating all three data sources, i.e., synthetic data, experimental data, and FEA data, as training samples. Specifically, the inclusion of the synthetic data led to a decline in model accuracy compared to *Experiment 5*, and MAPE also exhibited a moderate increased. The minor decline in model performance upon incorporating synthetic data can be attributed to several factors: CTGAN faces challenges in processing high-dimensional features, as the model struggles to learn and generate a large number of unique categories. Additionally, skewed distributions or distributions with a significant proportion of constant values (e.g., a preponderance of zeros in bending-to-torsion and axial compression ratios observed in this study) are difficult for the GAN architecture to capture. For small datasets, synthesis data may be less precise, as CTGAN, like any other deep learning model, thrives on substantial volumes of data. It is important to emphasize that the judicious selection and integration of FEA data with experimental data presents a viable strategy to mitigate the issue of overfitting in predictive models.

5. Conclusion and further work

This study delves into the effectiveness of model-centric and data-centric training strategies in mitigating overfitting issues within ML models, particularly in the context of predicting the torsional capacity of CFST columns. The specific conclusions are articulated as follows:

Firstly, two model-centric strategies were devised: replacing various model and eliminating the input feature parameters. However, under limited sample conditions, these strategies exhibited limited success in mitigating overfitting, highlighting the challenges in achieving significant performance gains solely through model structural optimizations in small datasets.

Subsequently, introduced a data-centric training approach that integrates CTGAN-based synthetic data with FEA-based data, aiming to augment the limited experimental dataset. Notably, training solely on CTGAN-generated data led to model instability and eventual collapse, whereas utilizing FEM data alone sustained model operation but yielded a modest prediction accuracy of 0.55 on the test set.

To further enhance data quality and mitigate model biases stemming from inaccurate training data, a sample selection strategy grounded in the minimum error criterion was devised. This strategy selects synthetic and FEA data that reflect true physical behaviors and exhibit minimal prediction errors, thereby optimizing the datasets. Specifically, a hybrid training approach utilizing the top 70% of FEA samples with the lowest errors, in conjunction with experimental data, notably improved the model's prediction stability and generalization ability, underscoring the efficacy of this strategy in bolstering model robustness.

It is noteworthy that while this study primarily focuses on the efficacy of data-centric training strategies, a detailed exploration of the specific sample selection algorithm was not undertaken. Nevertheless, the proposed method of sample screening based on a minimum error ratio provides a valuable insight and framework for future research endeavoring to efficiently and precisely filter high-quality training samples in big data scenarios, with potential for further development and refinement.

Declaration of competing interest

The authors declare that there is no conflict of interest regarding the publication of this paper.

Author statement

Mingxia Dang: Conceptualization, Methodology, Formal Analysis, Writing-Original Draft; Mengxue Guo: Validation, Data Curation, Writing-Original Draft, Supervision, Funding Acquisition; Ying Li: Investigation; Hua Li: Funding Acquisition; Shilin Yang: Resources.

Acknowledgments

This work was supported financially by Natural Science Basic Research Program of Shaanxi Province [Grant No: 2025JC-YBQN-470], Special Scientific Research Program of the Shaanxi Provincial Department of Education [Grant No: 24JX0486], Shaanxi Provincial Department of Science and Technology Talent Program [Grant No: 2024ZC-KJXX-011], Youth Projects of Xi'an Jiaotong University City College [Grant No: 2025Q05] and Research and innovation team of Xi'an Jiaotong University City College: Green Ecological Empowerment and Urban Resilience Innovation Team [Grant No: 037010].

Data availability statement

All data, models, and code generated or used during the study appear in the published article.

Reference

[1] El-Dakhakhni, W. Data Analytics in Structural Engineering. Journal of Structural Engineering, 2021. 147(8): 02021001.
[2] Feng, D.C. Implementing ensemble learning methods to predict the shear strength of RC deep beams with/without web reinforcements. Engineering Structures, 2021. 235: 111979.
[3] Nguyen-Sy T. Predicting the compressive strength of concrete from its compositions and age using the extreme gradient boosting method. Construction and Building Materials, 2020. 260: 119757.
[4] Liu K.H., Xie T.Y., Cai Z.K., et al. Data-driven prediction and optimization of axial compressive strength for FRP-reinforced CFST columns using synthetic data augmentation[J]. Engineering Structures, 2024, 300.
[5] Rahal, K.N. Torsional strength of normal and high strength reinforced concrete beams [J]. Engineering Structures, 2013. 56: 2206-2216.
[6] Deifalla, A. Refining the torsion design of fibered concrete beams reinforced with FRP using multi-variable non-linear regression analysis for experimental results[J]. Engineering Structures, 2021. 226: 111394.
[7] Fiore A , Berardi L , Marano G C. Predicting torsional strength of RC beams by using Evolutionary Polynomial Regression[J].Advances in Engineering Software, 2012, 47(1).
[8] Kim C. Torsional Behavior Evaluation of Reinforced Concrete Beams Using Artificial Neural Network[J].Applied Sciences, 2021, 11.
[9] Zhang T.J., Wang D.L., Lu Y. A data-centric strategy to improve performance of automatic pavement defects detection. Automation in Construction, 2024, 160,105334.
[10] Guo M.X., Huang H., Zhang W., et al. Assessment of RC frame capacity subjected to a loss of corner column[J]. Journal of Structural Engineering, 2022, 148(9):0422122.
[11] Lai D.D., Demartino C., Xiao Y. Interpretable machine-learning models for maximum displacements of RC beams under impact loading predictions[J]. Engineering Structures, 2023,281.
[12] Zakieh A., Hadi G., Amin S., et al. DCServCG: A data-centric sevice code generation using deep learning[J]. Engineering Applications of Artificial Intelligence, 2023, 123,106304.
[13] Sung S.H., Suh J.M., Hwang Y.J., et al. Data-centric arttificial olfactory system based on the eigengraph[J]. Nature Communications, 2024,15:1211.
[14] Li M., Jia G. Multifidelity Gaussian Process Model Integrating Low- and High-Fidelity Data Considering Censoring[J].Journal of Structural Engineering, 2020(3):146.
[15] Luo H. and Paal S.G. Reducing the effect of sample bias for small data sets with double weighted support vector transfer regression. Computer Aided Civil and Infrastructure Engineering, 2021. 36(3): p. 248-263.
[16] Marani A , Nehdi M L .Predicting shear strength of FRP-reinforced concrete beams using novel synthetic data driven deep learning[J].Engineering structures, 2022(Apr.15):257.
[17] Fu B.C., Gao Y.Q., and Wang W. Dual generative adversarial networks for automated component layout design of steel frame-brace structures[J]. Automation in Construction, 2022,146.
[18] Almustafa M.K., Nehdi M.L. Machine learning prediction of structural response for FEP retorfitted RC slabs subjected to blast loading[J]. Engineering Structures, 2021, 244.
[19] Song Z.M., Zhang C., and Lu Y.Y. The methodology for evaluating the fire resistance performance of concrete-filled steel tube columns by integrating conditional tabular generative adversarial networks and random oversampling[J]. Journal of Building Engineering, 2024,97.
[20] Zeng S.H., Wang X., Hua L.Q., et al. Prediction of compressive strength of FRP-confined concrete using machine learning: A novel synthetic data driven framework[J]. Journal of Building Engineering, 2024,94.
[21] Goodfellow, I., Pouget-Abadie, J., Mirza, M., et al. Generative adversarial nets[J],2014. arXiv preprint arXiv:1406.2661.
[22] Beck, J. and O. Kiyomiya. Fundemental pure torsional properties of concrete filled circular steel tubes. Doboku Gakkai Ronbunshu, 2003. 2003(739): 285-296.
[23] Han, L.H., G.-H. Yao, Z. Tao. Performance of concrete-filled thin-walled steel tubes under pure torsion. Thin-Walled Structures, 2007. 45(1): 24-36.
[24] Wang, Y.-H., G.-B. Lu, X.-H. Zhou, Experimental study of the cyclic behavior of concrete-filled double skin steel tube columns subjected to pure torsion. Thin-walled Structures, 2018. 122: 425-438.
[25] Chen, J., W.L. Jin, J. Fu, Experimental investigation of thin-walled centrifugal concrete-filled steel tubes under torsion. Thin-walled structures, 2008. 46(10): 1087-1093.
[26] Nie, X. Ultimate torsional capacity of steel tube confined reinforced concrete columns. Journal of Constructional Steel Research, 2019. 160: 207-222.
[27] Wang, Y.-H. Torsional capacity of concrete-filled steel tube columns circumferentially confined by CFRP. Journal of Constructional Steel Research, 2020. 175: 106320.
[28] Wang Y.H., Guo Y.F., Liu J.P., et al. Experimental study on behavior of concrete filled steel tube columns under torsion and eccentric compression[J]. China Civil Engineering Journal, 2017,50(7):51-61.
[29] Nie J.G., Wang Y.H., Fan J.S. Experimental study on concrete filled steel tubular columns under combined compression, flexure and torsion[J]. Journal of Building Structures, 2012,33(9):1-11.
[30] Wang Y.H., Nie J.G., Fan J.S. Study on the torsion behavior of concrete filled steel tube column with circular section[J]. Engineering Mechanics, 2014,31(3):222-227.

[31] Wang Y.H., Nie J.G., Fan J.S. Cross sectional shear strain disrtibution of rectangular concrete filled steel tubu columns subjected to torsion[J]. Engineering Mechanics, 2014,31(5):101-119.
[32] Wang Y.H., Li S., Zhou X.H., et al. Study on mechanical behavior of concrete filled steel tubular short columns under compound bending-shear-torsion load[J]. Journal of Building Structures, 2017, 38(11):1-12.
[33] Wang Q.L., Ling Z.N., Chen D. Experimental study on torsional behavior of concrete filled CFRP-steel tube with square cross-section [J]. Journal of Building Structures, 2017, 38,S1:478-484.
[34] Jamalpour R. and Hossain K.M.A. Torsion and Combined Torsion-Axial Load Behaviour of Concrete Filled Steel Tube Columns with and without ECC/CFRP Wrap[J]. Journal of Earthquake Engineering, 2024.
[35] Wang Q L, Peng K, Shao Y B. Research on Mechanical Properties of CFRP Confined Concrete-Filled SquareSteel Tubular Under Bending-Torsion Load[J]. Acta Materiae Compositae Sinica,2022, 39(11): 5557–5573.
[36] Wang YH., Wang Y Y., Zhou X H., et al. Coupled ultimate capacity of CFRP confined concrete-filled steel tube columns under compression-bending-torsion load[J]. Structures, 2021,31:558-575.
[37] Wang YH., Nie JG., and Fan JS. Theoretical model and investigation of concrete filled steel tube columns under axial force–torsion combined action[J]. Thin-Walled Structures, 2013,69:1-9.
[38] Nie X., Wang YH., and Li S., et al. Coupled bending-shear-torsion bearing capacity of concrete filled steel tube short columns[J].Thin-Walled Structures,2018,123:305-316.
[39] Yang ZC., Han LH., Zhao HY., et al. Performance of recycled aggregate concrete-filled high-strength steel tubular members under combined compression-bending-torsion[J].Engineering Structures,2025,335:120052.
[40] Zarringol M., Thai H.T. Prediction of the load-shortening curve of CFST columns using ANN-based models[J]. Journal of Buidling Engineering, 2022,51.
[41] Huang H., Xue C.L., Zhang W., et al. Torsion design of CFRP-CFST columns using a data-driven optimization approach[J]. Engineering Structures, 2022, 251:113479.
[42] Feng D.C., Wang W.J., Mangalathu S., et al. Implementing ensemble learning methods to predict the shear strength of RC deep beams with/without web reinforcements[J]. Engineering Structures,2021,235:111979.
[43] Xu L., Maria S., Alfredo C., et al. Modeling Tabular data using Conditional GAN[C]//Advances in Neural Information Processing Systems 32 (NIPS 2019) pre-proceedings, CA: NIPS, 2019.